UNIVERSITY OF LONDON THESIS

Degree PhD Year 2008 Name of Author SNELLER, Beatrix Irene

Artefacts in Longitudinal MRI of the Brain

Beatrix Irene Sneller

UCL

Submitted for the Degree of Doctor of Philosophy

2008

ProQuest LLC
789 East Eisenhower Parkway
P.O. Box 1346
Ann Arbor, MI 48106-1346

I, Beatrix Sneller, confirm that the work presented in this thesis is my own. Where information has been derived from other sources, I confirm that this has been indicated in the thesis.

Abstract

Many drugs are under development to treat Alzheimer's disease (AD), the prevalent cause of dementia. Cognitive tests are the established way of assessing drug efficacy. More sensitive, quantitative measures, biomarkers, are desirable for faster assessment of efficacy from smaller cohorts. AD is characterized by amyloid plaques, neurofibrillary tangles, neuronal cell death, memory deficits and brain volume loss detectable using longitudinal neuroMRI. This thesis focuses on acquisition artefacts which hinder the use of longitudinal structural MRI as an accurate, precise biomarker. It investigates change in artefact magnitude with field strength, prevalence of artefacts in clinical trials, influence of artefacts on quantification of atrophy, and correction of carotid flow artefacts.

A prospective study was used to quantitatively compare pulsatile flow artefact on images from a 3T scanner with those from a standard clinical 1.5T scanner. The artefact was significantly worse at the higher field strength ($p<0.01$).

In images from 837 clinical trial subjects, contrast issues, motion, and temporal lobe (occurring in up to 41% of scans) were the prevalent artefacts. The temporal lobe, particularly important in AD research, was affected predominantly by pulsatile flow artefact (60-70% of temporal lobe artefacts). Moving trials to higher field strengths may significantly increase these artefacts' occurrence.

I investigated the effects of artefact on computerized brain atrophy measurement techniques: the Boundary Shift Integral (BSI) and SIENA. I developed methods of simulating various types and severities of motion and pulsatile flow artefacts. Images simulated with known atrophy and artefacts were used to test the techniques. Rotational motion $\geq 3°$ at follow-up can result in apparent atrophy, of the order of AD relative to normal annual ageing, (1.5%), using SIENA. Increasing motion decreases measured atrophy using BSI: $\geq 3°$ can obscure atrophy of 1.5%.

An algorithm to remove pulsatile artefact was devised, implemented and tested on scans with simulated artefacts.

Acknowledgements

I would like to acknowledge the support and help of my supervisor, Derek Hill, without whom the work in this thesis would not have been possible. I would also like to acknowledge Nick Fox and all at the DRC for their help providing invaluable insight into the clinical aspects of neuroimaging. Particular thanks are due to Ellen Garde for her encouragement and support, and to Richard Boyes for his collaboration. I would like to acknowledge the help and support of Pablo Irrarazaval and the kindness he and his entire department showed me in warmly welcoming me over to Chile for a month. Thanks also to my second supervisor David Hawkes for offering advice on the thesis. Thanks are also due to Jo Hajnal, Alex Dresner, Rolf Heckemann, David Atkinson, Philip Batchelor, Oscar Camara, David Cash, Mark White and Ged Ridgeway for their helpful comments and discussions. I would like to thank everyone else at Guy's hospital and at CMIC, UCL who supported and encouraged me through this PhD. Particular thanks to Marc Miquel, Vivek Muthurangu, Nick Noble, Reda Boubertakh, Adam Chandler, Tim Carter, Jamie McClelland and Segolene Tarte. Many thanks are due to my friends and family for their incredibly patient support and prayers. I would like to acknowledge the encouragement to embark on a PhD provided by my father, who passed on to a better place during my studies, and to thank him for the unforgettable confidence he had in me. Finally, I acknowledge and thank Jesus for every ability, strength and incredible comfort He has given me during my PhD.

Table of contents

Abstract **3**
Acknowledgements **4**
Table of contents **5**
List of figures **8**
List of tables **10**
List of equations **11**
Table of abbreviations **11**
1 Introduction **13**
1.1 Motivation 13
1.1.1 Clinical background of Alzheimer's disease 13
1.1.2 Detection of structural brain change from MRI 14
1.1.3 Clinical dementia trials using longitudinal MRI 15
1.1.4 Influence of artefacts on clinical neuroimaging trials 17
1.2 Aims 17
1.3 Thesis overview 18
2 Background to MR neuroimaging **20**
2.1 Introduction to MRI 20
2.2 Magnetisation and spatial localisation 21
2.2.1 Magnetic field strength 21
2.2.2 Spatial localization 22
2.3 K-space 26
2.3.1 What is k-space? 26
2.3.2 Field of view 27
2.3.3 Rectangular field of view and parallel imaging 27
2.3.4 Resolution 27
2.3.5 Voxel size 28
2.3.6 Slow phase encode direction 28
2.3.7 Multiple 3D k-spaces for a single image 29
2.4 Different types of RF coils 29
2.4.1 Transmit coils 29
2.4.2 Receiver head coils 29
2.5 2D and 3D scans 30
2.6 Contrast mechanisms: T1 and T2-weighted images 31
2.6.1 Tissue contrasts 31
2.6.2 Uses of different contrasts 31
2.6.3 MR signal decay 32
2.6.4 T1-weighted images 32
2.6.5 T2-weighted images 33
2.7 MRI pulse sequences 33
2.7.1 Spin Echo 33
2.7.2 Gradient Echo 34
2.7.3 FLASH/SPGR 35
2.7.4 MP-RAGE 36
2.7.5 3D Turbo Field Echo Sequence, used in Chapter 4 36
2.7.6 MDEFT 38
2.7.7 Comparison of MDEFT vs. TFE 40
2.8 Summary 40
3 Background to artefacts in MR neuroimaging **41**
3.1 Noise in MR images 41
3.2 Imaging equipment artefacts 42
3.2.1 Intensity inhomogeneities 42
3.2.2 Gradient miscalibration 43

3.3 Object dependent artefacts 44
3.3.1 Bulk motion 44
3.3.2 Susceptibility artefact 44
3.3.3 Chemical shift artefact 44
3.3.4 Wrap around 45
3.3.5 Pulsatile motion/Flow artefact 45
3.3.6 Acquisition methods of reducing pulsatile flow artefact 48
3.4 Summary 51
4 Artefacts in longitudinal images at different field strengths 52
4.1 Introduction 52
4.1.1 Aims 53
4.1.2 Contribution 53
4.2 Literature review 54
4.2.1 Qualitative comparison of a variety of artefacts at 3T compared with 1.5T 54
4.2.2 Motion artefacts comparison 55
4.2.3 Chemical shift and susceptibility comparison 55
4.2.4 Intensity inhomogeneities comparison 55
4.2.5 Pulsatile flow artefacts comparison 56
4.3 Method 56
4.3.1 Image acquisition 56
4.3.2 Image analysis 57
4.4 Results 60
4.4.1 Quantitative analysis 60
4.4.2 Qualitative analysis 61
4.5 Discussion 62
4.6 Conclusion 63
5 Prevalence and automatic quantification of artefacts affecting longitudinal neuroimaging studies 64
5.1 Introduction 64
5.1.1 Aims 64
5.1.2 Contribution 64
5.2 Literature review 65
5.2.1 Literature on the frequency of artefacts in MRI trials 65
5.2.2 Literature on artefact quantification 67
5.3 Method 67
5.3.1 Prevalence of different artefacts in clinical data 67
5.3.2 Quantifying the severity of artefacts 68
5.4 Results 71
5.4.1 Prevalence of different artefacts in clinical data 71
5.4.2 Quantifying the severity of artefacts 75
5.5 Discussion 77
5.6 Conclusion 82
6 Simulation of a database of longitudinal MR head images with known atrophy and acquisition artefacts 83
6.1 Introduction 83
6.1.1 Aims 85
6.1.2 Contribution 85
6.2 Literature Review 85
6.2.1 K-t space 85
6.2.2 Simulating motion 86
6.2.3 Simulating noise 86
6.3 Method 86
6.3.1 Materials 86

6.3.2 Atrophy simulation ... 86
6.3.3 Simulation of motion artefact ... 89
6.3.4 Simulation of flow artefact ... 93
6.4 Results ... 93
6.4.1 Simulated images with motion artefact ... 93
6.4.2 Analysis of simulated images with motion artefact ... 96
6.5 Conclusions ... 101
7 Robustness assessment of global atrophy quantification techniques with a gold standard of atrophy and artefact simulated images 102
7.1 Introduction ... 102
7.1.1 Aims ... 103
7.1.2 Contribution ... 103
7.2 Literature Review ... 103
7.2.1 Overview of atrophy measurement techniques ... 103
7.2.2 Global techniques ... 104
7.2.3 Local brain volume change ... 110
7.2.4 The effect of artefacts in longitudinal imaging studies ... 111
7.3 Method ... 114
7.3.1 Materials ... 114
7.3.2 BSI ... 114
7.3.3 SIENA ... 115
7.4 Results ... 116
7.5 Discussion ... 118
7.6 Conclusions ... 120
8 Novel approach to simulating and removing pulsatile flow artefact 121
8.1 Introduction ... 121
8.1.1 Aims ... 122
8.1.2 Contribution ... 122
8.2 Literature ... 123
8.2.1 Simulating pulsatile flow artefact ... 123
8.2.2 Computational pulsatile flow artefact correction techniques ... 124
8.3 Method ... 128
8.3.1 Model ... 128
8.3.2 Implementation and Results ... 131
8.4 Results ... 149
8.4.1 Pulsatile flow artefact simulation ... 149
8.4.2 Pulsatile flow artefact correction ... 157
8.5 Conclusions and further work ... 162
8.6 Examples of acquired flow artefacts for comparison with simulated artefacts . 164
9 Conclusions ... 167
9.1 Summary of findings ... 167
9.1.1 Chapter 4 - Artefacts in longitudinal images at different field strengths 167
9.1.2 Chapter 5 - Prevalence and automatic quantification of artefacts affecting longitudinal neuroimaging studies ... 168
9.1.3 Chapter 6 - Simulation of a database of longitudinal MR head images with known atrophy and acquisition artefacts ... 169
9.1.4 Chapter 7 - Robustness assessment of global atrophy quantification techniques with a gold standard of atrophy and artefact simulated images 170
9.1.5 Chapter 8 - Novel approach to simulating and removing pulsatile flow artefact 172

9.2 Clinical impact 173
9.3 Future work 174
9.3.1 Implementation of an automated quality checking system 174
9.3.2 Effect of artefacts on atrophy measurement techniques 174
9.3.3 Improving image quality obtained from the scanners 175
9.4 Overall summary 176
References: 177
Publications list 184

List of figures

Figure 1-1 Dr Alois Alzheimer 13
Figure 2-1 Directions of magnetic field gradients 23
Figure 2-2 Slice select gradient 24
Figure 2-3 Phase encode gradient 25
Figure 2-4 Frequency encode gradient (readout gradient) 26
Figure 2-5 Relationships between k-space and image space 27
Figure 2-6 A linear Cartesian acquisition of a 3D image, and the order of acquisition of k-space planes giving the slow phase encode direction. 28
Figure 2-7 Example of contrast in a T1-weighted image 32
Figure 2-8 Example of contrast in a typical T2 scan weighted image 33
Figure 2-9 Example of images from a dual echo sequence 34
Figure 2-10 The 3D inner phase encoding loop for FLASH type sequences 35
Figure 2-11 K-space acquisition directions for the 3D TFE sequence used in Chapter 4. 37
Figure 2-12 Timing of one shot of the TFE sequence 37
Figure 2-13 Pulse sequence timings for TFE spatial encoding 38
Figure 2-14 Overview of 3D MDEFT sequence used by Deichmann, 2003 39
Figure 3-1 Visual example of Normal and Rician distributions 42
Figure 3-2 Coil array malfunction 42
Figure 3-3 Intensity inhomogeneity effecting an automatic segmentation algorithm 43
Figure 3-4 Pulsatile flow artefacts running head foot shown arising from the carotid arteries, using a 3D TFE sequence 48
Figure 4-1 Measuring severity of flow artefact from difference image 58
Figure 4-2 Flow artefact at different field strengths 61
Figure 5-1 Examples of artefact in clinical trials. From left to right: flow artefact, susceptibility artefact and incorrect contrast 68
Figure 5-2 Automatic quantification masks: Bottom ROI: Region of pulsatile flow artefact, Top ROI: Region free from flow artefact. 70
Figure 5-3 Prevalence of artefact in an historical trial. 72
Figure 5-4 Prevalence of artefact in a current trial 73
Figure 5-5 Temporal lobe artefacts in images rejected and accepted into analysis 74
Figure 5-6 Causes of temporal lobe artefacts in scans rejected from analysis .. 74
Figure 5-7 Causes of temporal lobe artefacts in scans accepted into analysis . 75
Figure 5-8 Assessment of automatic flow artefact tool 76
Figure 5-9 SNR pair results for motion affected scans from the historical trial .. 77
Figure 5-10: Well registered regions of interest from automatic quantification tool in a scan affected by pulsatile flow artefact: 79

Figure 5-11 Example of underestimation of pulsatile flow artefact severity by automatic tool 80
Figure 5-12 Example of overestimation of pulsatile flow artefact severity by automatic tool 81
Figure 6-1 Example of motion artefact 84
Figure 6-2 Atrophy simulation 87
Figure 6-3 Example of atrophy simulation on the cohort 88
Figure 6-4 Simulation of step rotational motion 90
Figure 6-5 Simulation of periodic step motion 91
Figure 6-6 Comparison of simulated motion artefact with 10° periodic step motion (left) with acquired motion artefact (right) 93
Figure 6-7 Baseline scan from one volunteer with different amounts of simulated atrophy from left to right and simulated motion artefact. Each pair of rows shows a different type of simulated motion artefact of 2 degrees rotation. 94
Figure 6-8 SNR levels with increasing angle of simulated rotational motion 96
Figure 6-9 Baseline scan of one volunteer with simulated motion of increasing rotational angle 99
Figure 7-1 Example of a BSI growth/atrophy map. 107
Figure 7-2 Comparing SIENA (pink) and BSI (blue) errors with increasing rotational angle of simulated motion. 116
Figure 7-3 BSI error with and without modified parameters for different levels of atrophy simulation 117
Figure 7-4 BSI overlay showing apparent regions of growth (green) and atrophy (red) 120
Figure 8-1 Sensitivities of two coils 127
Figure 8-2 Intensities against position along a randomly selected line in the left right direction from an MR head image. This line is nominally called $m(x)$ 131
Figure 8-3 Simulated 3D coil intensity profiles for array coil elements 3, $s_1(x,y,z)$ and 6, $s2(x,y,z)$ 133
Figure 8-4 Simulated coil intensity profiles in the x direction 133
Figure 8-5 $p(k_x)$: the intensity variation of voxel x_0 over time t 134
Figure 8-6 Simulated coil modulated lines without artefact. 134
Figure 8-7 $m_1(x,t)$: coil 3, modulated image with a voxel, $x_0 = 30$, varying intensity over time 135
Figure 8-8 $m_2(x,t)$: coil 6, modulated image with a voxel, $x_0 = 30$, varying intensity over time 135
Figure 8-9 $M_1(k,t)$: coil 3 modulated line with one voxel varying intensity over time, shown in the k t domain 136
Figure 8-10 $M_2(k,t)$: coil 6 modulated line with one voxel varying intensity over time, shown in the k t domain 136
Figure 8-11: coil modulated views with final artefact 136
Figure 8-12 Coil views, with coil intensity profiles corrected, with artefact compared to original image without artefact, $m(x)$ 137
Figure 8-13 Original line $m(x)$ and recovered m, (blue, real; red, imaginary) 139
Figure 8-14 Recovered $p(t)$ 140
Figure 8-15 $m_1(x,t)$, coil 3 modulated image with 6 voxels varying over time 141
Figure 8-16 $m_2(x,t)$, coil 6 modulated image with 6 voxels varying over time 141

Figure 8-17 $M_1(k,t)$ coil 3 modulated image with 6 varying voxels in k t domain 142
Figure 8-18 $M_2(k,t)$ coil 6 modulated image with 6 varying voxels in k t domain 142
Figure 8-19 $m_1'(x)$and $m_2'(x)$ artefact simulated from 6 varying voxels 142
Figure 8-20 Original $p(t)$ 144
Figure 8-21 Recovered $p(t)$ for 6 varying voxels 144
Figure 8-22 Original and recovered $m(t)$ for 6 varying voxels 144
Figure 8-23 Original line $m(t)$ and line recovered with side voxel correction, for 6 varying voxels 145
Figure 8-24 Peak velocity of the blood flow in the carotid artery 146
Figure 8-25 Simplified model of blood flow velocity 147
Figure 8-26 $p(t)$ as determined using the carotid flow model described above. 147
Figure 8-27 Simulation of an artefact generated from carotid flow artefact shown in two coil views, from two different axial slices 148
Figure 8-28 Simulation of an artefact generated from carotid flow artefact shown in two coil views, on a coronal slice 148
Figure 8-29 3D pulsatile flow artefact simulations with varying simulated pulse rates shown in two different axial slices 150
Figure 8-30 3D pulsatile flow artefact simulations with varying simulated pulse rates shown in two different coronal slices 153
Figure 8-31 Simulation and correction of artefact without noise shown in two axial slices 158
Figure 8-32 Simulation and correction of artefact without noise shown in two coronal slices 159
Figure 8-33 Coronal images showing the correction of artefact simulations, each simulated with the same artefact and increasing levels of noise 161
Figure 8-34 Axial images showing the correction of artefact simulations, each simulated with the same artefact and increasing levels of noise 162
Figure 8-35 Examples of acquired flow artefacts for comparison with simulated artefacts 164

List of tables

Table 1-1 Selected studies reporting annual mean (SD) brain and ventricle atrophy rates in AD and control subjects [Preboske 2006] 15
Table 2-1 Comparison of MDEFT vs TFE 40
Table 4-1 Artefact scores at 1.5T and 3T from Nobauer-Huhmann, 2002 55
Table 4-2 Comparison of artefact level at different field strengths: Birdcage coil results 60
Table 4-3 Comparison of artefact level at different field strengths: Array coil results 60
Table 4-4 Comparison of artefact level at different field strengths: Averages 60
Table 4-5 SNR measures 60
Table 7-1 Table from Anderson et al, 2007, summarizing the difference and similarities between BSI and SIENA. 105

List of equations

$m(x,t) = s(x)m(x) + s(x_0)p(t)\delta(x - x_0)$ Equation 1 130

$M(k_x,t) = S(k_x) * M(k_x) + s(x_0)p(t)e^{-i2\pi x_0 k_x}$ Equation 2 130

$M_1'(k_x) = S_1(k_x) * M(k_x) + s_1(x_0)p(k_x)e^{-i2\pi x_0 k_x}$ Equation 3 130

$M_2'(k_x) = S_2(k_x) * M(K_x) + s_2(x_0)p(k_x)e^{-i2\pi x_0 k_x}$ Equation 4 130

$m_1'(x) = s_1(x)m(x) + s_1(x_0)P(x - x_0)$ Equation 5 130

$m_2'(x) = s_2(x)m(x) + s_2(x_0)P(x - x_0)$ Equation 6 130

$$P(x - x_0) = \frac{s_2(x)m_1'(x) - s_1(x)m_2'(x)}{s_1(x_0)s_2(x) - s_2(x_0)s_1(x)}$$ Equation 7 130

$$m(x) = \frac{s_2(x_0)m_1'(x) - s_1(x_0)m_2'(x)}{s_2(x_0)s_1(x) - s_1(x_0)s_2(x)}$$ Equation 8 130

$$Coil\ sensistivity\ map = \exp\left(\frac{-\ sum\ of\ squares\ dist\ from\ coil\ centre}{coil\ diameter^2}\right)$$ Equation 9 132

$m_1(30,t) = m_1(30) + s_1(30) * p(t)$ Equation 10 135

$m_2(30,t) = m_2(30) + s_2(30) * p(t)$ Equation 11 135

$m_1'(x) = s_1(x)m(x) + s_1(x_0)P(x - x_0) + s_1(x_1)P(x - x_1) + \ldots$ Equation 12 140

$m_2'(x) = s_2(x)m(x) + s_2(x_0)P(x - x_0) + s_2(x_1)P(x - x_1) + \ldots$ Equation 13 140

$m_1'(30,t) = m_1(30,t) + s_1(30)p(t)$ Equation 14 141

$m_1'(x) = s_1(x)m(x) + s_1(x_0)P(x - x_0) + s_1(x_1)P(x - x_1) + \ldots$ Equation 15 143

$m_2'(x) = s_2(x)m(x) + s_2(x_0)P(x - x_0) + s_2(x_1)P(x - x_1) + \ldots$ Equation 16 143

Equation 17 143

$p(t) = carotid\ output\ sequence * 3400$ Equation 18 146

Table of abbreviations

2D	2 Dimensional
3D	3 Dimensional
AD	Alzheimer's Disease
ADNI	Alzheimer's Disease Neuroimaging Initiative I
AP	Anterior to Posterior
BET	Brain Extraction Tool
BSI	Boundary Shift Integral
BVC	Brain Volume Change
CMIC	Centre for Medical Image Computing
CNR	Contrast to Noise Ratio
CSF	CerebroSpinal Fluid
DRC	Dementia Research Centre
FEM	Finite Element Methods

FID	Free Induction Decay
FLASH	Fast Low Angle SHot
FOV	Field Of View
GM	Grey Matter
HF	Head to Foot
IXI	Information Extraction from Images
LR	Left to Right
MCI	Mild Cognitive Impairment
MDEFT	Modified Driven Equilibrium Fourier Transform
MR	Magnetic Resonance
MRI	Magnetic Resonance Imaging
MS	Multiple Sclerosis
MP-RAGE	Magnetisation Prepared RApid Gradient Echo
MT	Magnetisation Transfer
NIH	National Institutes of Health
PBVC	Percentage Brain Volume Change
PET	Positron Emission Tomography
QC	Quality Control
RF	Radio Frequency
ROI	Region Of Interest
SAR	Specific Absorption Rate
SD	Standard Deviation
SE	Spin Echo
SIENA	Structural Image Evaluation using Normalization of Atrophy
SNR	Signal to Noise Ratio
SPGR	SPoiled Gradient Recalled acquisition in the steady state
T	Tesla
TE	Echo Time
TFE	Turbo Field Echo
TI	Inversion Time
TR	Recovery Time
WM	White Matter

1 Introduction

1.1 Motivation
1.1.1 Clinical background of Alzheimer's disease
1.1.2 Detection of structural brain change from MRI
1.1.3 Clinical dementia trials using longitudinal MRI
1.1.4 Influence of artefacts on clinical neuroimaging trials
1.2 Aims
1.3 Thesis overview

1.1 Motivation

1.1.1 Clinical background of Alzheimer's disease

Alzheimer's disease (AD), discovered in 1906 by Alois Alzheimer, is the most common cause of dementia (progressive impairment of multiple cognitive domains) in the world today. The highest risk factor for this dementia is age, making it of particular concern to societies with ageing populations with huge associated medical and social care costs. 24 million people were estimated as having dementia in 2005, and this is predicted to double in the next 20 years [Ferri 2005]. It is a neurodegenerative disease characterized by progressive memory loss (amnesia): starting as forgetfulness with a relative sparing of older memories, leading to increasing problems with tasks such as constructing meaningful sentences, and resulting in an inability to perform normal daily tasks or even recognise care givers. Its end stage is immobility and death. The diagnosis of AD can be confirmed on autopsy by the presence of amyloid plaques and neurofibulary tangles which are thought to lead to neuronal cell death. Neurofibrillary tangles and Neuropil threads have distribution patterns that differentiate 6 stages of AD progression [Braak 1991]. Amyloid distribution patterns seem to be of a more limited significance. Cell death is associated with decreasing brain volume (atrophy) which can be seen in longitudinal magnetic resonance (MR) brain scans. Brain atrophy caused by AD progresses faster in certain regions of the brain than others [Braak 1991]. Initially, the hippocampus and entorhinal cortex both suffer substantial atrophy; both have a crucial role in memory function. Next, the disease spreads through the temporal and medial parietal lobes, and eventually the frontal lobes are affected too. The sensory motor strip is relatively spared until the end stages of the disease.

Figure 1-1 Dr Alois Alzheimer [1]

[1] Image from Kalamazoo Center for Medical Studies: http://hod.kcms.msu.edu

There is, at present, no disease modifying treatment for Alzheimer's. To try and address this need many drugs are in the development pipeline. A current issue is the necessity for tools to distinguish a drug's disease modifying effect from purely symptomatic benefits. As previously mentioned brain atrophy is a known downstream effect of AD, correlating with disease progression. At present the use of structural MR images to determine this atrophy is the most established biomarker for studying disease progression, and therefore for assessing new drugs [Jack 2003, Fox 1999a].

1.1.2 Detection of structural brain change from MRI

Longitudinal neuro magnetic resonance imaging (MRI) involves acquiring repeated magnetic resonance (MR) brain scans, a certain period of time apart, on the same subject. When this period of time is months or years, structural changes to the brain may be clearly visible between scans. In normal ageing there is a slow but progressive loss of brain volume of the order of 0.2-0.5% brain volume per year in elderly controls (See Table 1-1, [Preboske 2006]). With some neurological and psychiatric diseases, such as frontotemporal and semantic dementias [Rosen 2002], Multiple Sclerosis (MS) [Losseff 1996], Schizophrenia [Thompson 2001] and Alzheimer's disease [Fox 1999] there is acceleration in the rate of brain volume loss. For example, rates of 1-3% brain volume atrophy per year for elderly patients with AD were measured in studies collated by Preboske et al, 2006. Silbert et al, 2003, who found annual rates of global brain atrophy of 2% in Alzheimer's disease compared with 0.4% in age-matched controls, also found that this excess atrophy predicted the accumulation of Alzheimer's disease pathology at post-mortem. Rates of brain atrophy have been shown both to increase before the onset of symptoms [Schott 2003, Fox 1999a, Silbert 2003, Fox 1999b] and to accelerate as the disease progresses [Fox 2004]. This rate of atrophy can be determined using longitudinal structural MR imaging. This type of imaging, therefore, helps determine the onset and measure the progression of AD.

Study	Year	Structure	Control			AD		
			Mean (SD)/year (%)	Mean age	*n*	Mean (SD)/year (%)	Mean age	*n*
Bradley, KM et al.[a]	2002	Brain	0.2 ± 0.23	73.5	32	2.1 ± 0.5	61.7	5
Fox, NC et al.	2000	Brain	0.41 ± 0.47	65	18	2.4 ± 1.1	65	15
O'Brien, JT et al.	2001	Brain	0.5 ± 0.7	75.8	20	2.0 ± 0.9	74.3	9
Wang, D et al.[b]	2002	Brain	0.4 ± 0.5	71.5	14	2.4 ± 1.2	66.9	14
Fox, NC et al.	1999	Brain	0.4 ± 0.7	55.3	15	2.4 ± 1.4	58.1	29
Gunter, JL et al.	2003	Brain	0.54 ± 0.74	78.8	29	1.09 ± 0.93	76.2	32
Jack Jr, CR et al.	2004	Brain	0.4 ± 0.3	79	40	1.0 ± 0.9	78	65
Ezekiel, F et al.	2004	Brain	0.49 ± 0.39	76.7	22	1.28 ± 0.80	75.3	20
Fox, NC et al.	1997	Brain	0.24 ± 0.32	54.4	9	2.78 ± 0.92	54.3	9
Schott, JM et al.	2005	Brain	NA	69.3	19	2.1 ± 1.8	69.8	38
Bradley, KM et al.[a]	2002	Ventricle	4.1 ± 0.9	73.5	32	13 ± 2.4	61.7	5
Wang, D et al.[b]	2002	Ventricle	1.9 ± 4.2	71.5	14	13.8 ± 4.8	66.9	14
Gunter, JL et al.	2003	Ventricle	2.96 ± 1.79	78.8	29	6.35 ± 3.77	76.2	32
Jack Jr, CR et al.	2004	Ventricle	1.7 ± 0.9	79	40	5.4 ± 3.5	78	65
Ezekiel, F et al.	2004	Ventricle	3.34 ± 3.77	76.7	22	10.97 ± 4.7	75.3	20

Table 1-1 Selected studies reporting annual mean (SD) brain and ventricle atrophy rates in AD and control subjects [Preboske 2006]
[a] ROI-based measurements.
[b] ROI and segmentation based measurements

1.1.3 Clinical dementia trials using longitudinal MRI

As the use of structural MRI to determine atrophy is the most established biomarker for studying the progression of AD and therefore for assessing new drugs, it is of great importance to the pharmaceutical industry. In this industry there is high demand for reliable biomarkers which are able to monitor the efficacy of drugs, in vivo, against a placebo treated control group, more rapidly and with fewer subjects than needed using traditional techniques such as cognitive testing. Structural MRI has also been shown to be sensitive to the effects of novel therapies, for example in the AN1792 vaccination trial [Fox 2005].

Clinical trials of new drugs, involving imaging biomarkers, are often performed at many different hospitals, enabling large numbers of appropriate subjects to be recruited in a short timescale, allowing trials to be sufficiently statistically powered. Also any local effects which may bias results are more likely to be balanced out. These multi-centre

clinical trials acquire large quantities of image data. This data can be processed quicker, and in a more cost efficient and more consistent manner, by automated image analysis tools. Many such automated or semi-automated image analysis tools have been developed, including ones for longitudinal analysis. The use of these longitudinal image analysis tools is an area of particular focus in this thesis (See Chapter 7, Section 7.2 for more details on these tools).

Until recently most neuroimaging trials were performed on MR scanners with a magnetic field strength of 1.5 Tesla (T). New technological advances, however, have enabled the use of scanners with a magnetic field strength of 3T. Using scanners with this higher field strength can produce images with higher signal to noise ratios compared to images acquired on 1.5T scanners at the same resolution using similar acquisition times (See Chapter 2, Section 2.2.1 for more background on the benefits and drawbacks on using scanners of higher magnetic field strengths). Some neuroimaging trials are now using these higher field strength scanners to take advantage of their ability to either increase the signal to noise or the resolution of the images. It is therefore important that all the effects of moving trials to this higher field strength are fully evaluated. The effect of higher field strength on artefacts is another area of focus in this thesis.

At the present time there is a large National Institutes of Health (NIH) funded project running which is trying to determine the best biomarker for AD. It is the largest US public-private partnership on brain research to date. 800 adults, aged 55-90, are being scanned longitudinally over 3 years at 58 sites across North America. The $60 million project is funded by many of the large pharmaceutical companies as well as the NIH. Many potential biomarkers for AD are being investigated simultaneously: biochemical markers, including cerebrospinal fluid (CSF) and blood levels of amyloid and other proteins, and imaging markers consisting of positron emission tomography (PET) and MRI. This trial, known as the Alzheimer's Disease Neuroimaging Initiative[2] (ADNI) [Mueller 2005], is a current example of a study involving the management and analysis of large quantities of longitudinal MR image data. Other smaller current examples include the BIRN[3] [Grethe 2005], IXI[4] [Rowland 2004], and Neurogrid[5] [Geddes 2005] initiatives. The work in this thesis is born out of the IXI project, whose focus is particularly in storing, accessing and analysing large quantities of image data in an

[2] http://www.adni-info.org/
[3] http://www.nbirn.net/
[4] http://fantail.doc.ic.ac.uk/index.php
[5] http://www.neurogrid.ac.uk/

efficient and recordable manner, using a distributed computer infrastructure. The IXI project has informal links with ADNI, and contributed to discussions regarding their imaging protocol.

1.1.4 Influence of artefacts on clinical neuroimaging trials

The influence of artefacts on clinical dementia trials using MR images is demonstrated by the Vitamin E and Donepezil trial for the treatment of Mild Cognitive Impairment [Petersen 2005]. Out of 138 scan pairs acquired 36 months apart, 34 had to be discarded from whole brain atrophy analysis (using the boundary shift integral (BSI) algorithm) because one or both members of the scan pair exhibited artefacts which rendered them unusable. That is approximately 25% of patient data lost due to image artefacts. Preboske, 2006, reflecting on this trial, comments "Methods to maximize consistency of image quality over time are an essential component of any quantitative MRI study". (For further background on artefacts which affect neuroimaging trials see Chapter 3). This topic of the influence of artefacts on longitudinal clinical dementia trials using MR imaging is the main focus and context of this thesis.

1.2 Aims

This thesis aims to investigate artefacts in longitudinal MRI of the brain. The focus is acquisition artefacts affecting longitudinal dementia trials. The first topic I research is the effect on artefacts of moving from a 1.5T to a 3T scanner. I aim to qualitatively and quantitatively assess the increase in pulsatile flow artefact levels when moving between these two field strengths. The motivation for this is to investigate the potential problems which may be encountered when moving dementia trials to higher field strengths. Next, I aim to assess the frequency of occurrence of different types of artefacts in clinical dementia trials at 1.5T. During this assessment I investigate images which are excluded from analysis due to artefacts and those which are included with potentially confounding effects. I also determine the main causes of artefacts occurring in the temporal lobe in dementia trials, as this region of the brain is particularly affected in Alzheimer's disease. I aim to devise methods to quantify artefacts, such as those occurring in the temporal lobe, which have the potential to be used in an automated quality control system. To investigate further the potentially confounding effects of artefacts on the analysis of dementia trials, I aim to create a gold standard database with known levels of simulated atrophy and artefact. I use this database to test the robustness against artefacts of two whole brain atrophy measurement techniques commonly used in clinical trials. This involves simulating different types of motion

artefact. I also aim to develop a novel method to simulate pulsatile flow artefact which could also be used to test the robustness of atrophy tools to artefact. Finally, I aim to propose a novel technique to remove pulsatile flow artefact, and test it on simulated data.

1.3 Thesis overview

In describing the motivation for this thesis, I have discussed the necessity of being able to obtain large quantities of reliable longitudinal MRI scans. As mentioned, there is currently evidence in the literature of substantial degradation of these longitudinal scans by artefacts at 1.5T.

In Chapter 4 of this thesis I assess the effect on artefact levels of moving image acquisitions from 1.5T to 3T. In particular, I use qualitative and quantitative artefact assessment methods to investigate the effect on pulsatile flow artefact. I presented the work in this chapter at the Alzheimer's Association International Conference on Prevention of Dementia (ICAD) in 2005. I also presented it at the meeting of the International Society of Magnetic Resonance in Medicine, 2005. A preliminary version of the work was presented at MIUA in Sep 2004. The images I acquired using the method in this Chapter were also used by other collaborators to produce work on segmentation and classification of brain tissue across field strengths which was presented at MIUA, 2004 and SPIE 2005.

In Chapter 5 of this thesis, I carry out further assessment of artefact prevalence in longitudinal clinical trials. I determine the principle causes of artefact in recent longitudinal MR trials, and find ways to assess these both qualitatively and quantitatively. The work assessing the principle causes of temporal lobe artefact in this chapter was presented at ICAD, 2006.

In Chapter 6, I develop a gold standard database with simulated atrophy and different types of simulated motion artefact. This work has been published as part of a paper in IEEE transactions on medical imaging.

In Chapter 7, I investigate the robustness of two well-known automated tools of atrophy measurement to artefact using the gold standard database. The work in Chapter 6 and early work using the techniques in Chapter 7 were presented at the Medical Imaging Understanding and Analysis conference (MIUA) in July 2006, where it was awarded best paper at conference. This work was also presented at the 9th International

Conference on Medical Image Computing and Computer-Assisted Intervention (MICCAI), 2006.

In Chapter 8, I propose a novel method for simulating pulsatile flow artefact and also a novel method for removing this artefact from 3D MR brain images which I then test on simulated data. Preliminary work on this chapter was presented at ICAD 2006 and also as part of a presentation at the ESMRMB in Warsaw, 2006.

The next two chapters following this introduction provide the background to MRI (Chapter 2) and to acquisition artefacts in longitudinal imaging (Chapter 3) relevant to the work in this thesis. The next five chapters (Chapters 4 - 8) present the main contributions of this thesis. Chapter 9 provides final discussion and conclusions.

The list of publications arising from the work presented here can be found at the back of this thesis after the references section. This work was kindly funded by the ESPRC.

2 Background to MR neuroimaging

This chapter gives a brief introduction to MRI and looks at the particular details of MRI relevant to understand the work presented in this thesis. It is not intended to give the reader a full understanding of the physics behind MRI. Below is a summary of each section of this chapter:

2.1 Introduction to MRI.

2.2 Magnetisation and spatial localisation: explains the principles needed to understand the comparison of artefacts at different field strengths (Chapter 4) and the simulation of artefacts (Chapters 6 and 8).

2.3 K-space: describes k-space in sufficient detail to understand the methods described in Chapters 6 and 8 regarding the simulation and correction of artefacts.

2.4 Different types of RF coils: explains the properties of the different types of coils used in this thesis.

2.5 2D and 3D scans: explains the difference between these two different types of scans giving a better understanding of the benefits and limitations of the MR acquisition sequences used in this thesis.

2.6 Contrast mechanisms: T1 and T2-weighted images: describes contrast mechanisms and the differences between T1 and T2-weighted images, providing an explanation for the majority of scans acquired and used in this thesis being T1-weighted.

2.7 MRI pulse sequences: sets in context and explains the types of pulse sequences used in this thesis.

2.8 Summary

2.1 Introduction to MRI

Sir Peter Mansfield and Paul Lauterbur were awarded the 2003 Nobel Prize in Physiology or Medicine for their discoveries concerning Magnetic Resonance Imaging. The technique was first used to image the human body in the early 1970s and has been developing ever since, coming into regular clinical use from the late 1980s. Substantial progress has been made decreasing the average scanning time and increasing the quality of the images. MRI has no known, long term, harmful effects and is very useful in inspecting soft tissue without the need for invasive procedures. Different types of tissue are visualised in the scans with different intensities, as they have varying nuclear magnetic resonance properties and this results in images with high contrast between tissue types. The brain's structure can be depicted clearly using

MR. This is due to the high contrast enabling, for example, good differentiation of grey and white matter within the brain. The spatial resolution of MRI is not as high as that of CT, nor the equipment as portable and affordable as that of ultrasound, but its benefits lie in its ability to provide contrast between tissue types. These contrasts can also be manipulated for different purposes (See Section 2.6 on contrast mechanisms: T1 and T2-weighted images).

2.2 Magnetisation and spatial localisation

MRI involves a large static magnetic field (B_0), magnetic field gradients (small linear magnetic fields superimposed on B_0 which perform spatial encoding, by slightly varying the frequency at which different voxels will resonate), and radio frequency (RF) pulses (time varying magnetic fields known as B_1) that are used to align and manipulate the spins of hydrogen nuclei within the subject being imaged; the nuclei then emit small RF signals, which when detected and recorded can be used to produce an accurate image of the subject.

2.2.1 Magnetic field strength

Images are collected with the subject in a strong magnetic field (B_0), usually produced by a helium cooled superconducting magnet. The magnetic field strength within a clinical MRI system is much higher than that of the earth's magnetic field of 5×10^{-5} Tesla (T) [Schenck 2000]. The most common strength of magnetic field used in MR scanners at present is 1.5T. 3T scanners are becoming increasingly common in both clinical and research settings.

An advantage of using higher field strength is a proportional increase in the signal to noise ratio (SNR). See also Chapter 4, Section 4.2 on the literature comparing artefacts at 1.5 and 3T. This increase in SNR is due to an increase in the MR signal proportional to the square of the field strength, caused by a larger proportion of the hydrogen spins aligning with the stronger field. The absolute noise level also increases but only proportionally to the field strength increase. Therefore the SNR increases in proportion to the increase in field strength. SNR also increases in proportion to voxel volume (1/resolution), and in proportion to the square root of the number of phase encodings (see Section 2.2.2 regarding phase encoding). As higher magnetic fields provide higher signal to noise ratios than lower field systems, this gain in SNR from field strength can be traded against a loss in SNR from higher imaging resolution or from a decrease in scan time. For example, by increasing the resolution at the higher field strength the scan will have comparable SNR levels to a scan of lower resolution at the lower field

strength. Alternatively if higher resolution is not required the additional signal can be used in conjunction with an array coil to speed up the acquisition by acquiring fewer phase encodes instead.

However, there are also some problems with 3T scanners. The first is often a less homogeneous B_1 field which may result in increased signal intensity distortions (see Chapter 3, Section 3.2.1 on image artefacts). Next, there is an increase of RF exposure to the subject, proportional to the square of the magnetic field increase, which can result in tissue heating. RF exposure is measured as the Specific Absorption Rate (SAR) which is a measure of the rate of energy deposition per kilogram of body weight. There are SAR safety limits to reduce the risk of overheating tissue. SAR depends not only on field strength but is proportion to the pulse duty cycle, and proportional to the square of the flip angle used. Some sequences at 3T have to be slowed down (lowering the pulse duty cycle) compared to at 1.5T to stay within the SAR safety limits. Lower flip angle excitation pulses also help reduce SAR but have the disadvantage of potential SNR loss. Another problem of increased field strength is the effect on T1 and T2 relaxation times (see Section 2.6). T1 relaxation times of grey and white matter increase and T2 relaxation times decrease with field strength. This can lead to decreased grey/white matter contrast for an identical scan sequence acquired at 3T compared to at 1.5T [Crooks 1984]. Finally, susceptibility and chemical shift artefacts are significantly larger (see Chapter 3 for more details on artefacts).

In Chapter 4, I investigate the effect of moving from 1.5T to 3T on longitudinal neuroimaging in particular. First, I review papers which compare artefacts at increased field strengths: motion (Section 4.2.2), chemical shift and susceptibility (Section 4.2.3), intensity inhomogeneities (Section 4.2.4) and flow artefacts (Section 4.2.5). Next I carry out an experiment to quantitatively and qualitatively determine the effects of moving from 1.5T to 3T on flow artefacts: Section 4.3 describes the method, 4.4 the results and 4.5 the discussion.

2.2.2 Spatial localization

Hydrogen nuclei are used in MRI due to their natural abundance in the human body, particularly in water molecules (a lean adult body consists of 73% by weight of water; an increase in fat content lowers this percentage [Clarys 1999]). The hydrogen nucleus consists of a single proton; this proton gives the nucleus spin and charge, which induces a magnetic moment. Other MR visible nuclei are certain isotopes of carbon,

nitrogen, oxygen, fluorine, sodium, and phosphorous, which also possess a magnetic moment.

The large magnetic field of the scanner (B_0) aligns the net magnetic moment of the hydrogen nuclei to itself. The magnetic moments precess around B_0 with a defined frequency. This is called the Larmor frequency; it is calculated as the gyromagnetic ratio of the nuclei (a specific constant for each type of nuclei) multiplied by the applied magnetic field strength (B_0). A short radiofrequency (RF) pulse (B_1) of the same Larmor frequency is then applied. The RF pulse has a flip angle determined by the shape and length of the pulse applied, often a flip angle of 90° to B_0 is used. This RF excitation pulse (B_1) imparts energy to the hydrogen nuclei causing the magnetic moments to now precess around B_0 at an angle given by the flip angle. The excitation pulse also brings the magnetic moments into phase with each other, giving a rotating net magnetic moment. Magnetic field gradients, in the x, y and z directions, are applied to spatially encode the image (see Figure 2-1). For a 2D image this involves slice selection, frequency encoding and phase encoding; for a 3D image this involves frequency encoding in one direction and phase encoding in two directions (see Section 2.5 for more details on 2D and 3D imaging).

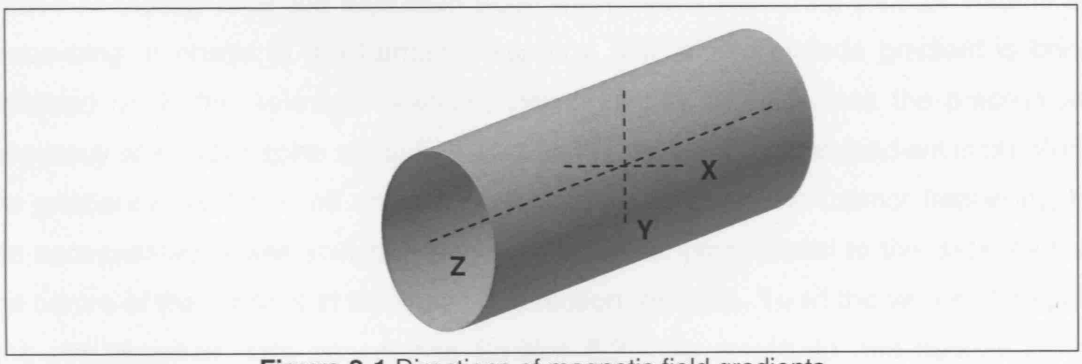

Figure 2-1 Directions of magnetic field gradients

Slice selection: In 2D imaging the slice select gradient is switched on during the delivery of the RF pulse. The gradient affects the magnetic field strength linearly in that selected direction. This causes the exact precessional frequency to vary along that direction because precessional frequency is directly proportional to magnetic field strength (Larmor's equation). A slice is selectively excited by transmitting RF at the desired precessional frequencies. The RF excitation pulse is chosen to include a range of frequencies; the greater the range of frequencies selected (the transmit bandwidth) and the shallower the gradient, the wider the slice that will be selected. The frequency on which the RF pulse is centred determines the slice location. Slices of equal thickness but different locations in the slice selection direction can be selected using different frequency RF pulses of the same bandwidth (See Figure 2-2).

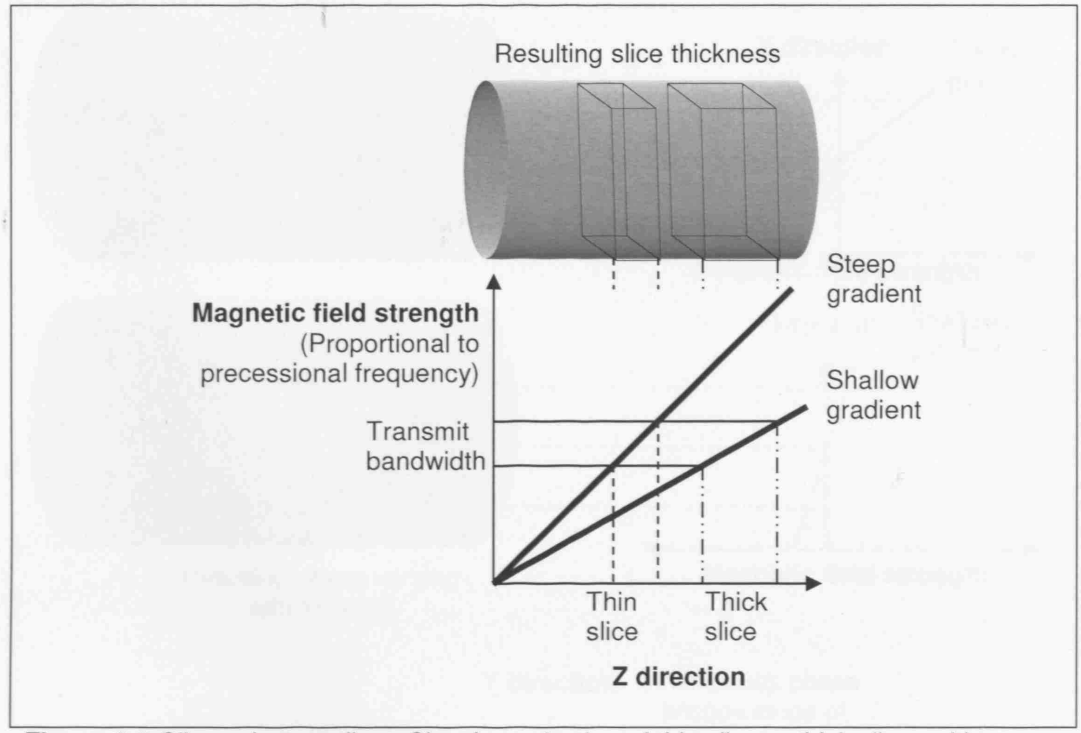

Figure 2-2 Slice select gradient: Showing selection of thin slice or thick slices with steep or shallow magnetic field strength gradients

Phase encoding: After the excitation pulse the protons within the slice or volume are precessing in phase at the Larmor frequency. The phase encode gradient is briefly switched on in the selected direction, this increases or decreases the precessional frequency of nuclear spins along this gradient for the duration this gradient is on. When the gradient is switched off and the nuclear spins return to the Larmor frequency, but the accumulated phase shift between nuclear spins, proportional to the distance from the centre of the magnet in the gradient direction, remains. To fill the whole of k-space (the raw acquired data space, see Section 2.3), the amplitude and polarity of this gradient is altered, for numerous phase encoding steps. This results in phase encoding being much slower than frequency encoding, so this is often chosen to be the direction(s) where the smallest number of distinct encodings are required. (See Figure 2-3).

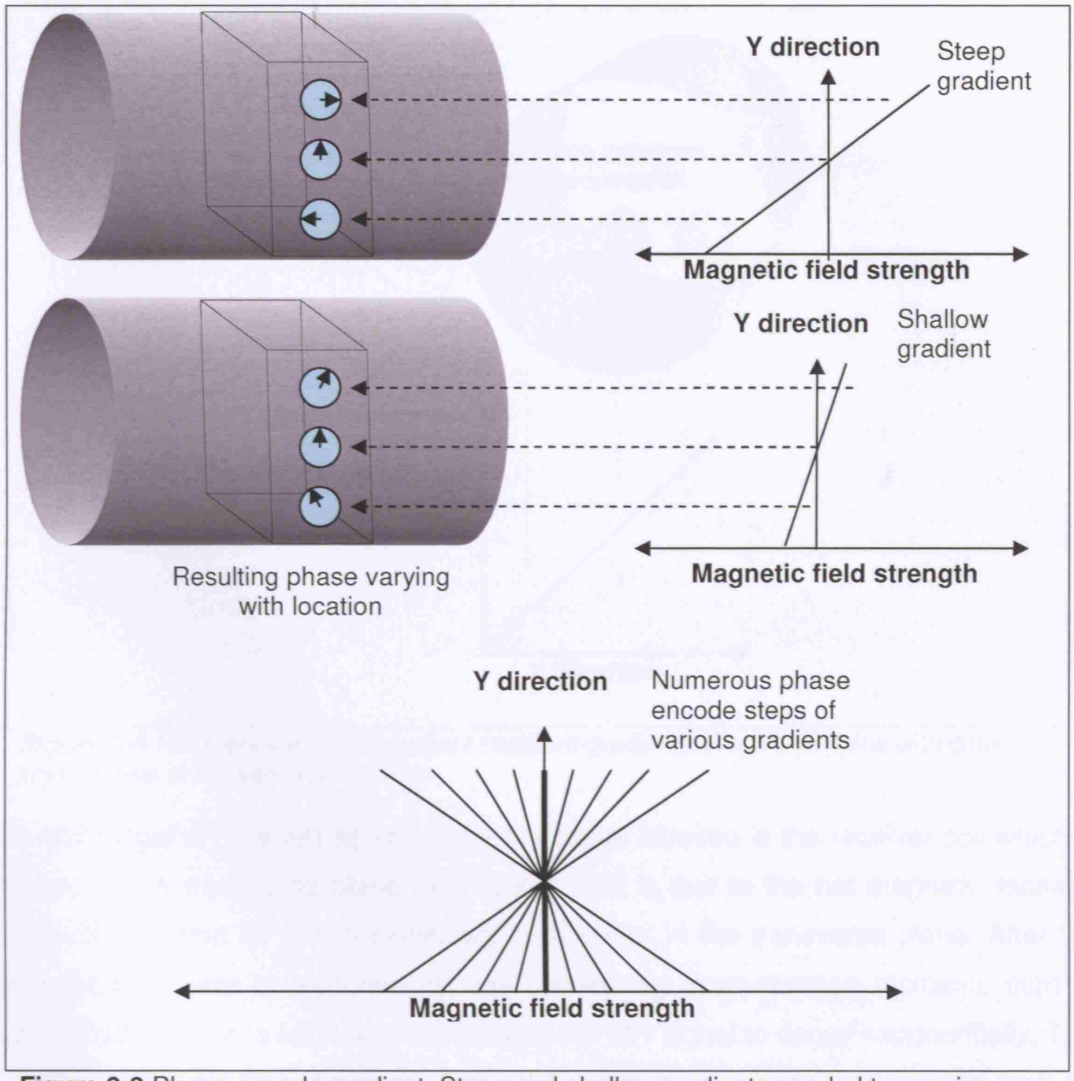

Figure 2-3 Phase encode gradient: Steep and shallow gradients needed to acquire numerous phase encoding steps to fill k-space

Frequency encoding: To locate signal, along the remaining axis during signal readout, the frequency encoding gradient is turned on. This shifts the frequencies of spins with respected to their location along the selected direction. An increased magnetic field, caused by the magnetic field gradient, increases the frequency and a decreased one reduces the frequency. The frequency encoding gradient pulse is centred with the signal echo. (See Figure 2-4).

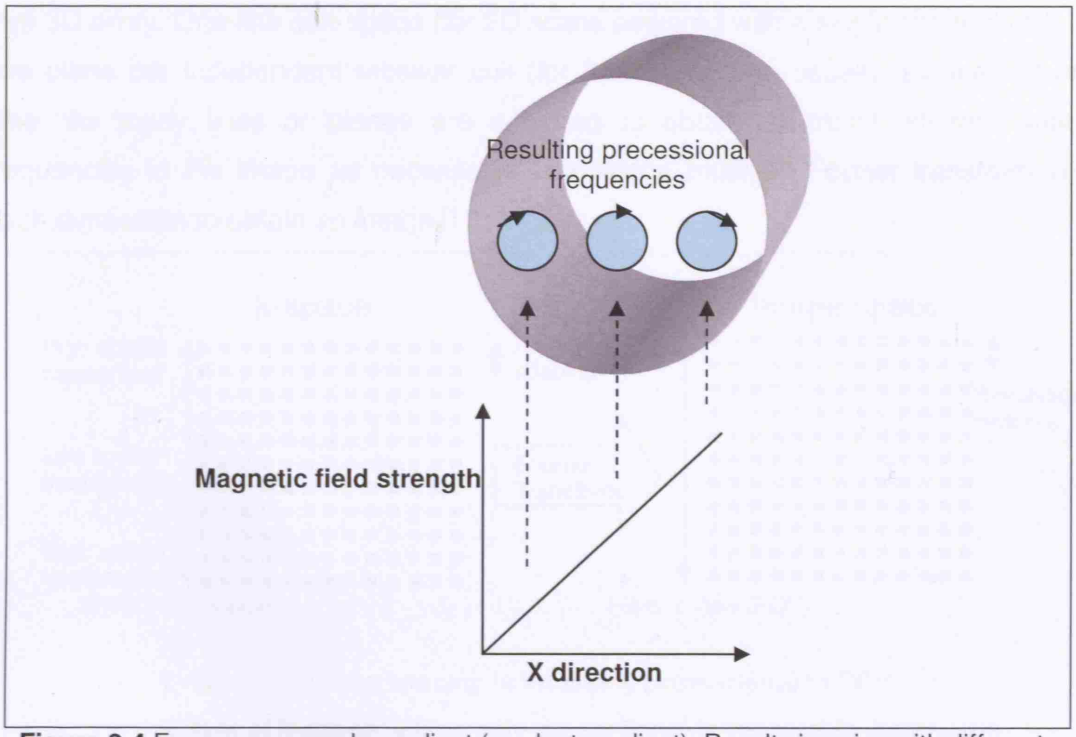

Figure 2-4 Frequency encode gradient (readout gradient): Results in spins with different frequencies in the selected direction

The MR signal is received as an electrical voltage induced in the receiver coil which is situated in the transverse plane (90° to B_0). This is due to the net magnetic moment precessing around B_0 with a significant component in the transverse plane. After the RF excitation pulse is switched off, the precessing magnetisation moments start to dephase and return to align with B_0, causing the MR signal to decay exponentially. This signal is called the free induction decay (FID) and is usually not used in this form for imaging, due to the speed with which it dephases making it difficult to obtain images with the desired tissue contrasts. For imaging the MR signal is usually rephased using either a spin echo or gradient echo sequence. (See Section 2.7 for more details on rephasing using different types of pulse sequences).

2.3 K-space

It is important to gain an understanding of k-space to fully appreciate the nature of MR artefacts and how to best to simulate and remove them from scans. It also provides insight into the effects of varying different parameters of MR sequences.

2.3.1 What is k-space?

K-space is an array of data comprised of the digitally sampled RF signal received back from the subject. A 2D array is used for 2D scans, a 3D array for 3D scans. Multiple 3D arrays can also exist for a single 3D scan acquired with array coils, as each coil has its

own 3D array. One line of k-space (for 2D scans acquired with a single channel coil), or one plane per independent receiver coil (for 3D scans), are usually acquired at one time. As many lines or planes are acquired to obtain as many different spatial frequencies in the image as necessary. This space must be Fourier transformed in each dimension to obtain an image.

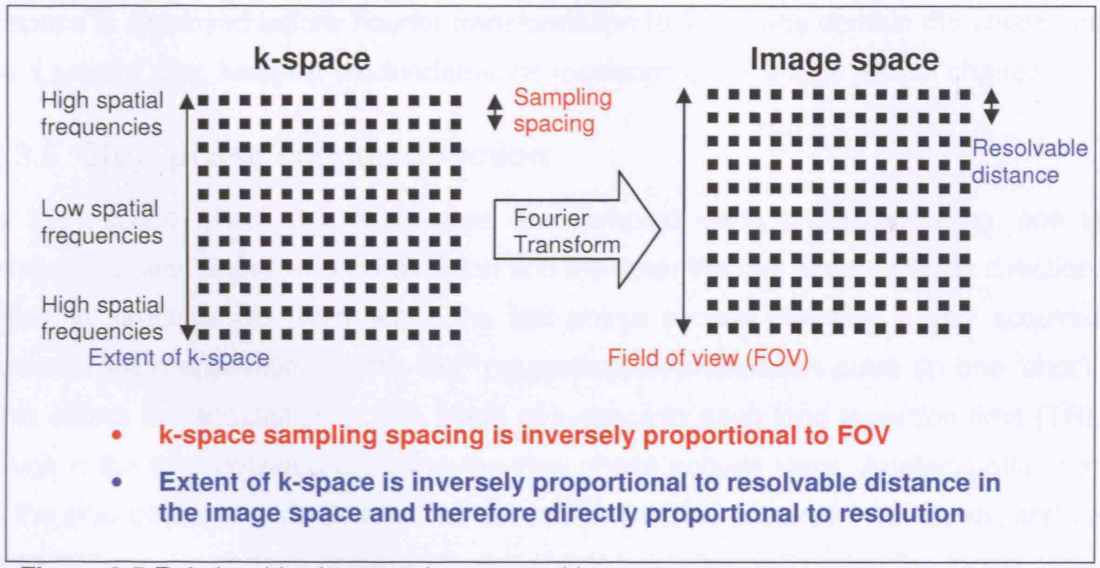

Figure 2-5 Relationships between k-space and image space

2.3.2 Field of view

Field of view (FOV) is the extent of the acquired image. It is determined by the spacing of the acquisition sampling in k-space; the narrower the spacing the larger the field of view (See Figure 2-5).

2.3.3 Rectangular field of view and parallel imaging

A rectangular field of view is obtained by using different spacing in the k-space directions; using larger spacing and thus fewer samples in the phase encode direction reduces scan time, and decreases the FOV in this direction, without affecting the resolution. Parallel imaging techniques can be used, in conjunction with larger spacing in the phase encode direction, to resolve aliasing (signal being placed in the wrong part of the image due to sampling at to low a frequency) due to reduced FOVs and unwrap the image, providing a full field of view in a reduced scan time.

2.3.4 Resolution

Resolution is the minimum distance required between two objects to detect them as separate objects. It is determined by the extent of acquisition in k-space; if high spatial frequencies are collected then the image is of higher resolution. This means that if

there is reduced acquisition in the phase encode direction with the outer portions of k-space not being collected then resolution in that direction will decrease.

2.3.5 Voxel size

Voxel spacing is determined by the reconstruction options. If zero filing of the edges of k-space is employed before Fourier transformation to the image domain the voxels will be a smaller size, however the fundamental resolution of the image will not change.

2.3.6 Slow phase encode direction

In 3D k-space where two dimensions are sampled using phase encoding, one is termed the slow phase encode direction and the other the fast phase encode direction. Often in structural 3D brain scans the fast phase encode direction is fully acquired between each application of the 180° magnetisation preparation pulse (in one 'shot'). This allows the acquisition of one plane of k-space in each long repetition time (TR), which is the time between encoding the slow phase encode steps. Artefacts often run in the slow phase encode direction as this is the direction acquired most slowly, and so most change could have occurred to the object being imaged during the longer time. The centre of k-space encodes low spatial frequency (contrast) and the outside, high spatial frequency (edges). Thus the collection of the centre portion of k-space in a relatively instantaneous time frame determines the image contrasts component from that shot. This concept is used in the simulation of pulsatile flow artefacts in Chapter 8. In Figure 2-6 an example slow phase encode direction for a linear Cartesian acquisition of a 3D image is shown.

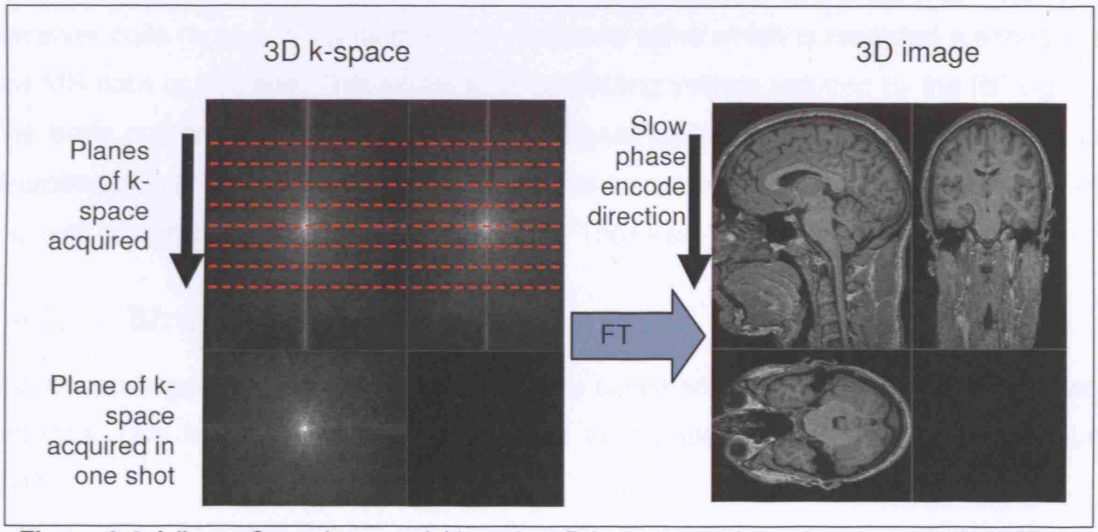

Figure 2-6 A linear Cartesian acquisition of a 3D image, and the order of acquisition of k-space planes giving the slow phase encode direction.

2.3.7 Multiple 3D k-spaces for a single image

Multiple 3D k-space data can be acquired for a single image. These multiple data sets can be acquired at certain time intervals, often used to image moving structures such as the heart. They can also be used to record the images from different coil views, from a parallel array coil. This data can either be treated as separate images for each coil which are reconstructed independently and then added together to give a sum-of-squares image, or they can be reconstructed together using a method such as SENSE [Pruessmann 1999] (see also Section 2.4.2.2). These methods allow the use of the extra information gained from the multiple coils to compensate for sub-sampling in k-space, providing good SNR levels in shorter scan times.

2.4 Different types of RF coils

2.4.1 Transmit coils

These transmit RF at the Larmor frequency of hydrogen, resulting in an oscillating magnetic field at 90° to B_0, which flips the spins and brings them into phase. The body coil, within the scanner bore, is often used as the transmit coil. Certain types of head coil can also be used as transmit coils. These produce RF fields which are very homogeneous in the radial direction, although homogeneity decreases in an axial direction towards the ends of the coil. Transmit coils can also generally be used as receiver coils.

2.4.2 Receiver head coils

Receiver coils receive a signal from the rephased spins which is recorded creating the raw MR data or k-space. This signal is an oscillating voltage induced by the RF signal. The body coil can be used to receive the signal but usually a head coil is used in neuroimaging as it can provide a higher signal to noise ratio. There are two types of receiver head coils which are in common use. These are described below.

2.4.2.1 Birdcage head coil

A birdcage head coil comprises one electrical circuit with axial wire paths joining two endrings. Due to their geometry they result in images with spatially homogeneous SNR.

2.4.2.2 Phased array coil

Phased array coils comprise many electrically separate but often spatially overlapping circuits, or coils. Each coil acquires a distinct set of data simultaneously as the echo is produced. If k-space is fully sampled then a separate image can be created from each coil's data. If k-space is sub-sampled in the phase encode direction, allowing a faster acquisition, the distinct sets of data from the multiple coils can still be used to reconstruct an image with a full field of view. There are various reconstruction techniques; the one used by the Philips scanners on which the majority of the work in this thesis was performed is called SENSE. The different SENSE factors correspond to the level of sub-sampling in the phase encode direction; for example a SENSE factor of 1 means that every line in k-space was acquired, a factor of 2 means that every other line in k-space was acquired etc. Phased array coils were developed more recently and are often used in conjunction with higher field strength magnets. This is because the combination of higher SNR (produced by higher field strengths) and multiple different images collected simultaneously can significantly reduce scan times while still providing images with high SNR. In general head array coils provide higher SNR at the periphery, and similar SNR at the centre, compared to birdcage coils of the same dimensions.

2.5 2D and 3D scans

In T1-weighted, whole brain MRI, 3D scans are often acquired rather than 2D multislice scans. In this thesis the images used are mainly 3D scans. Below follows an explanation of the differences in the two techniques and the advantages of using the 3D method for this application.

In 2D scans, thin slices are selected using magnetic field gradients during excitation and encoded in two directions using frequency encoding in one direction and phase encoding steps in another. The slice profiles are not perfectly rectangular and slice cross talk may occur. 2D data can be acquired sequentially (all data from slice 1 acquired then all data from slice 2 etc.) or in an interleaved manner, where several distant slices can be acquired simultaneously during one TR (e.g. one line of k-space acquired from slice 1, same line acquired from slice 2, etc). This speeds up acquisition by making use of the 'dead time' between excitation and readout. 2D images generally have a lower SNR than 3D scans as signal is only received from one physical slice. If any motion occurs during a 2D acquisition, it appears as steps or discontinuities in the through plane direction, which can cause problems in aligning images from different

time points [Hajnal 2001]. These discontinuities can result in certain spatial areas being under-sampled, making perfect correction of these inconsistencies impossible.

In 3D scans the whole volume is encoded using a secondary phase encoding direction. Signal and noise are therefore obtained from the entire volume, increasing the signal to noise ratio compared to the 2D multi-slice technique, as the secondary phase encode serves as a signal averaging process. Also the problems of imperfect slice profiles and slice cross talk are removed; phase encoding can define many slices without any gap or interleaving being necessary. If motion occurs during the scan its affects are spread throughout the whole image, causing general loss of image quality but still allowing reasonable alignment and comparison of longitudinal images, as long as the motion is not too severe.

2.6 Contrast mechanisms: T1 and T2-weighted images

2.6.1 Tissue contrasts

The intensities of different types of tissue in an MR image depend on the magnitude of the transverse component of each tissue's magnetic moment at the time that the MR signal is read, and the density of hydrogen nuclei (proton density). The contrast between different types of tissues is determined by both the tissue's intrinsic properties and scanner acquisition parameters. These scanner acquisition parameters can be varied to change the relative intensities of different tissue types. This enables the acquisition of differing images of the same region, providing complementary information to facilitate clinical diagnosis and research tasks.

2.6.2 Uses of different contrasts

T1-weighted volumes are good for inspecting neuroanatomy as they can provide good contrast between grey matter, white matter and cerebrospinal fluid (See Figure 2-7); for example, this allows observation of the separate lobes, the deep grey matter and the ventricles. T2-weighted scans (See Figure 2-8) are sensitive to many types of brain pathology. Multiple sclerosis (MS) lesions and many types of malignant tumours are clearly visible in T2-weighted scans. Angiograms depict the brain's blood supply and may be used to assess the patient's risk of suffering a stroke. A useful method for determining fibre orientation and neuronal connections within the brain is diffusion tensor imaging. This thesis mostly focuses on longitudinal image applications using structural information obtained from T1-weighted volume acquisitions.

2.6.3 MR signal decay

As mentioned in the Section 2.2.2.2, after the RF excitation pulse is switched off the MR signal starts to exhibit the free induction decay (FID). This decay occurs in two separate ways: the magnetisation moments start to dephase, and the net magnetisation moment returns to align with B_0. The first of these is called T2 decay and the second T1 relaxation. T2 decay occurs due to magnetic interactions between adjacent nuclei, and inhomogeneities in B_0 (also termed T2* decay). T1 relaxation is due to energy dissipating from the excited nuclei to their surrounding environment. As well as having different proton densities, different tissues exhibit different rates of T1 and T2 decay, which can be used to produce different contrasts between tissue types.

2.6.4 T1-weighted images

Figure 2-7 Example of contrast in a T1-weighted image, note high contrast between grey and white matter

In T1-weighted image acquisition, T1 relaxation is interrupted, by the application of the next excitation pulse, before the net magnetisation moment has returned to align with B_0. Tissues with a fast rate of T1 relaxation, for example fat, have a high intensity in T1-weighted images, as they almost fully recover to align with B_0 between excitation pulses. Tissues with a slow rate of T1 relaxation, for example water, have a low intensity because they only recover partially. If there is a long time between excitation pulses, which allows full recovery of all the tissues' T1 relaxations, then the principle differences in tissue intensities are not due to T1 weighting. For this reason, the time between excitation pulses called Repetition Time, or TR, is kept short in T1-weighted acquisitions: typically less than 600ms. To minimize T2 decay effects, the time between the excitation pulse and the signal acquisition called the Echo Time, or TE, is kept short, typically less than 30ms.

2.6.5 T2-weighted images

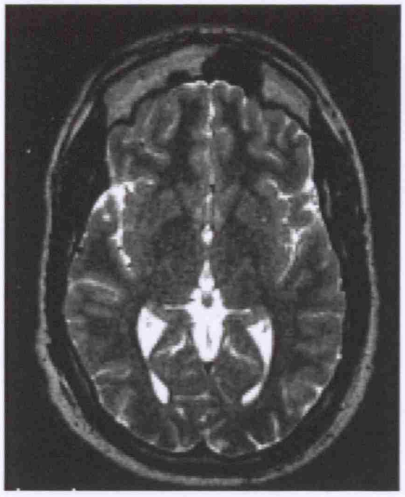

Figure 2-8 Example of contrast in a typical T2 scan weighted image. Note the bright cerebrospinal fluid.

In T2-weighted images TE is typically longer than 70ms, allowing the magnetic moments of the tissue's nuclei to start to dephase at their different rates. For example, the nuclei within fat dephase quickly resulting in lower intensities, compared to water whose nuclei dephase slower resulting in higher intensities for the same TE. To minimise the effects of T1 relaxation a long TR is used, typically of more than 2000ms. Dephasing occurs due to magnetic interactions between adjacent nuclei and because of inhomogeneities in B_0. To rephase the spins in order to obtain an MR signal, either a 180° RF pulse (spin echo), or a gradient (gradient echo) are used.

2.7 MRI pulse sequences

2.7.1 Spin Echo

A 90° RF pulse is applied to flip the magnetisation into the transverse plane. The spins then start to dephase. A second RF pulse with a flip angle of 180° is used to refocus the signal and eliminate the T2* dephasing effects. At a time TE after the initial RF pulse the spins revert to being back in phase, and a maximum signal is produced called the spin echo. Spin echo sequences can also be used to acquire two differently weighted images concurrently, by using an extra 180° pulse after the acquisition of the first echo, to create a second echo. These are called dual echo sequences (See Figure 2-9). A 180° inverting pulse can also be applied at the beginning of the spin echo sequence to manipulate image contrasts; this technique is known as Inversion Recovery.

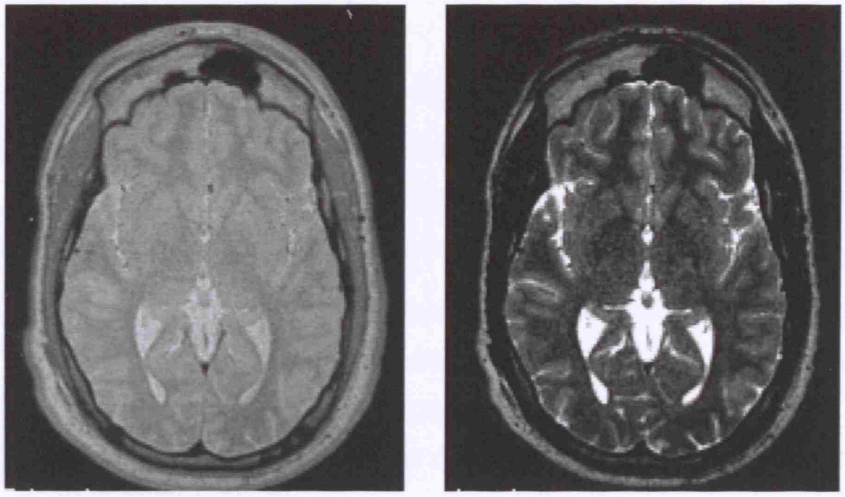

Figure 2-9 Example of images from a dual echo sequence. On the left is a slice from the first echo, in this case proton density weighted. On the right is the second echo image, a T2-weighted image.

2.7.2 Gradient Echo

An RF pulse, of operator-determined flip angle α, produces a signal which is subjected to a magnetic field gradient. The signal is refocused by reversal of an applied gradient rather than a second RF pulse. The repetition time is generally shorter than for a spin echo sequence, as the flip angle is smaller. In successive applications of the RF pulse, since the repetition time is generally shorter than the average T1 for the tissue types in the image, the signal will contain a contribution that is the spin echo of the prior excitation, so the total signal equals the sum of the free induction decay (FID) and spin echo signal. In gradient echo sequences the flip angle in conjunction with the TR determines the T1 weighting. To control contrast behaviour it is possible to apply a spoiler gradient. This is an additional gradient pulse to dephase signals from either the FID component or the spin echo component. For T1-weighted images the spoiler gradients are applied to eliminate formation of spin echoes from previous RF excitations. For T2-weighted images spoiler gradients are used before the echo formation, removing the contribution from the FID and leaving only the spin echo signal from the previous two excitation pulses. An alternative means of spoiling the spin echo contribution in T1 gradient echo is by stepping the phase of the excitation pulses, termed phase cycling; this also gives improved efficiency in timing. The use of a magnetic field gradient, rather than a 180° pulse used in a spin echo (SE), to refocus the signal, results in a smaller signal as only the dephasing due to the magnetic field gradient is reversed, and not that due to the field inhomogenieties.

2.7.3 FLASH/SPGR

FLASH stands for Fast Low Angle Shot and SPGR stands for SPoiled Gradient Recalled acquisition in the steady state. They are similar gradient echo sequences which can acquire an image quickly due to low flip angles and spoiling (removing) any remaining transverse magnetization from the previous echo.

FLASH uses a semi-random spoiler gradient after the echo and removes transverse magnetization by causing a spatially dependent phase shift. This gradient spoiling is less effective than RF spoiling (used by SPGR) and so more T2* information is present in the signal. Vasculature is well demonstrated with flowing blood being very bright.

FLASH type acquisition [Haase 1990]
In this FLASH acquisition, the 3D phase encoding is located inside the 2D phase encoding loop.
3D phase encoding is acquired in two segments. Values acquired in first segment start at the centre of k-space and continue linearly outwards in a positive direction. The second segment acquires phase encode line -1 in k-space and works outward linearly in a negative direction.

One 3D phase encoding step/gradient echo shown below

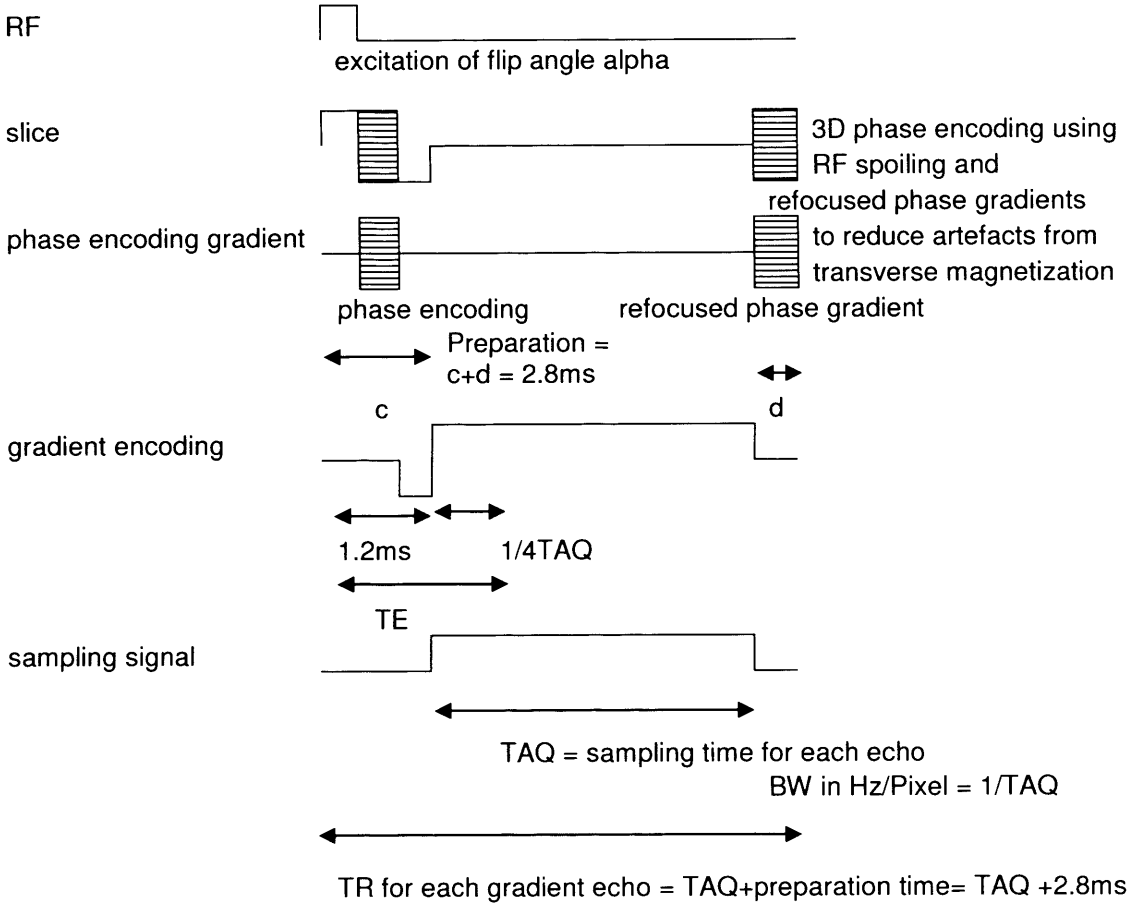

Figure 2-10 The 3D inner phase encoding loop for FLASH type sequences

SPGR uses semi-random changes in the phase of the RF pulses to produce a spatially independent phase shift. This sequence optimises the brighter tissue such as white matter.

The longitudinal magnetization is not affected in either spoiling protocol but, as normal, is a product of the T1 properties of the tissue and the flip angle. Consequently, these sequences can provide images with high T1 contrast if large flip angles and a short TR and TE are used. If a small flip angle is used the images will be more proton density weighted. The results from the preliminary tests for the ADNI trial show SPGR images generally result in better brain-CSF segmentation over MPRAGE images, and on some vendors machines result in superior SNR.

2.7.4 MP-RAGE

MP-RAGE stands for Magnetisation Prepared Rapid Gradient echo. It is another fast 3D gradient echo sequence which is good for fast acquisition of T1-weighted images. This sequence uses an inversion preparation pulse before each segment of k-space is collected instead of a spoiler gradient after each echo. It has a delay time after the acquisition to prevent saturation effects.

The results from the preliminary ADNI trial showed the MP-RAGE sequence is normally quicker than the SPGR sequence for a whole brain acquisition of the approximate dimensions used to acquire images for this thesis. MP-RAGE images also generally have superior grey-white contrast and SNR than SPGR images [Mugler 1990] [Deichmann 2000]. For these reasons the scans acquired specifically for this thesis were acquired using Philips (Philips Medical Systems, Best, The Netherlands) implementation of the MP-RAGE sequence, called the turbo field echo sequence (TFE).

2.7.5 3D Turbo Field Echo Sequence, used in Chapter 4

The sequence which we used to acquire the data for Chapter 4 at 1.5T is described by Philips as a "3D Turbo Field Echo Sequence" (TFE). This is a 3D fast gradient echo sequence which, with the parameters we used, had total scan duration of 4mins 27sec.

The sequence fills k-space in the order described below in Figure 2-11:

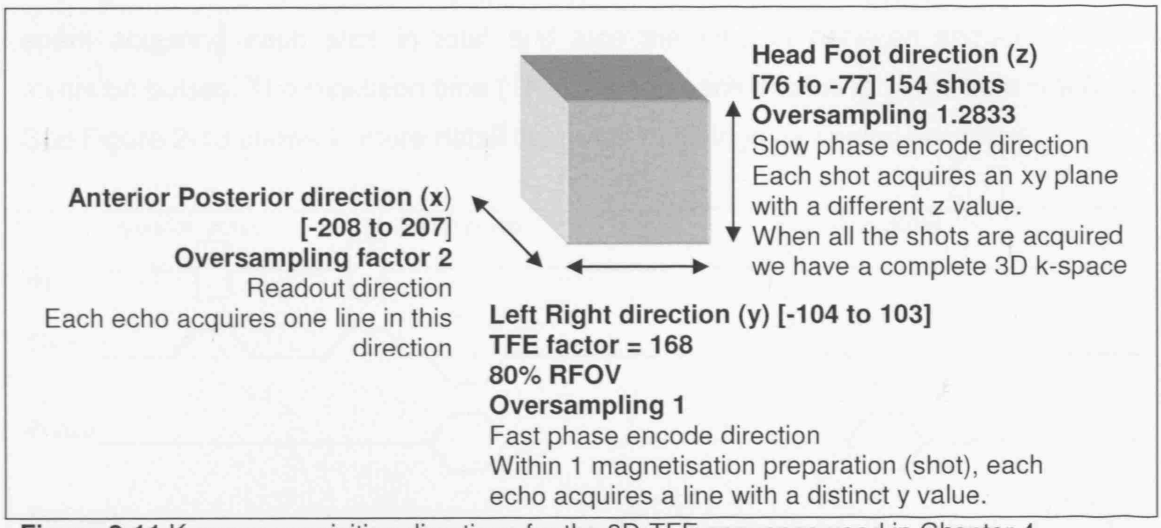

Figure 2-11 K-space acquisition directions for the 3D TFE sequence used in Chapter 4.

The measured voxels are 1.18 x 1.18 x 1.2 mm in size and the reconstructed voxels are 0.96 x 0.95 x 1.2 mm. The reconstructed image matrix is 256 x 256 x 120. The FOV is 245mm. The acquisition matrix after discarding oversampled points and zerofilling is 208 x 208 x 120.

It is comprised of distinct shots which each acquire one plane of k-space perpendicular to the head/foot direction. Each shot is comprised of one 180° inversion prepulse, followed by a train of 8° flip angle excitations, encodings and readouts. As shown in Figure 2-12 below:

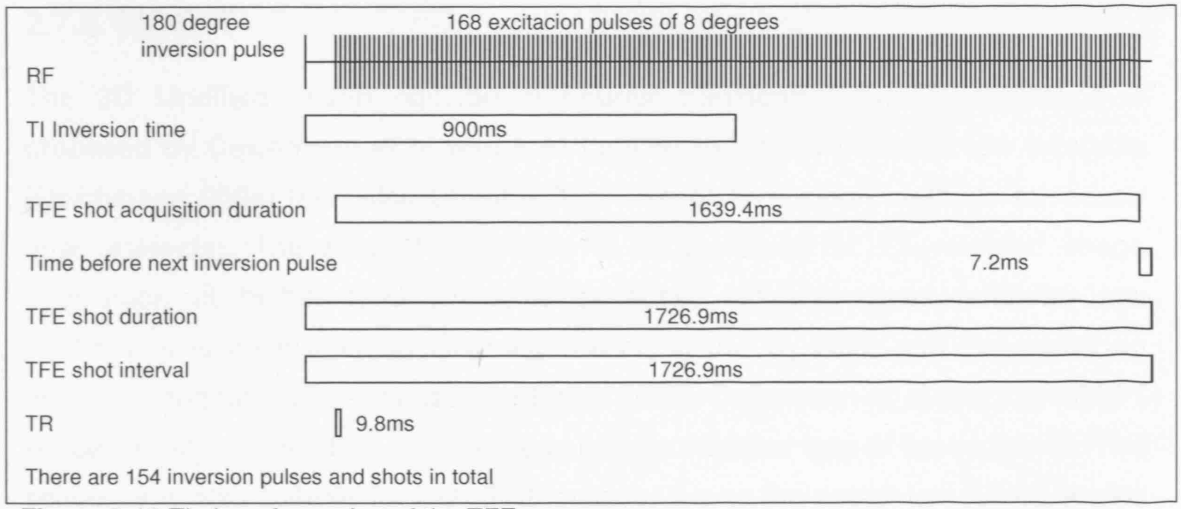

Figure 2-12 Timing of one shot of the TFE sequence

The prepulse inversion time (TI) is defined as the time between its application and the acquisition of the centre k space, which in this sequence occurs in the centre of the train of excitation pulses. At 1.5T TI using this sequence was set to 900ms. The shot

acquisition duration is the time taken to acquire each of the 168 lines in the x direction, starting from the first excitation pulse. The TFE shot duration or interval is the time spent acquiring each shot in total and also the time in between sequential 180° inversion pulses. The repetition time (TR) between each excitation in the train is 9.8ms. See Figure 2-13 shows in more detail the gradient timings for spatial encoding

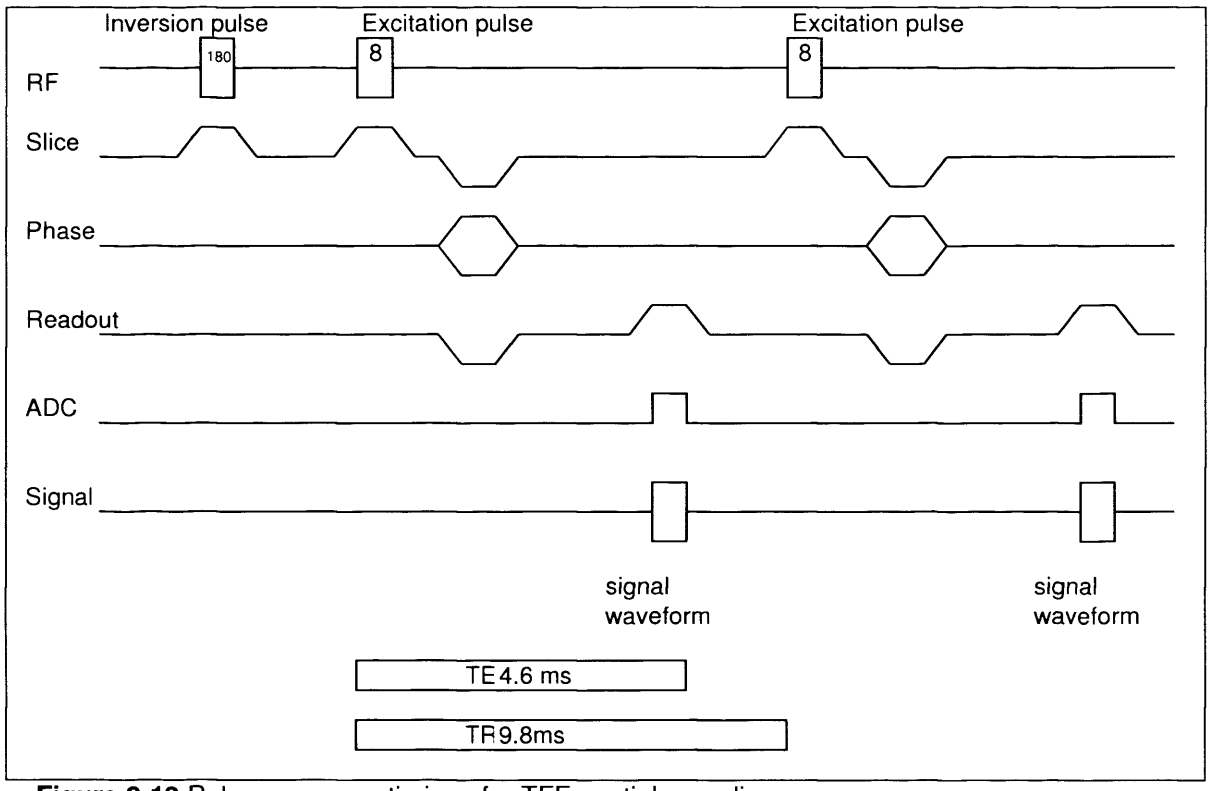

Figure 2-13 Pulse sequence timings for TFE spatial encoding

2.7.6 MDEFT

The 3D Modified driven equilibrium Fourier transform (MDEFT) sequence is proposed by Deichmann et al with spin tagging to reduce pulsatile flow artefacts [Deichmann 2004] (see also Chapter 3 for use of acquisition methods to reduce flow artefacts). The MDEFT sequence is widely used for T1-weighted image acquisition at higher field strengths because, although gives relatively low contrast, it is insensitive to inhomogeneities in the B_1 field, and generates no negative longitudinal magnetization [Norris 2003]. Deichmann et al use the MDEFT sequence with a FLASH type sequence to acquire the inner loop of the sequence. This sequence is also suitable for high field imaging, due to the use of low RF flip angles and short echo times keeping specific absorption rate (SAR) to a minimum.

Acquisition matrix and gradient directions			
NR	Read	head/foot	256
N2D	2Dphase	anterior/posterior	224
N3D	3Dphase, partition	left/right	176

Sequence timings

Below, are sequence timing diagrams generated from the description given in Deichmann's paper. These give an overview of how the 3D MDEFT sequence works.

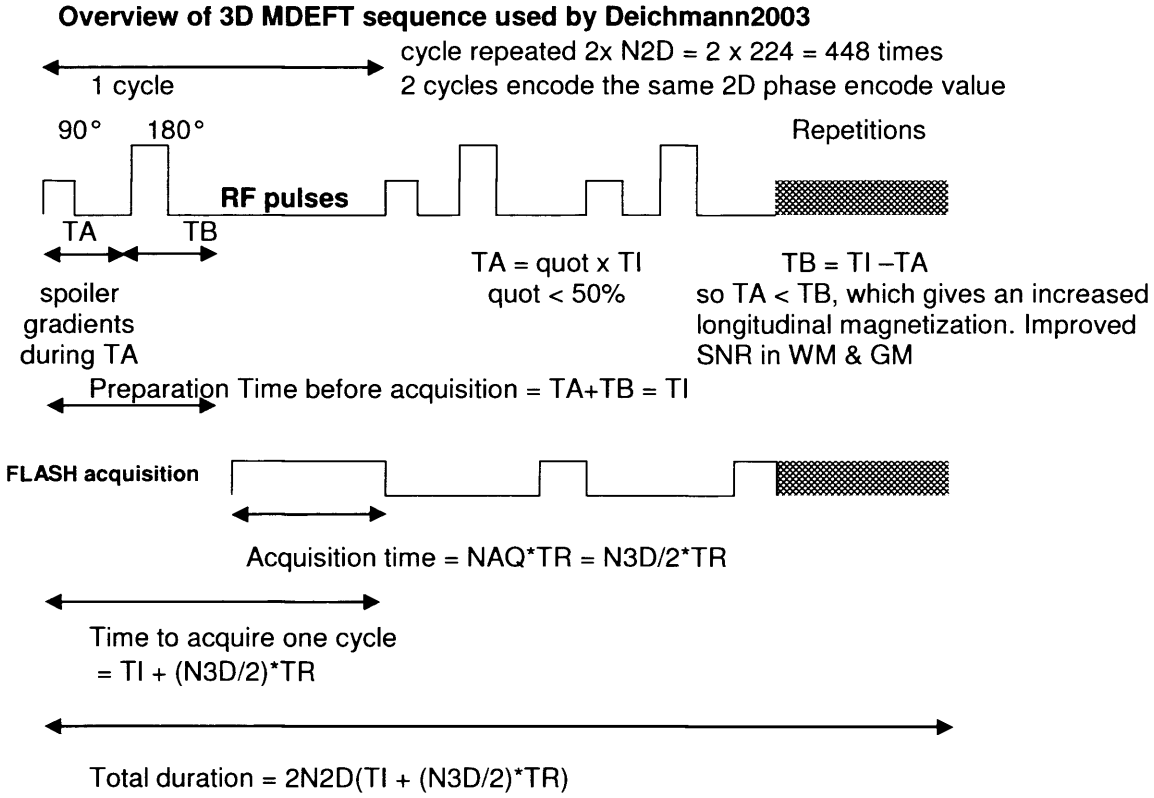

Figure 2-14 Overview of 3D MDEFT sequence used by Deichmann, 2003

Deichmann et al propose using spin tagging during TB (the time interval between inversion and acquisition), successively saturating an axial slice, 5cm thick, through the subject's neck every 80ms. They calculate that this should suppress the signal of spins with velocities of up to 63 cm/s, and therefore effectively saturate the flowing blood during the major part of the cardiac cycle, if normal blood velocities measured in the carotid artery are assumed [Lee 1999]. However, the application of RF pulses with a frequency offset can lead to magnetization transfer (MT) effects. MT affects white matter more than grey matter, leading to a reduction of contrast to noise ratio (CNR).

2.7.7 Comparison of MDEFT vs. TFE

Table 2-1 summarises the differences between the MDEFT and TFE sequences described previously:

	MDEFT	TFE
K-space acquisition	centric	linear
No of outer loop cycles to acquire 1 plane of k-space	2 shots	1 shot
Time needed to prepare each outer loop cycle	tA+tB = TI longer	TI - TAQ/2 shorter
Preparation pulses in outer loop cycle	90 and 180	180
Total scan time	12 mins	4mins 27sec
Acquired voxel dimensions	1mm isotropic	1.2 mm isotropic
Readout	Head foot	Anterior posterior
Outer loop	Anterior posterior	Head foot direction
Inner loop	Left right	Left right direction

Table 2-1 Comparison of MDEFT vs TFE

2.8 Summary

This chapter has given a brief introduction to MRI. It provides an understanding of the particular details of MRI relevant to the work presented in the rest of this thesis. The topics include magnetisation and spatial localisation, k-space, different types of RF coils, 2D and 3D scans, contrast mechanisms, pulse sequences and details of the particular sequence which I used to acquire images for the field strength comparison study in Chapter 4. In the next Chapter, Chapter 3, I provide the background on different types and causes of acquisition artefacts in longitudinal MR neuroimaging.

3 Background to artefacts in MR neuroimaging

I define an artefact to be anything appearing in an image which does not reflect the physical reality of the object being imaged, both in terms of location and intensity. In MRI there are many different types of artefacts which can occur. There are those which may occur due to problems with the imaging equipment, there are also artefacts which occur as a result of the object being imaged.

This chapter provides the background necessary to understand the different types and causes of artefacts discussed in Chapter 5, and to understand the simulation and correction of artefacts in Chapter 6 and 8, as well as providing a general background to all the work in this thesis.

Below is a summary of the sections of this chapter:

3.1 Noise in MR images: this looks at the nature of noise in the MR images used in this thesis, providing the background necessary to simulate different levels of noise such as in Chapter 6 and 8.

3.2 Imaging equipment artefacts: this provides some background for Chapter 5 and for the entire thesis.

3.3 Object dependent artefacts: including motion artefacts, pulsatile flow artefact and acquisition methods of reducing pulsatile flow artefact, which are specifically referred to in this thesis.

3.4 Summary

3.1 Noise in MR images

Noise in MR images of high intensity voxels is a Normal distribution of both the real and imaginary components centred on the true voxel intensity. In regions where the true voxel intensity is zero the modulus images exhibits Rician distributed noise (see Figure 3-1 for a visual example of a Rician distribution). Rician noise occurs as MR images are displayed as modulus images. In regions of zero signal, the raw noise is a Normal distribution centred on zero for both the real and imaginary components. However, when the modulus image is calculated (by squaring both of these distributions, adding them together and then taking the square root) a Rician distribution results. Low intensity voxels in modulus images do not therefore exhibit a perfect Normal distribution but rather tend towards a Rician distribution.

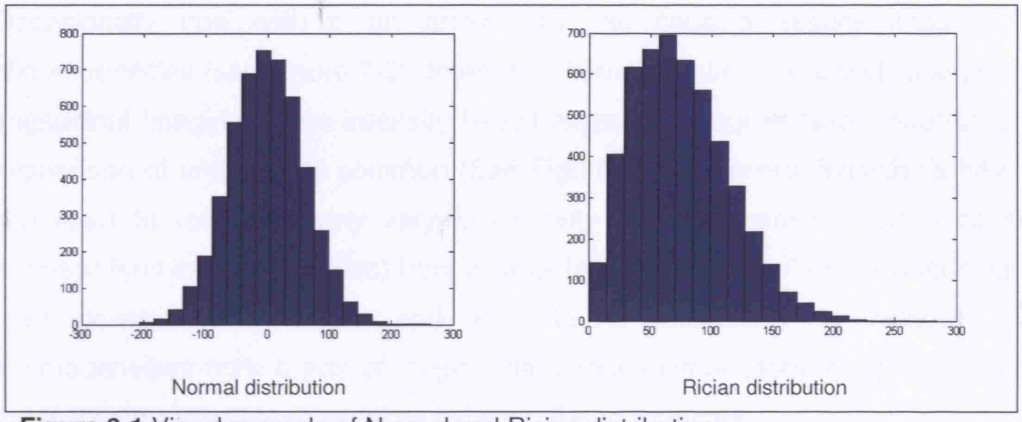

Figure 3-1 Visual example of Normal and Rician distributions

3.2 Imaging equipment artefacts

3.2.1 Intensity inhomogeneities

Intensity inhomogeneities, in MR images, are mainly cause by B_1 (transmit coil) field inhomogeneities. Equipment which provides a more homogeneous field, for example transmit head coils in the radial direction, and 1.5T magnets rather than 3T (see Section 2.2.1 on magnetic field strength), will result in acquisition of scans with greater intensity homogeneity. Array coil images can also display intensity inhomogeneity across the field of view due to receiving different relative levels of signal received from different parts of the imaging volume. More signal is received from the peripheries of the imaging volume and less from the centre. Although many scanners reconstruct array coil images aiming to take account of this signal variation, often with the help of coil sensitivity maps acquired at the beginning of each imaging session, there is usually some residual intensity inhomogeneity across the images.

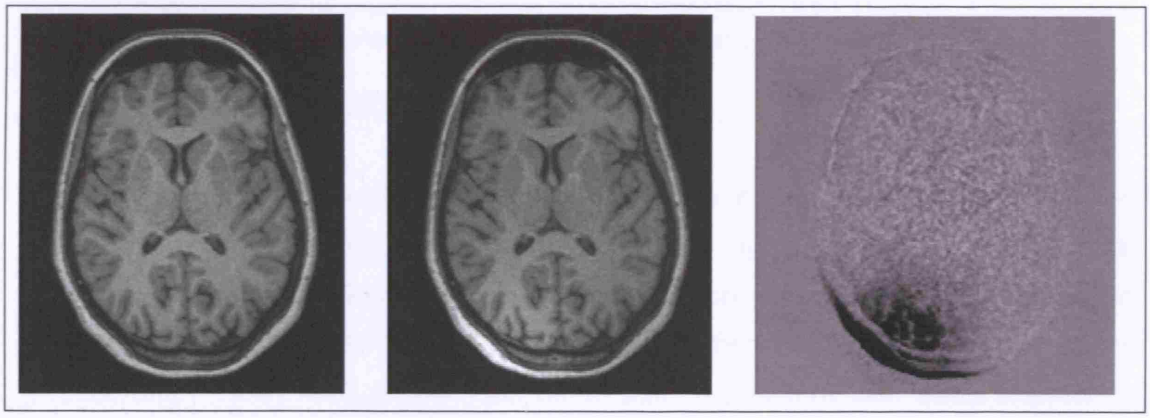

Figure 3-2 Coil array malfunction. One coil is a different intensity to the others.
Left image: Baseline scan. Centre image: Repeat scan with coil malfunction. Right image: Difference image showing the difference in intensity between scans.

Occasionally one coil in an array may fail causing severe image intensity inhomogeneities (see Figure 3-2). Intensity inhomogeneities are a particular problem in longitudinal imaging where intensity based alignment, segmentation, subtraction, and comparison of images are common (See Figure 3-3). Several algorithms have been developed to remove slowly varying intensity inhomogeneities (usually caused by magnetic field inhomogeneities) from images [e.g. Sled 1998]. One such technique has been developed by Lewis and Fox, 2004, particularly to remove differing inhomogeneities from a pair of longitudinal images simultaneously, by comparing the slowly varying intensity differences between the two images.

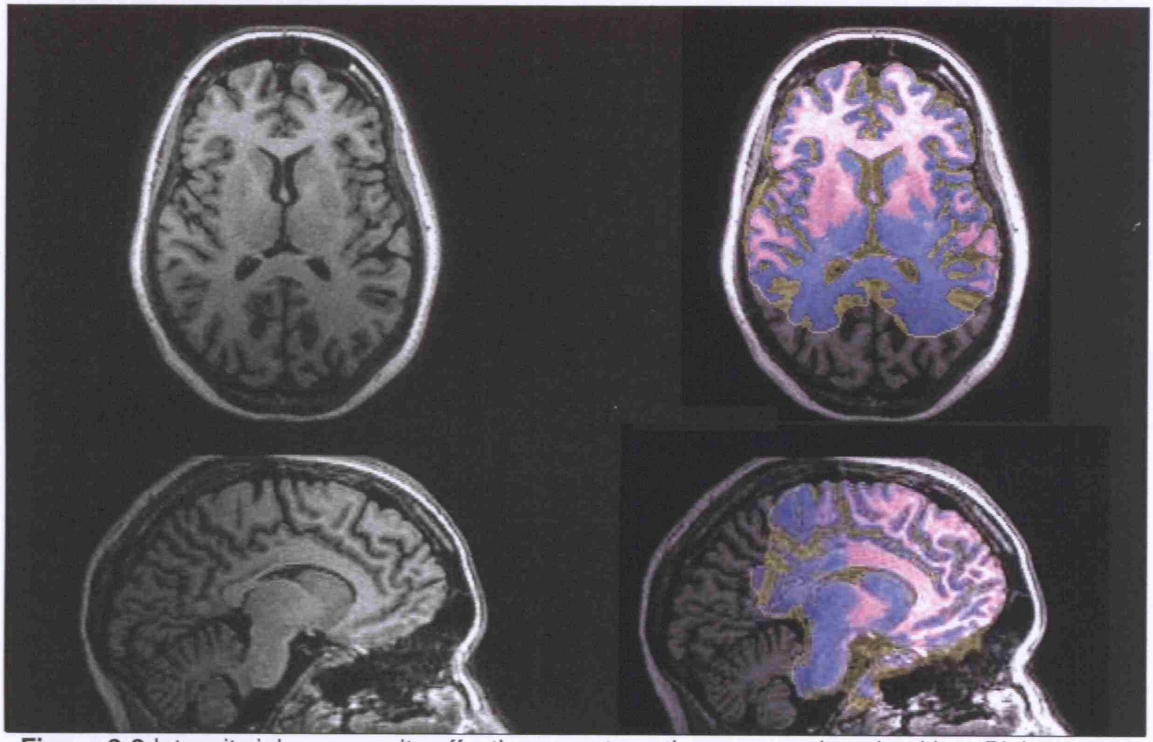

Figure 3-3 Intensity inhomogeneity effecting an automatic segmentation algorithm. Pink represents white matter, blue is gm, yellow is cerebrospinal fluid (CSF). However it can be seen that this segmentation has failed as these colours do not overlay the correct regions.

3.2.2 Gradient miscalibration

Linear gradient miscalibration can result in scaling errors. Voxel dimensions can change between timepoints, due to scanner instability, by up to 1-2% for a commercial scanner [Freeborough 1997]. The skull in conjunction with affine registration of the images can be used to normalise the voxel dimensions in longitudinal scans [Freeborough 1997]. Multicentre trials often scan a phantom with each scanner to determine any geometric differences between sites. Some MR systems have traded off gradient linearity for other performance characteristics. This nonlinearity causes spatial distortion also known as non linear stretch. Examples of systems with gradient non

linearity are the GE systems, which offer 2D in-plane distortion correction as default (called grad warp), however, there is no correction in the slice direction which can result in spatial distortion. The distortion correction algorithms can also result in different types of spatial distortion occurring.

3.3 Object dependent artefacts

3.3.1 Bulk motion

Bulk motion can be caused by a subject moving during acquisition. This could be due to relaxation of muscles, coughing, breathing, or the subject's inability to lie still. This is often a problem with younger children and older patients who may not remember, or understand, why they should remain still. Others may suffer from a residual tremor which will cause problems in obtaining good quality MR images. One problem with motion is that it can result in non-uniform sampling in the Fourier domain, with respect to the subject. This can result in many ghost images appearing periodically across the field of view in the phase encode direction, whose spacing and intensity depend on the pulse sequence timings and the velocity and periodicity of the motion [Ehman 1986]. This is usually seen most clearly as ringing of the scalp across the image. As well as ghost images, motion artefact can lead to image blurring which increases with the amplitude of the motion [Schultz 1984].

3.3.2 Susceptibility artefact

Different tissues have different magnetic susceptibilities; this causes local magnetic field variations, which can result in displacement within an image of the anatomy, particularly in areas of very different magnetic susceptibilities such as air/brain boundaries. For example, these susceptibility artefacts are often present at the interface between the petrous bone and the base of the brain [Xu 2000].

3.3.3 Chemical shift artefact

This is caused by hydrogen protons in different chemical environments exhibiting slightly different Larmor frequencies. This causes them to appear displaced in the image domain as the frequency is not just spatial dependent but also dependent on the composition of the tissue. This can be seen clearly at many fat/water boundaries, where the fat may appear displaced up to a few millimetres from where it is anatomically located along the frequency encode direction.

3.3.4 Wrap around

If the top of the head is outside the field of view this may wrap round into the bottom of the brain, or the nose may wrap around into the back of head. This can make alignment and analysis of images more difficult. Wrap occurs when any part of the imaged object lies outside of the selected field of view. This causes the range of frequencies in the received signal to increase beyond the Nyquist limit (the Nyquist limit is half the sampling frequency). This means that the frequencies above the Nyquist limit are incorrectly mapped to lower frequencies. Wrap can occur in any direction, but to avoid this oversampling is normally employed in the frequency encode direction as this can be done without changing the scan time. Wrap most often occurs in the phase encode direction as oversampling in this direction is time consuming. However, on Philips scanners, oversampling in the phase encode direction by a factor or 20-30% is still normally preformed.

3.3.5 Pulsatile motion/Flow artefact

Local motion or contrast change within the object being imaged such as non linear deformations of the pulsating brain, eye movement and pulsatile CSF and cerebral blood flow will result in aliasing of the structure involved in the phase encode direction. Unsaturated spins in blood and CSF entering the imaging volume appear much brighter than stationary blood. Pulsating flow artefacts appear due to the changing rate of flow in each shot, giving the vessels a different apparent intensity at the time each shot is acquired. This results in a striped artefact running in the slow phase encode direction. In the following sections I give more detail from the literature describing various flow artefacts.

3.3.5.1 Flow related intensity changes

To explain the formation of the ghost images associated with pulsatile flow artefact it is first necessary to describe the intensity changes which can be caused by flow.

In flow related enhancement, described by Bradely et al 1985, vessels with flowing blood appear bright relative to their surroundings. It occurs where unsaturated protons enter the imaging volume and emit a strong signal relative to the partially saturated adjacent tissue. The degree of flow related enhancement is proportional to the blood flow velocity and the TR of the sequence.

Two other effects which can darken the vessel are both phase related. The first is incorrect localisation of vessel signal due to the accumulation of phase as the spins move through the gradient field, and the second is loss of intensity caused by the dephasing of the blood signal. This effect occurs when spins within a single voxel are moving with different velocities through the gradient field, therefore acquiring different phases. The increasing variation of phases within a voxel causes increasingly substantial dephasing, resulting in considerable intravascular signal loss.

3.3.5.2 Pulsatility artefact in 2D MRI

Perman et al, 1986, investigated artefacts arising from the pulsating nature of blood flow. They describe pulsatile flow artefacts as having "characteristic bright and dark 'ghosting' patterns which appear close to vessels, usually arteries that generates the artefact". The ghosts are likened to periodic motion artefacts, such as those arising from the beating heart or from breathing, which propagate bright and dark ghosts in the phase encode direction.

The motivation behind their work was their concern that pulsatile flow artefacts may cause "serious confusion in the interpretation of a clinical MR image". They observe that these ghost artefacts are present on images acquired by scanners made by different manufactures, and they "come and go irreproducibly depending on minor, seemingly insignificant, changes in scan sequence parameters and sometimes with no changes".

Perman et al propose that the strength of the artefact depends on flow velocity and its degree of pulsatility, with steady flow conditions not exhibiting these artefacts. The spacing of ghost artefacts in the image is determined by the temporal beat pattern between the image gradient encoding steps and the pulsatile period. They use this to explain the observation of blood vessel pulsatile artefacts being "sporadic and seemingly irreproducible".

The mechanisms which produce these ghosts in 2D images were explained by Ehman in 1986. They involve the flow related intensity changes described in the previous section. He explained them as view-to-view modulation of the magnitude and of the average phase angle. Phase modulation is caused by the degree of phase mis-mapping varying from view-to-view. Magnitude modulation is caused by view-to-view differences in the quantity of relatively unsaturated spins that are washed into the imaging volume (flow related enhancement) and also by the variation in the degree of

intensity loss due to velocity related intravoxel dephasing.

Felmlee and Ehman, 1987, when working on their presaturation pulses to reduce pulsatile flow artefacts, concluded that flow related enhancement is the basic problem. By saturating flowing spins so that their longitudinal magnetization is very small when they enter the plane of section, flow artefact ghost are suppressed because the view-to-view intensity change is effectively removed.

3.3.5.3 Pulsatility artefacts in 3D MRI

Frank at al, 1993, describes the nature of pulsatile flow artefacts in 3D MRI. They create a numerical simulation of this artefact which is compared with experimental images of an elastic model of a human carotid artery under simulated physiological conditions, and also with images of 2 human subjects. He calculates where ghosts may occur within the 3D volume. Ghosts are located along a line, which extends from both sides of the causing vessel. A formula is given to calculate the angle of the line the ghost lie along (this formula is used in Chapter 8, Section 8.3.1 when simulating flow artefacts). The line lies in the plane defined by the two phase encode directions, and other imaging acquisition parameters define the angle of the line within this plane.

Petersson and Christoffersson in 1999, demonstrated clear pulsatile flow related ghost artefacts in image sets generated with pulsatile, plug flow. They also showed pulsatile flow related ghost artefact remains basically the same when the plug velocity profile is replaced by a laminar one. The only slight difference with the laminar flow profile was that the slowly moving spins in the outer part of the vessel become saturated, resulting in lower signal intensity, making the diameter of the vessel downstream appear smaller. As artefacts are shown to be basically the same for plug and laminar flow profiles I choose in my method to simulate the more straightforward plug flow.

3.3.5.4 Pulsatility artefacts in fast magnetization-prepared sequences

Tasciyan and Mitchell, 1994, investigate fast magnetization prepared sequences for abdominal imaging. The TR of these sequences tends to be too short to allow gradient moment nulling (for more detail on gradient moment nulling see Section 3.3.6.3), however the authors do not see this as a problem because TE is also short so that little within-view phase dispersion due to gradient moments occurs. However artefacts arise from view-to-view amplitude modulation caused by pulsatile blood flow.

View-to-view variations, in the mean phase and in the amplitude, cause ghost artefacts. The authors of this paper study the ghost artefacts as a function of amplitude modulation only. They do this because variation in phase will affect the relative contribution of the real and imaginary components but will not affect the magnitude of the artefacts. This is also the approach that I will take in my model in Chapter 8 choosing to only model amplitude view-to-view variations.

Tasciyan and Mitchell also show that pulsatile flow artefacts increase considerably with flip angle. Any repetitiveness in the magnetization pattern increases the artefacts, whether due to ordering of shots or faster pulse rate in same TR, or longer TR. Any method that disrupts the repetitiveness or narrows the magnetization range (difference between max and min magnetizations) will reduce pulsatile flow artefacts. When there is little periodicity, blurring due to modulation over the cardiac cycle is observed rather than distinct ghost artefacts.

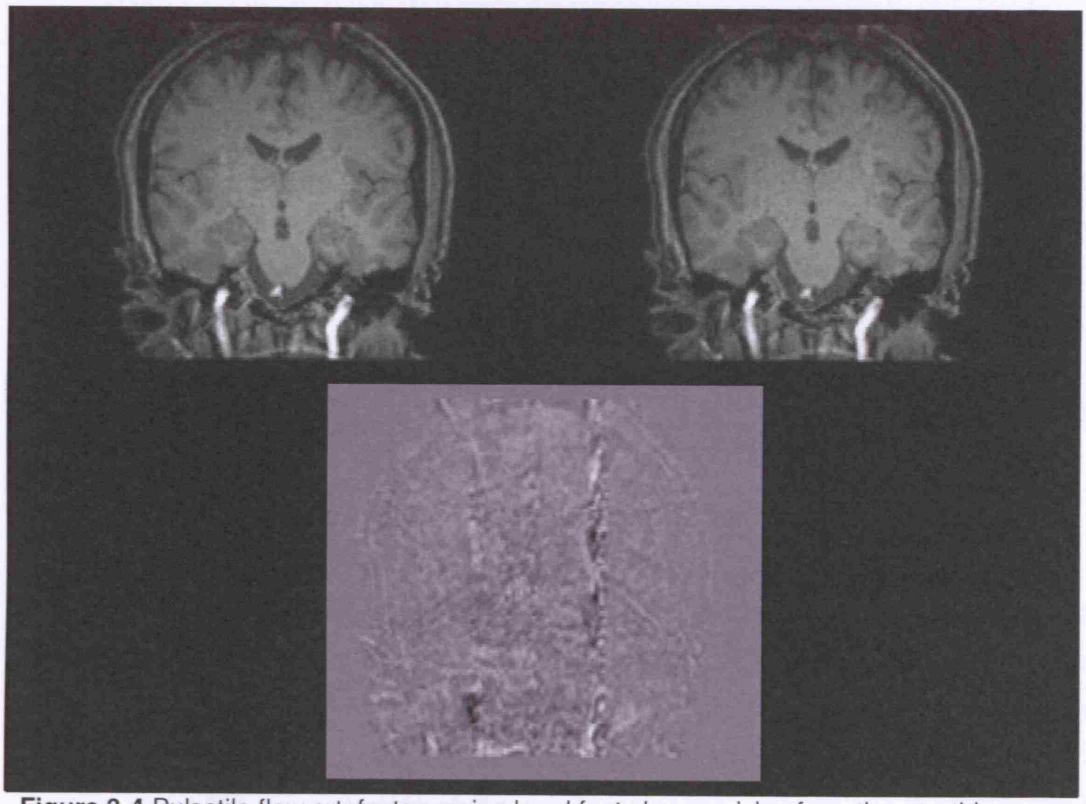

Figure 3-4 Pulsatile flow artefacts running head foot shown arising from the carotid arteries, seen in the baseline and follow up scan top row, and subtraction image bottom row using a 3D TFE sequence.

3.3.6 Acquisition methods of reducing pulsatile flow artefact

This section gives an overview of some acquisition solutions which can be used to reduce pulsatile flow artefacts for completeness. It is not intended to be an in-depth

study on sequence design. The majority of longitudinal multi-centre trials are carried out on a variety of manufacturer's scanners, of different models and running different software versions. This means that pulse programming and tailoring sequences is not a viable solution to reduce flow artefact. Spatial presaturation (available on the majority of scanners) could be used but potentially carries with it associated costs outlined in Section 3.3.6.4. Post-acquisition methods of correcting artefacts are discussed in Chapter 8 where a novel algorithm for reducing pulsatile flow artefact from 3D head images is proposed.

3.3.6.1 Change of slow phase encode direction

Changing acquisition direction can sometimes be used to relocate artefact away from a particular region of interest [Felmlee 1987]. However, this may not be suitable for all regions. In whole-brain analysis, any flow artefact is highly undesirable, regardless of its location.

3.3.6.2 Cardiac gating/pseudo-gating

Diastolic pseudo-gating, or synchronization of the cardiac cycle and the MR pulse sequence could both be used to reduce pulsatile flow artefacts. Felmlee and Elman, 1987 showed that cardiac gating of images consistently demonstrates improvement of flow artefacts. However, it would be time consuming and impractical to implement cardiac gating as a flow artefact reduction technique within a multicentre longitudinal study.

3.3.6.3 Flow compensation /Gradient Moment Nulling

Flow compensation, or gradient moment nulling as it is also known, uses gradient lobes to minimize the net phase accumulation of flowing blood. It ensures that during an echo the magnetization signal vectors for all pixels have zero phase angle independent of velocities, acceleration of the measured tissue. Anti-symmetrical gradient lobes are used to make the net moments of the amplitude of the waveform of the magnetic field gradients, zero at the time TE. [Felmlee 1987]. Flow compensation can partly reduce the amount of view-to-view phase modulation since it corrects the intensity variation caused by phase dispersion. It does not correct the component caused by flow related enhancement and so cannot by itself remove all pulsatile flow artefacts. This was demonstrated by Buxton et al in 1993 when using flow-compensated gradient

waveforms and still observing prominent image artefacts, including periodic ghosts caused from the periodic flow.

3.3.6.4 Flow saturation slabs

Flow saturation slabs can usually be used to reduce pulsatile flow artefacts, with a possible reduction of contrast to noise ratio (due to Magnetization transfer, MT, effects see Section 3.3.6.5), and depending on the exact sequence they can increase scan time. The idea of flow saturation slabs was suggested by Felmlee and Ehman in 1987. These slabs reduced pulsatile flow artefacts by controlling the spatial distribution of longitudinal magnetization outside the volume of tissue that is imaged. This is done by applying additional, interleaved, spectrally shaped radio frequency pulses during imaging, selectively saturating spins outside the image volume. The method is applicable to most MR pulse sequences on most scanners. The RF pulses are typically about 3ms long and designed to selectively saturate spins in regions exterior to the image volume. The spectral content of the RF pulses is determined by the location and dimension of the desired presaturation regions and is constant during image acquisition. The additional RF pulses increase the rate of energy deposition of the sequence, which can be an issue at high field strengths (See Chapter 2, Section 2.2.1 for more details on RF energy deposition). The cycle time for acquisition of each view is increased on the order of 3-6 milliseconds, or less if there is any free time between echoes in the sequence. There are contrast-to-noise ratio (CNR) losses with the use of flow saturation slabs with certain sequences, as shown in the following section where saturation pulses are used in conjunction with the MDEFT sequence.

3.3.6.5 MDEFT with Spin tagging in the neck

The use of spin tagging in the neck has been shown by Deichmann et al, 2004, to reduce blood flow artefact in conjunction with a saggitally orientated 3D Modified driven equilibrium Fourier transform (MDEFT) sequence (see Chapter 2, Section 2.7.6 for more details on the MDEFT sequence). The disadvantage of this approach is that it results in a considerable loss of CNR (12%), and is not applicable across different scanners as would be needed in a longitudinal clinical trial. This is because the MDEFT sequence cannot easily be implemented on all manufacturers' scanners. The spin tagging method is the insertion of RF pulses which successively saturate (every 80ms) an axial slice through the subject's neck with a thickness of 5cm. The loss in contrast-to-noise ratio (CNR) may be due to applying an RF pulse with a frequency offset

causing MT effects, as these affect white matter more than grey matter. The SNR loss was 9% in white matter and 6% in grey matter. (Magnetization transfer effects are caused by the application of an off resonance RF pulse saturating protons in macromolecules. During the pulse sequence this magnetization can be transferred to free water protons, decreasing the MR visible signal in areas of macromolecules affected by MT, such as normal grey and white matter).

3.4 Summary

This chapter has presented the background information necessary to understand the different types and causes of artefacts which will be discussed in Chapter 5, and to help understand the simulation and correction of artefacts in Chapter 6 and 8. It has provided the general background to the work with artefact covered in this entire thesis. The topics include a range of different artefact types from noise, through imaging equipment artefacts, to object dependent artefacts. Within object dependent artefacts, motion and pulsatile flow artefacts (focused on in Chapters 4, 6, 7 and 8) are specifically mentioned and acquisition methods of reducing pulsatile flow artefact are also included.

The next five chapters comprise the novel work of this thesis. In the next Chapter I investigate the effect of field strength on artefacts, focusing in my investigation on its effect on pulsatile flow artefact.

4 Artefacts in longitudinal images at different field strengths

4.1 Introduction
  4.1.1 Aims
  4.1.2 Contribution
4.2 Literature Review
  4.2.1 Qualitative comparison of a variety of artefacts at 3T compared with 1.5T
  4.2.2 Motion artefacts comparison
  4.2.3 Chemical shift and susceptibility comparison
  4.2.4 Intensity inhomogeneities comparison
  4.2.5 Pulsatile flow artefacts comparison
4.3 Method
  4.3.1 Image acquisition
  4.3.2 Image analysis
    4.3.2.1 Quantitative analysis
    4.3.2.2 Qualitative analysis
4.4 Results
  4.4.1 Quantitative analysis
  4.4.2 Qualitative analysis
4.5 Discussion
4.6 Conclusion

4.1 Introduction

There is substantial interest in using serial MRI as a biomarker to monitor the progression and treatment of dementias such as Alzheimer's [Fox 1999]. In large studies the analysis is often carried out using automated or semi-automated image analysis tools, which often give more consistent results compared to manual techniques. Automated techniques can make analysis of large study sizes more feasible due to their faster processing speed and their potential to exhibit higher reproducibility; however, they can be confounded by artefacts present in scans [Preboske 2006].

3T scanners are becoming increasingly common in both clinical and research settings because at 3T the signal to noise ratio (SNR) increases significantly relative to 1.5T levels [Ruggieri 2002, Maubon 1999]. SNR increases by a factor of approximately 2 depending on the exact sequences and scanners used. (See Chapter 2, Section 2.2.1 for further background on magnetic field strength of scanners). However, as well as changes in SNR the relative artefact levels present at 3T also change, as some types of artefacts are dependent on magnetic field strength [Farahani 1990]. While research has been directed at optimizing gradient echo volume sequences for structural neuroimaging at 3T [e.g. Deichmann 2004], the implications of higher field strength for

longitudinal neuroimaging studies have received less attention.

In this chapter I look at existing literature which compares artefacts at 1.5T and 3T. First, I look at a qualitative comparison of a variety of artefacts at 3T compared to 1.5T (Section 4.2.1). Next, I look at the effects of the increased field strength on specific different types of artefacts: motion (Section 4.2.2), chemical shift and susceptibility (Section 4.2.3), intensity inhomogeneities (Section 4.2.4) and finally, flow artefacts (Section 4.2.5), which I shall investigate further in the following sections.

4.1.1 Aims

I aim to compare both quantitatively and qualitatively the extent of flow artefacts in both 1.5T and 3T scans acquired using a typical 3D MP-RAGE sequence, in order to assess the likely consequences of moving longitudinal imaging studies to 3T scanners. To perform this quantitative comparison, I aim to develop a novel image processing technique to quantitatively compare relative artefact levels between longitudinal scans carried out at different field strengths.

4.1.2 Contribution

This chapter illustrates the increase in severity of flow artefacts in images from clinical trials acquired on scanners with a magnetic field strength of 3T, whose acquisition protocols have been moved from scanners with a magnetic field strength of 1.5T without considering the issues of change in relative artefact levels. It then introduces an artefact quantification technique (developed further in Chapter 5), which has many applications. First, this atrophy quantification has the potential to be used in producing an automatic quality check for scans obtained in high throughput clinical imaging trials. Second, the results from artefact quantification have the potential to be used as cost functions in artefact correction algorithms. Finally, this technique could provide adjustments or levels of confidence for automated measures, such as local atrophy quantification techniques.

The imaging sequences run at 3T and 1.5T were identical, with the exception that the inversion time (TI) was optimised to provide the best SNR and contrast to noise ratio (CNR) at both field strengths. Alex Dresner performed theoretical modelling for both field strengths to calculate the best TIs for both sequences. He then acquired test images at 3T. Derek Hill and I performed the test acquisitions at 1.5T. Julie Fitzpatrick also helped with scanning at both sites. Scans for the experiment were acquired by Alex Dresner, Marc Miquel, Derek Hill, and myself. The compilation and analysis of all

the images was my own work. For qualitative analysis, I randomised the images from different field strengths and presented them to a radiologist, Rolf Heckemann, who visually rated the severity of artefacts.

4.2 Literature review

There have been some studies in the literature exploring the effects of field strength on artefacts and the resultant problems they cause to image processing techniques in neuro imaging studies using MR. However, to the best of my knowledge there have not been any studies which carry out quantitative comparisons of acquisition artefacts that affect longitudinal dementia trials, across field strength in neuro MRI. In this section I review some studies which carry out qualitative assessments of artefacts across field strength.

4.2.1 Qualitative comparison of a variety of artefacts at 3T compared with 1.5T

The most comprehensive paper qualitatively examining differences in artefacts between 1.5T and 3T is the work of Nobauer-Huhmann, 2002. In this study, identical 2D T1- weighted spin echo protocols were acquired at both 3T and 1.5T on 16 patients with brain tumours, using a head birdcage transmit/receive coil. Three independent radiologists qualitatively assessed the images for artefact. Motion, susceptibility and other artefacts were graded as 1 (absent), 2 (mild), 3 (moderate) or 4 (severe). The mean values were calculated from the three radiologists' scores. The images were printed on films with field strength and patient name masked. Window settings were adjusted to minimize visual contrast differences in brain tissue between the two sets of images. While motion artefact did not significantly differ with field strength, the results for both pre and post contrast scans indicated that susceptibility and other artefacts (including observed pulsation and ringing artefacts) were significantly higher at 3 T than at 1.5 T (see Table 4-1).

Sequence	Median score at 1.5T	Median score at 3T	Significance at 5% level of difference in level between 1.5T and 3T
Motion artefacts T1 pre	1.0	1.1	No
Motion artefacts T1 post	1.1.	1.2	No
Susceptibility artefacts T1 pre	1.0	1.3	Yes
Susceptibility artefacts T1 post	1.0	1.3	Yes
Other artefacts T1 pre	1.5	2.1	Yes
Other artefacts T1 post	2.1	2.4	Yes

Table 4-1 Artefact scores at 1.5T and 3T from Nobauer-Huhmann, 2002

4.2.2 Motion artefacts comparison

Although the study above showed no significant relationship between motion artefacts and increased field strength on the sequences used, recent research on more modern sequences [Deichmann 2004, Howarth 2005] suggest otherwise. These studies point out that subject motion can cause a ringing artefact, which when using a 3D T1-weighted gradient echo sequence, such as FLASH, MP-RAGE or MDEFT, appear worse at 3T. As the T1 value of fat is lower at higher field strengths, the scalp and peripheral fat regions appear very bright, especially when using phased array coils which have improved sensitivity in peripheral areas. These studies suggest this artefact can be avoided by using a chemical shift selective, fat saturation pulse. It is interesting that while the Nobauer-Huhmann study shows no detectable increase in motion artefacts, it does report an increase in "other" artefacts, including ringing artefacts that can arise from motion.

4.2.3 Chemical shift and susceptibility comparison

Schmitt et al, 2004, highlight in particular how larger chemical shifts and stronger susceptibility effects need to be considered when using increased field strength. Frayne et al, 2003, also show that chemical shifts in gradient echo imaging result in regions of fat displaced twice as far compared with regions of water, than seen at 1.5T. Increasing the acquisition bandwidth at 3T can reduce the magnitude of this error, although with the penalty of reducing SNR.

4.2.4 Intensity inhomogeneities comparison

Cohen et al, 2000, highlight that 3T data, known to suffer from larger intensity inhomogeneities than 1.5T data, can degrade the performance of automatic segmentation tools. They suggest correcting inhomogeneities before using these tools.

4.2.5 Pulsatile flow artefacts comparison

Flow artefacts have been shown to cause problems in longitudinal neuroimaging. At 1.5T, these artefacts can obscure the boundaries of temporal lobe structures for manual delineation [Xu 2000] and can confound lesion change measurements in multiple sclerosis (MS) studies [Lemieux 1998]. I now look at the existing literature for the effect on this artefact of moving acquisition to 3T.

Felmlee et al, 1987, observed that pulsatile flow artefacts are very prominent when attempting to improve SNR using techniques such as the implementation of surface coils and acquiring at higher field strength. Their hypothesis is that the lack of saturation of flowing spins is the most basic cause of pulsatile flow artefact. This argument is supported by the observation that flow artefacts seem to be a greater problem at higher field strengths. At a given TR, tissues are more saturated at higher field strengths due to the longer T1 relaxation times. As a result, the degree of unsaturated blood flowing into the imaged section from outside is greater at higher field strengths. Therefore, the degree of intensity differences due to inflow effect results in greater flow artefact formation (for background on flow artefacts, please refer to Chapter 3, Section 3.3.5).

Deichmann et al, 2004, show that the 3D T1-weighted MDEFT sequence at 3T causes blood vessels to appear with very high intensities, giving rise to strong pulsation artefacts in the 2D phase direction (this is the outer acquisition loop encoding direction, see background Chapter 2, Section 2.7). These artefacts affect areas of brain tissue adjacent to the blood vessels. For example, in Deichmann's experiment, where the 2D phase direction is anterior/posterior, the readout direction is head/foot, and the corpus callosum and the brain stem were affected.

All the current studies in the literature on longitudinal dementia imaging only provide a visual comparison of artefact levels. Most papers comment in passing that artefacts seem worse at 3T according to visual inspection. Only a few studies provide visual ranking of artefact on a qualitative scale. I now provide a quantitative, as well as qualitative, analysis of flow artefact at different field strengths.

4.3 Method

4.3.1 Image acquisition

From 10 volunteers, 2 pairs of baseline and repeat scans were acquired after subjects

gave written consent as part of a local research ethics committee approved study. One pair of scans was acquired on a 1.5T and the other pair on a 3T Philips Intera scanner (Philips Medical Systems, Best, The Netherlands). Five of the volunteers were imaged at both field strengths with an eight-element (six channel) array coil and five with a birdcage coil (transmit-receive at 3T, receive only, with whole-body transmit coil at 1.5T). The array coil scans were corrected for RF inhomogeneity using a reference scan (SENSE factor 1). Scans were acquired with as little change in subject position as possible between baseline and repeat to minimize any confounding influences of extra-cranial soft tissue deformation and changes in B1 inhomogeneity.

The MR sequence protocol was matched as closely as possible between scanners, using the inversion time (TI) as the only parameter for optimisation. The test sequence was a 3D gradient echo sequence (MP-RAGE) with transverse orientation, anterior-posterior readout direction, and 1.2 mm cubic voxels (TR =9.8ms, TE=4.6ms, flip angle=8°, TFE factor (phase encoding steps after each inversion) =168, number of TFE shots (number of inversion pulses) =154). For background on this sequence, please refer to Chapter 2, Section 2.7. The inversion time (TI) was individually optimized at each field strength, within the constraints of the acquisition, to give good contrast between grey and white matter and a high signal to noise ratio (TI = 900 ms at 1.5T, TI = 1250 ms at 3T). This optimization was done using both a simulation (performed by Alex Dresner, Imperial College) and running five scans with different inversion times on a volunteer at both field strengths (acquired by Alex at 3T, Derek Hill and myself at 1.5T). The inter-shot repetition time was chosen to be as short as possible to accommodate the echoes, with the desired inversion time occurring in the middle of the echo train. The transverse orientation with the slow phase encode in the cranio-caudal direction was chosen to maximize the flow effects and to assess the flow artefacts at their worst.

4.3.2 Image analysis

The flow artefact was compared both quantitatively and qualitatively in scans acquired from the same 10 volunteers at 3T and 1.5T. The following method was used: pairs of scans acquired at the same field strength, from the same subjects, were aligned and subtracted to produce difference images. These difference images were re-formatted in the coronal plane, where these artefacts are most clearly visible. The slice with the most severe flow artefact was identified visually by an observer. The artefacts in these slices were then compared both quantitatively and qualitatively. The difference images were produced following a three-step procedure: First, scans were rigidly registered by

optimization of normalised mutual information using the vtkCISG software package [Hartkens 2002] with 3 resolution levels, 64 bins and a maximum of 100 iterations. The resulting transformations were then used in conjunction with Hanning windowed sinc interpolation (total width 12 voxels) to align repeat scans with baseline scans. In the third step, the aligned repeat scans were subtracted from baseline scans, creating two difference images per subject (one for each field strength).

4.3.2.1 Quantitative analysis

The difference image slices were chosen as those visually identified to have the most severe artefact in the volume. This slice selection method usually resulted in slices with slightly different anatomical location for the same subject at the different field strengths. Two regions of interest (ROI) were placed in the selected difference image slice. An artefact ROI was placed over an area in the difference image with the most severe flow artefact, and a reference ROI was placed over an area where no artefact was visually apparent (cf. Figure 4-1). The average size of the ROIs was 650 (504-880) voxels. The areas chosen for artefact ROIs were the largest possible regions that were only affected by the artefact. The reference ROIs were placed in a similar spatial location in each image to avoid confounding issues of varying signal to noise ratio in array coil images. The artefact level was quantified as the ratio of standard deviations of the intensity difference values, between the two ROIs. Artefact ratios were compared for each subject at both field strengths.

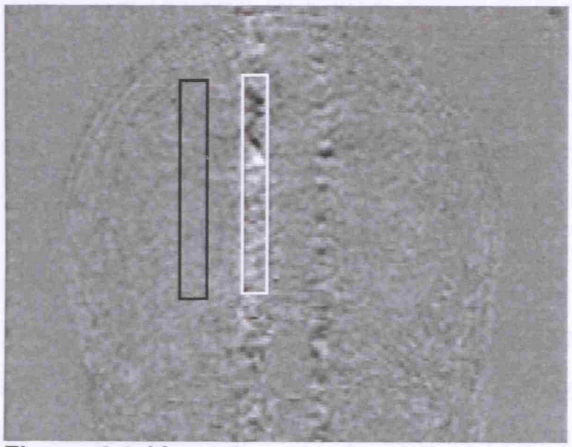

Figure 4-1 Measuring severity of flow artefact from difference image. Reference region of interest (ROI) (left, black rectangle) and artefact ROI (right, white rectangle)

Signal to noise ratio measurements

The signal to noise ratio (SNR) was measured for all the images using the difference image approach described by Firbank et al, 1999. For each baseline scan, the mean signal intensity was measured from a ROI placed in white matter, carefully avoiding regions where partial volume effects or artefacts might have distorted the results. The standard deviation of the intensities from the corresponding area on each of the difference images was also measured. This value was divided by the square root of 2 to obtain the measured noise. For each baseline image, the mean intensity of the ROI was divided by the measured noise from the corresponding difference image. The ratio of SNR 3T:1.5T was calculated for each subject. These ratios comparing SNR between field strengths were averaged for both types of coils separately and for all subjects.

4.3.2.2 Qualitative analysis

In order to compare the artefacts between the two field strengths, a radiologist visually rated the severity of artefacts across field strength. Visual assessment was performed on the same coronal slices that were described previously. Since the location of the artefacts can be more easily determined in the difference image, a comparative severity rating of the artefact was achieved by rating the baseline scan alongside the corresponding difference images. These baseline scans and difference images were presented to the rater. To ensure the radiologist was blinded to field strength, the 1.5T and 3T coronal slices were randomly labelled A and B and laid out where A is on the left and B is on the right. The relevant difference image slice was placed under its associated baseline slice. To enable a fair comparison between images acquired on different scanners, the baseline image slices were windowed so that the intensities in the scans from both field strengths appeared as similar as possible, and the difference image slices were windowed between +/- 35 % of the mean cortical grey matter intensity.

The comparative severity of the artefact was rated on a five-point scale: 1. A much worse than B, 2. A slightly worse than B, 3. A same as B, 4. A slightly better than B, 5. A much better than B. Finally, these results were translated into a comparative severity rating of artefact between field strengths by replacing the A and B labels with the acquisition field strength for each volunteer's images.

4.4 Results

4.4.1 Quantitative analysis

Tables 4-2 to 4-5 show the results of the quantitative analysis. The artefact level is, on average, more than twice as large at 3T than at 1.5T. The difference in artefact level between the two field strengths was found to be significant ($p<0.01$, paired Student's t-Test for all 10 subjects).

Table 4-2 Comparison of artefact level at different field strengths: Birdcage coil results

Artefact level (ratio of SDs of ROIs) at:	Vol1	Vol2	Vol3	Vol4	Vol5	Average	Standard deviation
1.5T	1.50	1.64	1.25	1.86	1.35	1.52	0.24
3T	3.12	3.91	3.22	3.80	2.80	3.37	0.47

Table 4-3 Comparison of artefact level at different field strengths: Array coil results

Artefact level (ratio of SDs of ROIs) at:	Vol6	Vol7	Vol8	Vol9	Vol10	Average	Standard deviation
1.5T	2.18	2.21	1.84	2.12	1.92	2.05	0.17
3T	5.00	3.76	4.49	6.26	4.83	4.89	0.92

Table 4-4 Comparison of artefact level at different field strengths: Averages

Artefact level (ratio of SDs of ROIs) at:	Average (±sd) artefact level for birdcage coil	Average (±sd) artefact level for array coil	Average artefact level for both coils
1.5T	1.52 ± 0.24	2.05 ± 0.17	1.79
3T	3.37 ± 0.47	4.89 ± 0.92	4.12
1.5T:3T	2.22	2.38	2.30

Table 4-5 SNR measures

	3T	1.5T	3T:1.5T ratio
Birdcage average SNR	88.8	46.6	1.90
Birdcage sd of SNR	10.4	5.79	
Array coil average SNR	95.2	55.7	1.71
Array coil sd of SNR	26.8	7.86	
Total average SNR	92.0	51.2	1.80
Total sd of SNR	19.5	8.07	

4.4.2 Qualitative analysis

In the visual assessment study, the radiologist ranked 8 of the 10 3T images as having worse flow artefacts than 1.5T images, 4 of the subjects being labelled as much worse. For one subject, the artefacts were rated the same and for one other subject the artefact was rated slightly better at 3T. A Wilcoxon matched pairs signed-rank test showed that this difference was significant ($p<0.05$).

Observations from images

Flow artefacts that arise from the carotid arteries dominate the 3T subtraction images. The most pronounced flow artefacts were located within 20mm of the midline, although clear artefacts were also visible further laterally when viewed in a coronal orientation. At 1.5T the artefacts are less pronounced, and in 9 of the 10 pairs of 1.5T images, lateral artefacts were visually assessed to be more prominent than medial ones. These patterns were found in birdcage coil as well as array coil studies.

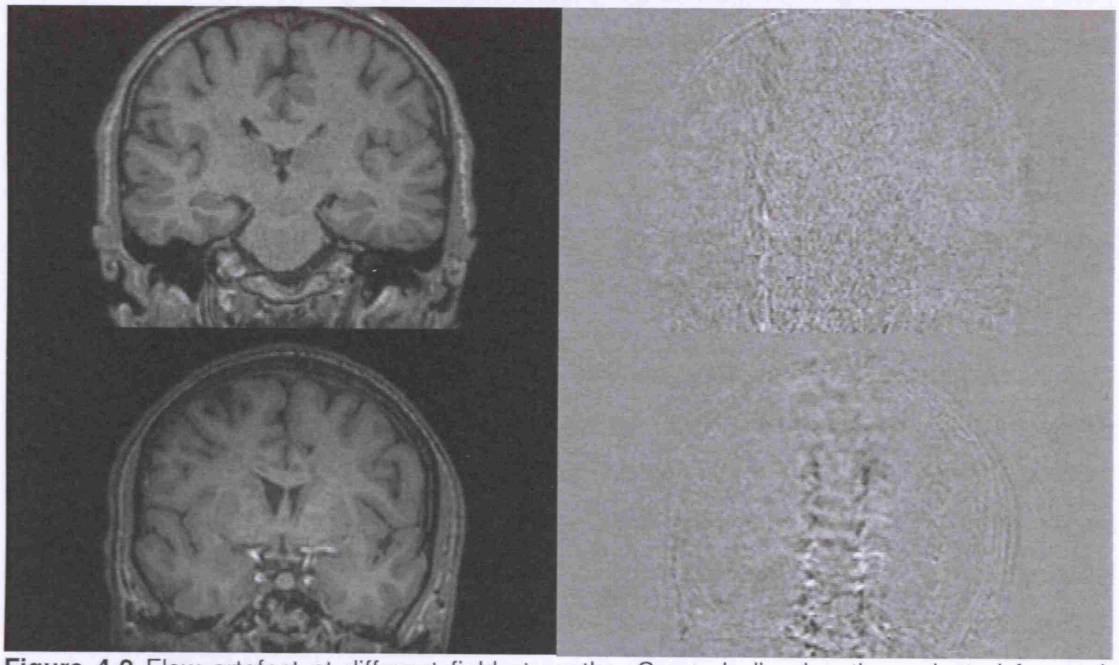

Figure 4-2 Flow artefact at different field strengths. Coronal slice location selected for each scan on the basis of containing the most severe flow artefact : baseline scans (left) and difference images (right) at 1.5T (top row) and 3T (bottom row). Images from subject 10.

Visual comparison of 1.5T and 3T images supported quantitative results for the expected differences in contrast to noise ratio (higher contrast to noise ratio at 3T (19.8 at 3T vs. 11.6 at 1.5T, ratio 1.7), signal homogeneity (signal more homogeneous at 1.5T) and SNR (higher at 3T by a factor of 1.8, see Table 4-5), see also Figure 4-2. The signal homogeneity was similar in all subjects, and, although the signal was non-uniform (particularly at 3T), the effect was stable between scans, and is therefore not

apparent in the difference images. Difference images visually showed more pronounced flow artefacts at 3T and more noise at 1.5T.

4.5 Discussion

The results of this study show significant differences in the magnitude of flow artefact in serial MRI for the widely used TFE sequence at 3T and 1.5T (also known as the MP-RAGE sequence, see Chapter 2, Section 2.7 for more details on pulse sequences). On average, the artefact level was more than twice as high at 3T as observed at 1.5T (2.22 times for the birdcage and 2.38 times for the array coil, Table 4-4). I suggest that some of the difference arises from the SNR at 3T being higher than at 1.5T (by a factor of 1.8, Table 4-5), but this does not fully explain the effect. It is worth noting that the blood vessels themselves (including the carotid arteries) appear relatively brighter in the 3T images than in the 1.5T images, which agrees with Deichmann's observation in 2004. This increase in field strength will lead to a greater difference in the signal from unprepared spins, resulting in a larger relative signal from flowing blood which is likely to result in a higher artefact level. This suggestion also builds on the theory proposed by Felmlee et al in 1987, in which they observed very prominent pulsatile flow artefact at high field strength and postulated that the tissues are more saturated at high field strengths, because the T1 relaxation times are longer. This leads to a greater degree of unsaturation of blood that flows into the imaged section from outside the image volume, resulting in more pronounced flow artefact than at lower field strengths.

The spatial location of the most prominent artefact appears to be dependent on field strength. All ten volunteers' images at 3T showed the most prominent artefact within 20mm of the midline. While in nine out of ten volunteers at 1.5T, the most prominent artefact was seen more laterally than in their 3T counterparts (see Figure 4-2). These flow artefacts run cranio-caudally in the field strength comparison study due to the axial orientation of acquisition. The direction of the artefact can be altered by changing the acquisition plane: in coronal sequences, for example, the artefact typically runs in a right-to-left direction through the region of the temporal lobes. Regardless of the orientation, the increased magnitude of this artefact through brain structures associated with the disease is likely to cause problems in the analysis of longitudinal changes. The impact on global measures of atrophy may be small, as only a limited proportion of the overall brain volume is affected, but local measurements (e.g. hippocampal volume or voxel-compression mapping of the temporal lobe) could be distorted by flow artefact arising from the carotid. In both the birdcage and array coil setup, flow artefact level depended on field strength; exhibiting similar artefact levels and spatial locations.

While the trial involves only a limited number of subjects, the difference in quantitative artefact level for each was substantial, leaving little doubt of a significant effect. A different birdcage coil was used on the two scanners, transmit-receive at 3T and a receive-only with whole-body transmit coil at 1.5T, which may have biased the results. However, a similar effect was seen on the five volunteers imaged with the array coils which were the same on both scanners.

The results also concur with the qualitative results presented in the literature by Parizel et al, 1995, Bernstein et al, 2001 and Deichmann et al, 2004, who all conclude that flow artefacts appear worse at higher field strengths. This effect partially diminishes the overall advantage in increased SNR provided by higher field strength imaging, particularly if trying to obtain accurate measures of volume for small structures such as the entorhinal cortex [Xu 2000]. As longitudinal neuroimaging trials in dementia are moving towards using 3T scanners more frequently, the elimination, or management of these pulsatile flow artefacts must be considered during the set up of these trials. The optimization of the pulse sequence protocol, the use of saturation pulses, the set up of quality control (QC) protocols, and image analysis should all be performed with the issues of pulsatile flow artefacts in mind. The prevalence of this and other artefacts in current imaging trials running at 1.5T should also be investigated.

4.6 Conclusion

I decided to qualitatively and quantitatively study the effects on pulsatile flow artefact, arising in a TFE (MP-RAGE) sequence, due to moving from a 1.5T to a 3T scanner. I devised an image processing method to quantify the comparative difference in severity of this artefact at the two field strengths. This method may also be useful for future automatic quality control systems to detect significant levels of artefacts in images. Using this method I determined that the severity of this artefact is, on average, more than doubled with the increase of field strength to 3T. These quantitative changes are supported by qualitative rankings which also show a visible difference between these artefact levels. This increase in severity has the potential to cause problems as longitudinal neuroimaging trials are moved to these higher field scanners.

In the next chapter I investigate the prevalence and severity of different types of artefacts, including pulsatile flow artefact, in current and historical trials at 1.5T. This will then provide insight into the scale of the problem in longitudinal imaging already caused by pulsatile flow artefact at 1.5T.

5 Prevalence and automatic quantification of artefacts affecting longitudinal neuroimaging studies

5.1 Introduction
5.1.1 Aims
5.1.2 Contribution
5.2 Literature Review
5.2.1 Literature on the frequency of artefacts in MRI trials
5.2.2 Literature on artefact quantification
5.3 Method
5.3.1 Prevalence of different artefacts in clinical data
5.3.2 Quantifying the severity of artefacts
5.4 Results
5.4.1 Prevalence of different artefacts in clinical data
5.4.2 Quantifying the severity of artefacts
5.5 Discussion
5.6 Conclusion

5.1 Introduction

MR images with features not representative of the original anatomy, due to acquisition artefacts, are a substantial problem in image analysis for multicentre trials. Quality control (QC) of the images is a critical step, but at present, is very subjective. Currently, there is little literature on the frequency with which artefacts occur within clinical trials. In this chapter, I address these issues by carrying out a meta-analysis of QC records from two trials and propose quantitative methods to assess artefact level.

5.1.1 Aims

In this chapter, I aim to assess the frequency of occurrence for different types of artefacts in historical and current clinical trials of dementia at 1.5T. I also aim to investigate the prevalence of artefacts in scans rejected from analysis, and in those accepted into analysis. I aim to determine the main types of temporal lobe artefacts, and to propose a tool which automatically quantifies the severity of the most common of these from longitudinal pairs of images.

5.1.2 Contribution

This chapter adds to the literature a more complete understanding of the prevalence of different types of artefacts which affect longitudinal neuroimaging trials. This work will enable future trials to prioritise the issues they consider when optimising their scanning acquisition parameters and protocols. I provide those designing MR neuro-imaging trial QC procedures with a better understanding of the most severe and the most common problems which need rapid and consistent detection. Also, I contribute a novel

prototype tool for automatically detecting and quantifying anatomically located artefacts in scan pairs. This tool could form part of an automatic QC system for use in longitudinal clinical trials. Finally, I use the technique proposed by Firbank et al in 1999 for SNR measures from repeat scans, to determine if this measure correlates with motion artefact levels in a pair of scans.

The trial QC records, and images used in this chapter were provided by the Dementia Research Centre (DRC), UCL, Institute of Neurology. An explanation of the methods and terminology used in compiling these records was provided by Dr Ellen Garde, DRC. I analysed these QC records and visually inspected all those with temporal lobe artefact to determine their cause. For any images that contained pulsatile flow artefact, I rated the artefact visually and then automatically, using a tool which I had designed and made. I analysed the prevalence of the different types of artefacts, in light of whether the scan had been rejected or accepted into analysis.

5.2 Literature review

5.2.1 Literature on the frequency of artefacts in MRI trials

The first aim of this chapter is to assess the frequency with which different types of artefacts occurred during historical clinical trials of dementia at 1.5T. In this section I will review the literature relevant to this aim. I will discuss the previous papers on longitudinal trials of dementia at 1.5T which have quantified the occurrence of artefacts in their scans. I will discuss both their contributions and the areas where further research is needed. Finally, I will discuss how my work in this chapter address what is lacking and adds to this literature.

The Vitamin E and Donepezil trial for the treatment of Mild Cognitive Impairment [Petersen 2005] and an investigation into using different regional image measurements as diagnostic markers of early AD [Xu 2000] are two neuro-degeneration clinical trials in the literature which quantify the incidence of artefact in scans. The Vitamin E and Donepezil trial quantifies the percentage of scans that were discarded from whole brain BSI analysis. The other trial, carried out by Xu et al, quantifies the percentage of scans with artefact that affect boundary delineation in the temporal lobe.

The Vitamin E and Donepezil trial for the treatment of Mild Cognitive Impairment carried out by Petersen et al in 2005 cites 25% of patient data as being discarded because of image artefacts. 34 out of 138 scan pairs acquired 36 months apart were deemed unusable with whole brain BSI analysis. However, this article did not

investigate the cause of these artefacts, or quantify their occurrence in images accepted into analysis.

The second trial by Xu et al, in 2000, investigated the usefulness of measuring the entorhinal cortex compared with the hippocampus as a diagnostic marker of early AD. (Both these structures are located in the temporal lobe). To do this they manually segmented the two regions from 3D spoiled gradient echo sequences of ninety subjects: 30 AD, 30 with Mild Cognitive Impairment (MCI), and 30 control subjects. They found that entorhinal cortex measurements were not as sensitive as predicted due to boundary ambiguity. 47% of scans suffered from anatomical variation which caused boundary ambiguity, while 60% of scans suffered from artefacts which caused boundary ambiguity. They observed two types of artefacts affecting this brain region. The first is flow artefact caused by arterial flow in the circle of Willis or by cerebro-spinal fluid (CSF) pulsation in the suprasellar cistern. The second is magnetic susceptibility artefact which hindered the measurement of the entorhinal cortex but not the hippocampus.

The current literature provides insight into the number of scans acquired in previous clinical trials which were rejected from analysis [Petersen 2005], or whose analysis were affected [Xu 2000], due to artefact. To the best of my knowledge, there is no detail in the literature comparing the relative prevalence of different causes of artefacts occurring in longitudinal imaging trials of dementia at 1.5T. It would be valuable to have details, for both the whole brain and for the temporal lobe, of the causes of artefacts which lead to images being rejected from or affecting analysis.

I selected the quality control records for longitudinal scans from 837 volunteers which have undergone whole brain volume analysis. The aim of the analysis was to assess the frequency of different artefacts in scans and to assess the severity of these artefacts. In the quality control artefact records, temporal lobe artefact was often recorded, but the specific cause of the artefact was not. Therefore, I visually inspected each of the images with temporal lobe artefact to determine its cause. My goal was to provide a more detailed quantification of the causes of artefacts affecting longitudinal MR Neuroimaging trials of dementia at 1.5T, from a much larger sample than previously investigated.

5.2.2 Literature on artefact quantification

There are numerous papers measuring signal to noise ratios, contrast to noise ratios, and g-factors; however, to the best of my knowledge there is nothing in the literature which has been used to quantify the severity of subject related artefacts occurring in 3D T1 weighted brain images. One exception is a method which has been used to quantifying motion by measuring the level of noise outside the skull. However, this is not appropriate for use with modern head array coils. There are a few papers such as [Blumenthal 2002] where artefact is visually rated but no automatic tools seem to exist to quantify their severity.

5.3 Method

5.3.1 Prevalence of different artefacts in clinical data

To study the prevalence of different artefacts in clinical data I investigated the QC records for a historical and a current trial.

Historical trial

In order to investigate the prevalence and severity of artefacts affecting longitudinal neuroimaging studies, I selected a historical clinical dementia trial involving 758 pairs of images acquired from subjects across multiple sites, utilizing different scanners models from a range of vendors. I obtained permission from the pharmaceutical company involved to investigate the trial images and publish my findings. The images were T1 weighted gradient echo volumes, acquired in the coronal plane, with readout direction from head to foot, and a matrix size typically of 256x256x124. There is some variation in the number of slices across patients ranging between 120 and 150. The reconstructed dimensions of the voxels are typically 1x1x1.8mm, with variation in the slice direction across different scanners, ranging between 1.5 and 1.8 mm.

The historical analysis of the images from this trial was performed at the Dementia Research Centre, UCL, Institute of Neurology. The BSI measure was used on each longitudinal scan pair to quantify brain atrophy for each subject. Any pair which produced unrealistic visual results during BSI analysis was further inspected and any artefacts present were recorded along with the reliability in the BSI measure being categorized as "unusable", "poor" or "acceptable".

I used these original records of artefact to quantify the prevalence of different artefacts in relation to the BSI reliability categories. Then, I selected all the scan pairs recorded

where artefact in the temporal lobe had affected BSI analysis to investigate the physical causes of this artefact. As certain types of dementia, such as Alzheimer's disease, can be detected earliest by volumetric changes to regions within the temporal lobe, it seems reasonable to assume that image quality in this region particularly affects the accuracy of atrophy quantification in the early stages of the disease. To determine the physical cause of the temporal lobe artefact, I visually inspected the image pairs and their resulting subtraction images. I used the location and texture of any non anatomical differences between the two images to determine the cause, or causes, of the artefact. Some examples images from this trial where artefacts are present can be found in Figure 5-1 below.

Current trial

The second clinical trial was in the process of acquiring images at the time of my research. So far, this trial has acquired 155 brain images. Scan quality was assessed on the receipt of each scan, and the scan was either accepted or rejected into the analysis. In either case, the nature of any scan problem or artefact was recorded. I analyzed these records to investigate the prevalence of different types of artefacts occurring in both the scans which were accepted and the scans which were rejected from analysis. I visually inspected any scans which were recorded as suffering from temporal lobe artefact, and recorded the cause of artefact.

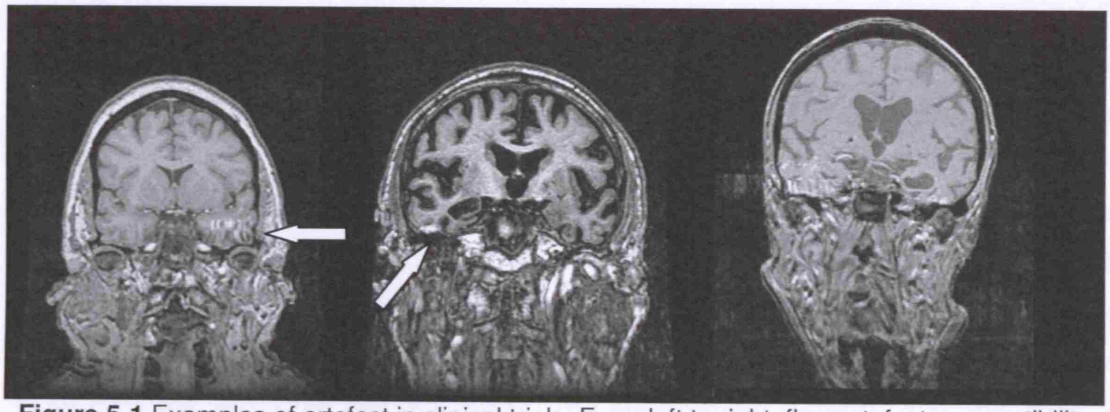

Figure 5-1 Examples of artefact in clinical trials. From left to right: flow artefact, susceptibility artefact and incorrect contrast

5.3.2 Quantifying the severity of artefacts

Visual quantification

During the visual inspection of each image with temporal lobe artefacts discussed in the previous section, I rated the visual severity of any pulsatile flow artefact arising from the carotid artery. I classified the artefact in images accepted into analysis as 'none',

'mild', 'moderate', 'severe'; all those which were rejected from analysis due to this pulsatile flow artefact I classified as 'rejected'.

Automatic quantification

To design an automatic image quality assessment system for detecting artefacts, it is important to be able to quantify artefact and to know the level of severity at which images are typically excluded from analysis. I designed a tool to quantify the severity of the most frequently occurring temporal lobe artefact, pulsatile flow artefact arising from the carotid artery (see results, Section 5.4.1 on Causes of temporal lobe artefact).

To automatically quantify the level of pulsatile flow artefact in a pair of images, I compared the standard deviation of two different regions of the difference image, which is created by subtracting the registered repeat from the baseline scan. These 3D regions are automatically selected by registering a template image to the baseline scan. Two masks made from the template image are then transformed onto the baseline scan to select these two regions.

To construct these masks, I selected one image, where artefacts did not cause any unusual results in the BSI analysis, as the "template image". This template image was then segmented twice to provide two 3D masks. Cross sections of these masks can be seen in Figure 5.2. One mask was created by segmenting regions of the temporal lobes, adjacent to the carotid arteries in the slow phase encode direction (left-right). These areas are where pulsatile flow artefact is most commonly seen. Areas near the scalp were not included to avoid anatomic variability issues in inter-subject registration. Areas near the hippocampal CSF spaces, and other brain/CSF boundaries were excluded as much as possible to avoid atrophy between the scans confounding flow artefact quantification. The second mask was created by segmenting a region of white matter in the parietal lobes from the same coronal slices as used in the first mask. Any brain/CSF interfaces were completely avoided in this mask by segmenting regions away from the ventricles and the cortex. The approximate distance from the edge of the skull was also chosen to be similar between the two masks to try and minimise differences in SNR due to acquisition location within an array coil.

To quantify the artefact, the tool first aligns the pair of images to be assessed using a 9 degree of freedom, affine registration. The template is also registered to the baseline, providing an affine transformation matrix which is then used to align both masks. A difference image is created by subtracting the transformed (sinc interpolated), and intensity normalised follow up scan from the baseline. The follow up scan intensities

are normalised according to the mean intensity of the artefact free ROI in the registered follow up scan, divided by the mean intensity of the same ROI in the baseline image. The transformed masks (trilinear interpolation) are then applied to the difference images. The tool automatically calculates the standard deviations of the voxel intensities in both regions of the difference image. The standard deviation of the temporal lobe region is divided by the standard deviation of the parietal lobe region to give a quantification of the severity of the artefact.

I also incorporated an automatic SNR measure in the tool based on the technique from Firbank et al, 1999, which measures SNR from a pair of scans. If the scanner, its scan parameters, and the acquisition coil are unchanged, a substantial decrease in SNR is a sign of image acquisition artefacts. The tool measures the standard deviation of the difference image parietal lobe region, which is then divided by the square root of 2 to give the noise level. The average intensity of the baseline parietal lobe region is used to give the signal level. The SNR is calculated as the signal divided by the noise level.

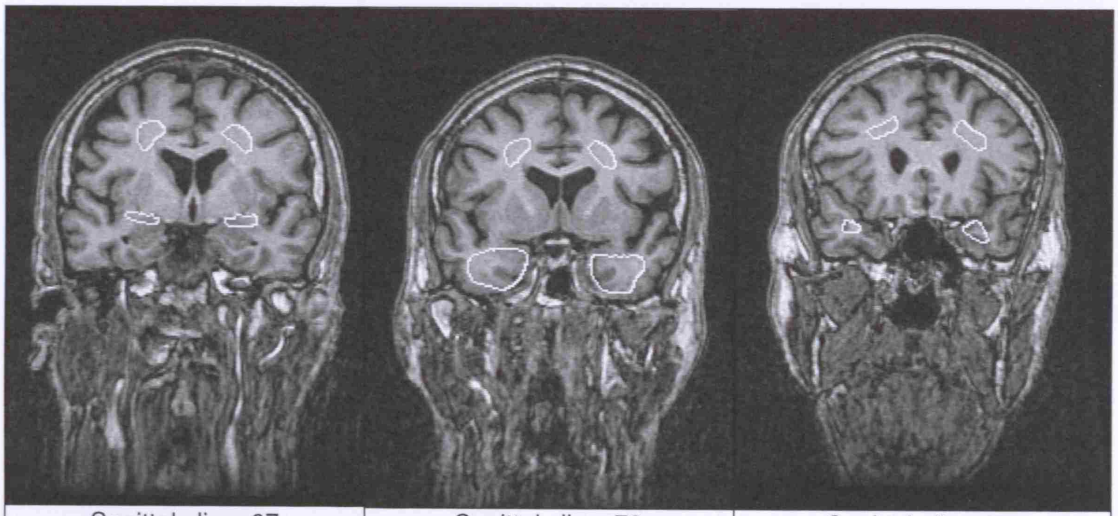

Figure 5-2 Automatic quantification masks: Bottom ROI: Region of pulsatile flow artefact, Top ROI: Region free from flow artefact. Flow artefact severity = standard deviation of difference image bottom ROI / standard deviation of difference image top ROI.

Assessing the automatic artefact quantification techniques

To assess the automatic pulsatile flow artefact quantification technique, I selected images from the historical trial which only had temporal lobe artefact caused by the pulsatile flow artefact arising from the carotid artery. Any which were recorded as suffering from other artefacts, or on visual inspection had displayed motion artefact, susceptibility or other types of artefact, were not selected.

This left 4 'rejected' images (rejected from analysis due to flow artefact), 4 'severe', 6 'moderate', 3 'mild', and 2 'none'. On inspection of these 18 images, 4 were of differing matrix size or voxel dimensions in the z-direction. To avoid introducing different types of registration errors between the template and the pair to be assessed, I decided to also exclude these 4 images from the comparison, which left 4 'rejected', 3 'severe', 4 'moderate', 2 'mild' and 2 'none'.

To test if the pair based SNR measure correlated with motion artefact levels in scan pairs, 6 image sets from the historical trial which did not cause any unusual results with the BSI analysis were selected. These images contained the same voxel dimensions and matrix size as the template image, and they were assumed to be free of substantial artefacts. Next, I selected image pairs from the same trial which were only specified as suffering from motion artefact (39 in total). From these 39, only the images with the same voxel dimensions and matrix size as the template image were then selected. As this left only 2 image pairs, I also selected those images which were recorded as only suffering temporal lobe artefact but on visual inspection were determined to be suffering from motion artefact. This final criterion included 7 more images, all of which had the same voxel dimensions and matrix size as the template image.

5.4 Results

5.4.1 Prevalence of different artefacts in clinical data

Historical trial

The records from the historical trial data were inspected. Of the 758 pairs of brain images recorded, 178 had good BSI results, 308 acceptable and 272 rejected. The records were found to contain non-specific classifications such as "scan artefact", "poor quality" and "quality differences". These terms occurred 93 times with rejected scans and 196 times with the accepted scans, or 289 occurrences in total. The frequency of specific artefact issues is shown in Figure 5-3.

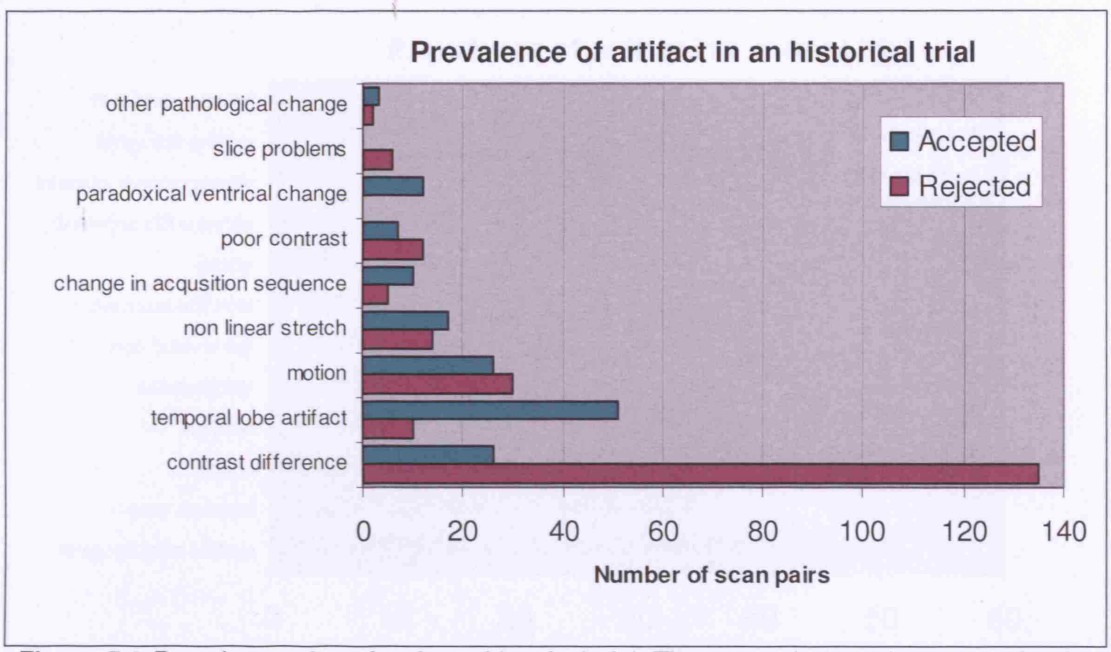

Figure 5-3 Prevalence of artefact in an historical trial. The categories are those used for the QC in this trial, excluding any non specific terms such eg, "scan artefact", "poor quality". For each category the number of scan pairs accepted into analysis suffering this type of artefact, and the number of scan pairs rejected from analysis exhibiting this artefact, are shown.

From Figure 5-3, contrast difference was the leading indicator cited to cause images to be rejected from BSI analysis. The artefacts which most often affected the BSI images which were still included into analysis were temporal lobe artefacts. Motion artefact, and non-linear stretch (see Chapter 3, Section 3.2.2 for an explanation of non-linear stretch) also contributed to the images being rejected from analysis, and affecting images which were accepted into analysis. To determine if these results were purely trial specific, I investigated the quality assessment records of a similar clinical trial which was running at the time of my research.

Current trial

155 images had been collected at the time of my research, 30 of which had been rejected from analysis, 105 accepted with recorded artefacts and 20 accepted with no recorded problems. The frequency with which different artefacts were recorded in these 155 images can be seen in Figure 5-4.

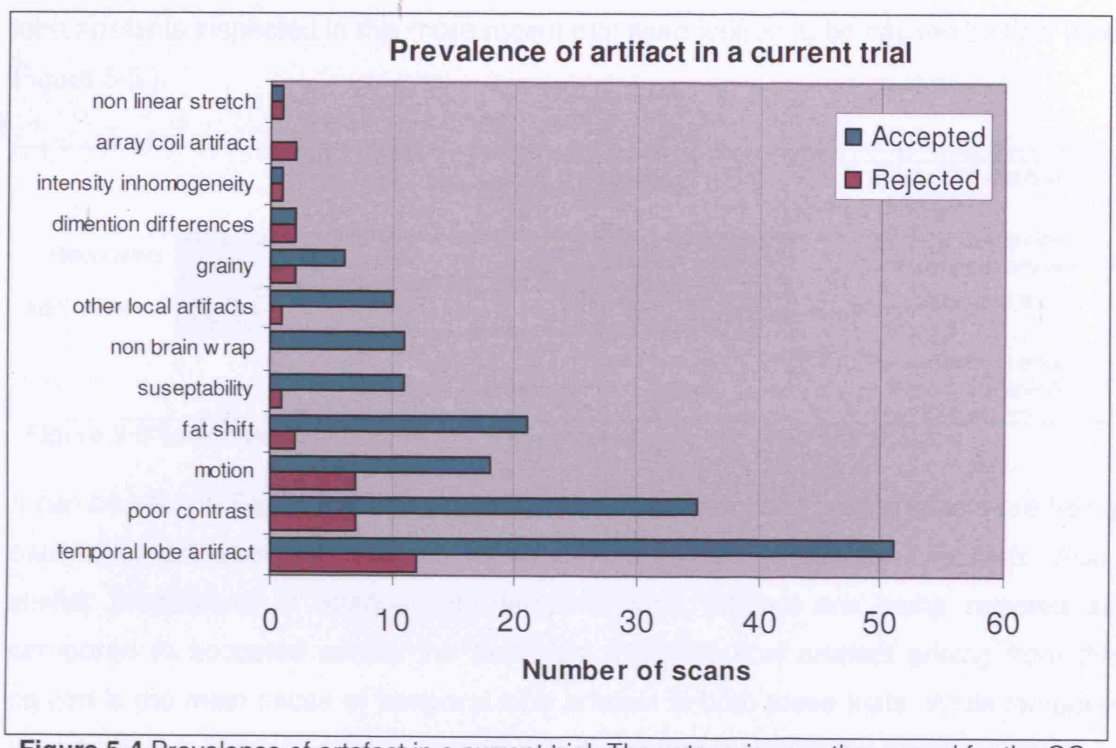

Figure 5-4 Prevalence of artefact in a current trial. The categories are those used for the QC in this trial. For each category the number of scan pairs accepted into analysis suffering this type of artefact, and the number of scan pairs rejected from analysis exhibiting this artefact, are shown.

The most frequent problems in this trial are temporal lobe artefact, poor contrast, motion artefact and fat shift. Non-linear stretch does not occur so frequently in this trial at this stage, as only single time points were available, and this artefact is much easier to detect when comparing multiple time-points for a subject. Temporal lobe artefact, problems with contrast, and motion artefacts are the three most prevalent artefacts in both the trials.

Causes of temporal lobe artefact

The prevalence of artefact occurring specifically in the temporal lobe is important given that this is one of the regions of the brain earliest affected by Alzheimer's disease. To determine the main causes of this artefact I visually inspected all scans recorded as suffering with temporal lobe artefact.

In the historical trial, 61 out of the 758 (8%) pairs of scans had been recorded as suffering from artefact in the temporal lobe. 35 (57%) of those recorded as suffering artefact in the temporal lobe were judged to be caused by pulsatile flow artefact.

In the current trial there were 63 records of temporal lobe artefacts from the 155 images (41%), of these 59 were available for inspection. 42 of the 59 (71%) temporal

lobe artefacts inspected in this more recent trial were judged to be caused by flow (see Figure 5-5).

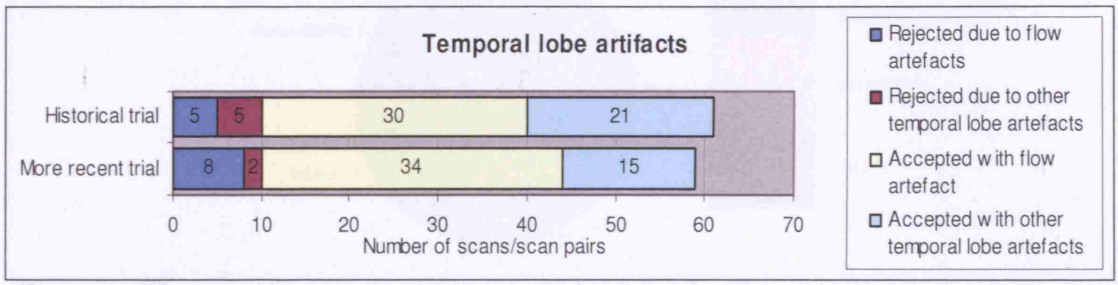

Figure 5-5 Temporal lobe artefacts in images rejected and accepted into analysis

It can be seen in Figure 5-5 that similar proportions of temporal lobe artefacts are being caused by pulsatile flow artefact, as by other artefacts across the two trials. Also, similar proportions of images with temporal lobe artefact are being rejected as compared to accepted across the two trials. Pulsatile flow artefact arising from the carotid is the main cause of temporal lobe artefact in both these trials. While temporal lobe artefact is more frequently recorded in the recent trial than the historical one, it is still the second most commonly recorded artefact in the historical one.

The Figures 5-6 and 5-7 below show further detail as to the other causes of temporal artefact. The first, Figure 5-6, shows the causes of temporal lobe artefact in scans which were rejected from analysis in both trials.

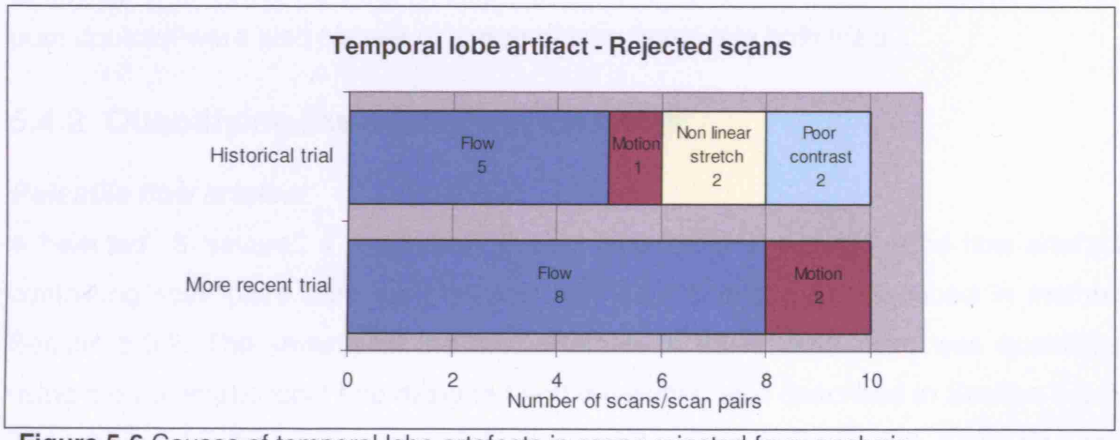

Figure 5-6 Causes of temporal lobe artefacts in scans rejected from analysis

Figure 5-7 shows the causes of temporal lobe artefacts in scans which were accepted for analysis. It also shows the proportion of flow artefacts which were visually rated severe, moderate and mild. There are similar proportions of these levels between both trials.

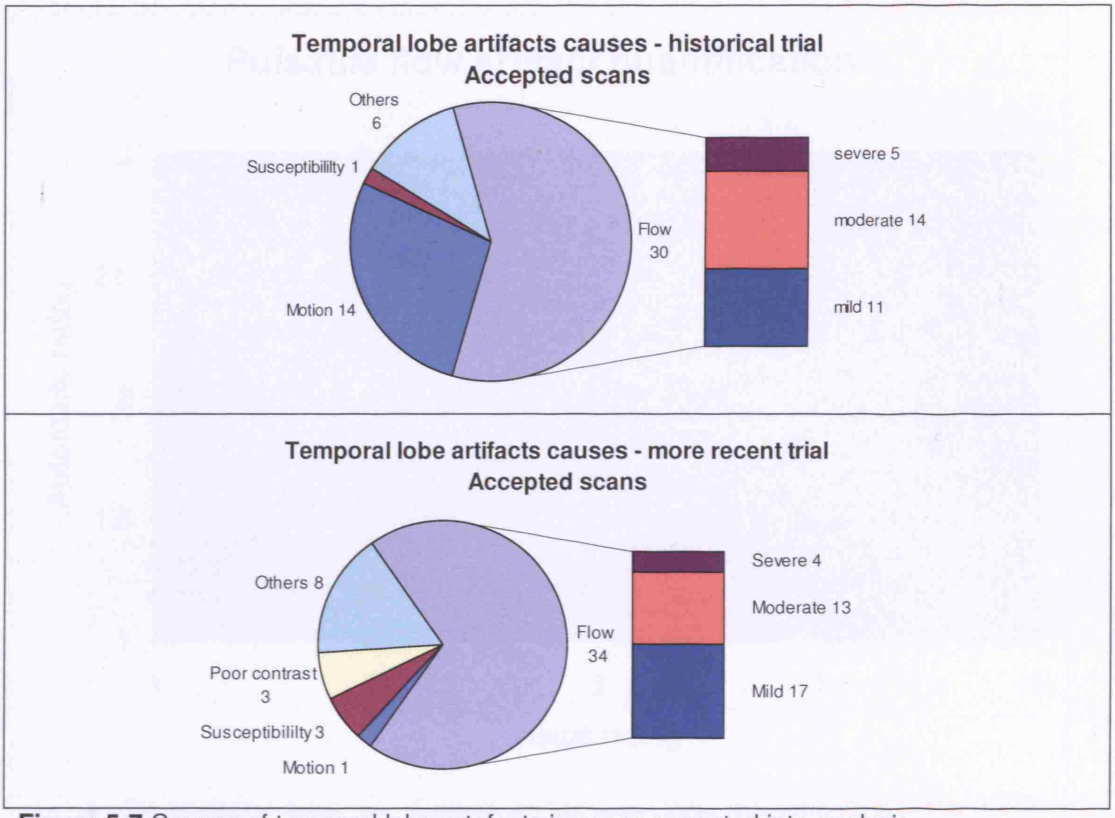

Figure 5-7 Causes of temporal lobe artefacts in scans accepted into analysis

The Figures 5-5, 5-6, 5-7 above show that pulsatile flow artefact arising from the carotid is the main cause of temporal lobe artefacts in both scans which are accepted and those which are rejected. Motion artefact was the second most common artefact occurring in both rejected and accepted scans across both trials. Susceptibility and poor contrast were also causes of temporal lobe artefact in both trials.

5.4.2 Quantifying the severity of artefacts

Pulsatile flow artefact

4 'rejected', 3 'severe', 4 'moderate', 2 'mild' and 2 'none' visually rated flow artefact containing scan pairs from the historical trial were selected as described in method Section 5.3.2. The severity of the flow artefacts in these scan pairs was quantified using the automatic tool I had designed and developed also described in Section 5.3.2. The results from the assessment of this tool can be seen in Figure 5-8. It can be seen from this figure that automatic rating of pulsatile flow artefact correlates well with the visual rating ($R^2 = 0.74$).

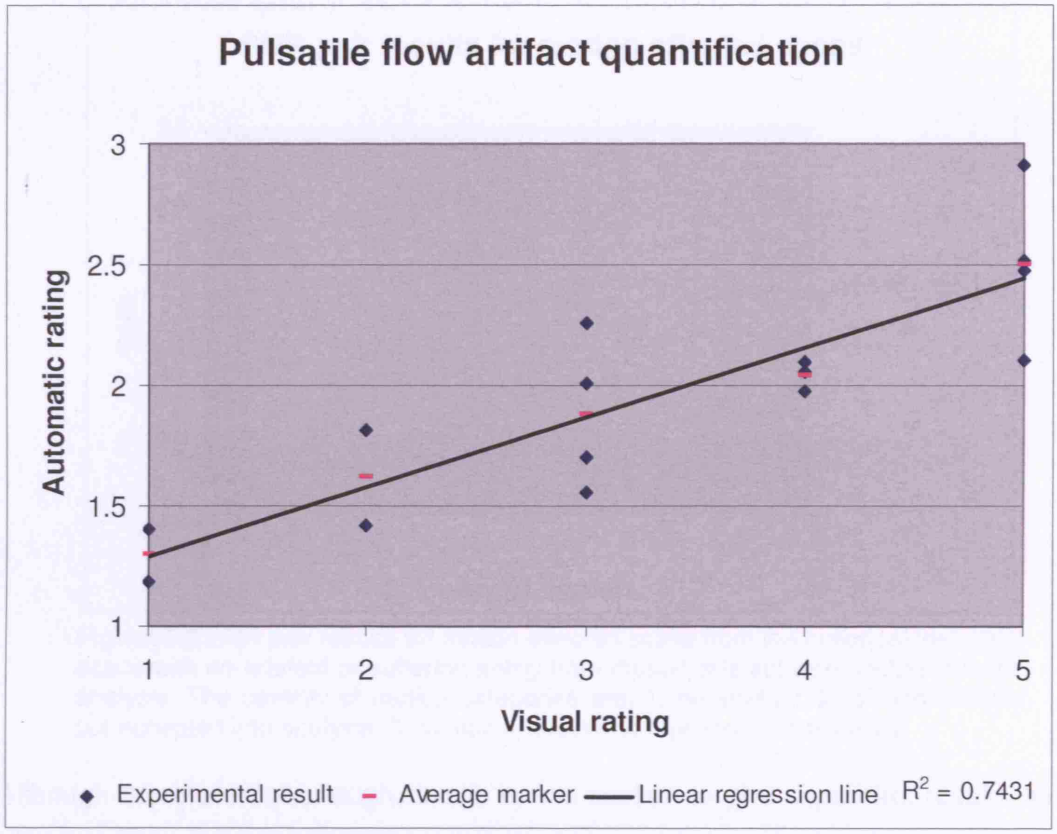

Figure 5-8 Assessment of automatic flow artefact tool by comparison of automatic and visual pulsatile flow artefact quantification. First the flow artefact in each image was visually rated between 1-5, where 1 was no artefact, 2 mild, 3 moderate, 4 severe but included in analysis and 5 was severe and rejected. Then the automatic algorithm was run on the image to give a quantitative measure, where a higher number reflects more severe artefact. Images were only included from the historical trial and only if flow artefact was the only artefact they were suffering from.

SNR pair measures correlation with motion

From the 6 randomly selected images assumed to be free of large artefacts, the SNRs measured had a mean of 30.5 and a range of 27.6 to 33.6. Out of the 2 image pairs with only motion specified as an artefact, one was accepted and the other rejected from analysis. The accepted one had an SNR of 31.1 and the rejected had an SNR of 14.4. The 7 pairs specified with only temporal lobe artefact, which on visual inspection were determined to be suffering from motion, had SNRs ranging from 19.8 to 31.9 with a mean of 24.8. None of these were severe enough to be rejected from analysis. I rated the 6 not marked as having any motion artefact as having a severity of motion artefact of 1, all 8 determined to be suffering from motion while still included into analysis a severity of 2, and the one excluded from analysis due to motion artefact as a 3. I have then plotted the SNR result for each image against the rating of the motion artefact severity, which is shown in Figure 5-9.

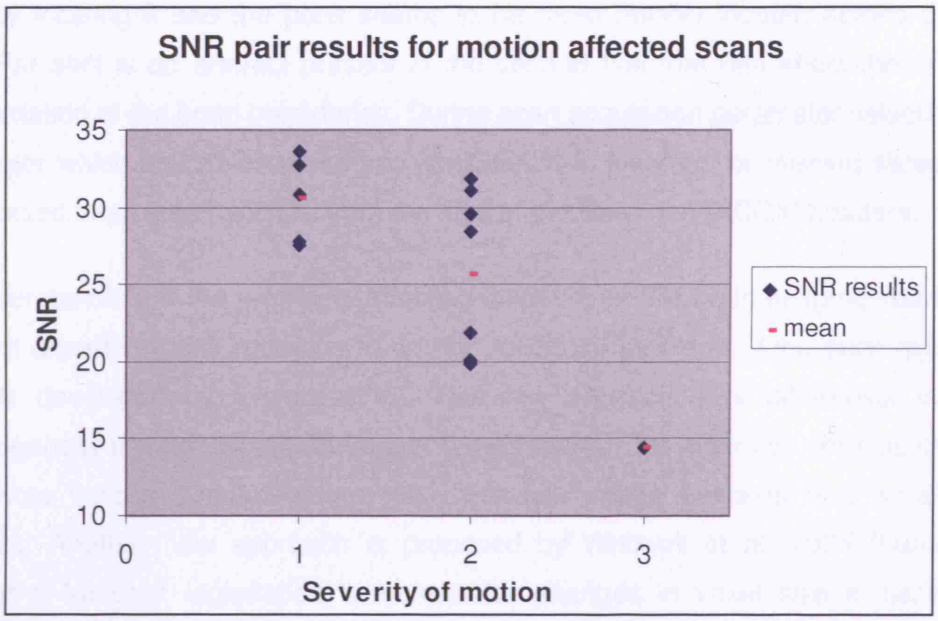

Figure 5-9 SNR pair results for motion affected scans from the historical trial. Only scans with no artefact or suffering solely from motion artefact were included in the analysis. The severity of motion categories are: 1, no artefact; 2, motion artefact but accepted into analysis; 3, motion artefact and rejected from analysis.

Although there are not enough results in this section to give significant results on the effectiveness of using this SNR measure as a tool for detecting motion artefact, these preliminary results seem to indicate that this method is worth exploring further in the automatic detection of motion artefact.

5.5 Discussion

Prevalence of artefacts in clinical trials

Temporal lobe artefact, problems with contrast, and motion artefacts are the three most prevalent artefacts in both the trials (Figures 5-3 and 5-4). Temporal lobe artefacts were the most commonly recorded problem in both rejected and accepted scans for the current trial. In the historic trial, temporal lobe artefacts were the most common specified artefact for scans accepted into analysis, with decreased confidence in the BSI result. The most common cause of rejecting a scan pair in the historic trial was that of differing contrast between scans. Motion artefact was the third most common problem in both trials, including both rejected and accepted scans.

Other problems identified were non-linear stretch, fat shift and incorrectly ordered or missing slices. Non-linear stretch is often caused by the subject being scanned in a different position within the magnet. One way of avoiding this artefact is to always centre the scan on the same part of the brain. The thalamus makes a good candidate as it is well located towards the centre of the brain. However many radiographers have

difficulty locating it and the pons seams to be more reliably located across different sites. Fat shift is an artefact present in the second trial that can affect the accurate segmentation of the brain boundaries. During scan acquisition parameter selection, this is a factor which should be taken into consideration. Incorrect or missing slices could be detected in an automatic QC from the size of the file or the DICOM headers.

An understanding of the problems affecting longitudinal MR brain imaging has lead to different algorithms and methods to correct for these problems. One such algorithm, recently developed by Emma Lewis, was the "Correction of differential intensity inhomogeneity in longitudinal MR image" [Lewis 2004]. This algorithm corrects intensity differences across scans so that the difference image contains only small local changes. Another new approach is proposed by Whitwell et al, 2004 "Using nine degrees-of-freedom registration to correct for changes in voxel size in serial MRI studies". This was developed to correct for the problem of scanner related drifts changing voxel sizes between scan pairs.

The more complete understanding provided in this chapter of the problems affecting longitudinal MR brain imaging led to further work, presented in Chapter 8 of this thesis, where I propose an algorithm to correct pulsatile flow artefact.

This understanding of the frequency and severity with which different artefacts occur in longitudinal MR trials provides insight to design future automatic QC systems. Effort should first be focused on designing components which detect the most common artefacts in images excluded from analysis, or the most common artefacts in images accepted into analysis which give unreliable results. The concept of an automatic QC system led to my work in this chapter on quantification of artefacts.

Causes of temporal lobe artefacts

In the historical trial, 61 out of the 758 (8%) pairs of scans had been recorded as suffering from artefact in the temporal lobe. In the current trial there were 63 records of temporal lobe artefacts from the 155 images (41%), of which 59 were available for inspection. These images indicated that the main cause of temporal lobe artefacts was pulsatile flow artefact. From the scans recorded as suffering temporal lobe artefact, 35 (57%) of the 61 scan pairs in the historical trial and 42 (71%) of the 59 scans in the current trial were caused by flow (see Figure 5-5). Other causes include motion, susceptibility artefacts, poor contrast and linear stretch (Figures 5-6 and 5-7).

In the current trial, susceptibility was also recorded 12 times as a distinct artefact category to temporal lobe artefact; this usually occurs in the temporal lobe however. It occurred in 1 rejected scan and 11 accepted scans. Even if this is added to the temporal lobe numbers, pulsatile flow is still the most common cause of artefact in the temporal lobe.

The occurrence of these artefacts is much more noticeable at 3T as the relative noise level decreases by approximately half. The increasing use of 3T scanners for serial neuroimaging makes the need to reduce these artefacts all the more urgent (see Chapter 4).

Quantification of artefacts: assessment of automatic tools

The tool that I designed to quantify pulsatile flow artefacts arising from the carotid artery correlates well with visual rating of the artefacts ($R^2 = 0.74$). There is a distinction between using the automatic rating between images with no or mild visually assessed artefact and those images which have artefact rated severe or rejected. There is scope for improvement in the automatic tool differentiating between different levels of moderate, severe and rejected artefact. Although visual rating is the current standard, it is certainly subjective, and it is more difficult to visually compare the severity of artefacts objectively across volumetric images, than across 2D images which may simply be compared side by side.

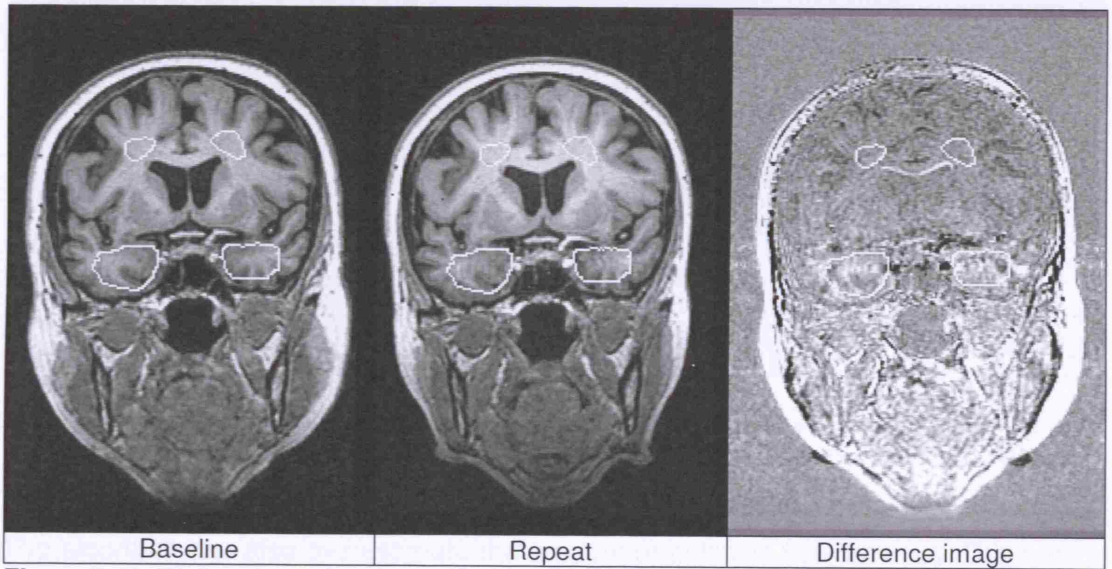

Figure 5-10: Well registered regions of interest from automatic quantification tool in a scan affected by pulsatile flow artefact: The top two regions over an area free of artefact or atrophy. The lower two regions over an area of flow artefact, visible in the temporal lobes of the repeat and difference image.

In Figure 5-10 is an example of a scan rejected from analysis with flow artefact. The

ROI boundaries, from the automatic quantification template, are overlaid on this example image. The region of interest templates can be seen to have registered well. No ventricle or brain boundary change is apparent in the artefact free region, very little is apparent in the flow artefact region (perhaps a very small amount of brain boundary change). N3 correction or differential intensity correction as suggested by Lewis, 2004 might improve the results further by remove intensity changes across the scans.

Sometimes the algorithm underestimates the flow artefact, see Figure 5-11. This scan was rated as suffering from moderate flow artefact but had a quantitative rating of 1.55 which would seem to correlate more with a mild rating. This can occur if the strongest part of the flow artefact appears outside the artefact ROI (see underneath the ellipse on the lower right of the difference and repeat images). It would be difficult to include this particular region in the analysis however as it is a brain boundary which may cause structure in the difference image if the two scans are taken at different time points. If two scans were acquired in the same session it would be much easier to use this tool to detect artefacts because any structure in the difference image would be due to artefacts. Another problem with the registration of the masks onto this scan is that some change in hippocampal ventricle is included and also some brain boundary in the lower left temporal lobe. Again, this would not be a problem if using two scans acquired in the same session.

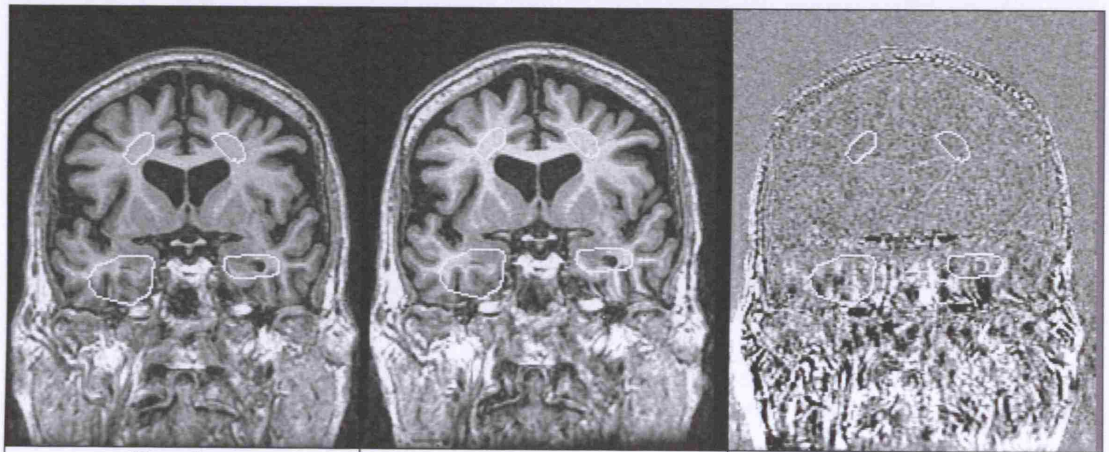

Figure 5-11 Example of underestimation of pulsatile flow artefact severity by automatic tool: Most severe part of artefact lies under the lower right ellipse on the repeat and difference image.

The algorithm can also overestimate the amount of pulsatile flow artefact. This can be seen in Figure 5-12, which was correctly identified as being rejected but had a score of 2.9 which was the highest score. This overestimation comes from the inter subject registration placing the temporal lobe area too high up and so including a bright vessels, see top row of Figure 5-12 (vessels usually appear with different intensities in

repeat scans and therefore appear with a large value in the difference image). It can be seen in the second row of Figure 5-12 that a large artefact is also caught within the ROI, so the high result is not purely due to the vessels being included. In my observations bright vessels appear to correlate with increased flow artefact, which agrees with Felmlee and Ehman's observation in 1987 that the intensity of the pulsatile flow artefacts decreased in direct proportion to the reduction of intensity in the flow channel as they were testing their flow saturation pulses. This effect means that inclusion of bright vessels, although overestimating the quantitative results, may not in many cases change the category in which these artefacts are automatically placed.

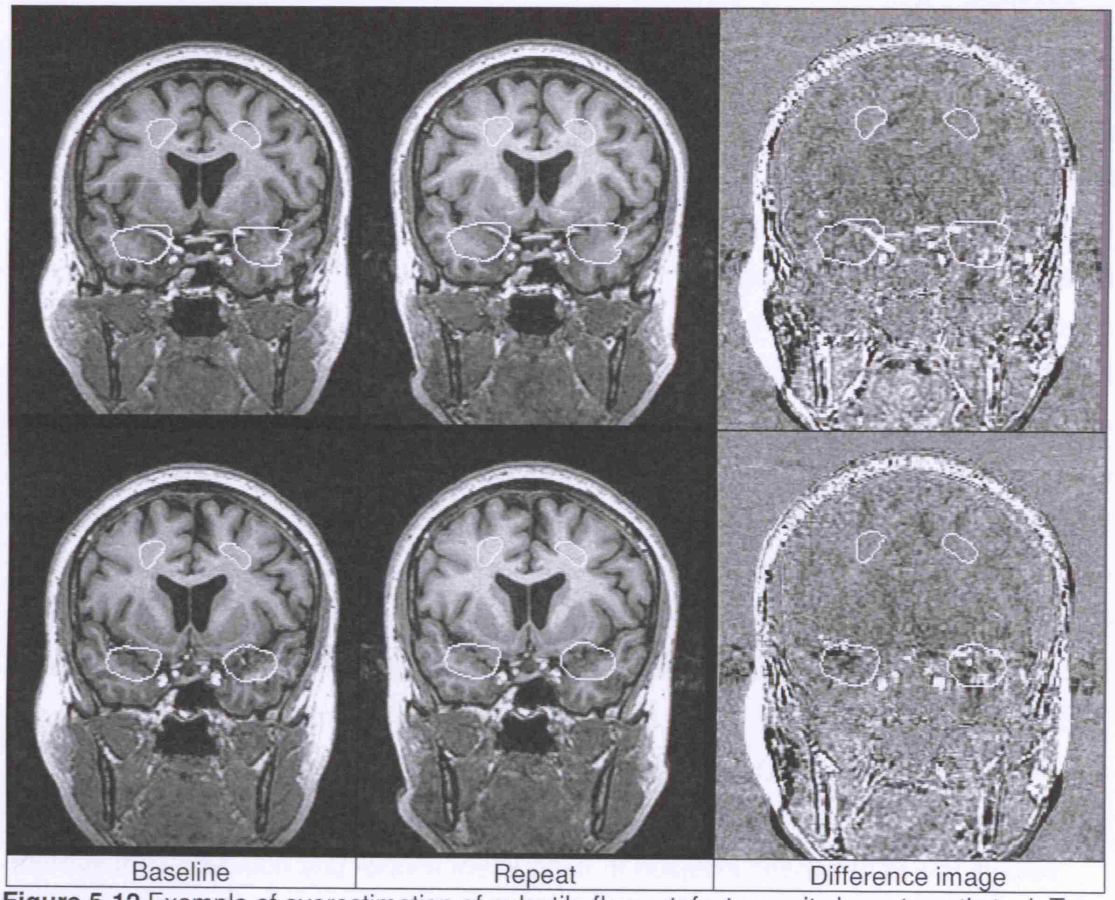

Figure 5-12 Example of overestimation of pulsatile flow artefact severity by automatic tool: Top row, artefact includes bright vessel; Bottom row, region also includes a good part of the artefact

To summarise, this tool already has good correlation with visual rating, although there are occurrences of slight over and underestimation. A new mask segmentation, further away from the brain boundaries and vessels, and a non rigid registration technique could further improve the results of this tool. However at present non rigid registration takes more time to process than the rigid type which I have used. If this tool is used on pairs of scans acquired at the same time point then it is not important if the brain boundaries are included in the region of interests.

The method used in this pulsatile flow artefact tool has the potential to be extended to detect eye ball motion in scans where artefacts run anterior/ posterior, or other types of artefacts which are located in a specific anatomical location.

The initial SNR pair measures, I have taken, correlate well with motion artefact severity. As well as increasing noise, motion artefacts can also result in ringing artefacts from the skull which can overlay the brain and cause severe problems for analysis or interpretation of the image. This measure could be improved by detecting the presence of these ringing bands.

5.6 Conclusion

This chapter has assessed the frequency of occurrence of different types of artefacts in historical and current clinical trial of dementia at 1.5T. The existing literature has been reviewed and lacks studies on the relative prevalence of various causes of artefacts in clinical dementia trials. To address this I have investigated the quality assurance records of scans from a large number of subjects (837) involved in clinical dementia trials. The frequency with which these artefacts occur in scans rejected and accepted into analysis was investigated. I have shown that temporal lobe artefact, motion artefact and problems with contrast are the most commonly occurring problems in the two trials investigated. The main cause of temporal lobe artefact was determined to be pulsatile flow artefact (responsible for 71% of temporal lobe artefacts in the more recent trial). The next most frequent temporal lobe artefacts are motion and susceptibility artefacts. Finally, I have designed and tested a tool to automatically quantify this pulsatile flow artefact, and proposed a tool to quantify motion artefact. Quantifying artefact is important for developing automated QC systems. Such systems could be used to reduce the frequency of artefacts in longitudinal trials which may improve their precision and reduce the number of subjects needed to power studies.

In Chapters 6 and 7, I simulate a cohort of scans with different levels of atrophy and artefact to determine the effect of accepting scans containing artefact into whole brain analysis, using both BSI and SIENA. As already shown in Chapter 4 pulsatile flow artefacts are significantly worse at 3T; this chapter has shown they are already a common occurrence at 1.5T in serial neuroimaging. This suggests that the issue of pulsatile flow artefacts ought to be considered in longitudinal trials using 3T scanners. In Chapter 8, I propose a novel method to correct this artefact.

6 Simulation of a database of longitudinal MR head images with known atrophy and acquisition artefacts

6.1 Introduction
- 6.1.1 Aims
- 6.1.2 Contribution

6.2 Literature Review
- 6.2.1 K-t space
- 6.2.2 Simulating motion
- 6.2.3 Simulating noise

6.3 Method
- 6.3.1 Materials
- 6.3.2 Atrophy simulation
- 6.3.3 Simulation of motion artefact
  - 6.3.3.1 Single step motion
  - 6.3.3.2 Periodic step motion
  - 6.3.3.3 Slow drift
  - 6.3.3.4 Adding noise to the simulation
  - 6.3.3.5 Simulating gold standard database with motion artefact
  - 6.3.3.6 Analysis of simulated images with motion artefact
- 6.3.4 Simulation of flow artefact

6.4 Results
- 6.4.1 Simulated images with motion artefact
- 6.4.2 Analysis of simulated images with motion artefact

6.5 Conclusions

6.1 Introduction

Artefacts are a common problem in longitudinal clinical dementia trials as shown in Chapter 5. They have the potential to affect results and conclusions of image-based analysis run on artefactual data. Whole brain atrophy quantification is one of the most used and critical image-based analysis applications in longitudinal dementia trials, and it is often performed using automatic or semiautomatic algorithms such as SIENA or BSI. To calculate the effect that motion artefacts have on these different algorithms, a quantifiable level of atrophy and artefact are needed, i.e. a gold standard. A database of longitudinal MR brain images with simulated atrophy and different simulated levels and types of motion artefact could provide these quantifiable levels. This cohort would also allow the assessment of post-processing artefact correction techniques [such as Howarth 2005, Atkinson 1999, Manduca 2000] and their incorporation in atrophy measurement methods. The main goal of this chapter is the generation of such a gold standard cohort of simulated images. In the Chapter 7, this cohort will be used to determine the effect of different levels of atrophy and artefact on SIENA and BSI.

Until recently this has not been possible because, apart from global scaling of the brain, there has been no effective atrophy simulation in existence. In 2006, Karacali et al, and Camara et al each described methods based on the combination of expert knowledge of clinical changes in brain with finite-element methods, providing valuable gold standard data for the objective validation of atrophy measurement techniques. Their techniques, however, did not take into account artefacts in the MR scans due to imperfections in the acquisition.

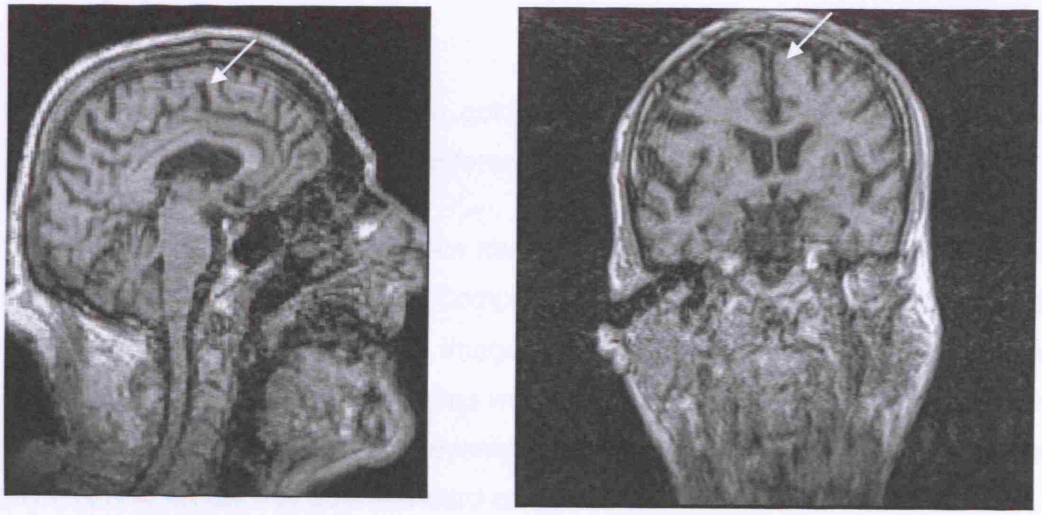

Figure 6-1 Example of motion artefact. Note skull ringing due to motion at edge of k-space, and intensity blurring due to motion near the centre of k-space

Acquisition artefacts may include movement during the acquisition of the edge of k space (domain in which raw MRI data is stored, the Fourier transform of this data is the MR image) leading to a ringing artefact from the scalp [Howarth 2005], global movement during the central portion of k-space which would blur image intensities (see Figure 6-1), or flow artefacts which may appear in the medial temporal lobes due to the pulsatile blood flow in the carotid arteries. Motion artefacts caused by the subject moving their head during image acquisition was shown to be one of the most common types of artefacts (Chapter 5, Sections 5.4.1), which is why it is chosen for simulation in this chapter. Another of the most common acquisition artefact identified in Chapter 5 was temporal lobe artefact, a region with a crucial role in Alzheimer's disease [Braak 1991]. The main cause of image degradation in the temporal lobe in 60 – 70% of temporal lobe artefacts is pulsatile flow artefact arising from the carotid arteries (Chapter 5, Section 5.4.1). Therefore, in Chapter 8, I develop a technique to simulate different pulsatile flow artefacts, which can be used on this cohort to provide a gold standard for testing atrophy techniques which measure local regions from the temporal lobe.

6.1.1 Aims

In this chapter, I aim to generate a cohort of longitudinal MR brain images with known levels of simulated atrophy and motion artefact of different types. This is to provide a gold standard database on which to test different atrophy quantification techniques. In doing this I aim to provide a method for generating gold standard cohorts with various different types of artefacts which can be used to test the robustness of atrophy quantification tools to these artefacts.

6.1.2 Contribution

My contribution is the generation of a gold standard database with known simulated atrophy and artefact on which to test different image analysis tools.

The technique used for simulating brain atrophy in this work was developed by Oscar Camara, Centre for Medical Image Computing (CMIC), UCL. Oscar performed the atrophy simulation on the baseline images from 7 subjects to provide simulated longitudinal scans. These baseline scans were acquired at the DRC, Queen's Square, UCL. I simulated different types and severity of motion on these baseline and simulated atrophy scans to create this gold standard cohort.

6.2 Literature Review

6.2.1 K-t space

The concept of using K-t space to simulate motion artefacts was proposed by Twieg et al in 1987, Riek and Tekalp in 1991, and Xiang and Henkelman in 1993. K-t space is the concept that the object being imaged is changing over time, therefore the true k space representation of that image is also changing over time. This can be represented for a 2D image by adding a third dimension, time. Most acquisition sequences sample different portions of k-t space at distinct times which acquires only part of this k-t space. This can lead to an inconsistent k-space which when transformed to the image domain can cause artefacts such as ringing, blurring and ghosting artefacts. Artefacts can be simulated by considering the object in k-t space, compiling the portions of k-t space which would be sampled using the simulated sequence, to give the simulated k space. When this k space is transformed to the image domain the resulting artefacts caused by the variation of the object over time will become apparent.

6.2.2 Simulating motion

Preboske et al, 2006, simulated motion in MR images by applying synthetic motion to the MR k-space. They divided k-space into 8 blocks, and added motion in the x direction to the second and eighth block, in the x and y directions to the third and seventh block, and in the y direction to the forth and sixth block, and no motion to the first and fifth block. Different magnitudes of the motion in image space were simulated: 0.3125, 0.625, 1.25, 2.5, and 5 pixels (pixels size 0.9 x 1.25mm).

6.2.3 Simulating noise

Preboske et al, 2006, simulated various levels of noise on MR images. They did this by transforming raw k-space data into the image space, using a proprietary program called MR-View. The image data had a dynamic range of 25 000. Noise was generated onto this image with a standard pseudo random number generator with a period of order 2^{32}. The range of the noise was from zero to the highest chosen value, which was 500, 1250, 5000 and 7500 for the various levels of noise. This is approximately equivalent to 2, 5, 10, 20 and 30% of the dynamic range of the image.

6.3 Method

6.3.1 Materials

The cohort is based on 7 MR scans of healthy elderly controls. The controls were enrolled in a longitudinal research project at the Dementia Research Centre, Institute of Neurology, UCL and underwent serial MRI, clinical and neuropsychological assessment over a period of at least one year. T1-weighted volumetric MR images were acquired on a 1.5 Tesla Signa Unit (General Electric, Milwaukee) using a 256x256 matrix to provide 124 contiguous 1.5mm coronal slices through the head (acquisition parameters: time to repeat, 15ms; time to echo, 5.4ms; flip angle 15°, field of view 24x24cm).

6.3.2 Atrophy simulation

To generate the ground truth cohort, I use a simulation technique proposed by Camara et al, 2006. Karacali et al., 2006 have also proposed a different approach to simulating atrophy. His technique is based on the generation of topology-preserving deformation fields with Jacobian determinants matching the desired volumetric changes on a specific region of interest. The main drawback of Karacali's technique is that it does not take into account the relationship between different structures. In Camara et al., 2006

atrophy is simulated in different tissue compartments or in different neuroanatomical structures with a phenomenological model. A thermoelastic model of tissue deformation is used to control the rate of progression of atrophy by means of a set of thermal coefficients (each corresponding to a tissue type). Camara's method requires a set of segmented structures to build the input of the finite element methods (FEM) solver, unlike Karacali's method, which does not necessarily need a segmentation step prior to simulation (the region of interest can be a sphere centred on a manually selected point in the image). On the other hand, in Camara's method the biomechanical readjustment of structures is modelled, using conventional physics-based techniques based on biomechanical tissue properties.

For these reasons I use Camara's approach to simulation. The simulation method can be divided into four phases: meshing of a labelled brain atlas; adaptation of the generated mesh to an individual MR scan; introduction of the individual-specific mesh into a finite element methods (FEM) solver that will generate the simulated deformations; and the application of such deformations to the MR scan. More details about this method can be found in Camara, 2006. Figure 6-2 shows an example of atrophy simulation.

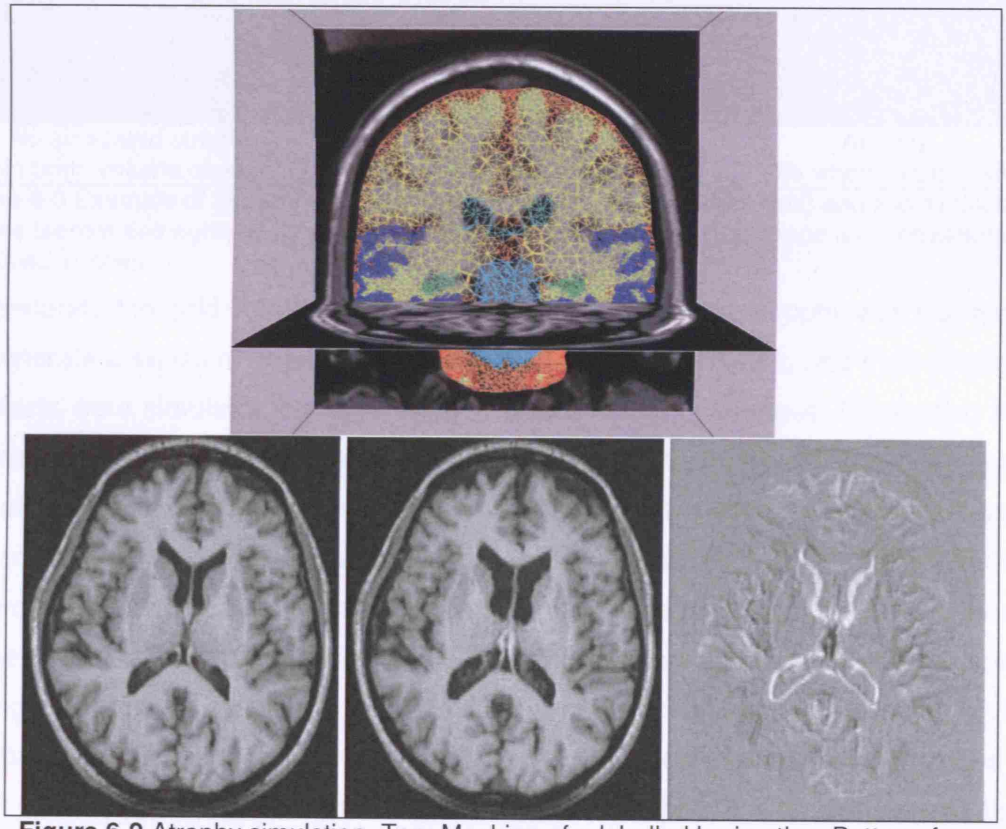

Figure 6-2 Atrophy simulation. Top: Meshing of a labelled brain atlas. Bottom, from left to right: baseline scan before simulation, atrophy simulated scan and difference image generated by subtraction of the baseline scan from the atrophy simulated scan.

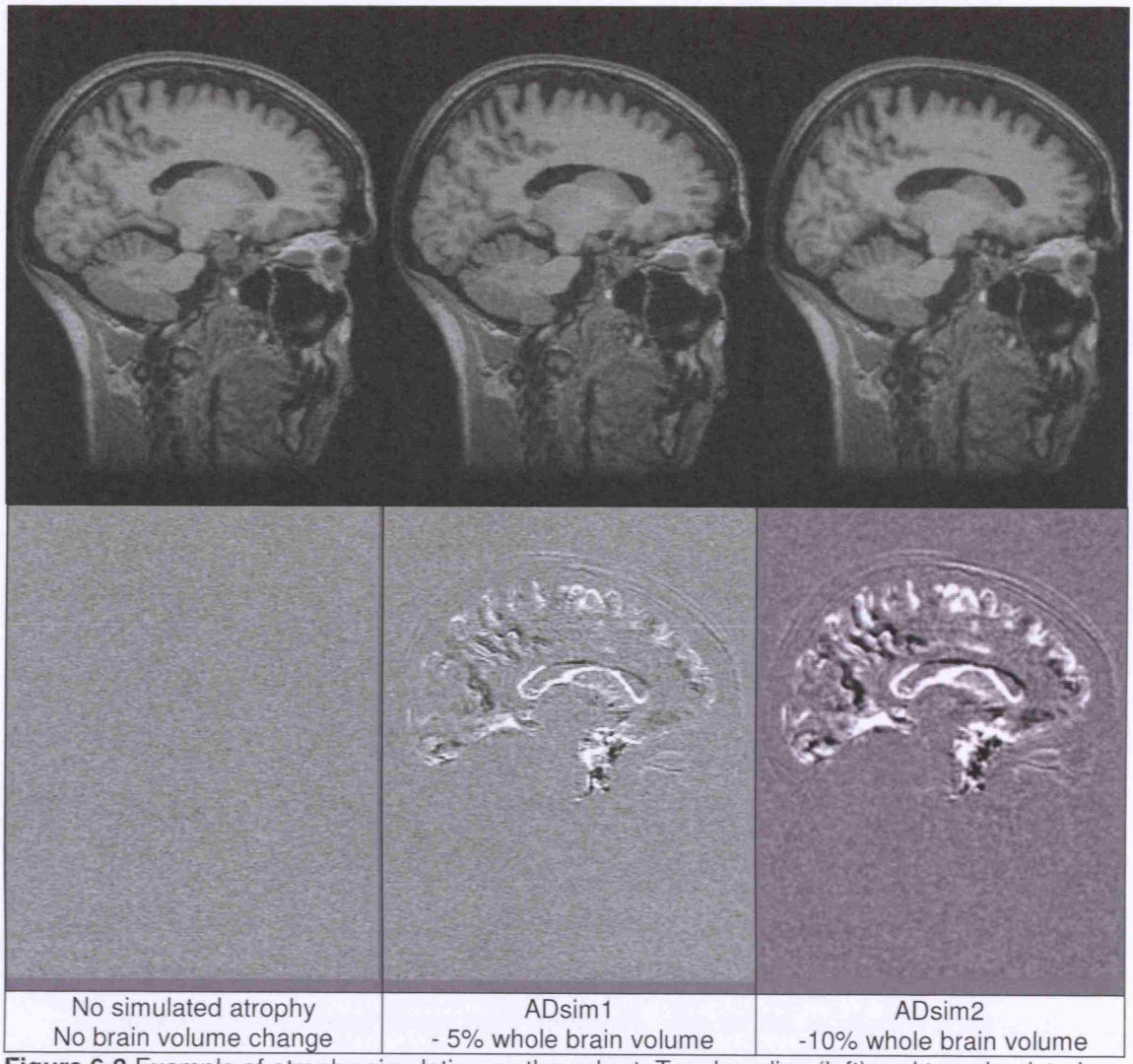

Figure 6-3 Example of atrophy simulation on the cohort. Top: baseline (left) and two simulated images (centre and right). Bottom: difference image between baseline image and corresponding simulated images.

To generate the gold standard database of simulated images, atrophy was first applied to generate a series of images for each of the 7 baseline images, and then acquisition artefacts were simulated on top of these atrophy simulated images. Generating these series of images for each baseline was done by Oscar Camara as follows. He applied the atrophy simulation technique [Camara 2006] to each of the 7 baseline MR scans, generating two new images, *ADsim1* and *ADsim2*, for each subject baseline scan, with different amounts of global atrophy, resulting in a dataset of 21 images. In this thesis, I make use of the atrophy simulation's ground truth values for the whole brain volume change, since I am going to study the effect of artefact on algorithms which give an estimation of the global atrophy rate. However, the atrophy simulation technique can also simulated different amounts of regional atrophy in several brain tissue compartments and structures. These ground truth values for local changes could be used to consider the effect of artefact on local atrophy measurement techniques. The

mean and standard deviation of the simulated whole brain volume change percentages are the following:

- ADsim1: brain volume reduction of 5.10% ± 0.26
- ADsim2: brain volume reduction of 10.82% ± 0.53

An example of simulating these levels of atrophy on one of the baseline images can be seen in Figure 6-3.

6.3.3 Simulation of motion artefact

Rotational motion during a scan causes inconsistencies in the sampled k-space signal that results in blurring and ghosting in the image domain. In this section, I describe how I simulate three types of rotational motion: a single step rotational motion, a periodic step rotational motion, and a slow constant drift motion throughout the scan.

The method I developed to simulate rotational motion is the following:

1. A motion-free 3D image volume is converted into a complex image, C, by treating the modulus image as the real part, and setting the imaginary component to zero (see top left of Figure 6-4)

2. This complex image, C, is then rotated by a set amount, between 0 and 10 degrees, about a central axis in the left/right direction (therefore approximately parallel to the internal auditory meatus), simulating a slight nodding of the patient during the scan. This produces a rotated, complex image, R (bottom left of Figure 6-4). Bicubic interpolation is used in the rotation, and voxels entering the volume are assigned the value zero.

3. The original, C, and rotated, R, images are then both Fourier transformed into k-space, giving c, and r. (second column of Figure 6-4).

4. A motion-corrupted k-space, m, is subsequently generated by assembling portions of the k-spaces corresponding to the un-rotated, C, and rotated images, R (third column of Figure 6-4).

5. The motion-corrupted k-space is then transformed back to the image domain (right image of Figure 6-4) to give the motion corrupted volume, A.

The k-space samples were combined as sagittal planes representing a sagittal MR acquisition orientation. Transverse or coronal planes could also have been simulated.

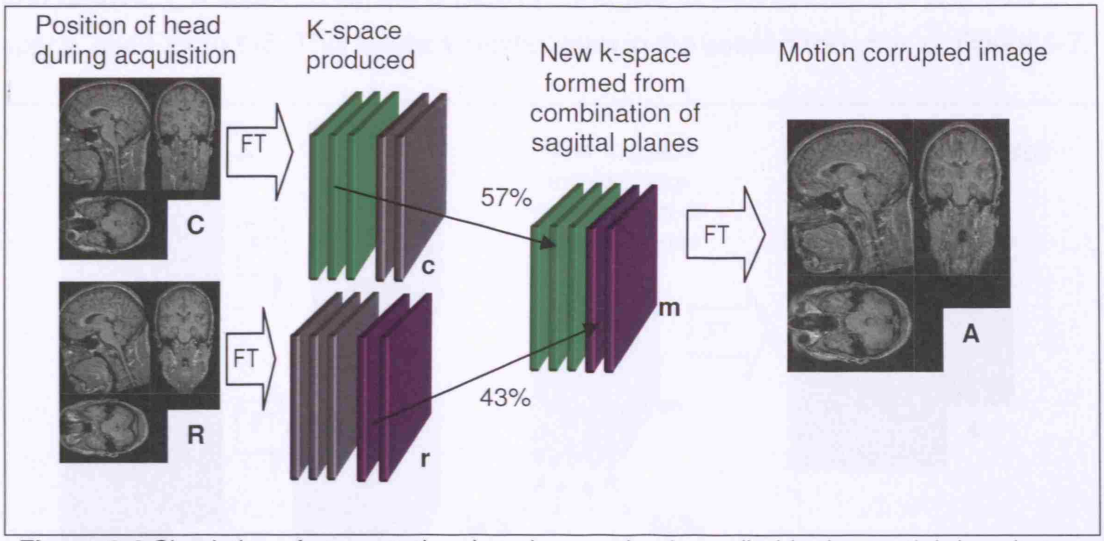

Figure 6-4 Simulation of step rotational motion: motion is applied in the spatial domain to a motion-free image volume, and the k-spaces re-combined to generate a motion-corrupted image volume.

The appearance of the motion artefacts is influenced by which region of k-space (its distance to the centre of the k-space) is being sampled as the motion takes place, and whether a single step motion, a periodic step motion, or a continuous slow drift occurs. The developed technique allows complete freedom in the selection of the k-space region in which the motion occurs.

For the generation of the gold standard cohort needed to evaluate the robustness of atrophy quantification techniques with respect to artefacts, single step motion, periodic step motion and slow drift are simulated using the parameters described below.

6.3.3.1 Single step motion

I simulate a single step motion since a single sudden movement can commonly occur, for example when the subject coughs or sneezes. This can cause troublesome motion artefacts, especially when the single step motion occurs near the middle of the scan. To simulate this single step motion, I combine the first 57% of the un-rotated k-space, c, with 43% of the rotated k-space, r, as shown in Figure 6-4. This results in the artefact seen in the first two rows of Figure 6-7.

6.3.3.2 Periodic step motion

Periodic motion in MR scans can often cause more severe artefacts than a single step motion. Defined ghosts and increased blurring can occur particularly in the phase encode direction. To simulate periodic step motion, representing a repeated nodding of the head, I generate the motion-corrupted k-space from portions of the un-rotated, c,

and rotated, r, k-space, alternating between the two at 44%, 48%, 52% and 56% of k-space, see Figure 6-5. This artefact can be seen in the second two rows of Figure 6-7.

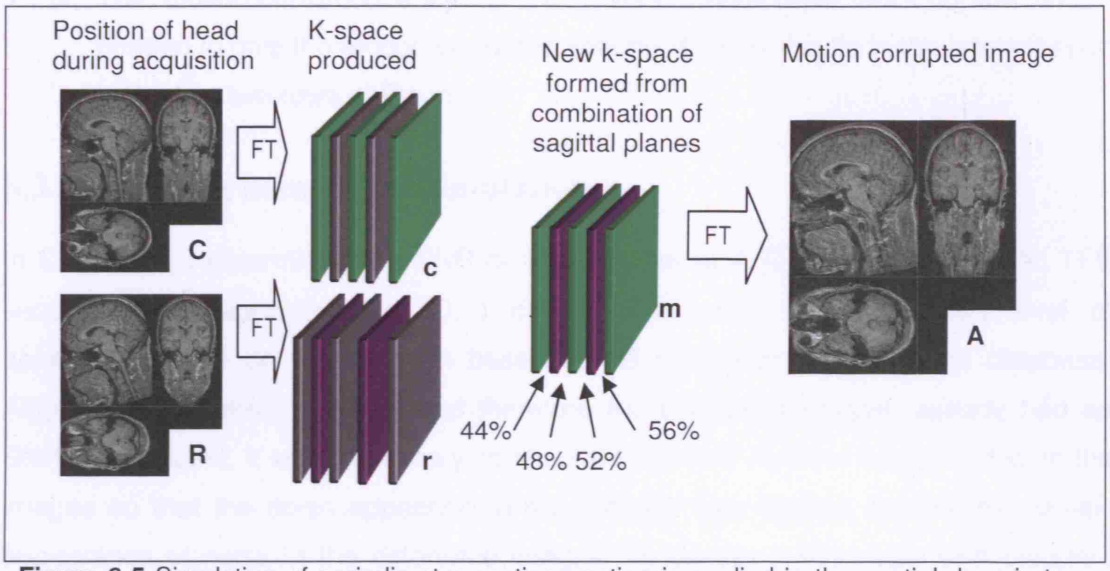

Figure 6-5 Simulation of periodic step motion: motion is applied in the spatial domain to a motion-free image volume, and the k-spaces re-combined in an alternating manner to generate a motion-corrupted image volume, simulating a repeated nodding of the head.

6.3.3.3 Slow drift

A slow drift is a very common type of motion during MRI acquisition as the subject slowly relaxes their muscles during scanning. I simulate a slow drift, representing a continuous, smooth rotation of the head around the left right axis, throughout the scan.

1. To simulate this type of motion, as many images as there are planes in k-space are created each with different levels of rotation, $R_{-N}...R_{-2},R_{-1}$, $C,R_1,R_2...R_N$ where 2N+1 is the number of planes in k-space.
2. The first image R_{-N} is rotated in the negative direction by $\alpha/2$, where α is the specified angle of rotation. The last image R_N is rotated in the positive direction by $\alpha/2$. The angle of rotation of each image is given by $\alpha n/2N$, where n is the number of the image, R. The central image, R_0, therefore remains unrotated and is equivalent to C.
3. All the images, $R_{-N}...R_{-2},R_{-1}$, $R_0,R_1,R_2...R_N$, are then Fourier transformed into k-space giving, $r_{-N}...r_{-2},r_{-1}$, $r_0,r_1,r_2...r_N$.
4. A motion-corrupted k-space, m, is generated by assembling one plane from each of the rotated and unrotated k-spaces, $r_{-N}...r_{-2},r_{-1},r_0,r_1,r_2...r_N$. The first plane in m, is selected from r_{-N}, the second from $r_{-(N-1)}$, the central plane from c, and the last from r_N. The centre plane of k-space is therefore unrotated keeping the

bulk intensities of the motion corrupted volume unrotated with respect to the original image.

5. The motion-corrupted k-space, m, is then transformed back to the image domain to give the motion corrupted volume, A. This results in the artefact seen in the last two rows of Figure 6-7.

6.3.3.4 Adding noise to the simulation

In Chapter 4, I determined the SNR of white matter at 1.5T using the specified TFE sequence was approximately 50. I chose to simulate a similar SNR level of approximately 50 on top of each baseline and simulated image in the database. Although the baseline images, and therefore the simulated images, already had an SNR of this level, it was necessary to simulate different random noise on top of the images so that the noise appearing in each image was distinct, leading to realistic appearance of noise in the difference images. To do this I add noise with standard deviation 2 to each of the real and imaginary components, resulting in modulus data with noise of a standard deviation of approximately 2.8. The white matter intensity in the baseline images in my cohort is approximately 135 (dynamic range of image 0-268), which means that an SNR of approximately 48 is simulated. To generate the random noise I use a pseudo random noise generator within Matlab (MathWorks, Natick, MA.) 'normrnd' which generates random numbers chosen from a normal distribution, which I select to have a mean of zero, and a standard deviation of two. Matlab claims that theoretically this pseudo random generator can generate over 2^{1492} values before repeating itself.

6.3.3.5 Simulating gold standard database with motion artefact

To simulate motion artefact, I applied the methods described previously to the whole dataset of baseline and atrophy simulated images. I simulated single step, periodic step and slow drift rotational motion of varying severity (i.e. changing degrees of rotation: every 1 degree interval, between 1 and 10) on each of the baseline and atrophy simulated images. This involved simulating 3 types of motion artefact with 10 different angles at 3 time points for each of 7 baseline images, giving a total of 630 images with simulated motion artefacts.

6.3.3.6 Analysis of simulated images with motion artefact

In order to quantify the general image degradation effect of increased angle of rotational motion artefact on the images, I measured the signal and noise in a region of

white matter. I used a region of white matter so that the noise would be Gaussian (rather than Rican as in the lower intensity regions, see Chapter 3 Section 3.1). I measured this for one subject's baseline and atrophy simulated images with all the different types and angles of rotations applied. The method I used to calculate the signal and noise is detailed in Chapter 4, Section 4.3.2 and Chapter 5, Section 5.3.2. The region of white matter, over which I measured the signal and noise, was segmented from the baseline image and used to mask all the other images. Obtained results can be seen in Figure 6-8. Examples of the images resulting from simulated single step, periodic step, and slow drift rotational motion are shown in the results section.

6.3.4 Simulation of flow artefact

As well as simulating motion artefact on the cohort, which is the most common cause of acquisition artefact, I also simulate pulsatile flow artefact from the carotid arteries, which is the most common cause of local artefact in the temporal lobe (see Chapter 5). The simulation of this artefact is detailed in Chapter 8.

6.4 Results

6.4.1 Simulated images with motion artefact

Figure 6-6 compares a simulated motion artefact with an acquired motion artefact. Similar ringing and blurring artefacts can be seen in both.

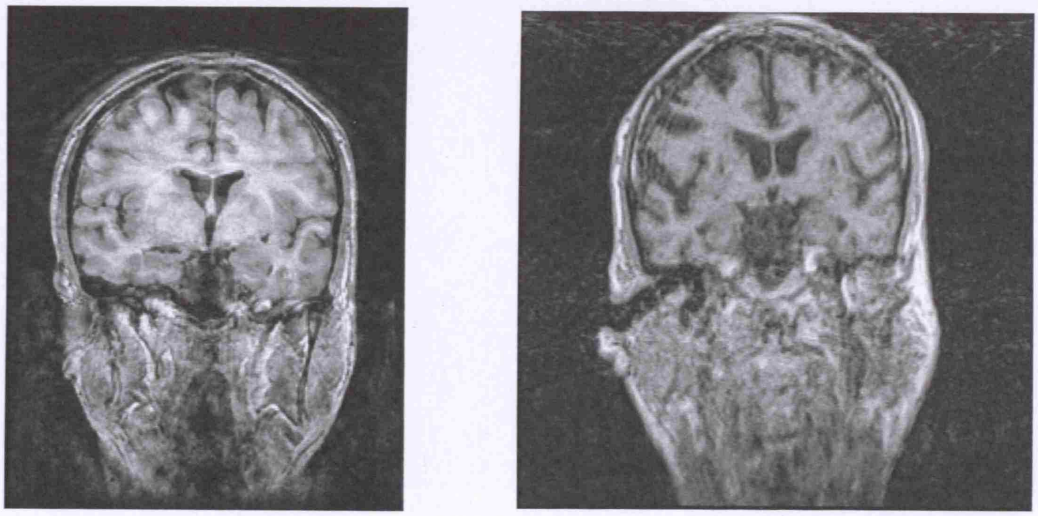

Figure 6-6 Comparison of simulated motion artefact with 10° periodic step motion (left) with acquired motion artefact (right)

Figure 6-7 shows the three different types of motion artefacts, all at 2 degrees of rotational motion, on the baseline and different atrophy simulated, longitudinal images from one volunteer. The images are sample sagittal slices, all taken from images based on the same subject, and from the same position. The difference images are windowed to +- 35% of the grey matter intensity. These images can be compared to Figure 6-9 to see how the images with artefacts differ to those without. The figure starts on the next page and runs over onto the following page. It shows images with different amount of atrophy from left to right and each pair of rows shows a different type of simulated motion artefact.

Figure 6-7 Baseline scan from one volunteer with different amounts of simulated atrophy from left to right and simulated motion artefact. Each pair of rows shows a different type of simulated motion artefact of 2 degrees rotation. The first row of each pair shows simulated images. The second row displays the difference between the image directly above and the original baseline scan without artefact and atrophy simulation. The first pair of rows displays single step motion, the next pair simulated periodic step motion and the final pair drift motion.

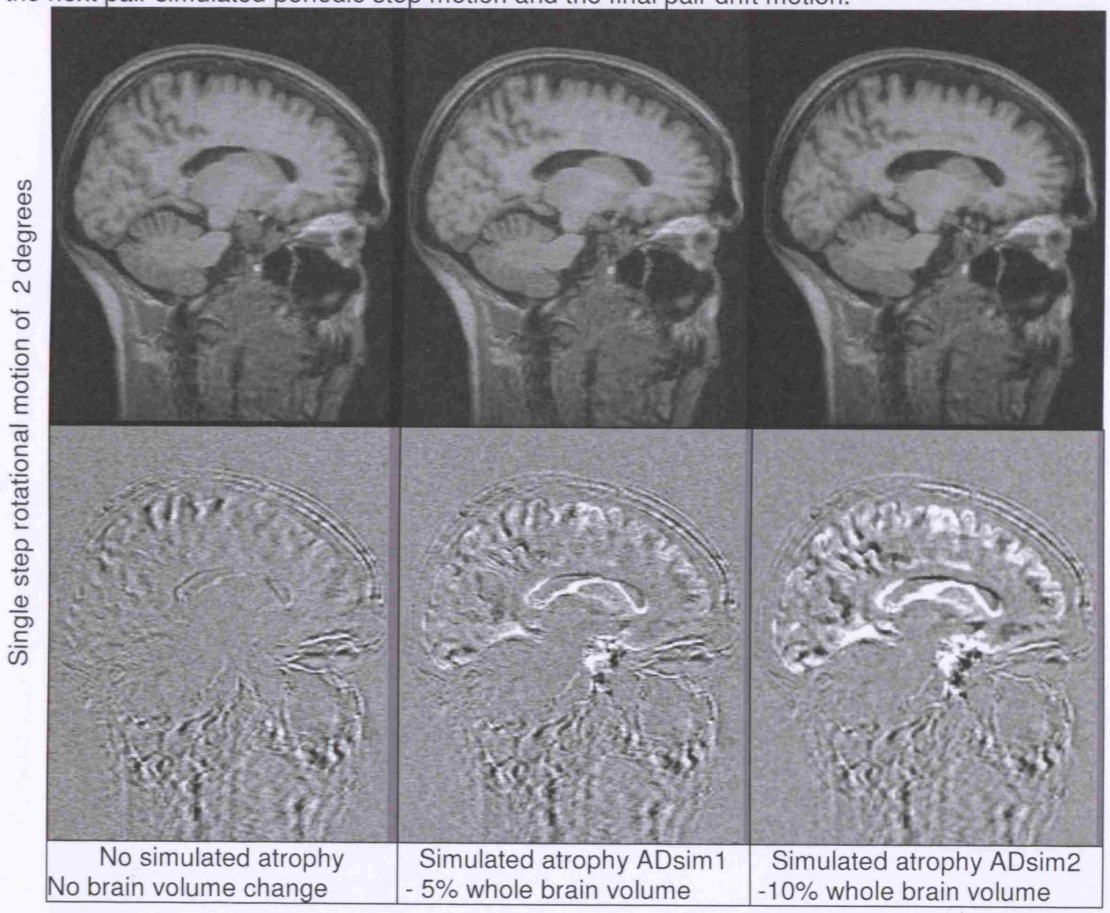

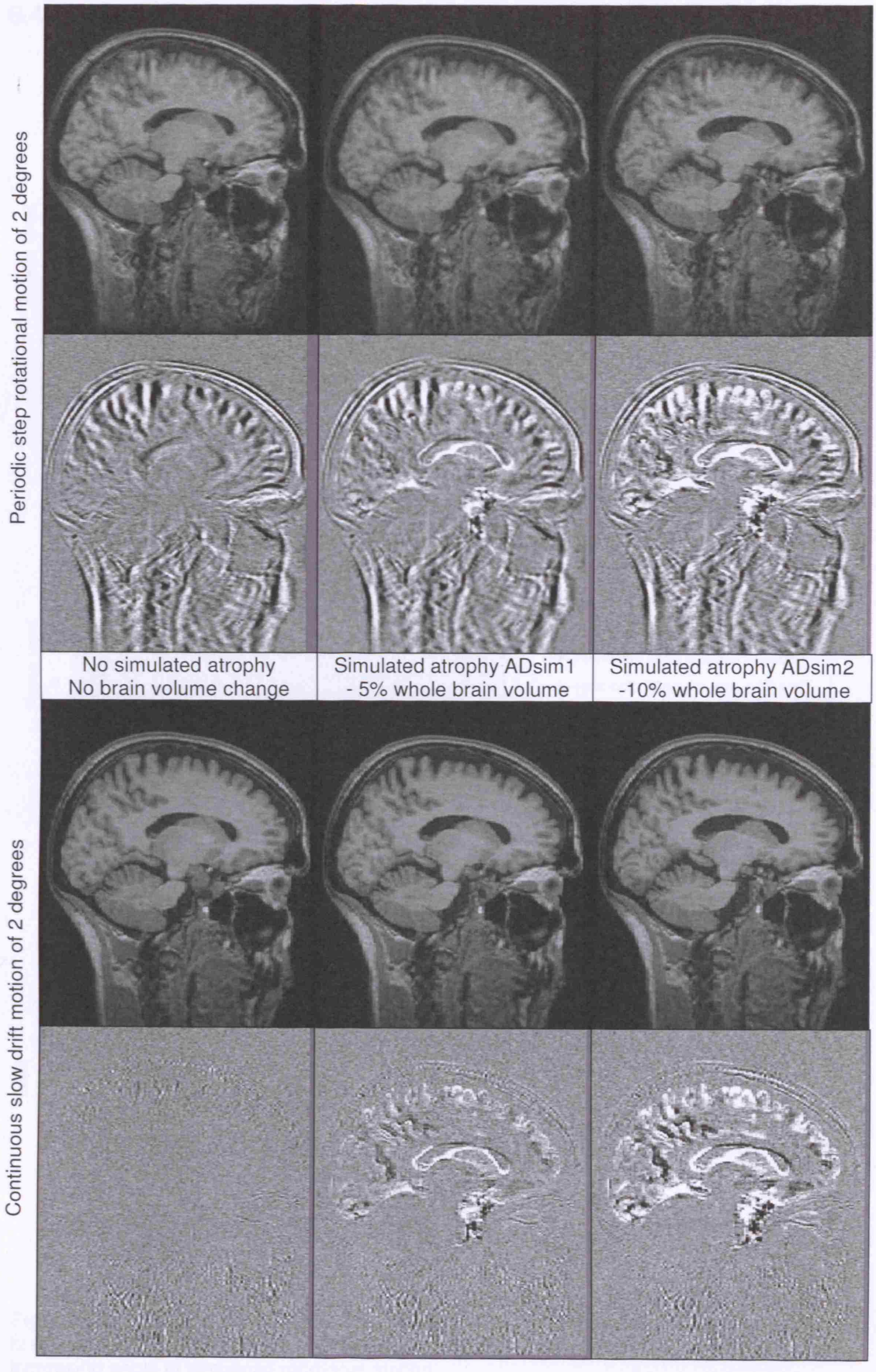
Periodic step rotational motion of 2 degrees
No simulated atrophy
No brain volume change
Simulated atrophy ADsim1
- 5% whole brain volume
Simulated atrophy ADsim2
-10% whole brain volume
Continuous slow drift motion of 2 degrees

6.4.2 Analysis of simulated images with motion artefact

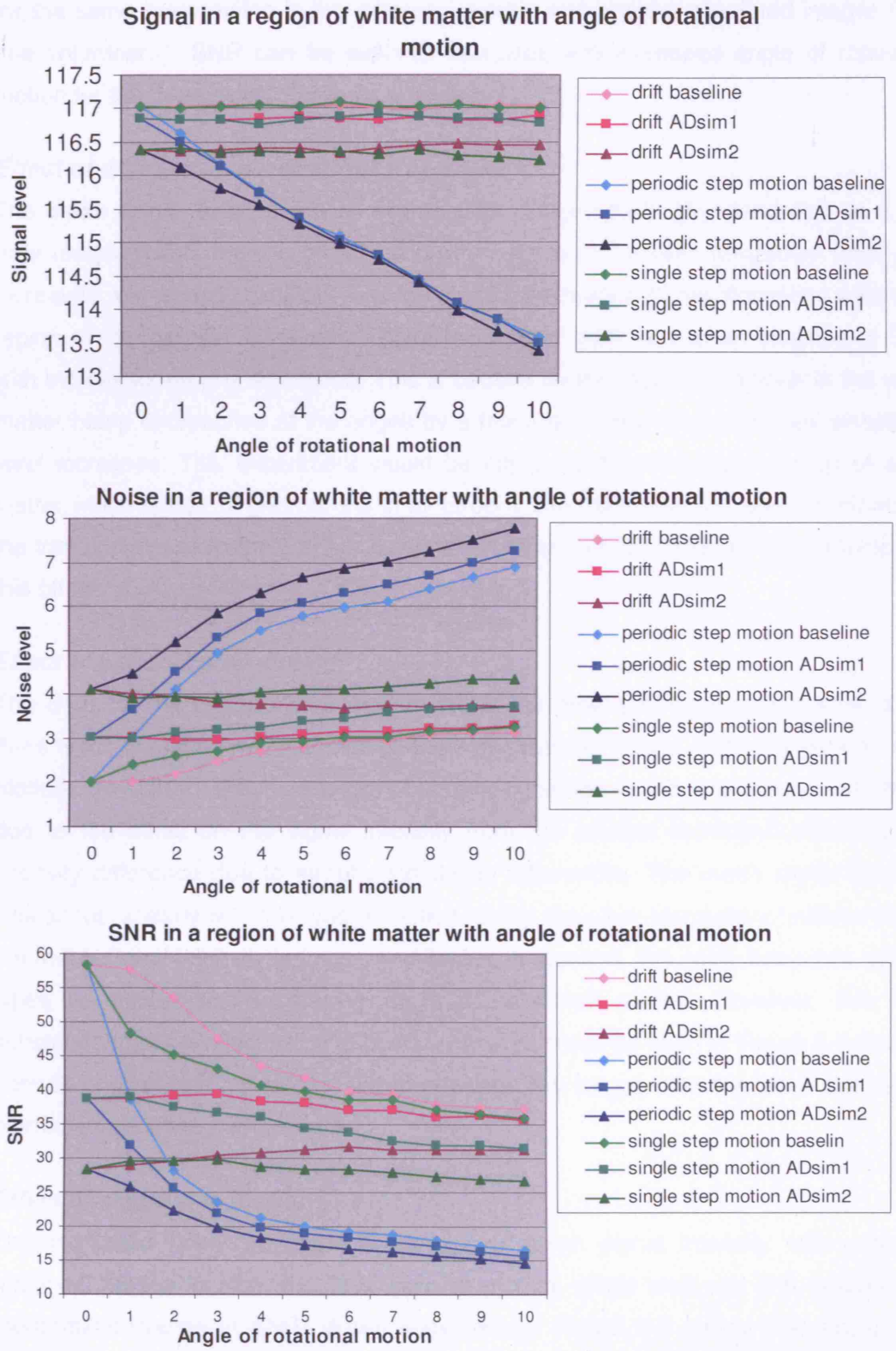

Figure 6-8 Top: Signal levels Middle: Noise levels Bottom: SNR. All shown for the same brain region, in the different atrophy and artefact simulated images from one volunteer, with increasing angle of simulated rotational motion.

In Figure 6-8 the SNR (signal to noise ratio), the signal and the noise levels are shown for the same brain region in the different atrophy and artefact simulated images from one volunteer. SNR can be seen to decrease with increased angle of rotational motion for the three types of rotational motion.

Effect of different levels of atrophy simulation

The mean signal level decreases slightly with increased atrophy simulation as a few grey matter voxels have encroached on the region of interest. The noise level also increases with atrophy simulation as the standard deviation of the intensities within the region of interest also increases. These two factors both lead to an increase of SNR with increased atrophy simulation. This is caused by the region of interest in the white matter being encroached at the edges by a few grey voxels as the atrophy simulation level increases. This experiment would be improved by selecting a region of white matter which is free of grey voxels in all atrophy simulation without artefact. However, the trends and conclusions of this analysis are clear and do not seem to be affected by this offset.

Effect of periodic step motion

The SNR for the periodic step motion shows the most pronounced decrease of the three types of motion with increase of angle of rotational motion. With this periodic step motion, the SNR for the three levels of atrophy converge as the angle increases, this is due to the effect on the signal intensity from the artefact blurring dominating any intensity difference due to atrophy simulation differences. The mean signal intensity falls almost linearly with this type of motion, unlike the other two types of motion where the mean signal intensity is largely unaffected. In general, the noise increases with all types of motion with increasing angle of rotational motion. However, this is a substantially larger effect with the periodic motion. It can be seen in Figure 6-9 that the periodic motion has the largest visual effect on the image, with the most substantial blurring in the white matter tissue.

Effect of single step motion

The increased noise and lack of change of mean signal intensity with angle of rotational motion for the other two types of motion, single step and drift, results in a moderate decrease in SNR. Visual inspection of Figure 6-9 shows that single step motion has a mild visible effect on blurring the intensities across the image, only apparent in the difference image or by comparing an affected image closely with the original one without artefact.

Effect of drift motion

Drift motion is most visible at the grey/CSF boundaries; it has a negligible visible effect on the white matter away from the boundaries, unlike the periodic step motion. It is the only type of motion where, for ADsim2 (i.e. the more severe atrophy simulation) the noise level actually slightly decreases with increases angle of rotation and the SNR slightly increases as a result. This could be due to a smoothing effect of the artefact blurring the intensity of the few grey voxels in the region of interest (see Section 'Effect of different levels of atrophy simulation'). This could potentially cause a greater decreasing effect on the standard deviation of the voxels' intensities than the increase due to the artefact introduced in this internal region. The effect of drift motion on noise in the region of interest across the other two levels of atrophy is the usual increase in noise with increase in angle of motion. This leads to the different levels of atrophy simulation converging to a noise level of 3.3 with increased angle of rotational motion.

Figure 6-9 shows the visual increase in blurriness of the simulated scans with increased rotational angle for the three types of motion artefact.

Figure 6-9 Baseline scan of one volunteer with simulated motion of increasing rotational angle. The first row shows the baseline image without artefact and its difference image for comparison purposes. Each following pair of rows shows a different type of simulated motion artefact. The first row of each pair shows simulated images. The second row displays the difference between the image directly above and the original baseline scan without artefact simulation. First pair of rows: single step motion. Second pair: periodic step motion. Final pair: continuous drift motion

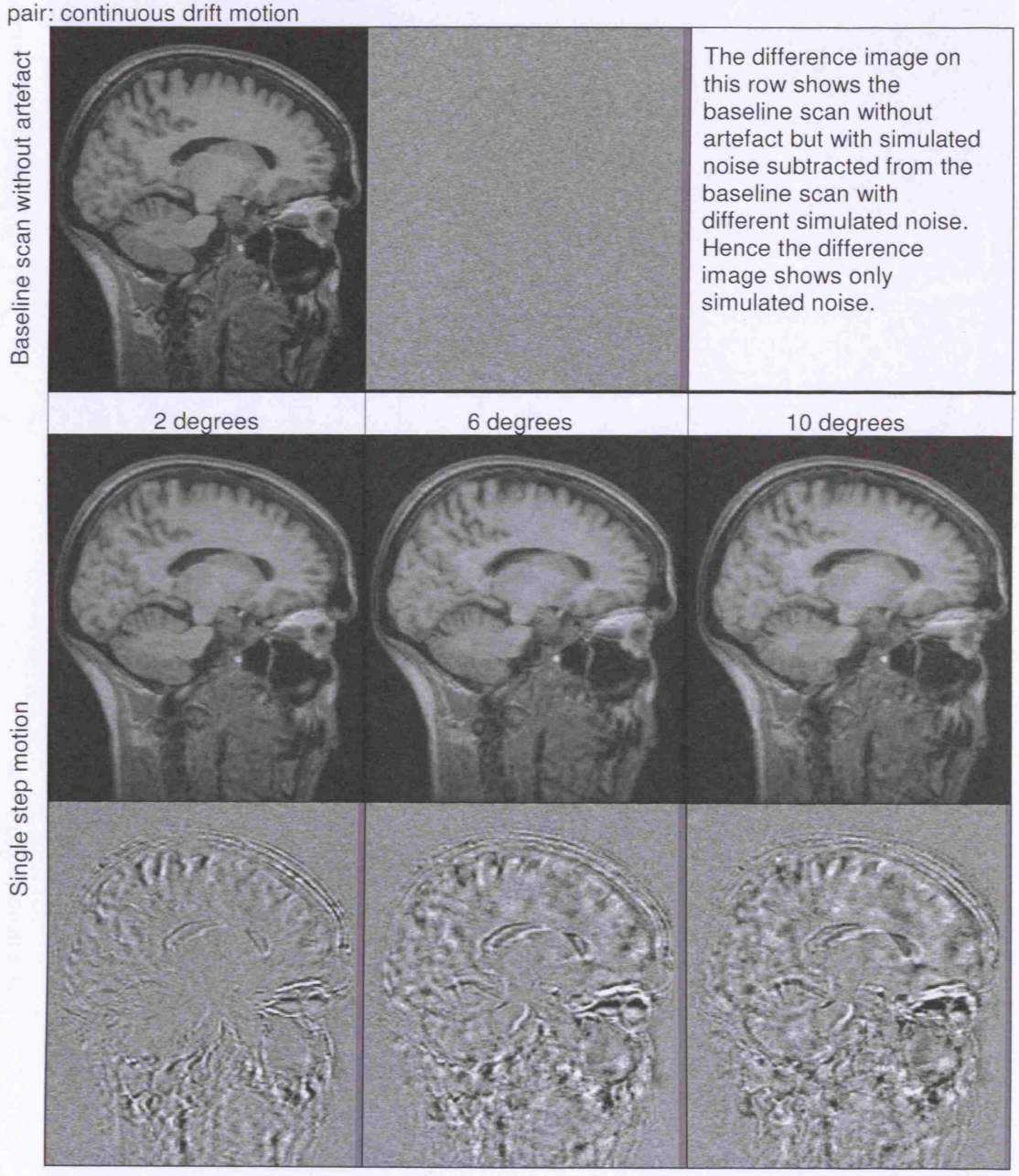

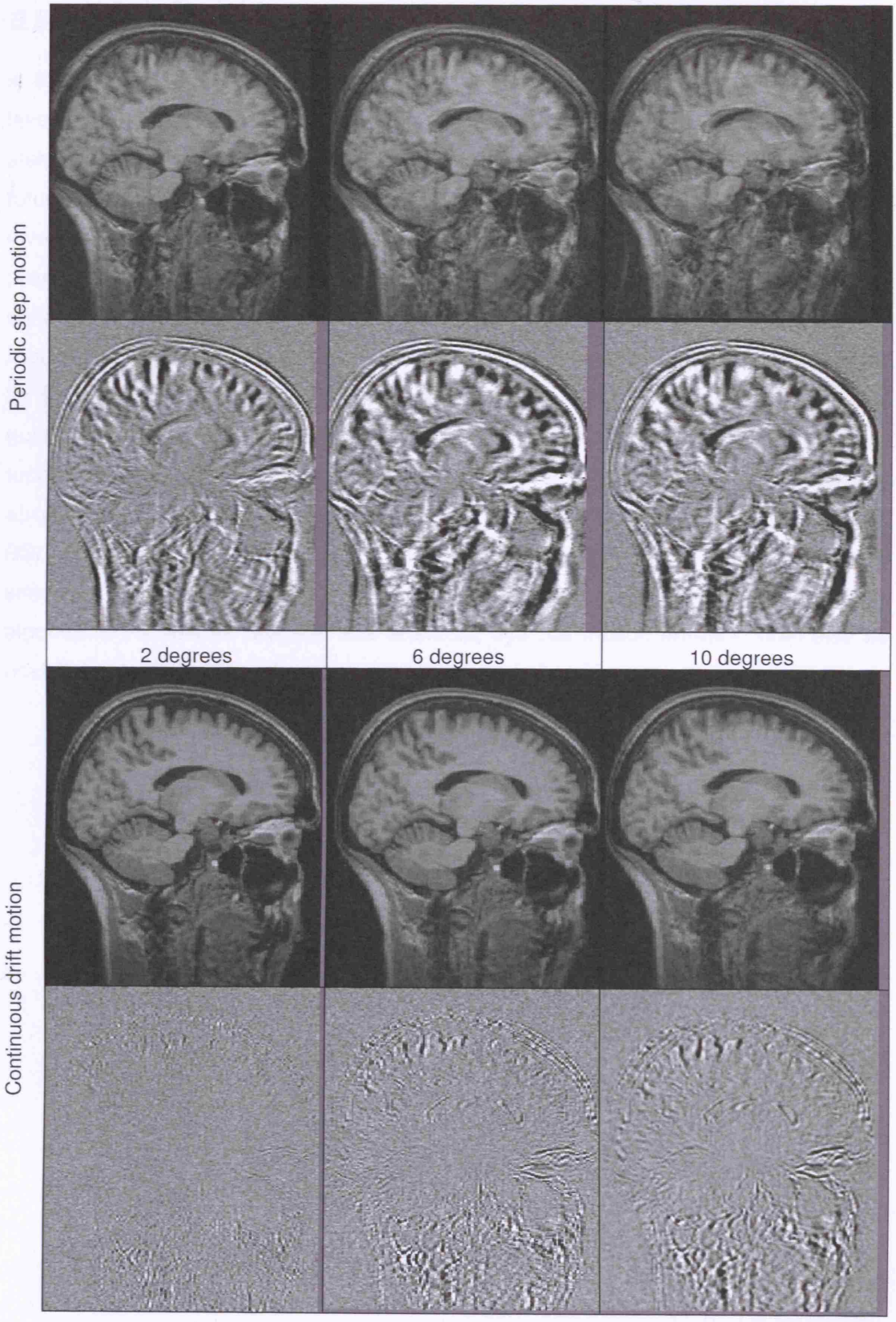
Periodic step motion
2 degrees
6 degrees
10 degrees
Continuous drift motion

6.5 Conclusions

In this chapter I have generated a cohort of longitudinal MR brain images with known levels of simulated atrophy and motion artefact of different types, to provide a gold standard set of data on which to test different atrophy quantification techniques. In future work I would suggest using smaller levels of atrophy more consistent with normal levels for 6 months, or a year of brain atrophy from AD. As a result of the work presented in this chapter, a method has been provided for generating gold standard cohorts with various different types of artefacts which can be used to test the robustness of atrophy quantification tools to these artefacts. In Chapter 8, a technique for simulating pulsatile flow artefacts is developed to enable the generation of a similar gold standard cohort with the potential for testing the robustness of local atrophy techniques to this type of artefact. In the next chapter, Chapter 7, I use the simulated atrophy and motion data to investigate the effect of motion on whole brain atrophy tools BSI and SIENA. There is scope for future work investigating how localised artefacts simulated on a gold standard cohort affect regional atrophy measures from various algorithms. As well as pulsatile flow artefacts, eye ball motion artefact could also be usefully generated on a cohort for such a purpose.

7 Robustness assessment of global atrophy quantification techniques with a gold standard of atrophy and artefact simulated images

7.1 Introduction
- 7.1.1 Aims
- 7.1.2 Contribution

7.2 Literature Review
- 7.2.1 Overview of atrophy measurement techniques
- 7.2.2 Global techniques
  - 7.2.2.1 Boundary Shift Integral
  - 7.2.2.2 SIENA
- 7.2.3 Local brain volume change
  - 7.2.3.1 Manual or automatic delineation of hippocampus
  - 7.2.3.2 Jacobian of deformation field from nonrigid registration
- 7.2.4 The effect of artefacts in longitudinal imaging studies
  - 7.2.4.1 Effect of artefact on manual delineation
  - 7.2.4.2 Effect of artefact on automatic segmentation
  - 7.2.4.3 Effect of artefact on difference images
  - 7.2.4.4 Effect of artefact on BSI measures of scans without atrophy

7.3 Method
- 7.3.1 Materials
- 7.3.2 BSI
- 7.3.3 SIENA

7.4 Results

7.5 Discussion

7.6 Conclusions

7.1 Introduction

In this chapter I use the cohort generated in the previous chapter to investigate the effect of acquisition artefacts on atrophy quantification techniques.

Structural magnetic resonance imaging (MRI) can be used to estimate the progression of neurodegenerative disease since brain atrophy is a measurable macroscopic feature of the most common forms of dementia such as Alzheimer's disease (AD) (see Chapter 1, Section 1.1.1 for background on AD). Several computerized techniques [Freeborough 1997, Smith 2001, Davatzikos 2001, Freeborough 1998] for the quantification of cerebral atrophy in MR scans are available in the literature. Nevertheless, there is a lack of consensus on the most appropriate method to be used since there have been no gold standard data sets with which to test the different methods. In the previous chapter I have generated a gold standard cohort with known levels of atrophy and artefacts, allowing an investigation into the effect of these artefacts on different atrophy quantification techniques. There is a prevalence of motion artefact with AD patients, and we should be fully aware of the effects of motion on

atrophy quantification techniques. It is important that atrophy quantification results are not biased due to any relationship between increasing motion and increase severity of dementia.

7.1.1 Aims

To compare the robustness to artefacts of two different atrophy quantification techniques, I use the generated gold standard cohort with simulated atrophy and artefacts described in the previous chapter, as my evaluation cohort. The first evaluated method is a fully automatic technique, SIENA [Smith 2001], and the second is a semi-automatic technique which is most commonly used in clinical trials, BSI [Freeborough 1997]. To the best of my knowledge, this is the first time a direct comparison of atrophy quantification techniques with respect to robustness to artefact has been made. Some authors [Preboske 2006] investigated the error of atrophy measurements obtained with the BSI algorithm when there is no atrophy between images. Here, I aim to investigate the error of measurements with different levels of known atrophy and determine if different types of rotational motion (single, periodic step and slow continuous drift motion) have different effect on the evaluated atrophy quantification techniques. I also aim to determine the effect of increasing the rotational distance causing these artefacts on the assessed algorithms.

7.1.2 Contribution

This chapter adds to the literature a more complete understanding of the effects of motion artefacts on global atrophy quantification techniques. It also provides a methodology for assessing the effects of different types and severities of artefacts on whole and local brain atrophy quantification tools.

I determined the method of this chapter, collated and analysed all the results. I also ran the SIENA technique on the cohort of images, while Richard Boyes (DRC, Queen's Square) ran the BSI technique and Tracey Pepple (DRC, Queen's Square) segmented the brains.

7.2 Literature Review

7.2.1 Overview of atrophy measurement techniques

In this section I look at atrophy measurement techniques commonly employed in longitudinal dementia imaging trials, which provide rates of atrophy that can be used as biomarkers of dementia.

Atrophy measurement techniques can be categorized according to which parts of the brain they are investigating. For example, atrophy can be calculated over global structures, such as the whole brain, the ventricles and the cortex thickness or over local structures, including the hippocampus, the caudate nucleus, and the putamen. Techniques can also be categorized according to the level of user interaction. Those which involve no user interaction, apart from providing the algorithm with its inputs, are called fully automated. Some which do not use computer algorithms at all to calculate atrophy but rely entirely on measurements performed by a human are fully manual techniques. Finally, those which use computer algorithms with some human interaction are called semi-automatic.

7.2.2 Global techniques

There are different types of global techniques such as those which measure the cortical thickness [MacDonald 2000, Fischl 2000], and others which measure the volume of the ventricles [Barra 2002, Freeborough 1997]. However I will focus on structural whole brain atrophy quantification techniques, and in particular BSI and SIENA as these are the techniques which we are testing.

The early techniques in this field enabled improved visualization of atrophy between longitudinal brain images, facilitating expert observers in giving a qualitative assessment of atrophy. One of the simplest ways to accurately visualize whole brain atrophy was developed by Hajnal et al in 1995, using accurate alignment and subtraction of images. This technique assumes that the sequential scans are identical apart from real structural change, which is therefore assumed to be the cause of any structure in the resulting difference image. Lemieux et al. used a similar technique in 1998 to quantify changes in multiple sclerosis lesions. The authors pointed out that a significant quantity of structure in difference images is caused by image acquisition artefacts. Lemieux et al. suggested using maps of the likelihood of artefact being present, histogram matching and bias field correction to be able to use this technique more quantitatively. The techniques currently used in dementia imaging trials, such as the boundary shift integral (BSI) and SIENA, attempt to overcome some of these initial problems caused by artefacts. They do this by quantifying atrophy based on brain tissue boundaries, rather than based on all the intensities in the difference image. The main differences between BSI and SIENA are summarized by Anderson et al, 2007 and shown in Table 7-1.

Similarities	Differences	
	BSI	**SIENA**
Automated registration-based technique	Scaling changes optimized using brain	Scaling changes optimized using brain and skull
Segmentation of brain required before registration and atrophy quantification	Semi-automated brain segmentation using MIDAS image analysis software	Automated brain segmentation using brain extraction tool (BET)
Atrophy quantification based on movement of brain edges	Quantification based on intensity differences between brain edges	Quantification based on distance moved by brain edges
Small segmentation errors should not affect quantification	Intensity changes from baseline to repeat images may affect BSI	Relatively insensitive to intensity changes

Table 7-1 Table from Anderson et al, 2007, summarizing the difference and similarities between BSI and SIENA.

7.2.2.1 Boundary Shift Integral

The boundary shift integral (BSI) is a semi-automatic technique for measuring atrophy from longitudinal structural MRI scans, first proposed by Freeborough and Fox in 1997. In this chapter I use this technique as a global technique to measure whole brain atrophy. However, it is also designed to measure volume change of segmented brain regions which have an intensity defined boundary, such as the ventricles or the hippocampus. It is therefore not only a whole-brain atrophy measurement technique. It is the most commonly used atrophy quantification technique in clinical trials at present. It has been widely used by the neuroimaging community in a huge variety of studies [Chan 2003, Schott 2003, Fox 1999a], being considered as a robust and reliable technique providing results that correlate with disease progression. BSI, however, can be time consuming when processing large cohorts since it requires a semi-automatic brain segmentation stage.

BSI is designed to work on images acquired with the same sequence and directly comparable image intensities. However, due to variations in the scanner and the acquisition environment over time the image intensities of a scan pair may not be directly comparable. To address this, images are intensity normalized during the calculation. The BSI measures atrophy by calculating the volume through which the brain tissue boundaries move between baseline and repeat scans.

The technique works as follows:

Baseline | Repeat

Segmentation [Freeborough, Fox, Kitney 1997]

- Required structure (whole brain, hippocampus etc) is segmented with interactive software, and edited manually if necessary.
- The internal region is defined as a region of voxels, within the segmented structure in both baseline and registered repeat scan, eroded slightly by a morphological operator.
- The boundary region is defined as the region of voxels within either segmented structure, dilated slightly, and not comprising any internal region voxels

Registration AIR 3.0 [Woods 1998]

- Automated image registration (number of degrees of freedom can be selected)
- Segmented brain images are used as input for the registrations
- Cost function for registering baseline to repeat and vice versa averaged and minimised
- Final re-sampling done with renormalized sinc (Thacker et al)
- Trilinear interpolation used to compute the cost function during minimization
- Smoothing with a 2 mm isotropic Gaussian filter
- The scaled least-squared difference image is used as the cost function.

Boundary Shift Integral

- Area under the intensity profile across a tissue boundary region in image1 subtracted from that of image2, normalized by the boundary height to give the boundary motion.
- Assumes a monotonic intensity change across the boundary

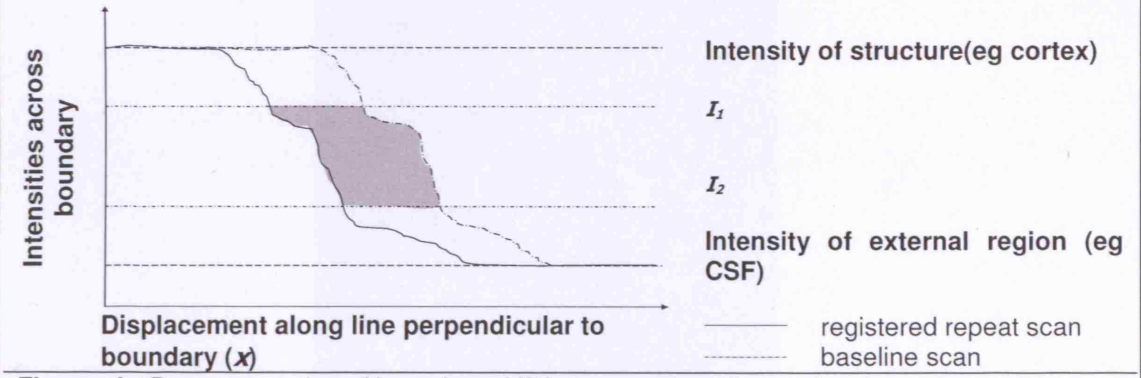

Figure: A 1D representation of boundary shift between a baseline and registered repeat scan. An estimate of the shift, can be obtained as the area of the shaded region divided by $I_1 - I_2$ (the intensity window)

$$BSI = \frac{K}{I_1 - I_2} \sum_{x,y,z \subset E} \left(clip\left(I_{base}(x,y,z), I_1, I_2\right) - clip\left(I_{reg}(x,y,z), I_1, I_2\right) \right)$$

Where BSI approximates the total volume displaced over the boundary of a structure

K is the voxel volume, E is the set of voxels in boundary region

$I_{base}(x,y,z)$ normalised voxel intensities on the baseline scan

$I_{reg}(x,y,z)$ normalised voxel intensities on the registered repeat scan

I_1 High intensity boundary of window, I_2 Low intensity boundary of window

We used 6 degrees of freedom in the registration as opposed to 9 or 12 as we found the simulated atrophy had a significant global scaling component when registering

brain to brain. BSI as often implemented with 9 or 12 degrees of freedom removes this global scaling component, unlike SIENA which uses skull constraint to avoid this. This is a limitation of BSI which could be corrected by using a skull registration constraint.

The intensity window must fall within the intensity transition associated with tissue boundaries. If the window is too narrow a small "signal" will be provided as most of the boundary will be missed and the technique will not be very robust to noise. Too big a window will reduce the gain as intensities not associated with tissue boundaries may be selected. However, the gain for whole brain BSI is always less than one and so brain volume change is always slightly underestimated.

The BSI gives more reliable results than comparing absolute volumes obtained from the segmentation because segmentation errors do not introduce large biases to the BSI results. Instead, they only influence the sensitivity of the technique by distorting the boundary region. Motion artefact is shown to be significantly correlated to the residual registration mismatch and therefore the BSI will represent a less reliable measure of volume change [Freeborough 1997].

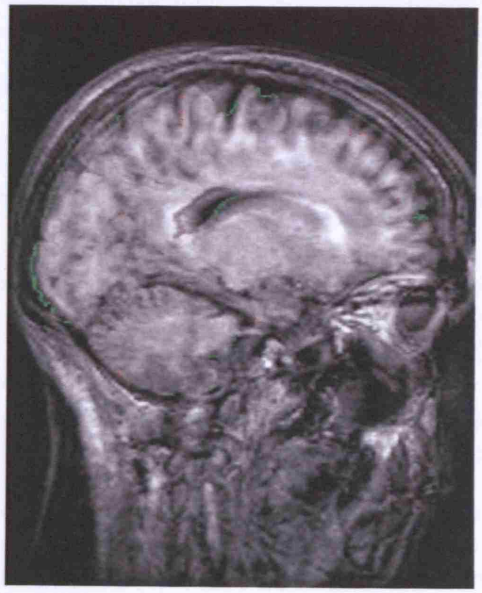

Figure 7-1 Example of a BSI growth/atrophy map, overlayed on a grey-level image. Green represents areas of growth, red represents areas of atrophy.

7.2.2.2 SIENA

SIENA (Structural Image Evaluation, using Normalization, of Atrophy) is a fully automatic brain atrophy quantification technique, proposed by Smith et al [Smith 2001, Smith 2002]. It is part of the open source FSL package [Smith 2004]. Unlike the BSI

technique, SIENA can be applied to data acquired with different sequences. It also seems to be relatively insensitive to slice thickness. Its authors quote accuracy, with "reasonable quality MR images", of the order of 0.2% brain volume change (BVC). Intensity normalisation between scans and intensity inhomogeneity correction within scans is not necessary for using this technique. They claim the technique to be fairly robust, functioning with "less than ideal MR images". The technique is described below:

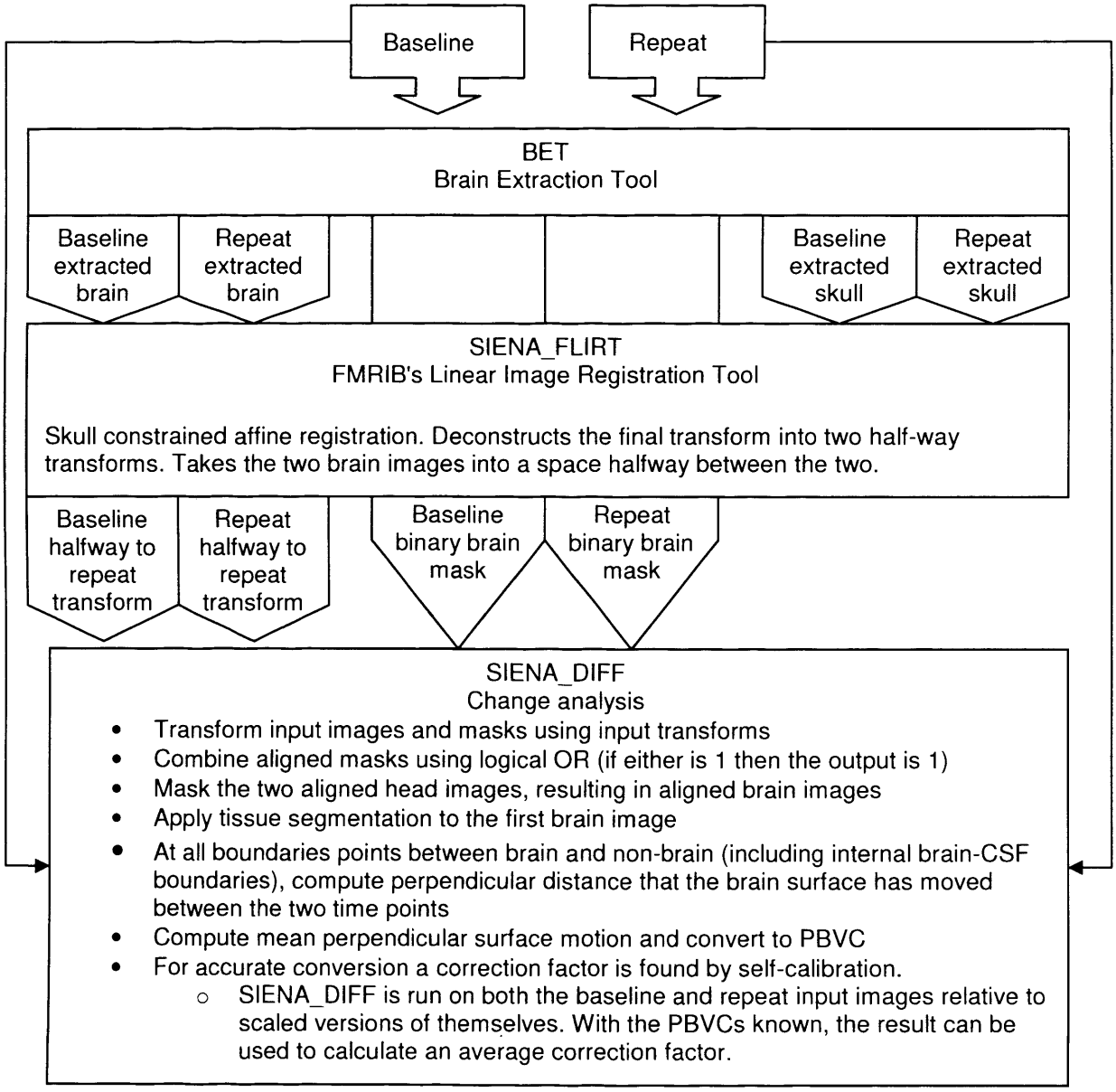

1. SIENA extracts binary brain masks, segmented brain images, and skull images from the two-timepoint input images [Smith 2002] using the Brain Extraction Tool (BET) [Smith 2000]. BET uses a tessellated mesh modelling surface which deforms in a constrained way to optimally fit the brain surface.
2. The two brain images are then aligned to each other [Jenkinson 2001, Jenkinson 2002] (using the skull images to constrain the registration scaling).

Jenkinson's global optimisation method uses the correlation ratio cost function, with a multiscale search. This first alignment is a full affine transformation including scaling and skew. Next, scaling and skew are constrained using the skull surfaces. The brain images are then realigned, allowing only translation and rotation to vary.

3. Both original scans are transformed into the space halfway between the two so that both have the same interpolation effects.
4. The two brain masks are also transformed half way and combined to produce one new mask. This is then applied to both transformed images from step 3.
5. Next, tissue-type segmentation is carried out (on the transformed, masked baseline scan) [Zhang 2001] in order to find brain/non-brain edge points.
6. Perpendicular edge displacement (between the two timepoints) is estimated at these edge points. The direction perpendicular to the brain surface is determined as the direction of maximum intensity gradient.
    a. A 1D array of intensities values perpendicular to the brain surface is created for both the aligned scans.
    b. Arrays are differentiated to give arrays of intensity gradients, which are less sensitive to intensity inhomogeneities across and between scans.
    c. Each array is multiplied by a high power exponential profile so that larger motions are less likely than smaller ones.
    d. Brain surface motion is defined as the shift between the two arrays that produces maximum correlation. Sub-voxel accuracy is obtained by fitting a quadratic through the correlation peak and its two neighbours.
7. The mean perpendicular brain surface motion is calculated by summing the brain surface motions over all brain surface points, multiplying by the volume of a voxel, and dividing by the number of detected brain surface points, times the voxel cross sectional area.
8. Finally, the mean edge displacement is converted into an estimate of percentage brain volume change between the two timepoints. This is calculated as 100 times the mean surface motion, times the ratio of actual area to volume.
    a. This ratio of actual area to volume is calculated as follows: a single image is scaled by a known amount and then compared with the unscaled version using the above technique. This gives a mean surface motion which together with the percentage brain volume change (PBVC) (known from the applied scaling) can be used to determine the ratio of actual area to volume. This method ensures there is no bias in the reported estimates of the percentage brain volume change.

7.2.3 Local brain volume change

I now look at the second group of brain atrophy measurement techniques: those which focus on measuring atrophy of particular brain regions, which are known or believed to be affected by the particular pathology we wish to study. In Alzheimer's disease studies the change in volume of the hippocampus and amygdala is often observed due to their importance as biomarkers in dementia. I do not assess these techniques in my work, but include them as relevant background to suggest that further work should be carried out to investigate the robustness of these techniques to artefacts.

7.2.3.1 Manual or automatic delineation of hippocampus

Delineation and quantification of the volume of the hippocampus and amygdala from sequential MRI scans had been used as a research tool in many disorders including epilepsy, schizophrenia, depression and AD [Bogerts 1990, Jack 1994, Bremner 1995, de Leon 1996, Sheline 1996]. Manual delineation is a time consuming technique. More automated techniques can save some time but still need verifications by an expert observer.

Comparing results from these techniques across different studies and groups is recognized to be problematic due to many factors which introduce high levels of variability [Pruessner 2000]. One problem is variability introduced because different software packages are often used to trace the target structure. These visualise the structures in a variety of ways, some with different level of enlargement, some with a varying number of orientations in which the structure can be viewed, as well as 2D or 3D visualisations. Using different visualisation tools may influence the accuracy with which the brain structures are delineated. Different calculating algorithms within the packages might also introduce variability [Jack 1995]. Another cause of variability, which Pruessner et al highlight, is that different groups disagree in definitions of the borders of the hippocampus and amygdala [Cendes 1993, Kates 1997].

7.2.3.2 Jacobian of deformation field from nonrigid registration

Another more recently developed, local brain volume change quantification technique uses complex non rigid registration techniques. These registration techniques more accurately localise where atrophy or growth is occurring, than the automatic whole brain measures presented so far. The result of this technique is a voxel compression map comprised of the Jacobian determinants of the deformation field, which is needed to warp one scan into the other. Different types of non rigid registration algorithms can

be used. For example, to map atrophy in AD, Freeborough et al, 1998, have used a fluid registration technique and Studholme et al, 2004, have used a cubic b-spline registration technique. Non rigid registration techniques determine a set of points or features on one image and try to determine their corresponding locations in the second image. To do this the deformation field that will map one to the other most efficiently is determined. Different algorithms use different cost functions to optimise the similarity of the transformed and target image. Most algorithms favour small displacements and do not allow displacements to overlap.

In a direct comparison study by Boyes et al, 2006, a technique based on the integration of Jacobian determinants from non-rigid registration was shown to be able to distinguish between control and AD subjects more clearly than with BSI ($P<0.01$). BSI is still currently the method of choice for most clinical trials, however, as it has been used and tested more extensively.

The voxel compression maps generated by these techniques are intended to visualise rates of tissue growth and atrophy. However, they should be treated with caution as they represent the lowest cost method of warping one image into the other, according to the cost function used. They do not necessarily accurately visualise growth or loss of tissue, particularly when mapping a large region of homogeneous tissue, lacking detailed structure. Unrealistic maps can be computed due to spatial distortion, and intensity inhomogeneities in images; this has been observed particularly in the brain stem, thalamus and ventricles [Yanovsky 2007].

7.2.4 The effect of artefacts in longitudinal imaging studies

In this section we consider the effect of artefacts on the tools used to measure atrophy and on longitudinal neuroanatomical MRI in general. Artefacts in MR images may interfere with accurate measurement of cerebral atrophy from longitudinal MR images, either by affecting these automated tools or also by increasing the difficulty of manually segmenting these images. I now review some studies which investigate, to a limited extent, the effect of artefact on specific tools. These include Lemieux looking at artefacts in difference images, Blumenthal et al in 2001 investigating the correlation between grey matter volumes measured with a segmentation tool and motion, and Preboske et al in 2006 investigating the effects of differing contrasts between scans and different levels of simulated noise and motion on BSI whole brain and ventricular volume measures.

7.2.4.1 Effect of artefact on manual delineation

When manually segmenting entorhinal cortex from 3D spoiled gradient echo sequences of ninety subjects, Xu et al 2000 reported that 60% of scans had boundaries affected by blood and CSF pulsatile flow artefacts and susceptibility artefact. These artefacts decreased the sensitivity of using the entorhinal cortex volume as a diagnostic marker of early AD.

7.2.4.2 Effect of artefact on automatic segmentation

Blumenthal et al. carried out prospective analysis on scans acquired from 180 healthy children. Each image was segmented and classified using an algorithm called ANIMAL + INSECT [Collins 1999], a combination of ANIMAL: automatic non-linear image matching and anatomical labelling [Collins 1997] and INSECT: intensity normalised environment for the classification of tissue [Zijdenbos 1998]. Each image was assigned a motion artefact rating on a 4 point scale: "none" little or no detectable motion artefact; "mild" enough to result in subtle concentric bands to appear in the automated classification; "moderate" significant banding; "severe" so extreme the data was deemed unreliable for analysis. An inverse correlation of grey matter volume with motion was found. Even mild motion was found to decrease grey matter values by over 4% which is within the range of between-group differences in some studies.

Blumenthal et al. reason that motion artefact may blur image intensities in narrow regions of grey matter such as cortical grey matter into the relatively large areas of white matter and not be detected by automatic algorithms. This would result in the observed increasing underestimation of grey matter volume with increasing severity of motion artefact.

7.2.4.3 Effect of artefact on difference images

Lemieux, 1998, used a difference image based method to detect changes in brain lesions in 3D T1 weighted gradient echo images. They used a technique to filter out noise from the difference images and leave only voxels classified as structure; structure ideally being caused solely by structural brain change. In controls with no significant structural brain change an average of 1.57% of brain voxels (range 0.44-3.51%) were classified as structure. This structure was arising from imaging artefacts. Lemieux aligned these difference images from 20 controls into a common brain space to create an anatomical distribution map of artefact occurrence. This map was then

used, with the difference images from 7 patients, to reduce the misclassification of structure caused by artefact as lesion change.

In his paper, Lemieux comments "Maximum sensitivity to subtle signal changes may be achieved by removing non-biological variation between successive scans". He details the cause of some of these non-biological variations as signal intensity non-uniformity, geometric distortion, magnetic susceptibility artefact and changes in signal from vessels. More specifically he argues "In T1-weighted gradient echo images, head movement during scanning, flow, pulsation and susceptibility artefacts can cause random signal variations resulting in differences in matched images. As previously mentioned, such differences will reduce the ability to detect changes (ie differences) due to pathological processes".

He suggests that these artefacts may be distinguishable from pathological changes by their anatomical location; citing the example of pulsation artefacts often appearing as mixed signal bands across the temporal lobes.

7.2.4.4 Effect of artefact on BSI measures of scans without atrophy

Preboske et al, 2006 investigate how 3 types of image acquisition problems affect the output of the BSI. They look at MR protocol inconsistencies between baseline and follow up scans, simulated head motion, and simulated images acquired with relatively low signal to noise ratio.

To investigate protocol inconsistencies they acquire scans from each of 10 normal volunteers with various flip angles and other parameter changes, resulting in contrast changes and increased susceptibility artefacts. They simulated 5 different levels of the motion in image space of between 0.3125 and 5 pixels (pixels of size 0.9 x 1.25mm) to investigate motion artefacts. To simulate low signal to noise ratio, the baseline scan were simulated with five different levels of noise.

The BSI results increasingly deviated from zero the greater the mismatch in the contrast between the two scans. The results also deviate more from zero with an increase in simulated motion and noise. Increasing noise levels lead to measurements suggesting apparent smaller brain volume and larger ventricles. Large motions lead to suggested smaller brain volumes, and smaller motions lead to suggested larger brain volumes. Any increase in simulated motion resulted in smaller ventricular volume being measured.

7.3 Method

This section describes how I use the gold standard cohort of atrophy and artefact simulated images (see Chapter 6) to investigate the effect of motion artefact on two different atrophy quantification tools commonly used in longitudinal dementia trials, BSI (see Section 7.2.2.1) and SIENA(see Section 7.2.2.2).

7.3.1 Materials

The cohort is comprised of images based on 7 subjects baseline scans with three different levels of simulated atrophy: no atrophy, moderate atrophy, ADsim1: brain volume reduction of 5.10% ± 0.26, and severe atrophy, ADsim2: brain volume reduction of 10.82% ± 0.53. On each of the images, with and without atrophy simulation, 3 different types of motion have been simulated with 10 different rotational distances causing the artefact. These 3 types of motion are a single sudden movement, repetitive sudden movements and a slow head drift at constant speed through the scan.

Each of the two algorithms requires two time-point images as inputs. In this experiment the first time-point image is always the relevant subject's baseline scan without any simulated artefact, except noise simulated at the same level as in the follow-up scan. The second time-point is the corresponding atrophy and artefact simulated image we have generated. To gain a repeatability measure one of the generated second time-point images was the same as the first time-point image but with different simulated noise of the same level.

7.3.2 BSI

The analysis of cohort of images with BSI is sometimes performed with modified thresholds for the intensities in the clipping function of BSI to give optimum results. To evaluate if we should modify these thresholds in this experiment we performed a small study to investigate if changing one of these threshold from the predefined value had a large effect on the algorithms accuracy and its response to artefact. We did this by using one subject's scans and calculating the percentage brain volume change using the standard, predefined parameters (0.25, 0.75) and one set of modified parameters (0.45, 0.75). Figure 7-3 shows the results for this investigation.

On the basis of these results, and another recent paper which also shows that BSI consistently under-estimates severe atrophy [Camara 2007], I used the images without

atrophy and with the moderate atrophy simulation from the 7 subjects to compare the effect of motion artefact on the BSI and SIENA algorithms. The BSI algorithm was employed as it is usually done in clinical trials, without modified parameters, with the exception of the image segmentation step.

We decided, due to time and resource constraints, not to segment each of the images with simulated motion artefact but instead to segment the baseline scans and the two atrophy simulation images for each subject before artefact was added. These segmentations are then used as the masks for each of the related artefact corrupted images. This would give a best possible case scenario for the BSI algorithm, where the segmentation is not affected by the motion artefact. In the real life scenario it would be likely that segmentation accuracy would decrease with motion artefact increase, due to increased blurring of the brain boundary.

7.3.3 SIENA

To investigate the effects of motion artefacts on SIENA I ran the algorithm on the images without atrophy and with moderate atrophy simulation from the 7 subjects. I ran SIENA as it is most commonly used in clinical trials, with no parameters optimised.

7.4 Results

Figure 7-2 shows SIENA (pink markers) and BSI (blue markers) results comparing the effects of simulating different levels and types of motion artefacts on the atrophy measurement error. Atrophy is measured as negative percentage brain volume change (PBVC). Measurement errors are the algorithm result, minus the gold standard. Increasingly negative measurement errors show an increasing overestimation of atrophy; increasingly positive errors an increasing underestimation of atrophy. If the positive measurement error is greater than the absolute gold standard atrophy apparent brain growth is being measured.

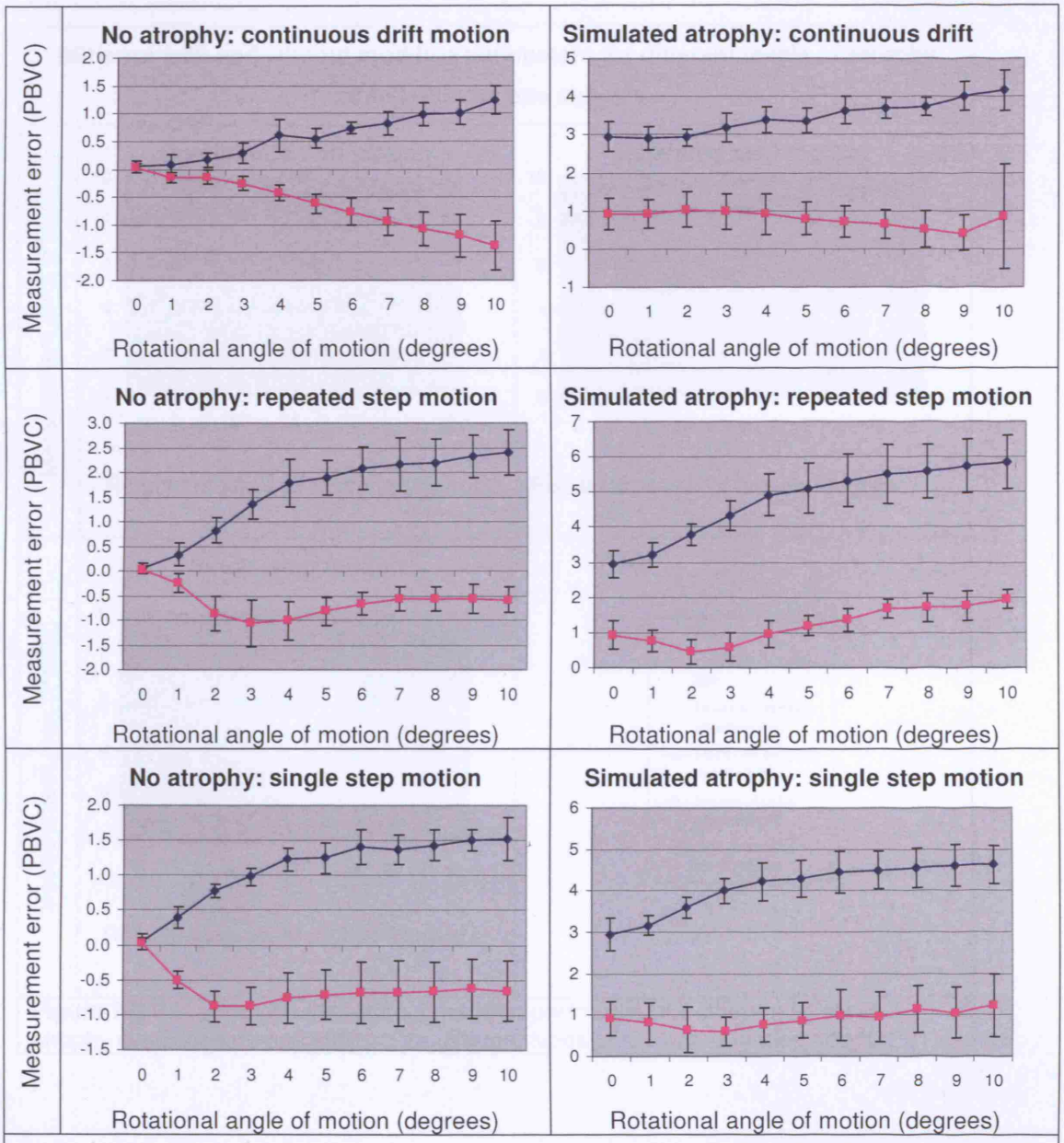

Figure 7-2 Comparing SIENA (pink) and BSI (blue) errors with increasing rotational angle of simulated motion, on images with no atrophy(left) and with simulated atrophy(right), when different types and levels of simulated motion artefacts are present on 7 subjects images.

It can be seen in Figure 7-3 that the modified parameters have a negligible effect when used to measure un-artefacted, images with and without atrophy simulation (ADsim1). The modified parameters slightly reduce the measurement error of un-artefacted severe atrophy, ADsim2, images.

When simulated motion artefact is present in the images, use of the modified parameters decreases the measurement error. The effect is greater the more severe the simulated atrophy. The only exception is the periodic step motion case, where for the no atrophy scan there is a slight increase in measurement error using the modified parameters.

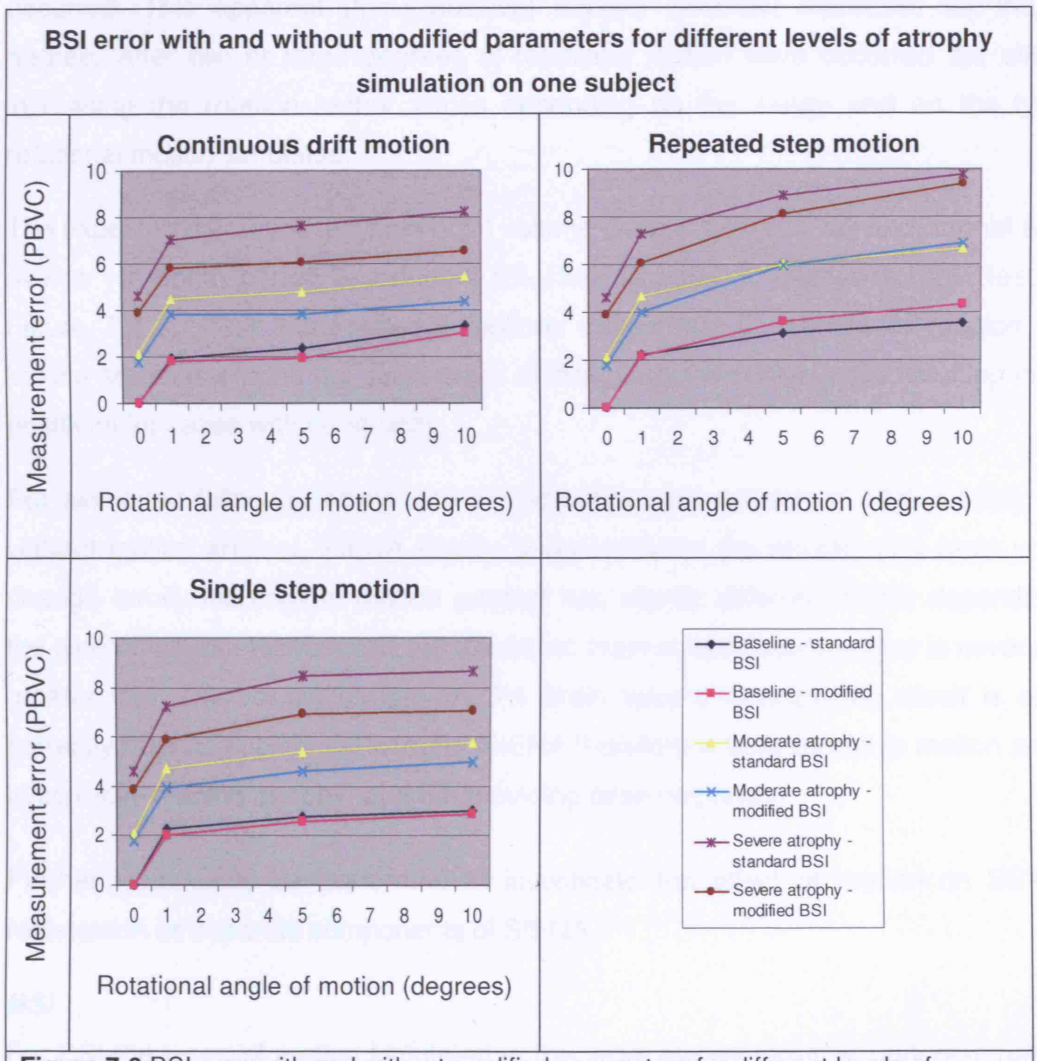

Figure 7-3 BSI error with and without modified parameters for different levels of atrophy simulation on one subject, for different types of simulated motion artefact

7.5 Discussion

SIENA

It must be pointed out that the accuracy obtained with SIENA in atrophy measurements of images without simulated atrophy and artefacts are consistent with results provided by the authors of this technique (accuracy of 0.2% of whole brain volume change). For the images without simulated atrophy, Figure 7-2 shows the results of the SIENA atrophy measurement as a function of magnitude of the rotational motion (rotation from 0° to 10° degrees in intervals of 1 degree). Small increases of one degree rotational motion seem to cause the SIENA algorithm to measure atrophy when none has occurred. This apparent (false positive) atrophy generally increases for the next degree. After two or three degrees of rotational motion have occurred the effect of increasing the rotation further varies depending on the image and on the type of rotational motion simulated.

The expected difference in whole brain volume change between AD and normal ageing over a 12 month period is around 1.5% (See Chapter 1, Section 1.1.2). Results in Figure 7-2 suggest that rotational motions larger than 2 degrees of rotation could induce artefacts around the same order of these expected differences resulting in false positives for cases with no atrophy.

For simulated follow-up scans with a moderated brain atrophy (5.10% ± 0.26), even without motion artefact, SIENA slightly underestimates the atrophy (1% brain volume change error). Increase in motion artefact has slightly different effects depending on the type of motion. However as the maximum brain volume change error is never much greater than 2%, for an atrophy of 5% brain volume change, the result is always correctly read as substantial atrophy. SIENA therefore is fairly robust to motion artefact in correctly reading atrophy, and not providing false negatives.

Further work could be performed to investigate the effect of motion on BET and registration as separate components of SIENA.

BSI

For BSI the types of motion simulated in this work always result in underestimation of brain atrophy and increased levels of variability with increased motion. For the images without atrophy this underestimation results in apparent brain growth, this will mean that false positives brain atrophy is never reported when motion artefact appears in the second scan. For the simulated follow-up scan with a brain atrophy of 5.10% ± 0.26 this usually results in the atrophy being progressively underestimated, with extreme

periodic step motion appearing as slight growth, meaning that false negative maybe a problem due to motion artefact. False negative due to motion maybe a substantial problem as motion is more likely to occur with AD symptoms, which will get worse with progression of time, so this is likely to hide the difference of brain volume change between AD and normal progression. It has also previously been shown that BSI underestimates atrophy of this magnitude, and our results from the simulated follow-up scans with atrophy but rotation angle of motion of zero confirm this (3% brain volume change error).

This apparent growth with increasing motion is due to the second scan having artefact while the first does not. The BSI is calculated over a 'between borders' region, which lies between the two registered scans, where intensities in the repeat are subtracted from the baseline. As there is no motion in the baseline, but quite a bit in the repeat, the intensities in the between borders region will be low for the baseline (CSF), while in the repeat they will be high (blurred WM/GM/CSF). This results in original regions of CSF intensity turning to blurred intensities, giving apparent growth. The overlay image below (Figure 7-4) shows the regions of growth and atrophy between a volunteer's baseline image and a simulated image without simulated atrophy but with simulated periodic step rotational motion of 10. The greyscale image beneath is the follow up scan with simulated motion artefact. This figure shows substantial regions of growth (green) at the brain/CSF interface supporting the theory above. The same artificial growth effect occurs with significant motion where Alzheimer's has been simulated, leading to underestimated atrophy measure results. As the BSI algorithm acts consistently with increasing motion artefact, across both image with and without simulated atrophy, it might be possible to quantify the level of artefact in an image and to compensate the BSI result proportionally.

The atrophy measurements errors from SIENA are generally smaller than those from the BSI. BSI, however, responds in a more consistent manner to increased motion artefact allowing for the possibility of quantifying artefact and adjusting the result.

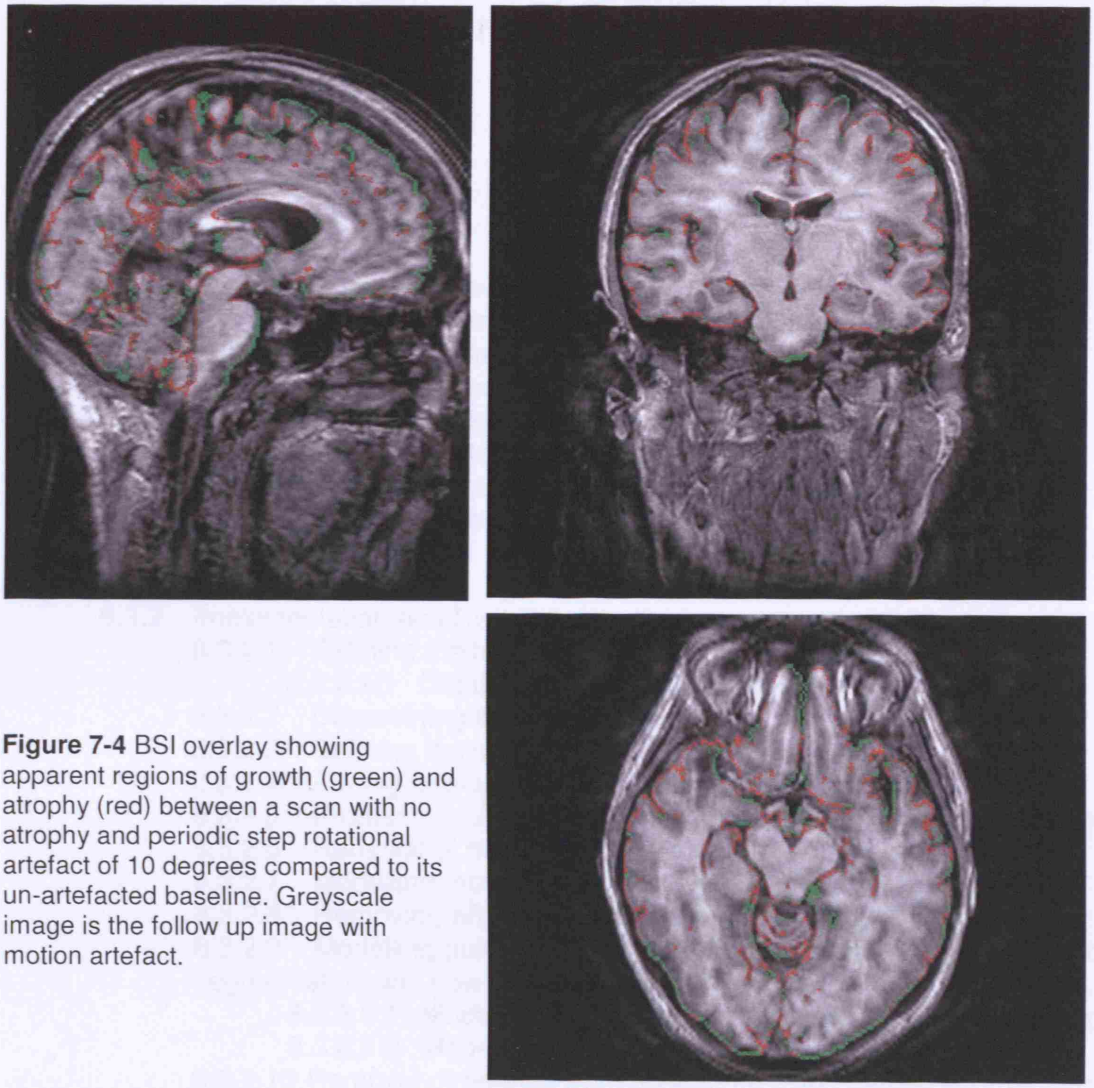

Figure 7-4 BSI overlay showing apparent regions of growth (green) and atrophy (red) between a scan with no atrophy and periodic step rotational artefact of 10 degrees compared to its un-artefacted baseline. Greyscale image is the follow up image with motion artefact.

7.6 Conclusions

The impact of motion artefacts is likely to be different with different algorithms, and especially for local atrophy measures (e.g.: from a non-rigid registration algorithm) or cortical thickness measurement methods. The value of the approach presented in this chapter is in predicting the sensitivity of methods to motion artefact (potentially valuable in a power analysis used in the design of a clinical trial), and also in comparing the relative merits of alternative atrophy measuring algorithms in the presence of common image artefacts. Further work includes the evaluation of techniques using non-rigid registration deformation fields between two serial images to measure atrophy, the assessment of post-processing artefact correction techniques and their incorporation in atrophy measurement methods.

In the next chapter I describe the simulation of pulsatile flow artefacts which can be used to generate a gold standard database to test local atrophy measurement tools. I also propose a method for the removal of these pulsatile flow artefacts.

8 Novel approach to simulating and removing pulsatile flow artefact

8.1 Introduction
- 8.1.1 Aims
- 8.1.2 Contribution

8.2 Literature
- 8.2.1 Simulating pulsatile flow artefact
  - 8.2.1.1 Flow phantoms
  - 8.2.1.2 Geometric simulation
  - 8.2.1.3 Full Sequence simulations
- 8.2.2 Computational pulsatile flow artefact correction techniques
  - 8.2.2.1 Two-point interference method
  - 8.2.2.2 Parallel imaging correction techniques
    - 8.2.2.2.1 Care

8.3 Method
- 8.3.1 Model
- 8.3.2 Implementation and Results
  - 8.3.2.1 Defining the true image and the coil sensitivities
    - 8.3.2.1.1 Details of simulating coil profiles
  - 8.3.2.2 Determining the remaining inputs
  - 8.3.2.3 Defining the space x-t
  - 8.3.2.4 Adding artefact in x-t
  - 8.3.2.5 Producing coil images with artefact through k-t space selection
  - 8.3.2.6 Removal of the artefact by solving linear equations
  - 8.3.2.7 Modelling more than one varying voxel
  - 8.3.2.8 Removing artefact caused by more than one varying pixel
  - 8.3.2.9 Modelling pulsatile flow artefact in a 3D image, using a carotid segmentation and flow velocity profiles
    - 8.3.2.9.1 Modelling of the carotid and scanner sequence timing
    - 8.3.2.9.2 Modelling artefact
  - 8.3.2.10 Removal of artefact from 3d volume using carotid segmentation

8.4 Results
- 8.4.1 Pulsatile flow artefact simulation
- 8.4.2 Pulsatile flow artefact correction
  - 8.4.2.1 Correction of artefact simulation without noise
  - 8.4.2.2 Correction of artefact simulation with noise

8.5 Conclusions and further work

8.6 Examples of real flow artefact occurring in longitudinal data for comparison

8.1 Introduction

Pulsatile flow artefact is a common problem in 3D fast gradient echo sequences acquired at 1.5T, as demonstrated in Chapter 5 of this thesis. This artefact becomes more pronounced at higher field strengths as shown in Chapter 4. The artefact can also interfere with analysis of longitudinal MRI scans. Particular when delineating local structures within the temporal lobes, as is common in analysis of dementia trial scans; see Chapter 4 regarding Xu's work on this in 2000.

I provide in this chapter a method for the simulation of pulsatile flow artefacts. The simulation of artefact can be used in conjunction with atrophy simulation to quantify the effects of pulsatile flow artefact on different measures of atrophy.

This chapter also describes a technique for removing these artefacts and an evaluation of the method on simulated data. As the technique would need the raw data from the different coils which comprise an array coil, to be practically used in trials it would require vendor-specific techniques for exporting the raw data from each site, or would have to be implemented into the scanner manufactures' platforms.

8.1.1 Aims

In this chapter I aim to develop a novel technique to simulate pulsatile flow artefact. This simulation technique should have the potential to be used in conjunction with atrophy simulation techniques to determine the effects of this artefact on atrophy quantification techniques.

I also aim to devise a novel, fully 3D technique for the removal of pulsatile flow artefacts arising from the carotid, and apply this to simulated data.

8.1.2 Contribution

My contribution is a novel, simulation method for determining the effects of the artefact on image analysis techniques and the proposal of a novel technique to remove these pulsatile flow artefacts in 3D brain imaging.

Pablo Irrarazaval, Derek Hill, David Atkinson, Philip Batchelor, Jo Hajnal and David Larkman contributed to the discussion of these techniques. I discussed CARE, Coil-based artefact reduction [Atkinson 2004] and how best to extend its principles to 3D with David Atkinson, Philip Batchelor and Derek Hill. Jo Hajnal and David Larkman discussed with me the issues surrounding parallel imaging and the practicalities of acquiring coil sensitivity maps. Initially I carried out work extending the CARE algorithm to a 3D volumetric brain image approach. First I simulated a 3D volume acquired in a low number of shots (40 or less), with flow artefact simulated using a multiplicative factor. With the extended 3D CARE algorithm I substantially reduced the ghost artefacts. However, this technique proved difficult to extend well to images with a high numbers of shots (as many as there are slices), which are usually used to acquire volumetric brain images. I then modified the method to use an additional rather than a multiplicative correction factor, which seemed to model the underlying physics better

(see method section), while allowing the problem to be solved as a linear equation. I implemented this idea, testing and developing it to work on simulations of a volumetric brain with flow artefact which I generated using an additive model. Further work is needed on this technique to test and optimise it for use on acquired data with artefact.

8.2 Literature

8.2.1 Simulating pulsatile flow artefact

This section describes existing methods in the literature which simulate pulsatile flow artefact. The method I develop in this chapter builds on the observations from the phantom simulations and geometric numerical simulations and is more generalised than the full sequence simulations proposed in Section 8.2.1.3. These full simulations are useful for comparing the relative effects of pulsatile flow on different existing sequences and for helping to design new sequences. However they are fully tailored to the particular sequence and scene on which they are designed.

8.2.1.1 Flow phantoms

Flow phantoms were the first method used to simulate pulsatile flow artefacts [Bradely 1985, Perman 1986]. These phantoms ranged from straight sections of tubing connected to a pump, to elastic models of the carotid artery bifurcation cast from fresh cadavers, accurately reproducing the shape of the human blood vessels [Buxton 1993].

8.2.1.2 Geometric simulation

Frank et al, 1993 provided a geometric simulation by numerically simulating the location where this artefact can occur in a 3D volume. These results are described in Chapter 3, Section 3.3.5.3. To validate his simulation, Frank compared his results with experimental images of an elastic model of a human carotid artery under simulated physiological conditions, and also with images of 2 human subjects.

8.2.1.3 Full Sequence simulations

Full sequence simulations involve using the Bloch equations to simulate signal intensities during a specific acquisition.

Tasciyan and Mitchell, 1994, used a matrix formulation of the Bloch equation to simulate an inversion recovery prepared GRASS sequence (gradient recalled acquisition in the steady state). The blood T1 and T2 values were assumed to be 930 and 170 msecs. Flip angles of 20, 45 and 60 were simulated and TRs of 7 and 12 ms.

They then calculated the flow effects resulting from spin displacements in the vessel and also the magnetization of the spins in the proximity (within 16 mm either side) of the vessel. They calculated the distance the spins traversed during each repetition period by using an aortic pulsatile velocity waveform based on published Doppler data from 40 health individuals and at a cardiac ate of 60, 80 and 100 beats per minute.

Petersson and Christoffersson, 1999, extended the Multi Dimensional Partition model (MDPM), which simulates the outcome of a given pulse sequence on a given object, to visualize flow related artefacts. To use the MDPM the imaged object must be divided into different types of tissue. Each tissue type must have at least one unique property. The calculation of the MR signal generated from each tissue type is then performed by using the partition concept. Partitions are used to model the separate magnetization components generated during the execution of a pulse sequence. For example the first partition is the longitudinal magnetization, z direction. The second partition represents magnetization in the xy plane. The third partition represents magnetization returned to the z direction. Other partitions are used to model the effect of pulsatile flow on the image over time. The outcome of any simulation is a function of flow velocity, flow profile, and pulse sequence parameters such as pulsatile period time, pulse sequence repetition time, echo time and acquisition bandwidth. The simulation is capable of outputting different SNR levels. To demonstrate the presence of ghost artefacts, the noise level during all calculations was kept low.

8.2.2 Computational pulsatile flow artefact correction techniques

The pulsatile flow artefact pattern is unpredictable without monitoring the subjects pulse relative to the scanner sequence timings which makes it difficult to remove with computational correction techniques. However if multiple images with different artefact intensity patterns can be obtained then it is possible to reduce or remove the artefact based on the redundancy of information obtained. Xiang et al, 1991, proposed the two point interference method where two interleaved sequences are obtained. Later, with the introduction of parallel array coils, the idea was developed of using the redundant information provided by the different coils acquiring fully sampled k-space.

8.2.2.1 Two-point interference method

Xiang et al, 1993, describe a two-point interference method to suppress ghosting due to motion and pulsatile flow in magnetic resonance imaging. The method requires two time-interleaved data acquisitions. A post processing technique is used to produce a

weighted sum of the two acquired images, in which ghosts are suppressed by interference through an automatic regional tuning procedure. The appropriate complex weighting factors are regionally chosen by minimizing the "gradient energy," which is defined as the sum of squared pixel values in the partial-derivative maps.

8.2.2.2 Parallel imaging correction techniques

There are different existing approaches in the literature which use parallel imaging to reduce ghost artefacts caused by bulk motion or pulsatile flow. Image correction can be performed in k-space [Bydder 2002, Bydder 2003, Atkinson 2004], or in the spatial domain [Kellman 2001, Winkelmann 2005]. These image correction algorithms have been demonstrated on 2D images, usually of the abdomen. In this chapter I propose a method to extend pulsatile flow artefact correction to 3D structural head images.

8.2.2.2.1 CARE

Coil based artefact reduction (CARE) a parallel imaging correction technique described by Atkinson et al, 2004, works by reconstructing multiple images using data from different combinations of coils. The comparison of these images shows artefacts because motion or flowing blood appear with different intensities due to the differing coil sensitivities. The artefact appears amplified in regions of low coil sensitivity. An optimization routine is used to find an unknown multiplicative factor, which corrects for flow. It does this by comparing reconstructions from various coil combinations and optimising for consistency between reconstructions. Atkinson et al demonstrate that 2D images containing artefacts from blood flowing in the aorta, or translational motion of the head, can be improved.

CARE is based on assuming k-space acquisitions are divided into shots, each containing one or more phase-encode line. Significant object changes are modelled as only occurring between shots. The data for any point in k-space is assumed to be received by all the coils simultaneously.

With no artefact, the image s^{γ} obtained from coil y with spatial sensitivity c^{γ} is:

$$s^{\gamma} = c^{\gamma} \cdot r$$

where r is the underlying object. In k-space this is:

$$S^{\gamma} = C^{\gamma} \otimes R$$

where S^{γ} is the k-space data acquired, $\otimes$ signifies convolution, C^{γ} is the k-space representation of the coil sensitivity and R is the k-space representation of the object.

In matrix terms S^{γ} can be stacked, for each coil, into a column vector **S** and R can be written as a column vector **R**. The convolution is represented as a matrix multiplication by the matrix **C** whose rows are shifted copies of the C^{γ} expressed as row vectors with periodic boundaries.

Solving the matrix equation below, to determine **R** is the "generalised SMASH" technique.

S = **CR**

The size of **S** is $[n_{coil} \cdot n_{pe} \times 1]$ where n_{coil} is the number of coils and n_{pe} is the number of phase encode lines acquired. The matrix **C** has size $[n_{coil} \cdot n_{pe} \times n_r]$ where n_r is the size of r. If the data is fully sampled, $n_{pe} = n_r$.

The k-space data received at the time of shot t is given by:

$$S_t^{\gamma} = E_t F\{c^{\gamma} \cdot r\}$$

where F is Fourier transform from the image domain to k-space. E_t selects only the phase-encode lines measured in shot t. The complete k-space for one coil, S^{γ}, is assembled from the k-space acquired from all shots:

$$S^{\gamma} = \{S_1^{\gamma}, S_2^{\gamma}, ...\}$$

The CARE optimisation scheme compares various estimates of r. These estimates are computed by solving the following matrix equations.

If at the time of acquisition of shot t, the object has changed from r to $\bar{r}_t$ then

$$\bar{S}_t^{\gamma} = E_t F\{c^{\gamma} \cdot \bar{r}_t\}$$

The bar specifies artefact corrupted data. The CARE method expresses the artefact as a change to the coils, rather than as a change to r:

$$\bar{S}_t^{\gamma} = E_t F\{c^{\gamma} \cdot \bar{r}_t\} = E_t F\{\bar{c}_t^{\gamma} \cdot r\}$$

In matrix terms

$$\bar{\mathbf{S}} = \bar{\mathbf{C}}\mathbf{R}$$

To simplify the processing, the data from just one column in the image domain is taken at a time. The column vector $\bar{\mathbf{S}}$ is formed from the actual measured data at each of the shots. Each row of $\bar{\mathbf{C}}$ is formed from the Fourier transform of the $\bar{c}_t^{\gamma}$ shifted to account for the convolution process.

$\mathbf{R}^{\gamma} = \overline{\mathbf{C}}^{\gamma} \backslash \overline{\mathbf{S}}^{\gamma}$ can be calculated with the data from only coil γ (if k-space is fully sampled) (\ denotes the left matrix divide function of Matlab (MathWorks, Natick, MA). A solution of the matrix equation AX=B is written X = A\B and this can be performed without explicit computation of the inverse of A). The calculation of $\mathbf{R}^{\gamma}$ is repeated for each coil. The generalised SMASH solution $\mathbf{R}^{G} = \overline{\mathbf{C}}^{G} \backslash \overline{\mathbf{S}}^{G}$ where G stands for data from all coils is also computed.

The optimization cost function which is minimised is

$$K = \sum_{\gamma} \left| r^{\gamma} - r^{G} \right|^2$$

where the reconstructed data has been Fourier transformed to the image domain and the sum is over all image domain pixels and coils. In the absence of noise, K would be zero at the solution.

To remove flow artefacts CARE assumes that the effect of the flow can be parameterized by a complex multiplicative value z_t that is the same across the whole vessel but can change from shot to shot. For only those pixels $\bar{x}$ within the vessel:

$\bar{c}_t^{\gamma}(\bar{x}) = c_t^{\gamma}(\bar{x}) z_t$

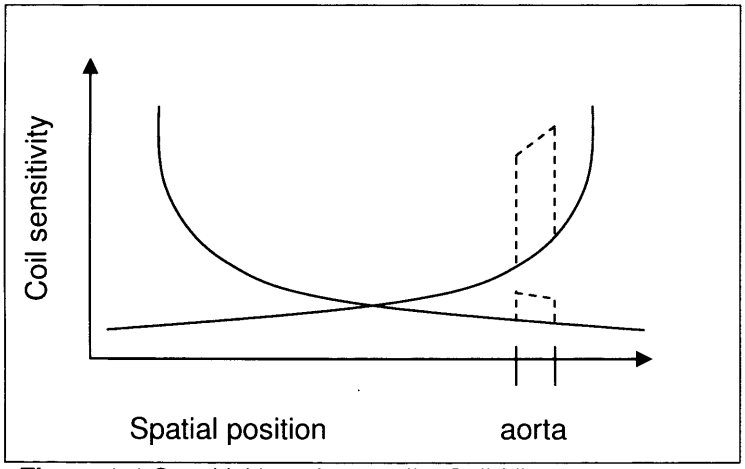

Figure 8-1 Sensitivities of two coils. Solid lines represent true sensitivities c^{γ}. In the region of the aorta, the sensitivities are multiplied by a factor z_t to give the sensitivities shown by the dashed line.

The method I propose in this chapter for removing pulsatile flow artefacts arising from the carotid in 3D structural head images was developed out of an understanding of the CARE technique.

8.3 Method

In this section I propose a new technique for simulating and removing pulsatile flow artefact. The assumptions and modelling have some similarities to that used in the CARE algorithm. These similarities are based on the common assumption that pulsatile flow artefacts are caused by view to view differences in intensities. To extend this concept to a 3D head image I modelled the TFE sequence (described in Chapter 2, Section 2.7.5) with the complete collection of planes of k-space occurring sequentially and distinctly. However, to match the most common acquisition parameters used in clinical trials, I modelled the slow phase encode direction as being the left right direction rather than the head foot direction. I chose to model each plane as being acquired instantaneously, which is an approximation. However, as previously described the pulsatile flow artefact only appears in the slow phase encode direction so this is an approximation which will give a realistic simulation. To simulate the artefact I assume that the whole vessel has the same intensity modulation over time; this is the same assumption made with the CARE algorithm. In CARE a multiplicative factor is used to vary the intensity of the vessel, in this method I propose the use of an additive factor. The use of an additive factor suits the proposed model for my simulation: the intensity of the vessel in the original image is modelled as the intensity of the vessel during the rest phase of the cardiac cycle, and the increase in intensity of the vessel during the active phase is an amount directly proportional to the carotid velocity at that time. With the use of an additive factor I can correct the simulated artefact by solving a linear system. I also use the principle behind CARE that all coil views should be the same if the artefact is completely corrected. CARE optimises its solution by minimizing the difference between coil views, while the method I propose solves the equations given from two different coil views.

8.3.1 Model

To model pulsatile flow artefact I assume that the intensity variation of the pulsating voxel can be expressed as an additive variable. To begin with, I assume that only one voxel in a line running in the slow phase encode direction has a pulsating intensity, although I later extend this to allow several voxels to vary in Section 8.3.2.7.

x is the slow phase encode direction, which in this case is left right, the direction along which the artefact spreads. I deal independently with each complete line of voxels in the x direction, in doing so I assume that the artefact does not spread in any other direction. I base this assumption both on observation from flow artefacts in acquired

images and from the literature. Frank et al, 1993, investigate the geometric location of ghost artefacts in 3D acquisitions arising from pulsatile blood flow. They show that the line along which ghost artefacts occurs lies in the plane defined by the two phase encode directions. The angle of the line in the plane depends solely on the imaging parameters. Frank et al assume for a sagittal acquisition that the whole range of volume encoding is completed before advancing to the next y encoding step. The angle between the artefact line and the slow phase encode (y) direction is calculated in their paper as follows. Current time = (nsNf + nf)TR, where ns is the number of complete slow phase encode lines acquired, nf is the number of fast phase encode lines acquired within the current slow phase encode cycle, and Nf is the number of fast phase encode lines in one slow phase encode cycle. TR is the repetition time between each fast phase encode acquisition. In my model I will simulate an MP-RAGE (TFE) sequence, such as is described in Chapter 3, in the sagittal orientation. Using Frank's theory, the time at any point during the scan is equal to (nsNf +nf)TR + (ns+1)TI, where TI is the time between the inversion pulse and the first fast excitation pulse. Frank calculates in his paper the angle of the line as $\tan^{-1}$(delta f/ delta s), where delta f and delta s are respectively the distances in the fast and slow phase encode directions which the next ghost will occur. Delta s = NfLsTR/tau0, where Ls is the field of view in the slow phase encode direction, and tau0 is the pulsation period. Substituting the acquisition details of a sagittal MP-RAGE sequence similar to that in Chapter 3 gives delta s = Ls(NfTR+TI)/tau0. Frank et al, show Delta f = LfTR/tau0, where Lf is the field of view in the fast phase encode direction, which would remain the same in the case of the MP-RAGE sequence. This results in an angle of $\tan^{-1}$(Lf/Ls(Nf+TI/TR). Using the acquisition parameters for a sagittal MP-RAGE sequence, similar to that described in Chapter 3, this is approximately equal to $\tan^{-1}$(245/144(168+(80.3/9.8)) which is approximately equal to 0.5 degree. Due to this negligibly small angle suggested by Frank's theory, as well as visual inspection of the artefacts in the images showing artefacts running parallel to the phase encode direction, I decided to model the artefact as occurring solely in the slow phase encode direction.

I also chose to simulate plug flow instead of the more complex laminar flow profiles in this work. Petersson and Christoffersson in 1999, show that pulsatile flow artefacts are almost the same for plug and laminar flow profiles.

So, if $m(x,t)$ is the representation of the object at location, x and time, t, $s(x)$ is the coil sensitivity, $m(x)$ is the true representation of the object and $p(t)$ is the function of intensity variation of voxel x_0.

The relationship between m(x) and m(x, t) can be defined as:

$$m(x,t) = s(x)m(x) + s(x_0)p(t)\delta(x - x_0) \qquad \textbf{Equation 1}$$

The Fourier transform of Equation 1 is:

$$M(k_x,t) = S(k_x) * M(k_x) + s(x_0)p(t)e^{-i2\pi x_0 k_x} \qquad \textbf{Equation 2}$$

I now assume that points along the slow phase encode direction, x, of k-space are sequentially acquired. This gives $k_x(t) = t$, and so we have $p(k_x) = p(t)$. So we can write the data acquired by two coils as

$$M_1'(k_x) = S_1(k_x) * M(k_x) + s_1(x_0)p(k_x)e^{-i2\pi x_0 k_x} \qquad \textbf{Equation 3}$$

$$M_2'(k_x) = S_2(k_x) * M(K_x) + s_2(x_0)p(k_x)e^{-i2\pi x_0 k_x} \qquad \textbf{Equation 4}$$

Equations 3 and 4 in the spatial domain are:

$$m_1'(x) = s_1(x)m(x) + s_1(x_0)P(x - x_0) \qquad \textbf{Equation 5}$$

$$m_2'(x) = s_2(x)m(x) + s_2(x_0)P(x - x_0) \qquad \textbf{Equation 6}$$

where $P(x - x_0)$ represents the Fourier transform of $p(t)$ displaced to position x_0. For example, if $p(t)$ were a rect function (a voxel changing its intensity for a fixed period of time), P would be a sinc centred on the voxel x_0 which would generate the expected artefacts. For every voxel, x, there is a linear system with two unknowns, $m(x)$ and $P(x - x_0)$ and using just two coils, two equations which can be solved:

$$P(x - x_0) = \frac{s_2(x)m_1'(x) - s_1(x)m_2'(x)}{s_1(x_0)s_2(x) - s_2(x_0)s_1(x)} \qquad \textbf{Equation 7}$$

$$m(x) = \frac{s_2(x_0)m_1'(x) - s_1(x_0)m_2'(x)}{s_2(x_0)s_1(x) - s_1(x_0)s_2(x)} \qquad \textbf{Equation 8}$$

This is solvable for all x, except for $x = x_0$ where the denominator becomes zero. This means the true voxel values can be accurately recovered for all voxels except the varying voxel.

8.3.2 Implementation and Results

8.3.2.1 Defining the true image and the coil sensitivities

First I define the true representation of the image, $m(x)$, and the coil sensitivities, $s_1(x)$ and $s_2(x)$. I set $m(x)$ to be one line of a 3D head image (in this example, a line running in the left right (LR) direction (slow phase encode direction) which was randomly selected from the volume, 120 voxels in the head foot (HF) direction and 120 voxels in the anterior posterior (AP) direction). An example $m(x)$ is shown below in Figure 8-2.

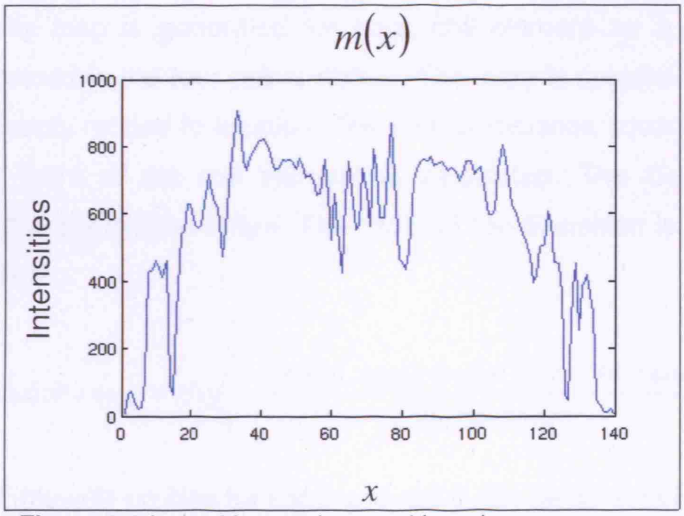

Figure 8-2 Intensities against position along a randomly selected line in the left right direction from an MR head image. This line is nominally called $m(x)$. This is the true representation of the line, without artefact.

To define $s_1(x)$ and $s_2(x)$ I simulate coil profiles and then select the same line from the profiles (in this case y =120, z =120), example $s_1(x)$ and $s_2(x)$ can be seen in Figure 8-4. I assume 6 coils in the array and choose coils 3 and 6 as $s_1(x, y, z)$ and $s_2(x, y, z)$ respectively. This is because they are located directly opposite across the mid AP line; therefore the two coil views should display the most differences in artefact appearance.

8.3.2.1.1 Details of simulating coil profiles

The diameter of the coil array is determined as the maximum size of the image in the x (LR) or y (AP) direction. The diameter of each element is determined by multiplying the diameter of the array by π, giving the array circumference, and divided by the number of coils.

The position of each coil is determined as follows:

1. The first dimension coordinate is given by the size of the image in the HF direction divided by 2/3, as all the coils are simulated at being at this height.
2. The next two dimension coordinates are calculated to place the centre of each element around the circumference of the array, at equal intervals.
3. The last element is always placed exactly half way along the AP direction.
4. An even number of coils is normally chosen, so each coil has a coil in a mirrored location on the opposite side of the medial AP line.

The coil sensitivity map is generated for each coil element as a Gaussian profile centred as determined in the four points above. This map is created by making a grid where value is directly related to location. The sum of distance squared for each voxel from the centre point of the coil element is calculated. The Gaussian profile is generated using the expression below. The width of the Gaussian is controlled by the coil element diameter.

$$Coil\ sensistivity\ map = \exp\left(\frac{-\ sum\ of\ squares\ dist\ from\ coil\ centre}{coil\ diameter^2}\right) \quad \textbf{Equation 9}$$

The resulting coil intensity profiles for coil 3 and coil 6 can be seen in Figures 8-3 and 8-4. This is a simplification of a 3D coil sensitivity map which I use to demonstrate the method being described.

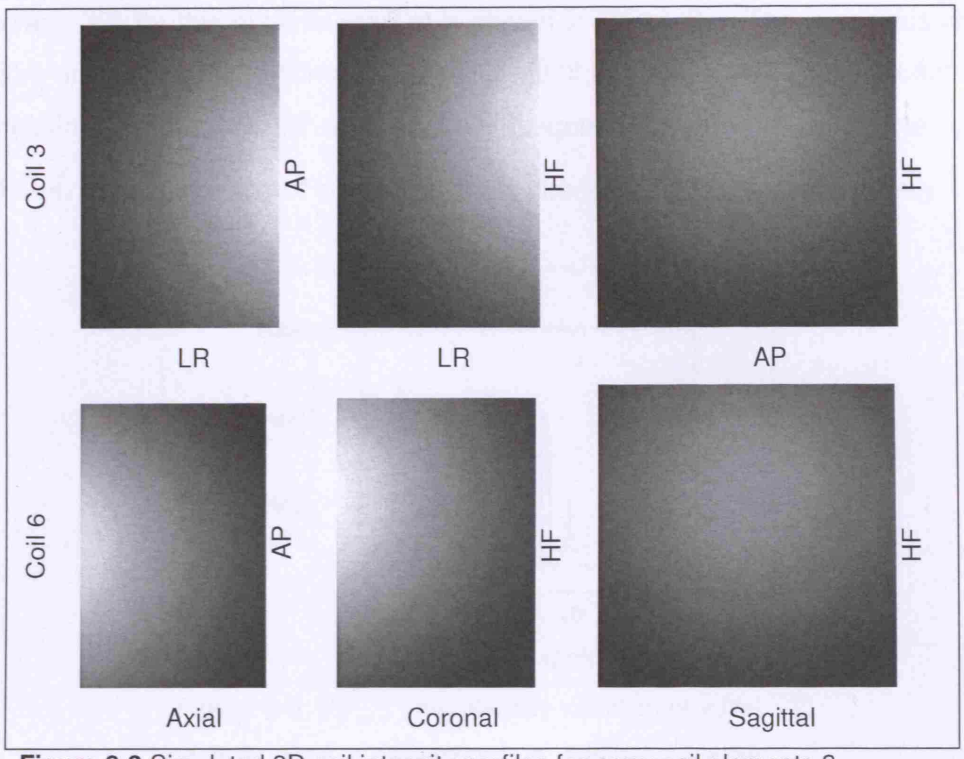

Figure 8-3 Simulated 3D coil intensity profiles for array coil elements 3, $s_1(x, y, z)$ and 6, $s2(x, y, z)$

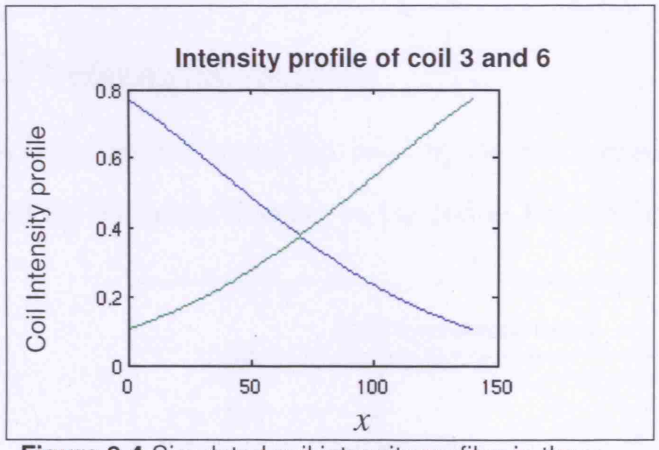

Figure 8-4 Simulated coil intensity profiles in the x direction, at y =120, z = 120. Coil3, $s_1(x)$, blue. Coil6 , $s_2(x)$, green

8.3.2.2 Determining the remaining inputs

I use the vessel mask to select the voxel which will vary, x_0. (In this example, x_0 = 30; later I use a segmentation of the carotid so determine a selection of varying voxels). In this simulation I set the size of the matrix $p(k_x)$ to be the same size as $m(x)$; this is because I model one slow phase encode step for each plane in the image. $p(k_x)$, which is the intensity variation of the varying voxel at each slow phase encoding step,

is arbitrarily set for this experiment and is shown in Figure 8-5. The intensities chosen were in a suitable range to simulate a similar effect to that from the carotid. Later I use a simulation of the carotid and scanner sequence timing to determine $p(k_x)$. $p(k_x) = p(t)$ as each plane of k-space in the x direction is acquired sequentially.

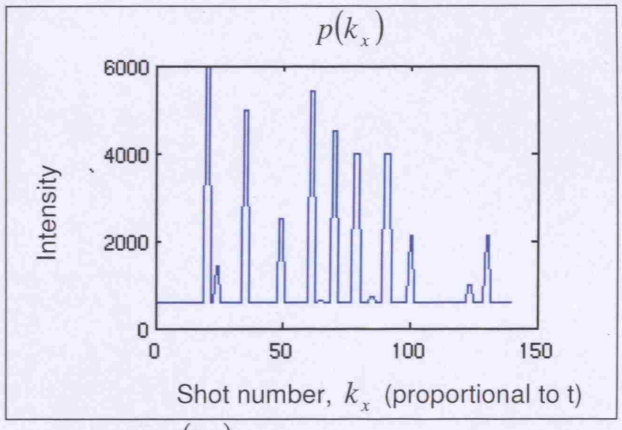

Figure 8-5 $p(k_x)$: the intensity variation of voxel x_0 over time t, measured in number of slow phase encoding steps, or shot number, which also correlates to time, $p(k_x) = p(t)$

8.3.2.3 Defining the space x-t

I multiply the original image line $m(x)$ by the coil sensitivity maps $s_1(x)$ and $s_2(x)$, to give two coil modulated images, $m_1(x)$ and $m_2(x)$ see Figure 8-6.

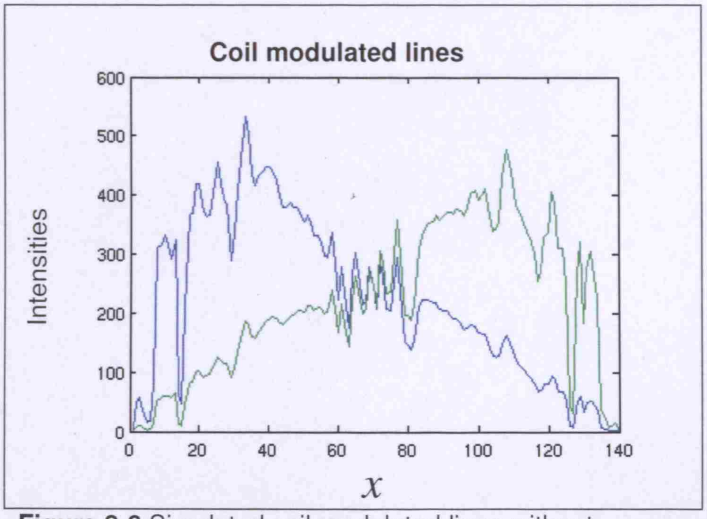

Figure 8-6 Simulated coil modulated lines without artefact. $m(x)\ s_1(x) = m_1(x)$, coil 3, blue. $m(x)\ s_2(x) = m_2(x)$, coil 6, green.

These lines are both replicated as many times as there are slow phase encodings (140 in this simulation) to form a matrix defining the space x-t

8.3.2.4 Adding artefact in x-t

Now I simulate artefact into this x-t space. This is done by adjusting the intensity of the varying voxel at each time point using the function p. So for example, when varying voxel $x = 30$ I use the following equations to calculate the new x-t space with artefact.

$$m_1(30,t) = m_1(30) + s_1(30) * p(t) \quad \textbf{Equation 10}$$
$$m_2(30,t) = m_2(30) + s_2(30) * p(t) \quad \textbf{Equation 11}$$

The resulting $m_1(x,t)$ and $m_2(x,t)$ can be seen in Figures 8-7 and 8-8 respectively.

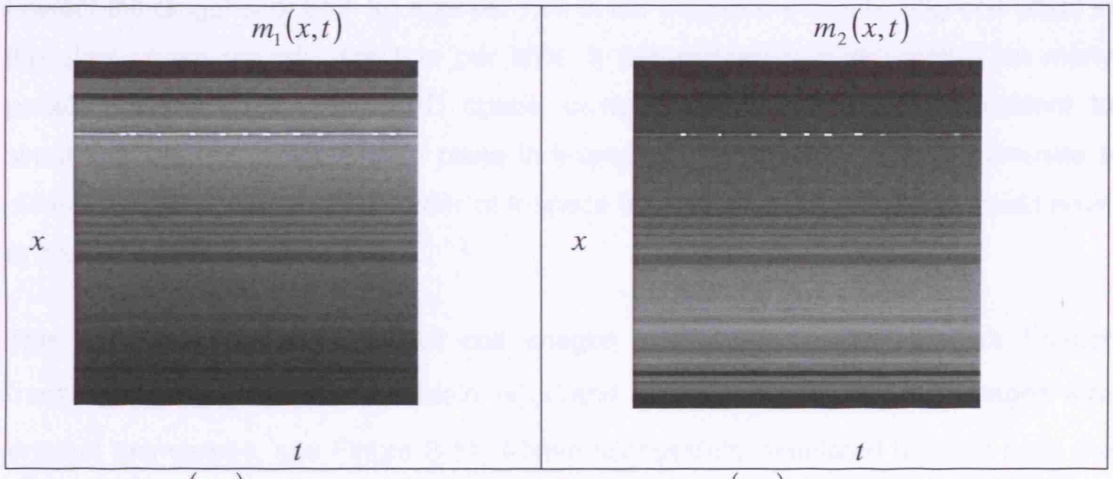

Figure 8-7 $m_1(x,t)$: coil 3, modulated image with a voxel, $x_0 = 30$, varying intensity over time

Figure 8-8 $m_2(x,t)$: coil 6, modulated image with a voxel, $x_0 = 30$, varying intensity over time

8.3.2.5 Producing coil images with artefact through k-t space selection

I then Fourier transform these two coil modulated, x-t spaces with artefact to give two coil modulated, k-t spaces with artefact, see Figures 8-9 and 8-10.

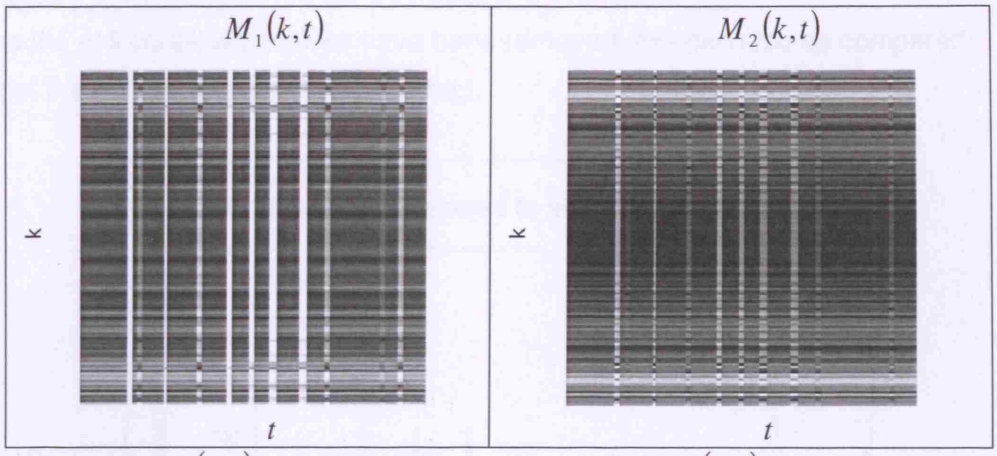

Figure 8-9 $M_1(k,t)$: coil 3 modulated line with one voxel varying intensity over time, shown in the k t domain

Figure 8-10 $M_2(k,t)$: coil 6 modulated line with one voxel varying intensity over time, shown in the k t domain

I select the diagonal of both k-t spaces. This is the equivalent of selecting one voxel in the slow phase encode direction per shot. If this operation is performed on many parallel lines from the same 3D space, using the same p, this is equivalent to simulating the acquisition of one plane in k-space per shot. If I wished to simulate a different sequence acquisition order of k-space this selection of k-t space would have to be modified accordingly.

This results in two k-spaces of coil images with artefact; after inverse Fourier transforming both of these we obtain $m_1'(x)$ and $m_2'(x)$ which are the coil images with artefact themselves, see Figure 8-11. I have successfully simulated artefact from the varying voxel.

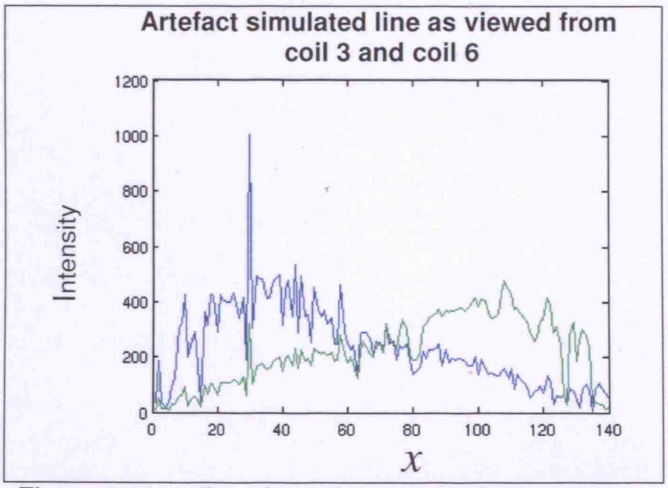

Figure 8-11: coil modulated views with final artefact: coil3: $m_1'(x)$ (blue), coil6: $m_2'(x)$ (green). Artefact causing pixel x= 30.

In Figure 8-12, the difference the artefact alone creates can be seen in the coil views where the coil sensitivity profiles have been removed; this can also be compared against the original image without artefact.

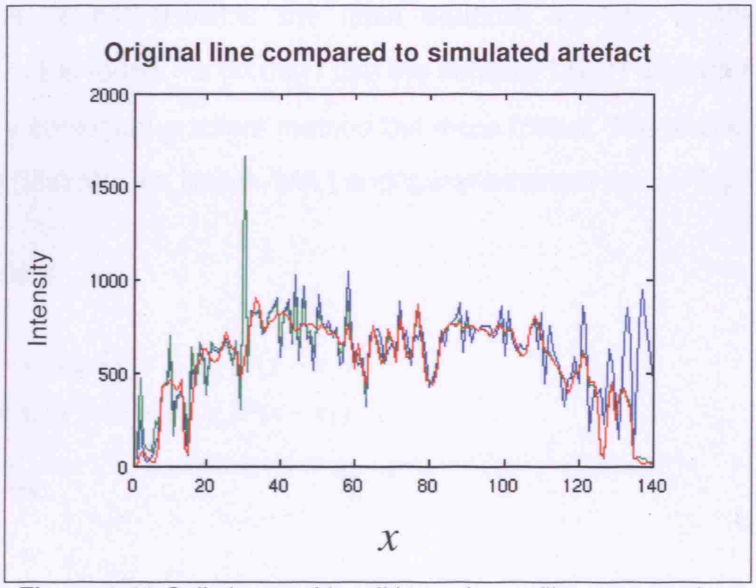

Figure 8-12 Coil views, with coil intensity profiles corrected, with artefact: Coil 3, $m_1'(x)/s_1(x)$, blue; coil 6, $m_2'(x)/s_2(x)$ green. Original image without artefact, $m(x)$ red

8.3.2.6 Removal of the artefact by solving linear equations

To remove the artefact I propose solving the system of linear equations $m' = Ax$, for x. Where this is not possible the least squares solution x that minimizes $norm(m'(x) - Ax)$ is found. To do this I use the iterative LSQR algorithm [Paige 1982], it is similar to a conjugate gradient method but more robust. The implementation I use is from Matlab (MathWorks, Natick, MA.) and is implemented as $x = lsqr(A, m'(x))$

Equations 5 and 6:

$$m_1'(x) = s_1(x)m(x) + s_1(x_0)P(x - x_0)$$
$$m_2'(x) = s_2(x)m(x) + s_2(x_0)P(x - x_0)$$

can be written as:

$m'(x) = A * x$

$$\begin{array}{|c|}\hline m_1'(x) \\ \hline m_2'(x) \\ \hline \end{array} = \begin{array}{|c|c|}\hline Diag(s_1(x)) & Diag(s_1(x_0)) \\ \hline Diag(s_2(x)) & Diag(s_2(x_0)) \\ \hline \end{array} * \begin{array}{|c|}\hline m(x) \\ \hline P(x - x_0) \\ \hline \end{array}$$

$$\begin{array}{|c|}\hline m_1'(x_a) \\ m_1'(x_b) \\ m_1'(x_c) \\ \ldots \\ \hline m_2'(x_a) \\ m_2'(x_b) \\ m_2'(x_c) \\ \ldots \\ \hline \end{array} = \begin{array}{|cccc|cccc|}\hline s_1(x_a) & 0 & 0 & 0 & s_1(x_0) & 0 & 0 & 0 \\ 0 & s_1(x_b) & 0 & 0 & 0 & s_1(x_0) & 0 & 0 \\ 0 & 0 & s_1(x_c) & 0 & 0 & 0 & s_1(x_0) & 0 \\ 0 & 0 & 0 & .... & 0 & 0 & 0 & .... \\ \hline s_2(x_a) & 0 & 0 & 0 & s_2(x_0) & 0 & 0 & 0 \\ 0 & s_2(x_b) & 0 & 0 & 0 & s_2(x_0) & 0 & 0 \\ 0 & 0 & s_2(x_c) & 0 & 0 & 0 & s_2(x_0) & 0 \\ 0 & 0 & 0 & .... & 0 & 0 & 0 & .... \\ \hline \end{array} * \begin{array}{|c|}\hline m(x_a) \\ m(x_b) \\ m(x_c) \\ \ldots \\ \hline P(x_a - x_0) \\ P(x_b - x_0) \\ P(x_c - x_0) \\ \ldots \\ \hline \end{array}$$

where $m'(x)$ is a column matrix created from $m_1'(x)$ written as a column matrix and vertically concatenate with $m_2'(x)$. A is a matrix comprised of a square matrix with $s_1(x)$ on the diagonal, horizontally concatenated with another square matrix with $s_1(x_0)$ on the diagonal, vertically concatenated with a square matrix with $s_2(x)$ on the diagonal which has been horizontally concatenated with a square matrix with $s_2(x_0)$ on the diagonal. The x output from the LSQR algorithm is a column vector of the same dimensions as $m'(x)$. It contains the vertically concatenated column vectors $m(x)$ and $P(x - x_0)$, which will be the solutions of the algorithm.

This gives the Equations 5 and 6 we require:

$$m_1'(x_a) = s_1(x_a)m(x_a) + s_1(x_0)P(x_a - x_0)$$
$$m_1'(x_b) = s_1(x_b)m(x_b) + s_1(x_0)P(x_b - x_0)$$
$$m_1'(x_c) = s_1(x_c)m(x_c) + s_1(x_0)P(x_c - x_0)$$
$$\ldots.$$
$$m_2'(x_a) = s_2(x_a)m(x_a) + s_2(x_0)P(x_a - x_0)$$
$$m_2'(x_b) = s_2(x_b)m(x_b) + s_2(x_0)P(x_b - x_0)$$
$$m_2'(x_c) = s_2(x_c)m(x_c) + s_2(x_0)P(x_c - x_0)$$

As it is impossible to recover $m(x)$, or $P(x - x_0)$ at the position of the varying voxel I interpolate using the two values either side. I also rotationally shift the matrix $P(x - x_0)$ left by the number of voxels before the varying voxel. This gives $P(x)$. I then Fourier transform this to obtain $p(t)$. This should recover the original waveform $p(t)$ which I used as my input. The original and recovered $m(x)$ can be seen in Figure 8-13. The only place the recovered does not quite exactly match the original is in the voxels which were varying.

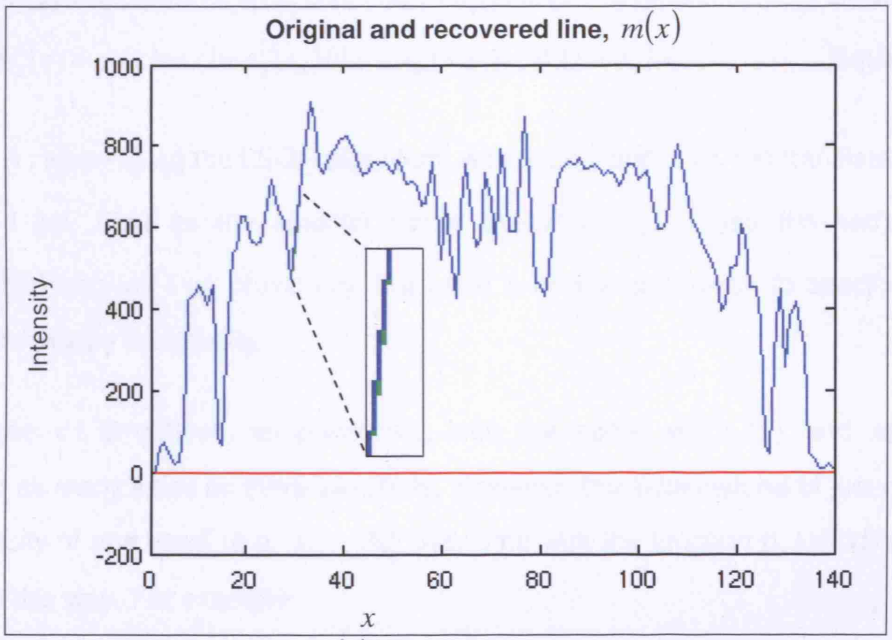

Figure 8-13 Original line $m(x)$, (green, but hidden behind the blue) and recovered m, (blue, real; red, imaginary)

The recovered $p(t)$ can be seen in Figure 8-14. Compared with Figure 8-5 which is the original $p(t)$, the function has been well recovered.

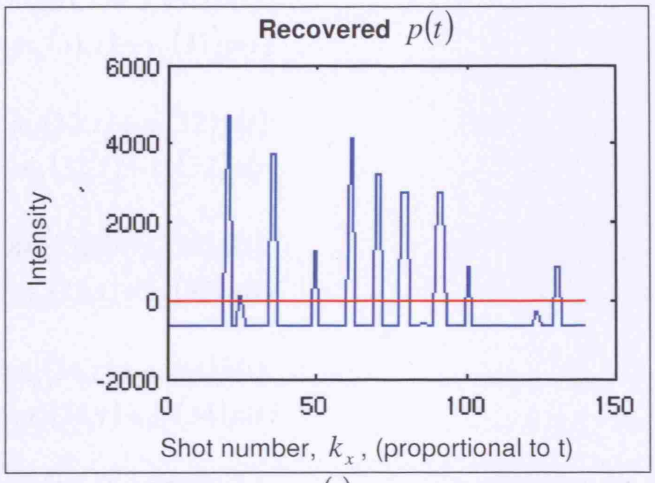

Figure 8-14 Recovered $p(t)$, real component (blue), imaginary component (red)

8.3.2.7 Modelling more than one varying voxel

To model more than one varying voxel I use the following equations, adding as many new terms to Equations 5 and 6 as there are new varying voxels.

$$m_1'(x) = s_1(x)m(x) + s_1(x_0)P(x - x_0) + s_1(x_1)P(x - x_1) + \ldots \quad \textbf{Equation 12}$$

$$m_2'(x) = s_2(x)m(x) + s_2(x_0)P(x - x_0) + s_2(x_1)P(x - x_1) + \ldots \quad \textbf{Equation 13}$$

I define A, when using the LSQR algorithm, with $s_1(x_0)$ and $s_1(x_1)$ in translated places so that I get $P(x)$ as the solution rather than $P(x - x_0)$. I use the same $m(x)$, $s1(x)$, $s2(x)$ and $p(t)$ as previously, but I use a new vessel mask to specify several voxels which vary in intensity.

The space x-t is defined, as previously, with the same $m(x)s_1(x)$ and $m(x)s_2(x)$ repeated as many times as there are shots. However, this time instead of just changing the intensity of one voxel (e.g. x_0 = 30) over time with the function p, I modify several voxels in this way. For example:

$$m_1'(30,t) = m_1(30,t) + s_1(30)p(t)$$
$$m_2'(30,t) = m_2(30,t) + s_2(30)p(t)$$

$$m_1'(31,t) = m_1(31,t) + s_1(31)p(t)$$
$$m_2'(31,t) = m_2(31,t) + s_2(31)p(t)$$

$$m_1'(32,t) = m_1(32,t) + s_1(32)p(t)$$
$$m_2'(32,t) = m_2(32,t) + s_2(32)p(t)$$

$$m_1'(33,t) = m_1(33,t) + s_1(33)p(t)$$
$$m_2'(33,t) = m_2(33,t) + s_2(33)p(t)$$

$$m_1'(34,t) = m_1(34,t) + s_1(34)p(t)$$
$$m_2'(34,t) = m_2(34,t) + s_2(34)p(t)$$

$$m_1'(35,t) = m_1(35,t) + s_1(35)p(t)$$
$$m_2'(35,t) = m_2(35,t) + s_2(35)p(t)$$

Equation 14

The results of the x t space can be seen in Figure 8-15, 8-16. When this space is Fourier transformed the results are different to before. See Figure 8-17 and 8-18.

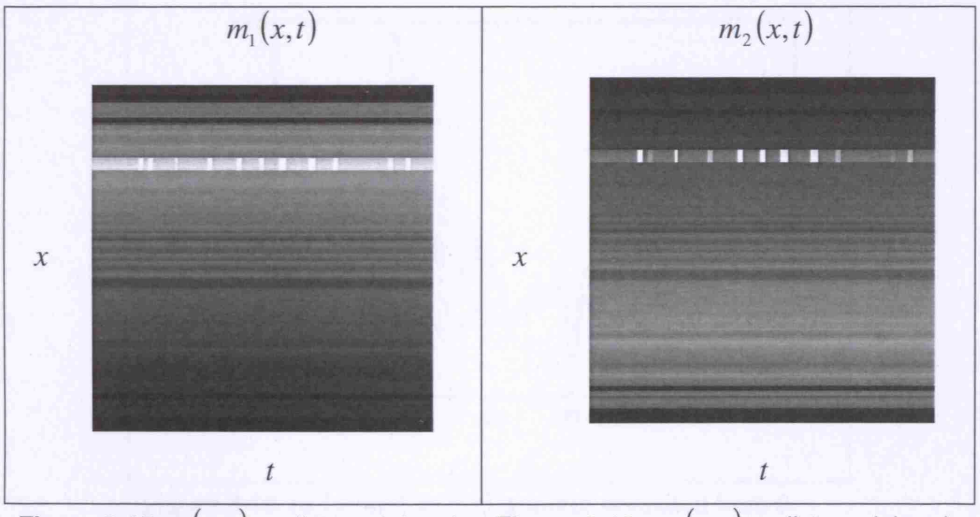

Figure 8-15 $m_1(x,t)$, coil 3 modulated image with 6 voxels varying over time

Figure 8-16 $m_2(x,t)$, coil 6 modulated image with 6 voxels varying over time

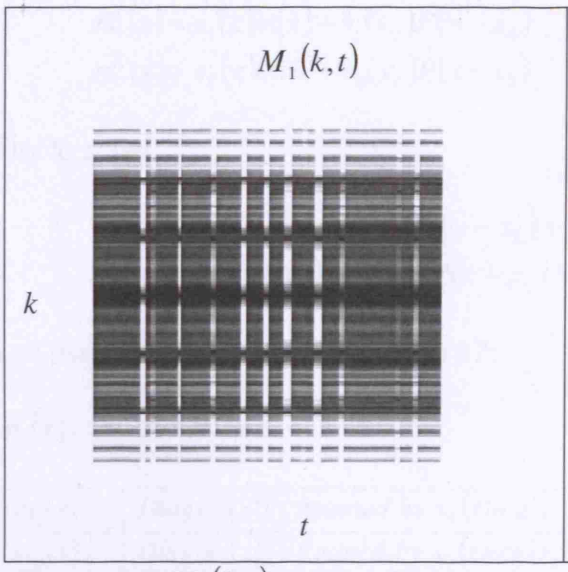

Figure 8-17 $M_1(k,t)$ coil 3 modulated image with 6 varying voxels in k t domain

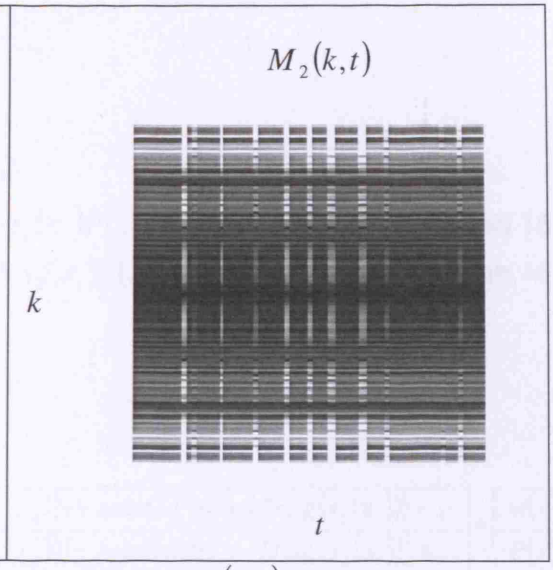

Figure 8-18 $M_2(k,t)$ coil 6 modulated image with 6 varying voxels in k t domain

I select just the diagonal of k-t space as before to give $M_1'(k)$ and $M_2'(k)$. After being inverse Fourier transformed this gives $m_1'(x)$ and $m_2'(x)$, see Figure 8-19.

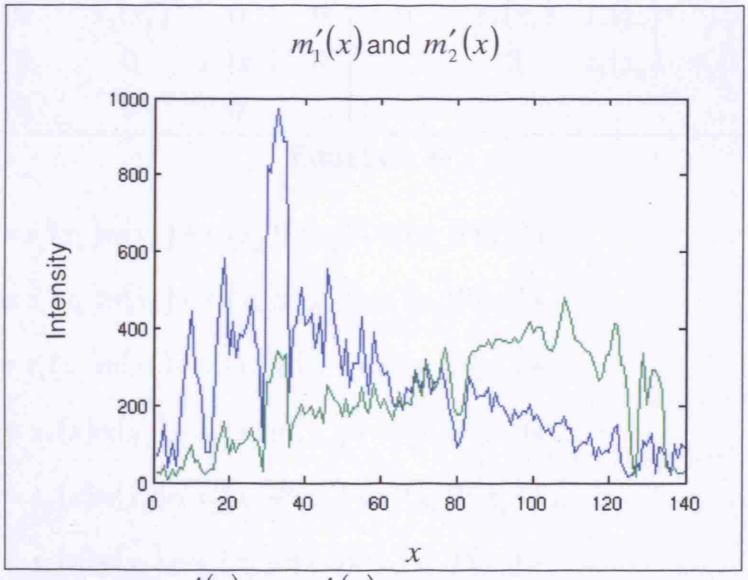

Figure 8-19 $m_1'(x)$ and $m_2'(x)$ artefact simulated from 6 varying voxels as viewed from both coils 3 and 6.

8.3.2.8 Removing artefact caused by more than one varying pixel

For removing this artefact I use the same LSQR method as before $x = lsqr(A, m'(x))$ to solve the system of linear equations $m' = Ax$. However, instead of trying to solve equations 5 and 6

$$m_1'(x) = s_1(x)m(x) + s_1(x_0)P(x - x_0)$$
$$m_2'(x) = s_2(x)m(x) + s_2(x_0)P(x - x_0)$$

I try to solve

$$m_1'(x) = s_1(x)m(x) + s_1(x_0)P(x - x_0) + s_1(x_1)P(x - x_1) + \ldots \quad \textbf{Equation 15}$$
$$m_2'(x) = s_2(x)m(x) + s_2(x_0)P(x - x_0) + s_2(x_1)P(x - x_1) + \ldots \quad \textbf{Equation 16}$$

so I use a new A see Equation 17:

$$m'(x) = A * x$$

$$\begin{array}{|c|} \hline m_1'(x) \\ \hline m_2'(x) \\ \hline \end{array} = \begin{array}{|c|c|} \hline Diag(s_1(x)) & Rotated\ by\ x_0(Diag(s_1(x_0))) + rotated\ by\ x_1(Diag(s_1(x_1))) + \ldots \\ \hline Diag(s_2(x)) & Rotated\ by\ x_0(Diag(s_2(x_0))) + rotated\ by\ x_1(Diag(s_2(x_1))) + \ldots \\ \hline \end{array} * \begin{array}{|c|} \hline m(x) \\ \hline P(x) \\ \hline \end{array}$$

$$\begin{array}{|c|} \hline m_1'(x_a) \\ m_1'(x_b) \\ m_1'(x_c) \\ \ldots \\ \hline m_2'(x_a) \\ m_2'(x_b) \\ m_2'(x_c) \\ \ldots \\ \hline \end{array} = \begin{array}{|cccc|cccc|} \hline s_1(x_a) & 0 & 0 & 0 & s_1(x_0) & s_1(x_1) & .... & 0 \\ 0 & s_1(x_b) & 0 & 0 & 0 & s_1(x_0) & s_1(x_1) & .... \\ 0 & 0 & s_1(x_c) & 0 & .... & 0 & s_1(x_0) & s_1(x_1) \\ 0 & 0 & 0 & .... & .... & .... & .... & .... \\ \hline s_2(x_a) & 0 & 0 & 0 & s_2(x_0) & s_2(x_1) & .... & 0 \\ 0 & s_2(x_b) & 0 & 0 & 0 & s_2(x_0) & s_2(x_1) & .... \\ 0 & 0 & s_2(x_c) & 0 & .... & 0 & s_2(x_0) & s_2(x_1) \\ 0 & 0 & 0 & .... & .... & .... & .... & .... \\ \hline \end{array} * \begin{array}{|c|} \hline m(x_a) \\ m(x_b) \\ m(x_c) \\ \ldots \\ \hline P(x_a) \\ P(x_b) \\ P(x_c) \\ \ldots \\ \hline \end{array}$$

Equation 17

$$m_1'(x_a) = s_1(x_a)m(x_a) + s_1(x_0)P(x_a) + s_1(x_1)P(x_a) + \ldots \quad \textbf{Equation 15}$$
$$m_1'(x_b) = s_1(x_b)m(x_b) + s_1(x_0)P(x_b) + s_1(x_1)P(x_b) + \ldots$$
$$m_1'(x_c) = s_1(x_c)m(x_c) + s_1(x_0)P(x_c) + s_1(x_1)P(x_c) + \ldots$$
$$m_2'(x_a) = s_2(x)m(x_a) + s_2(x_0)P(x_a) + s_2(x_1)P(x_a) + \ldots \quad \textbf{Equation 16}$$
$$m_2'(x_b) = s_2(x)m(x_b) + s_2(x_0)P(x_b) + s_2(x_1)P(x_b) + \ldots$$
$$m_2'(x_c) = s_2(x)m(x_c) + s_2(x_0)P(x_c) + s_2(x_1)P(x_c) + \ldots$$

This time the LSQR algorithm outputs $m(x)$, the recovered image, and $P(x)$ the input modulation function. $P(x)$ can be Fourier transformed without any extra rotation to give the original $p(t)$. The original $p(t)$ can be seen in Figure 8-20 and compared with the recovered $p(t)$ in Figure 8-21. The recovered $p(t)$ is slightly corrupted as the values corresponding to the varying pixels cannot be recovered.

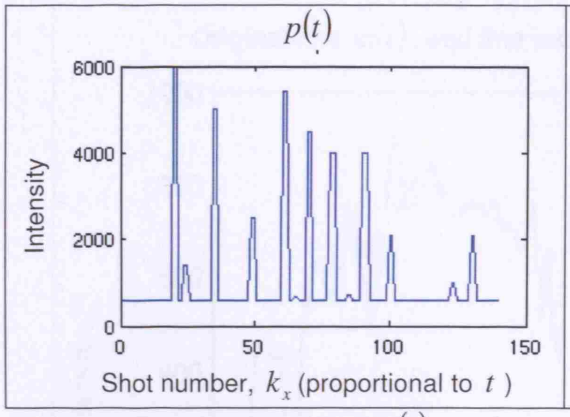

Figure 8-20 Original $p(t)$

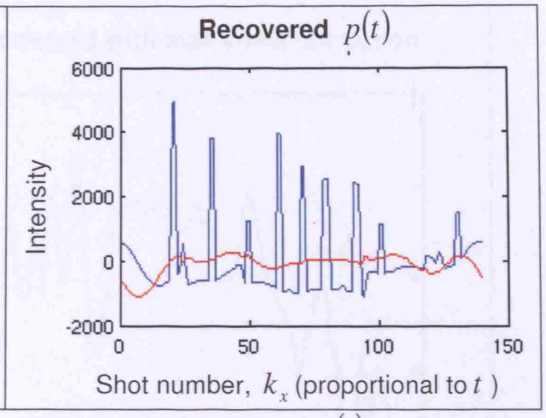

Figure 8-21 Recovered $p(t)$ for 6 varying voxels

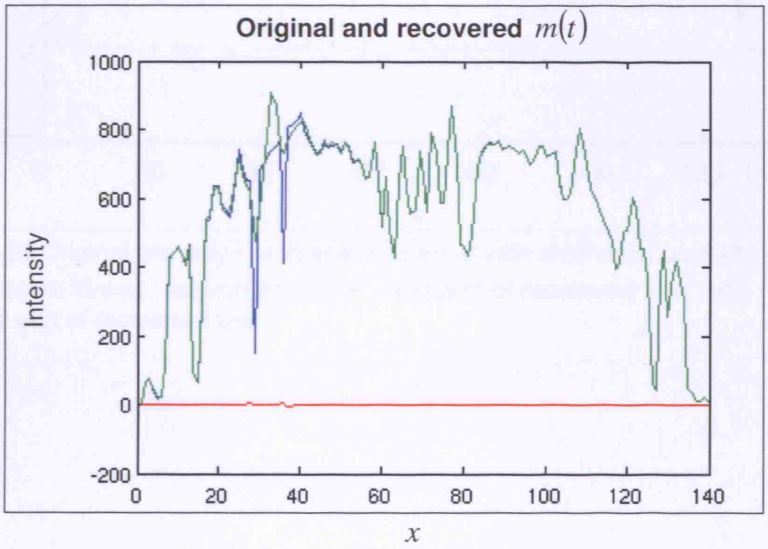

Figure 8-22 Original and recovered $m(t)$ for 6 varying voxels, original (green), recovered, real (blue), imaginary (red)

The original and recovered $m(t)$ in Figure 8-22 differ in the voxels either side of the intensity varying voxels. As the intensity varying voxels cannot be accurately recovered, and to reduce the error in the estimation of the voxels either side of these varying voxels, I smooth these intensities as shown in Figure 8-23. This smoothing is done by interpolating the values of these 8 voxels, using the intensity of the two voxels on either side. This reduces the discrepancy between the original and recovered lines.

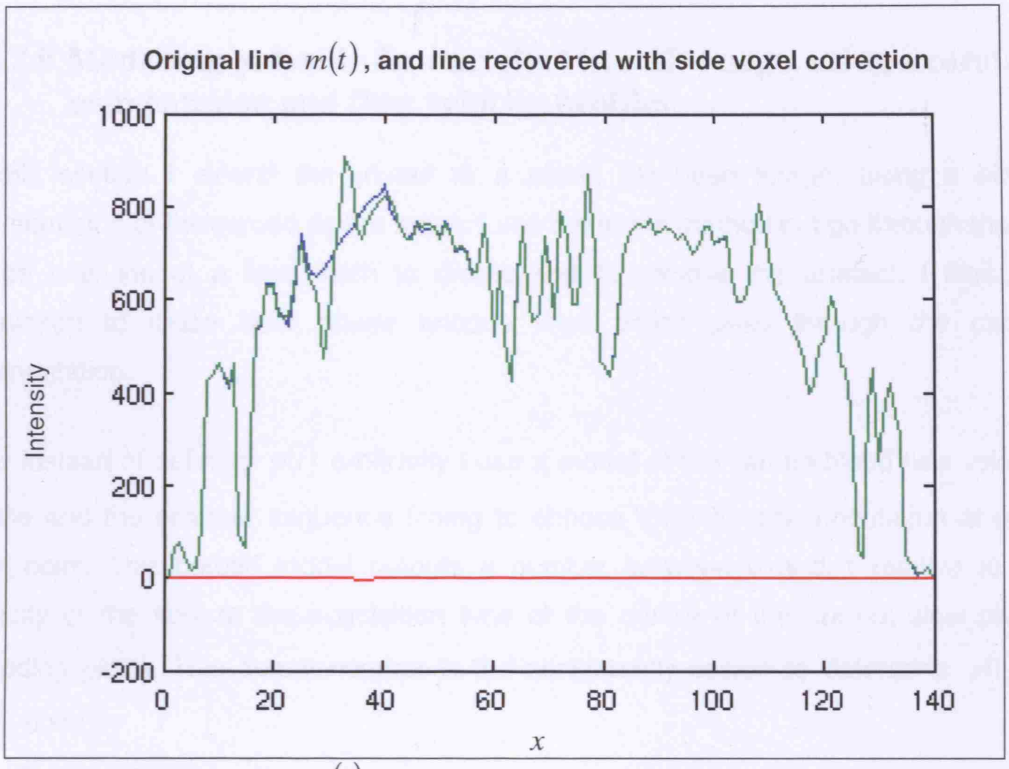

Figure 8-23 Original line $m(t)$ and line recovered with side voxel correction, for 6 varying voxels. Green - original line; blue - real part of recovered line; red - imaginary part of recovered line

8.3.2.9 Modelling pulsatile flow artefact in a 3D image, using a carotid segmentation and flow velocity profiles

In this section I extend the model to a whole 3D head image, using a binary segmentation of the carotid as the mask. I use the same method but go through the 3D image one line at a time, both to create and to remove the artefact. I limit this simulation to those slow phase encode lines which pass through the carotid segmentation.

Now instead of defining $p(t)$ arbitrarily I use a model of the carotid blood flow velocity profile and the scanner sequence timing to choose the intensity modulation at each time point. This carotid model outputs a number between 0 and 1 relative to the velocity of the flow at the acquisition time of the centre of the current slow phase encoding plane. This output number is the consistently scaled to determine $p(t)$ at each point by

$$p(t) = carotid\ output\ sequence * 3400 \qquad \textbf{Equation 18}$$

8.3.2.9.1 Modelling of the carotid and scanner sequence timing

The measured peak velocity of the blood flow in the carotid artery of a normal subject is shown in the following results from Holdworth et al, 1999, see Figure 8-24.

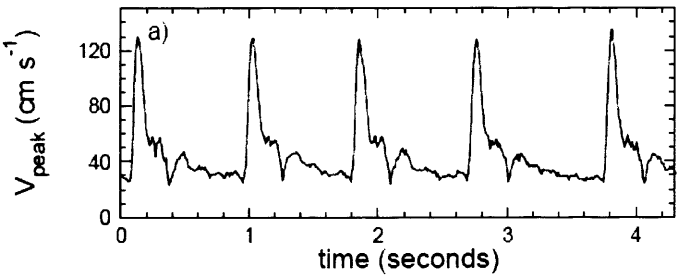

Figure 8-24 Peak velocity of the blood flow in the carotid artery of a normal subject from Holdworth, 1999

I simulated a velocity model for use in this simulation as a half sine wave followed by plateau, see Figure 8-25 below. I simulated a heart rate of 60bmp, and a scanner sequence with shots 1.73s apart, which gives the $p(t)$ function shown in Figure 8-26.

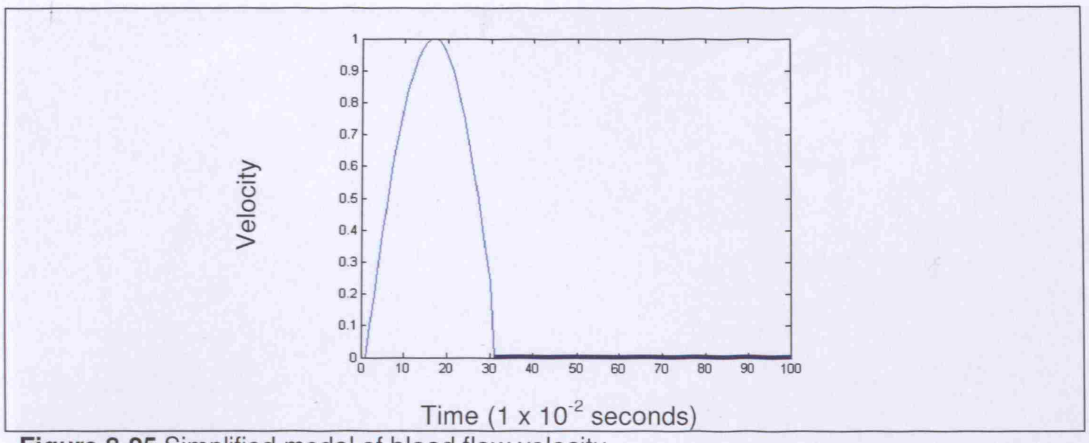

Figure 8-25 Simplified model of blood flow velocity

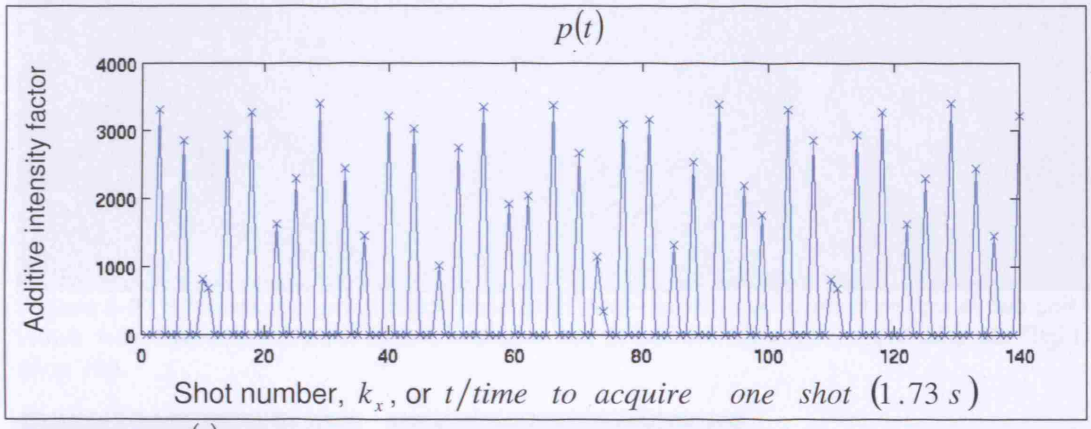

Figure 8-26 $p(t)$ as determined using the carotid flow model described above. This demonstrates the interference pattern between flow pulsatility and the MR acquisition.

8.3.2.9.2 Modelling artefact

I calculate the coil sensitivity maps as before but for all 6 coils. Then I select one slow phase encode line which goes through the carotid at a time, and generate suitable values for $m(x)$ *and* $s(x)$. Using the carotid segmentation I also know which vessels in each line vary over time. I simulate x-t space as before, varying the pixels in the carotid segmentation over time using the function $p(t)$. I Fourier transform to generate the k-t space for each of the six coils and select the diagonals just as previously.

I put all these lines with artefact together for each coil modulation to give a simulation of an artefact generated from carotid flow artefact in each coil view. Two coil views are shown in Figures 8-27 and 8-28. These 6 coil views are then added together to give a single sum of squares, artefact simulated image, see results section, Figure 8-29.

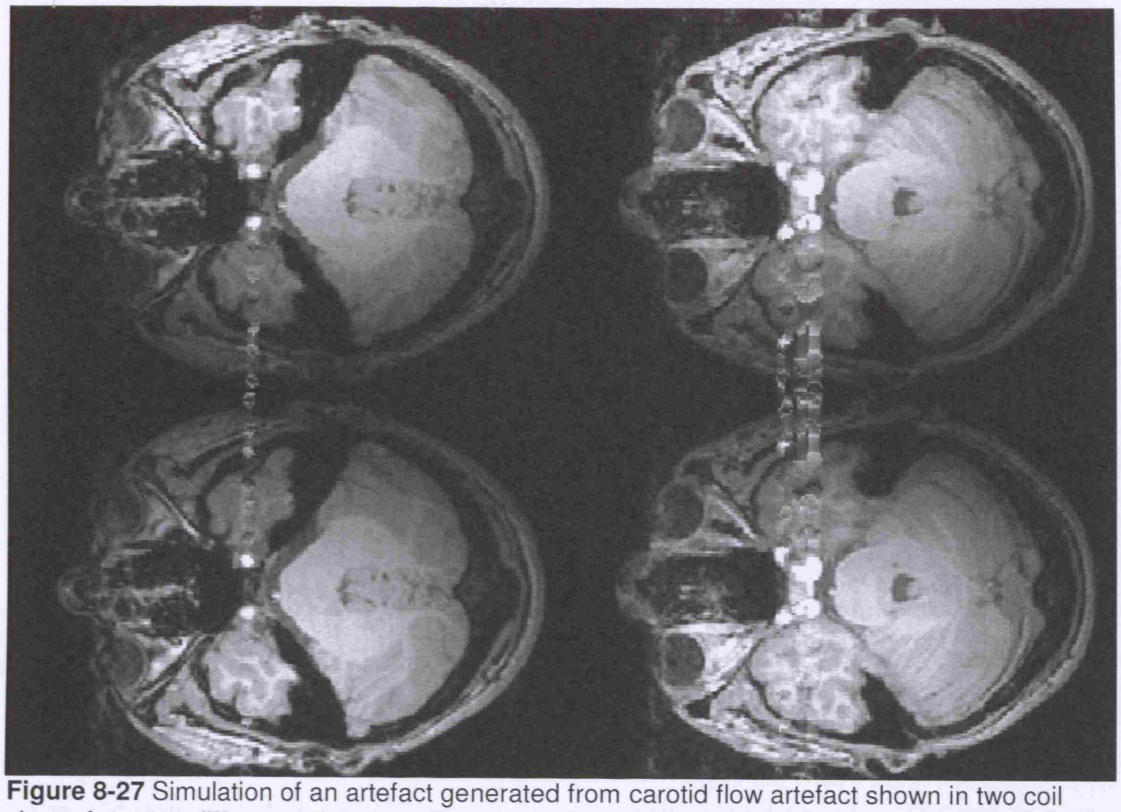

Figure 8-27 Simulation of an artefact generated from carotid flow artefact shown in two coil views, from two different axial slices. Top row: coil 3. Bottom row: coil 6. Left: slice 99, Right slice 106.

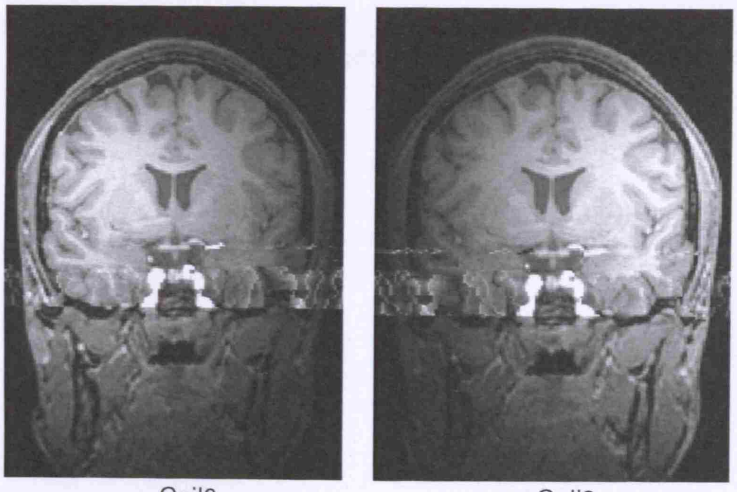

Coil6 Coil3

Figure 8-28 Simulation of an artefact generated from carotid flow artefact shown in two coil views, on a coronal slice (slice 118)

8.3.2.10 Removal of artefact from 3d volume using carotid segmentation

To remove the artefact I use a similar method of correcting one slow phase encode line which passes through the carotid at a time. I calculate $s_1(x)$ and $s_2(x)$ as above and $m'(x)$ is one line of the whole image with artefact. I replace all the slow phase encode

lines with simulated artefact, which pass through the carotid, with their respective recovered $m(x)$.

8.4 Results

All native images in this section are windowed to 1000, all difference images are windowed to +/- 35% of the cortical grey matter intensiy, 210.

8.4.1 Pulsatile flow artefact simulation

Below in Figure 8-29 and 8-30 are images from my simulations. The first row is the original image before I simulate artefact. I have simulated noise on this original image, at the same level which it is simulated on the images with artefact. The difference images are created by subtracting this original image from the simulated image directly above. The scanner sequence long TR is simulated at 1.73s. The various images are simulated with pulse rates between 55 and 85 bpm. To simulate this change in pulse rate a different $p(t)$ is generated, which simulates a different pattern of ghosts. This pattern is determined by the difference between the pulse frequency and the sampling frequency. If there is no difference between the two, no ghosts will be produced.

For comparison longitudinal images with real pulsatile flow artefacts are included in Section 8.6.

Figure 8-29 3D pulsatile flow artefact simulations with varying simulated pulse rates shown in two different axial slices. The difference images show the difference between the simulated image directly above them and the original image with noise.

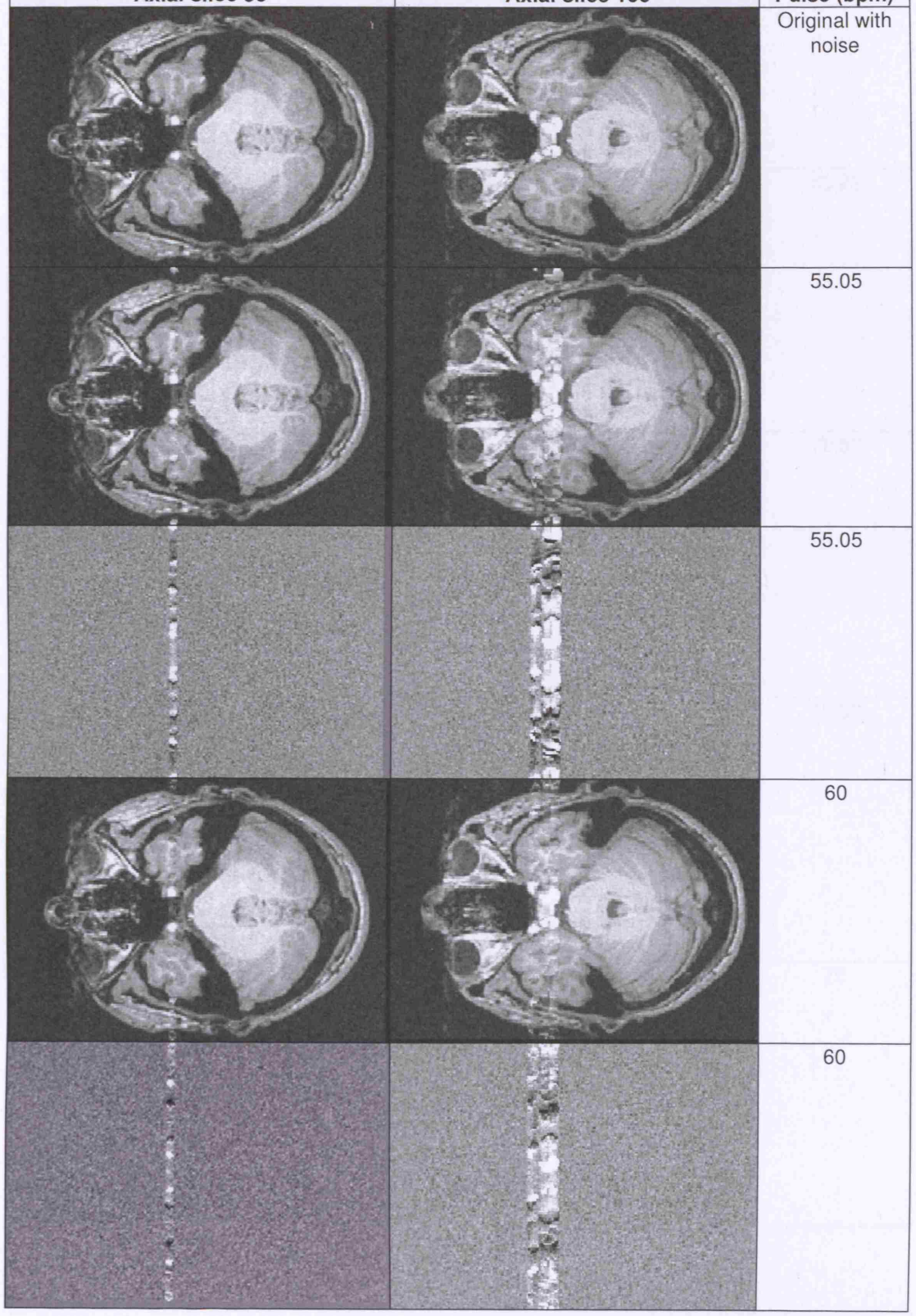

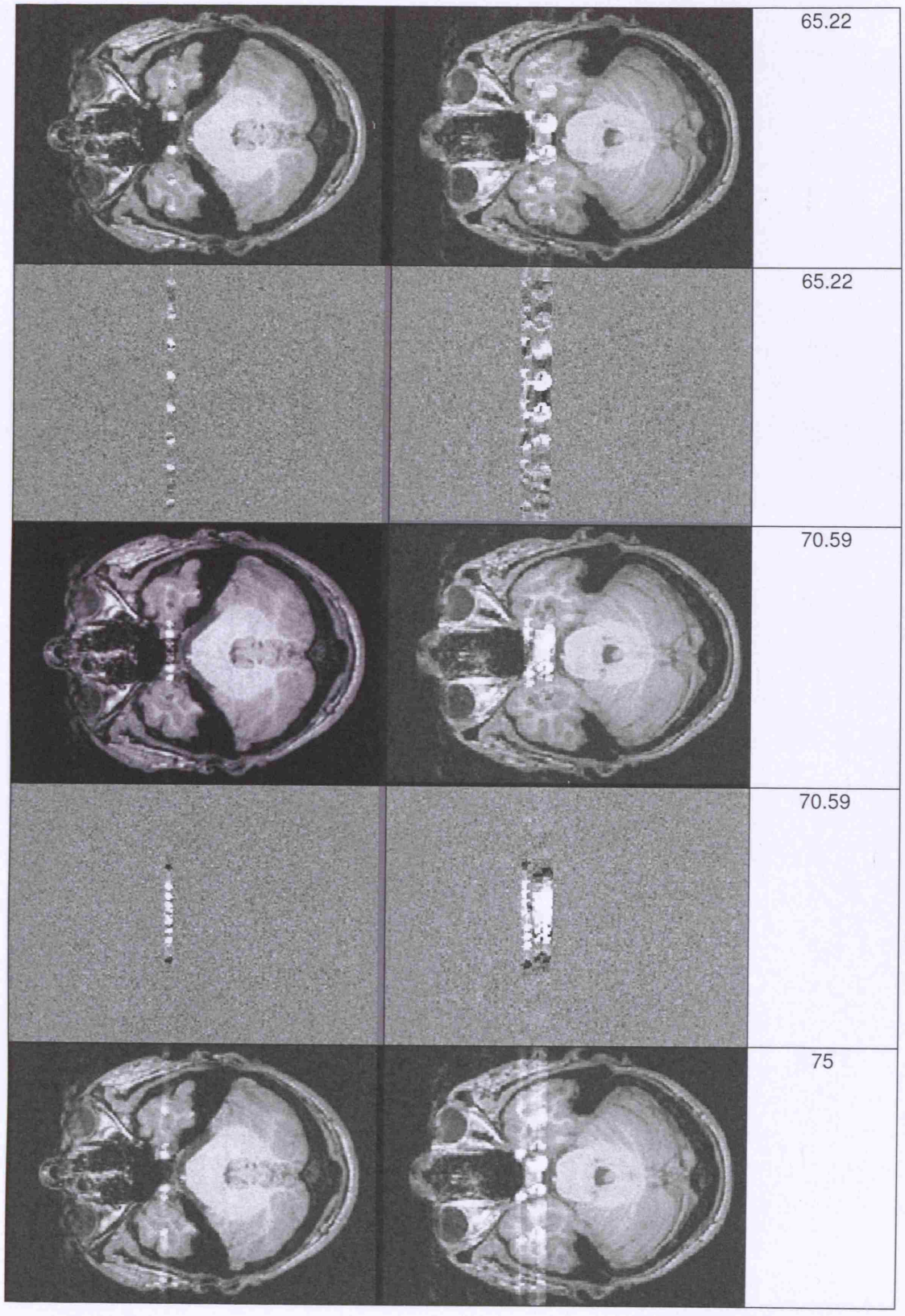
65.22
65.22
70.59
70.59
75

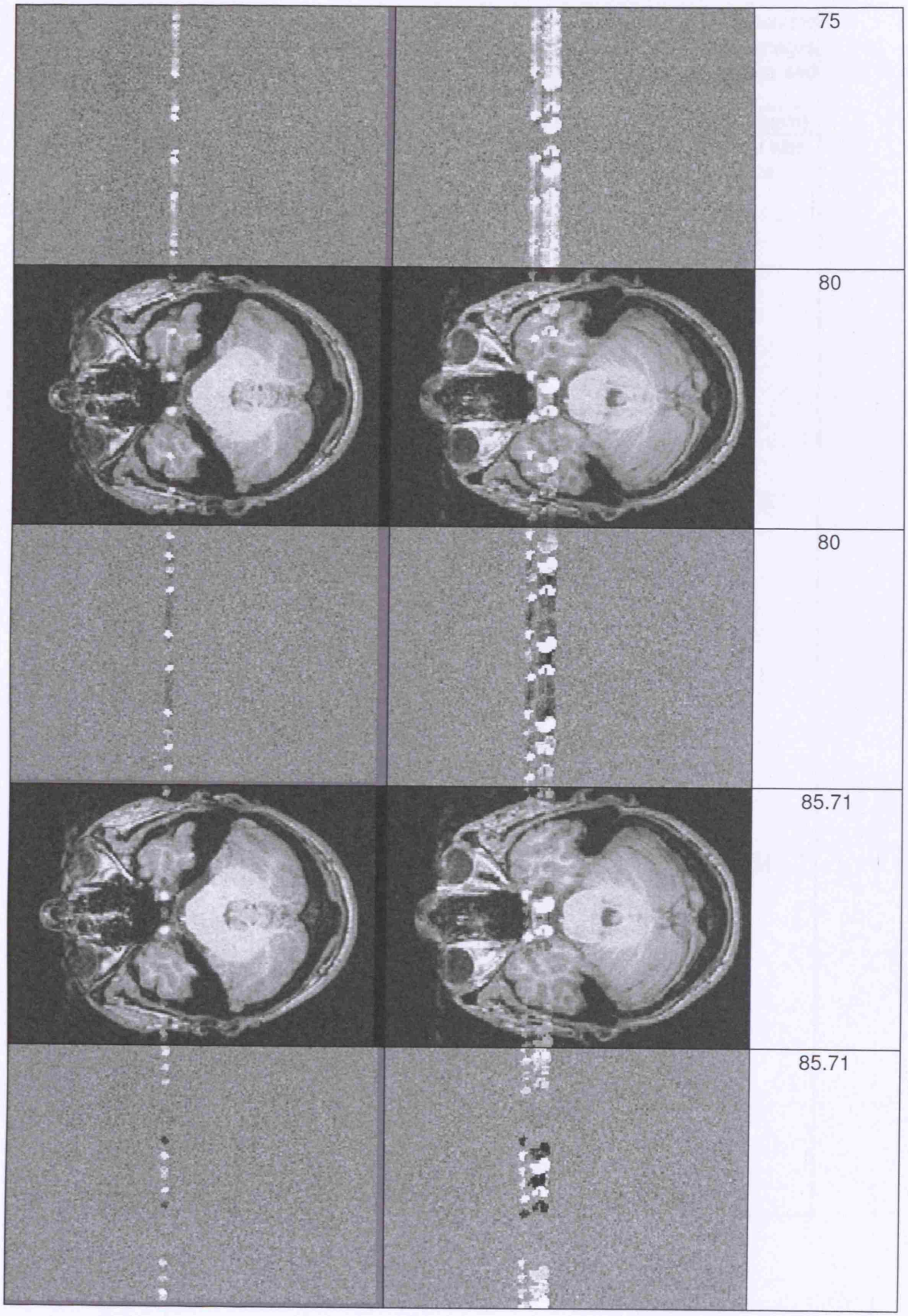
75
80
80
85.71
85.71

Figure 8-30 3D pulsatile flow artefact simulations with varying simulated pulse rates shown in two different coronal slices. The difference images show the difference between the simulated image directly above them and the original image with noise.

Coronal slice 103	Coronal slice 118	Pulse (bpm)
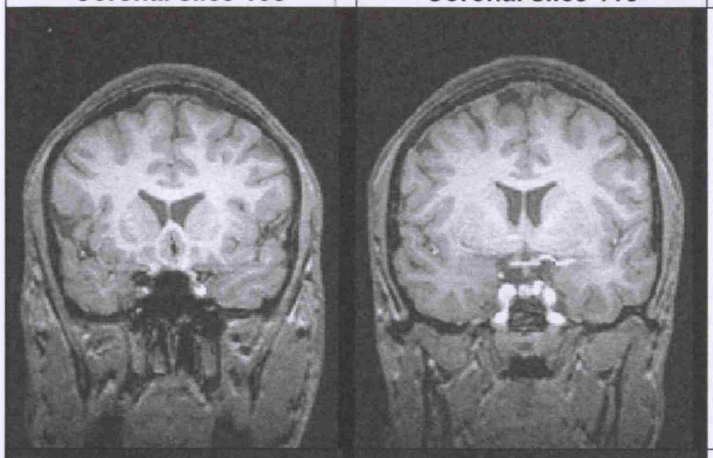		Original with noise
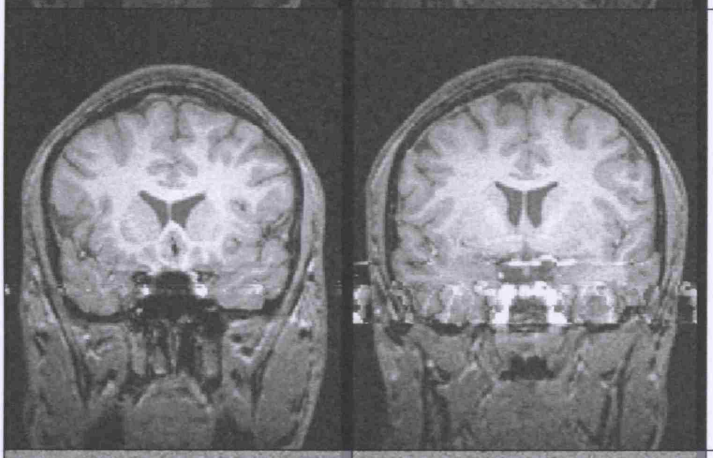		55.05
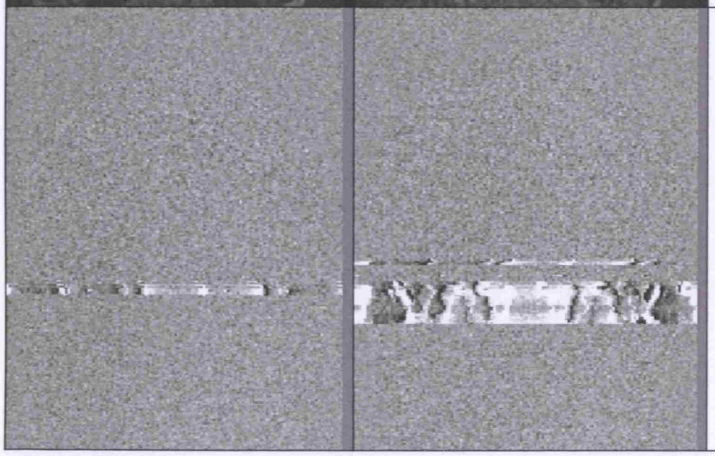		55.05

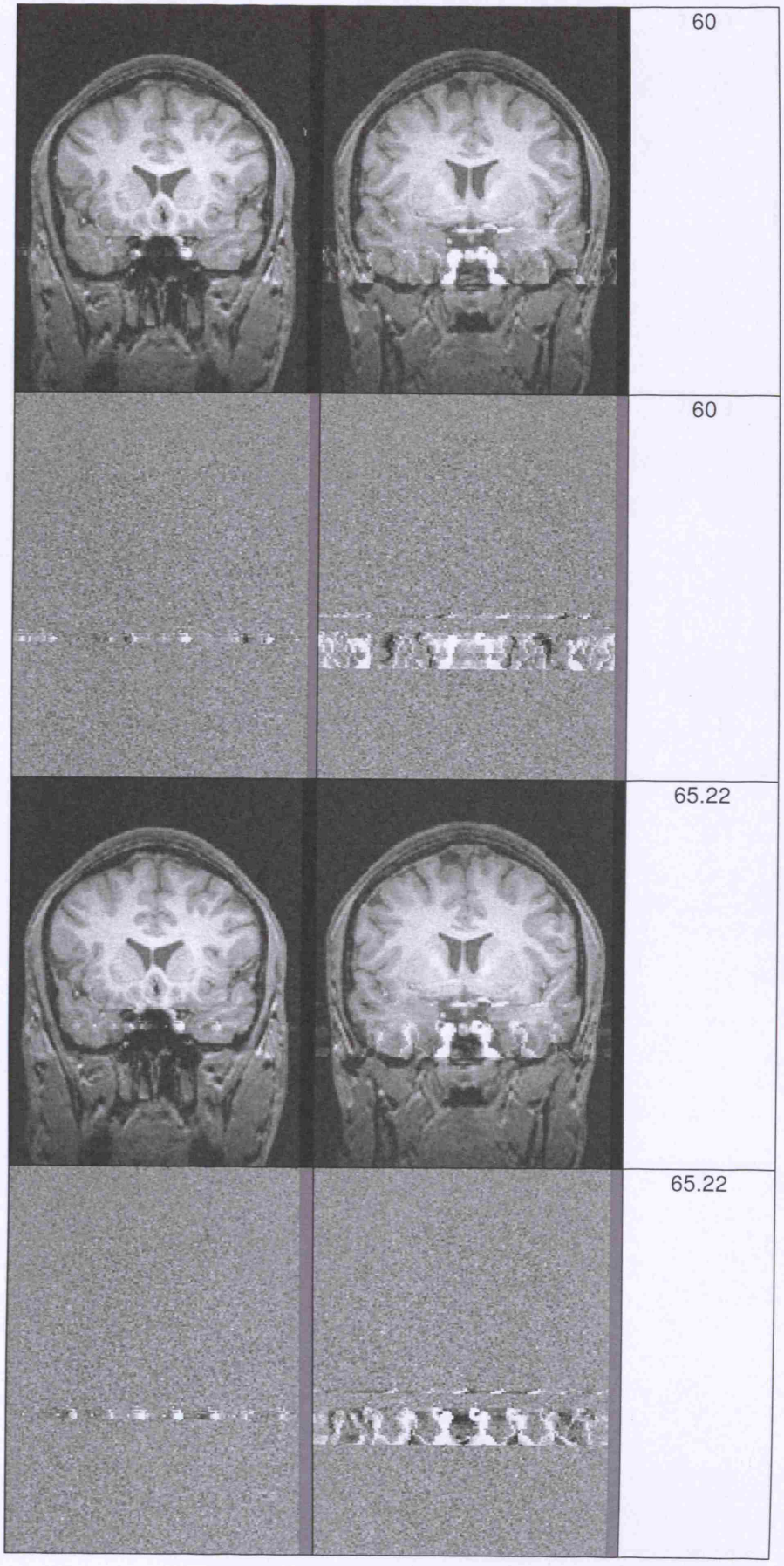
60
60
65.22
65.22

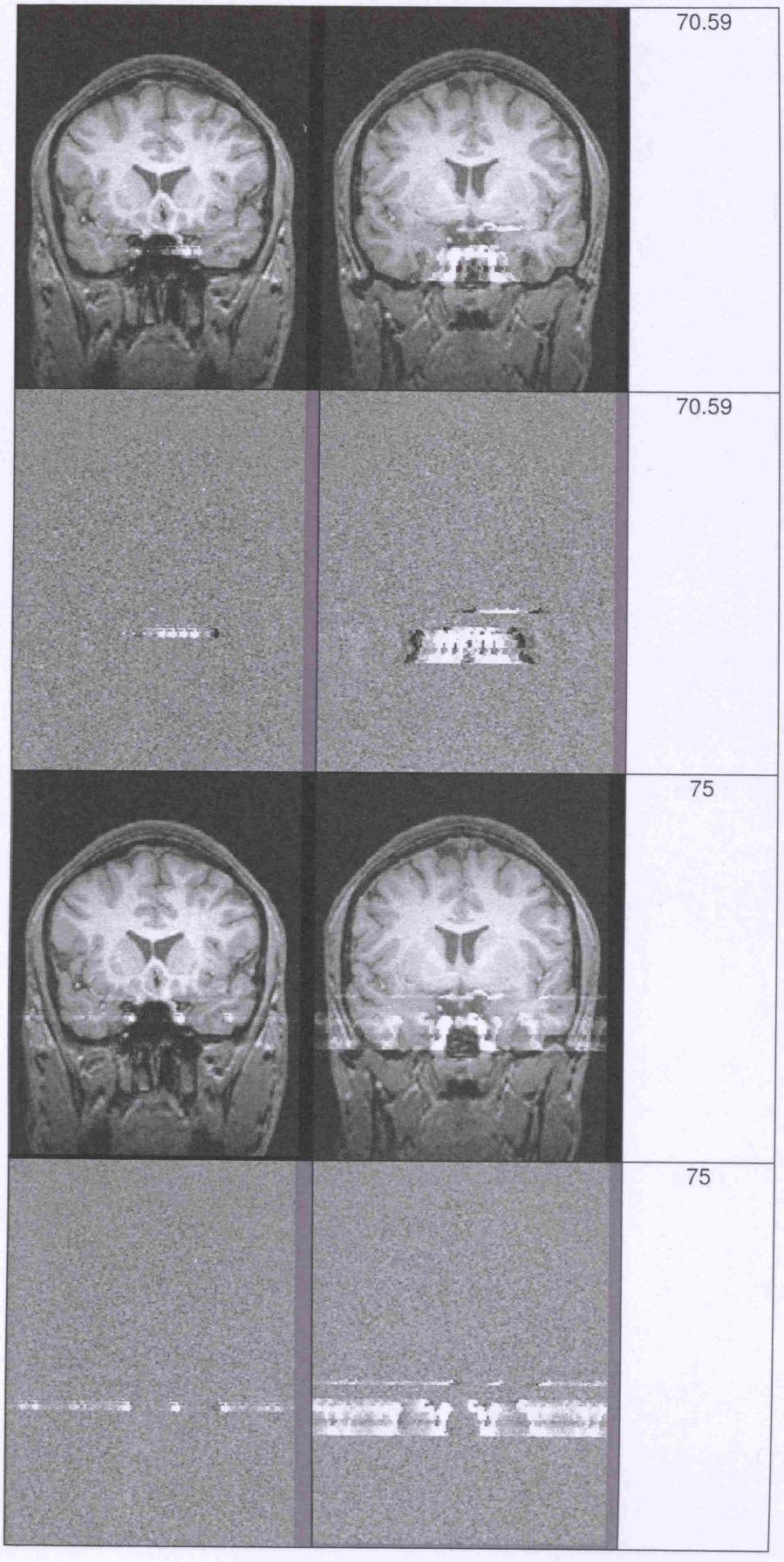
70.59
70.59
75
75

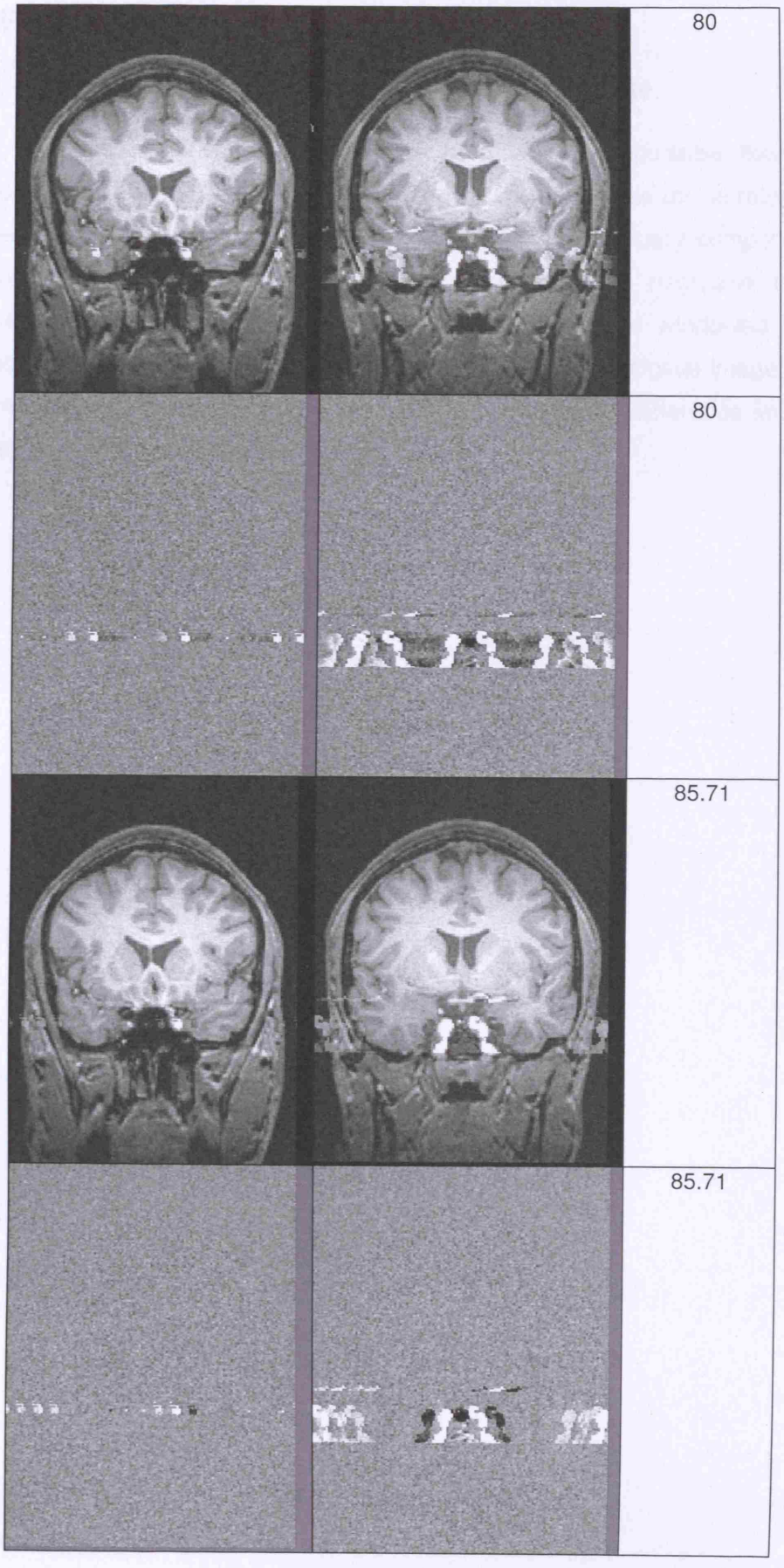
80
80
85.71
85.71

8.4.2 Pulsatile flow artefact correction

8.4.2.1 Correction of artefact simulation without noise

Figures 8-31 and 8-32 show some results from using the pulsatile flow artefact correction technique on simulated artefact without simulated noise (pulse rate 60). The simulated artefact is entirely real and does not have an imaginary component. The correction of the artefact simulation without noise has a negligible imaginary component, max of +23, -23, compared to the native image windowed to 1000. Difference images were, therefore, created by subtracting the original image from the real component of the above image. The backgrounds of the difference images are plain grey as no noise has been simulated.

Figure 8-31 Simulation and correction of artefact without noise shown in two axial slices, in native and difference images. The top row shows the original images, the following pair of rows the image with artefact and the final pair of rows the image with corrected artefact

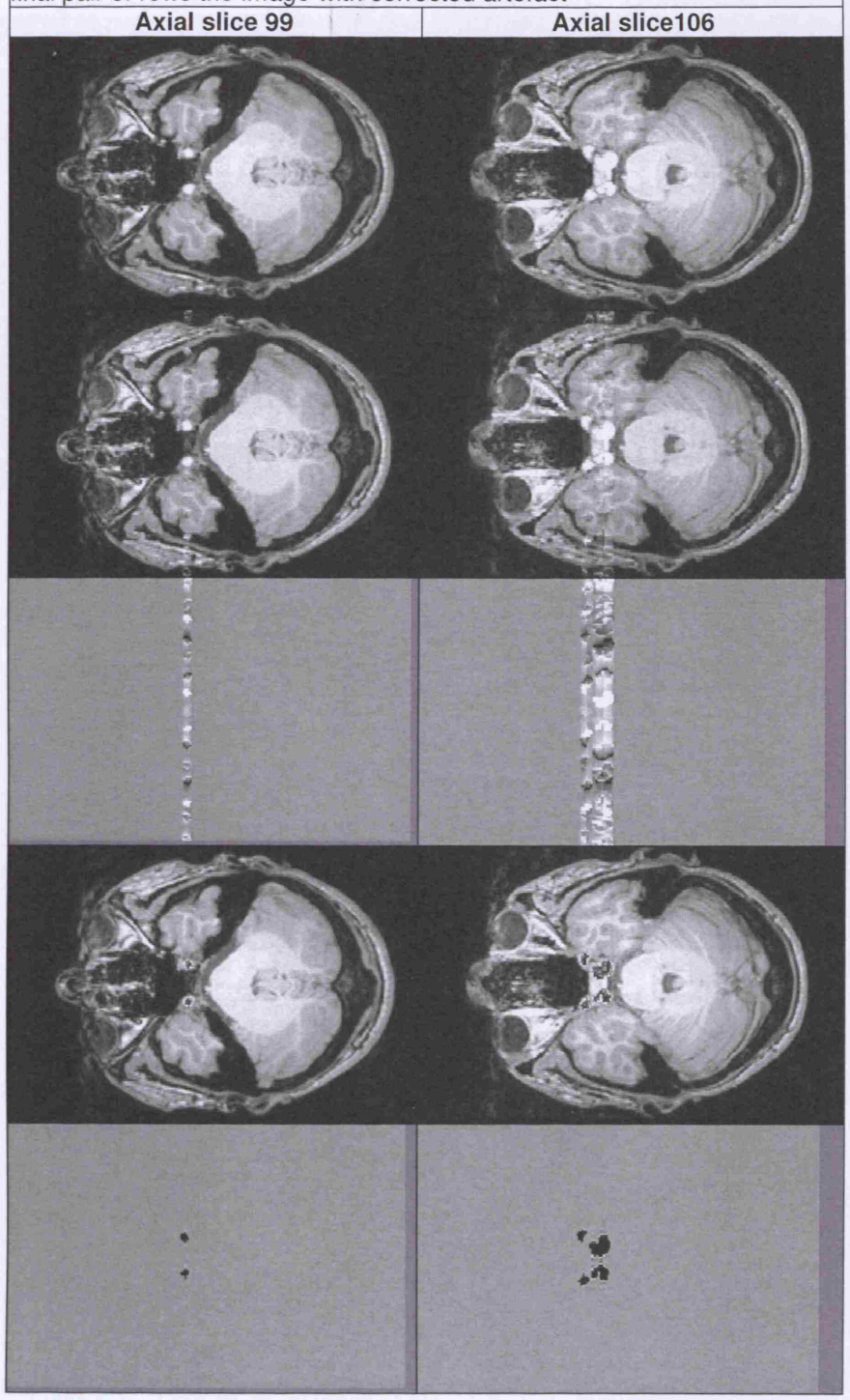

Figure 8-32 Simulation and correction of artefact without noise shown in two coronal slices, in native and difference images. First pair of rows coronal slice 118, second pair of rows coronal slice 103

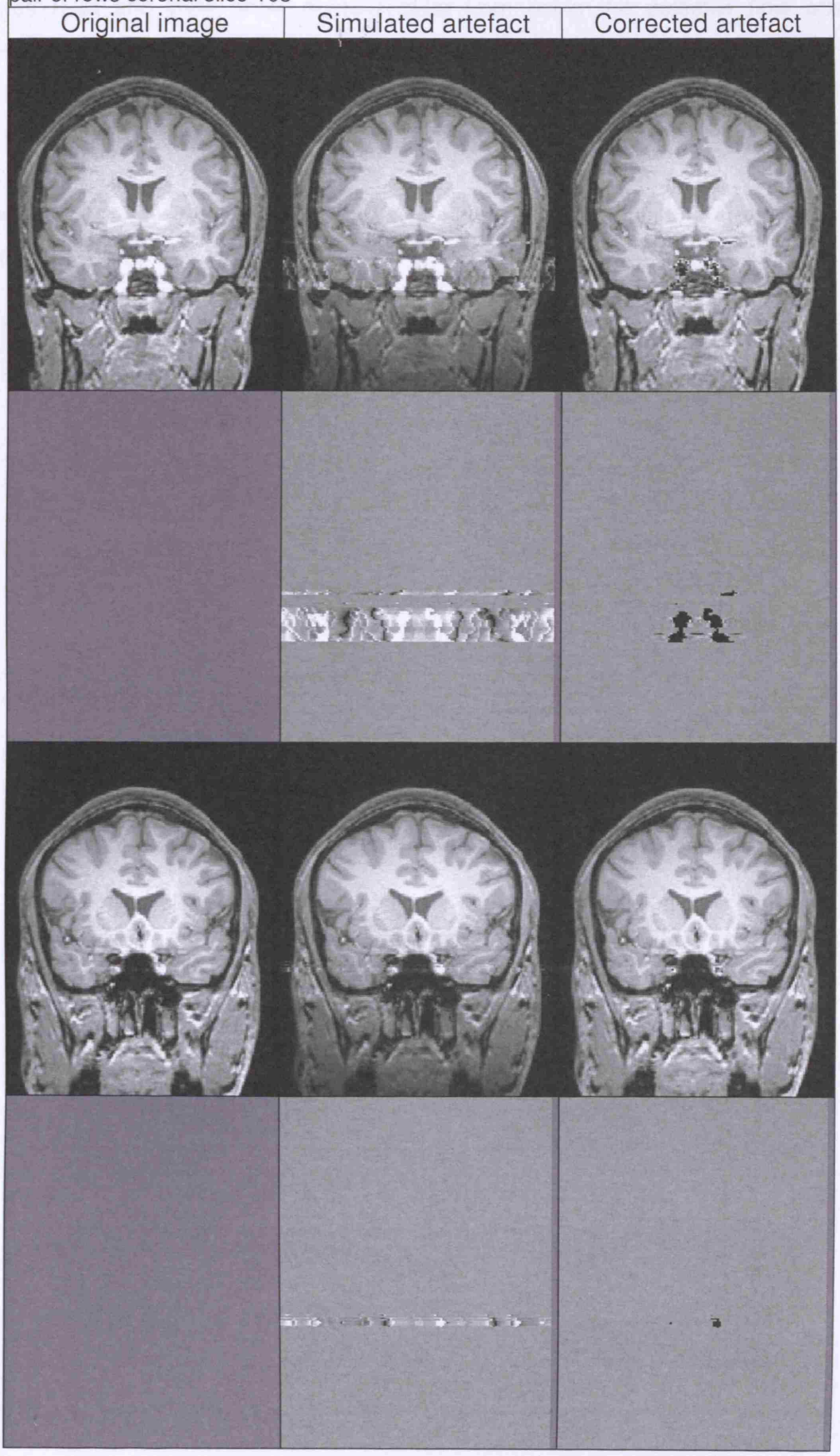

8.4.2.2 Correction of artefact simulation with noise

Figures 8-33 and 8-34 show some results from using the pulsatile flow artefact correction technique on simulated artefact (pulse rate 60) with various levels of simulated noise. The simulated noise had a real and an imaginary component. In these figures I show the real and imaginary components of the difference images. I do this because the errors in the correction are in both components rather than in just the real component as they were for the correction on an artefact simulation without noise (see Section 8.4.2.1).

Figure 8-33 Coronal images showing the correction of artefact simulations, each simulated with the same artefact and increasing levels of noise.

Noise level	Coronal slice 103	Coronal slice 118
Original image		
2		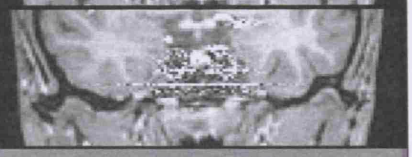
Difference image: real component		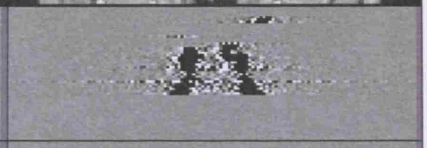
Difference image: imaginary component	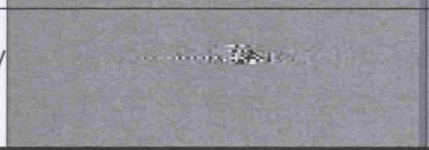	
10		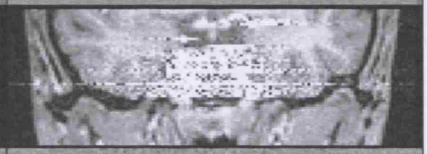
Difference image: real component		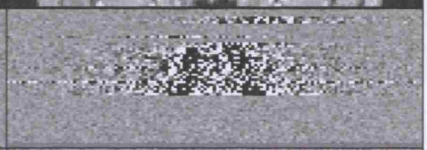
Difference image: imaginary component		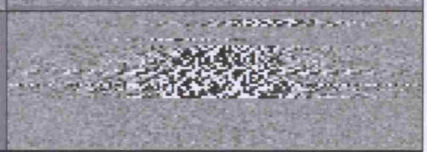
25		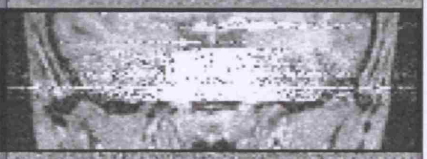
difference image: real component		
difference image: imaginary component		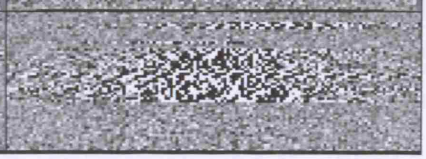

Figure 8-34 Axial images showing the correction of artefact simulations, each simulated with the same artefact and increasing levels of noise.

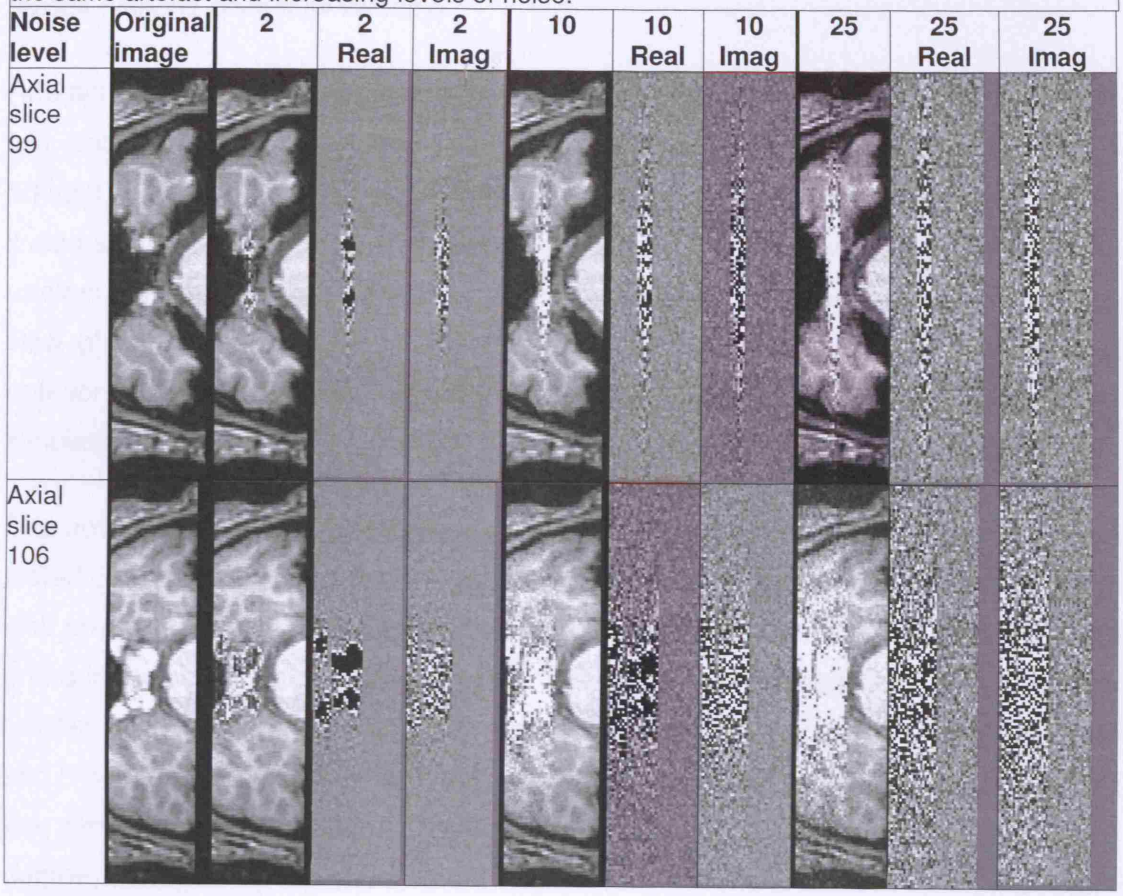

8.5 Conclusions and further work

In this chapter I have developed a novel technique to simulate pulsatile flow artefact. In the future this simulation technique could be used in conjunction with atrophy simulation techniques to determine the effects of this artefact on different atrophy quantification techniques.

In order to simulate these pulsatile flow artefacts on the cohort, the carotid artery in each of the baseline images should be segmented and the algorithm described in this chapter to simulated pulsatile flow artefact should be applied. The technique models the timing of the velocity profile of the carotid relative to the scanner acquisition parameters (modelled on a sagittal TFE sequence). This timing model can be adjusted with one parameter to simulate different pulse rates, (as demonstrated in Figures 8-29 and 8-30). The timing model determines the value of an additional intensity factor for the segmented carotid artery at each time-point where the centre of a plane of k-space is modelled as being acquired. This scaling of this factor can be modified to simulate

different levels of intensity of pulsatile flow artefact which can reflect different strengths pulses (varying peak flow velocity).

Artefact is simulated for each of six views representing the six elements of an array coil, and then summed together using the sum of squares method. The pulsatile flow artefact simulation is similar in principle to that of the slow drift motion simulation in that it also assumes every plane of k-space comes from a different image, to comprise the artefact corrupted images k-space. As the pulsatile flow artefact only spreads in the slow phase encode direction, only the volume of the image in the head foot and anterior posterior direction containing the segmented carotid artery is used for simulating the artefact.

The novel technique to remove flow artefacts in 3D structural head images has been tested on simulated artefacts (shown in Figures 8-31 to 8-34). The correction works well on the image with artefact but without added noise simulated. There are slight errors in the voxels close to the carotid arteries which can be seen also in Figure 8-22. Further work is needed to more fully understand why this is occurring. In Figures 8-33 and 8-34 it can be seen that as the level of noise simulated on the image is increased the performance of the correction algorithm decreases. This is expected to some degree, however, the algorithm needs further work to increase its robustness to noise. In this proof of concept study, I have only used information from two coils to correct the artefact. In the presence of noise using data from all 6 coil elements would be beneficial. Using more iterations of the LSQR algorithm, and using side voxel correction, similar to the correction shown in Figure 8-23, might also improve the robustness of the algorithm.

Other suggestions for improving this work include incorporating the Fourier transform into the A matrix to obtain directly p instead of P. The method I have proposed is expandable to different pulse sequences for example where more than one plane is acquired within one TR. This would mean that you need less points in time (for two lines per shot you would need to define only one p(t) every other time point). The sampling of the k-t matrix would be a stair pattern.

The simulation and correction methods described in this chapter could also potentially be used to model eye ball motion artefact which can decrease image quality in longitudinal trial images when the slow phase encode direction is Anterior - Posterior.

8.6 Examples of acquired pulsatile flow artefacts for comparison with simulated artefacts

No two acquired flow artefacts appear the same as they are a function of the vessel shape, the carotid pulse, the scanner sequence timing, and the timings relative to each other. Figure 8-35 shows a selection of acquired and simulated artefacts for comparison. The acquired difference images show non-brain misregistration artefacts which are not present in the simulated images.

Figure 8-35 Examples of acquired pulsatile flow artefacts for comparison with simulated artefacts. Comparisons are made across a pair of rows. The top row shows an acquired artefact and the lower row of the pair shows the simulated artefact which is the best comparison. Acquired images are from the historical trial referred to in Chapter 5. The left column contains acquired images with less apparent flow artefact and images without simulated artefact. The right row exhibits acquired images with more severe flow artefacts, and simulated artefacts. The central column contains difference images which are created with the images from either side.

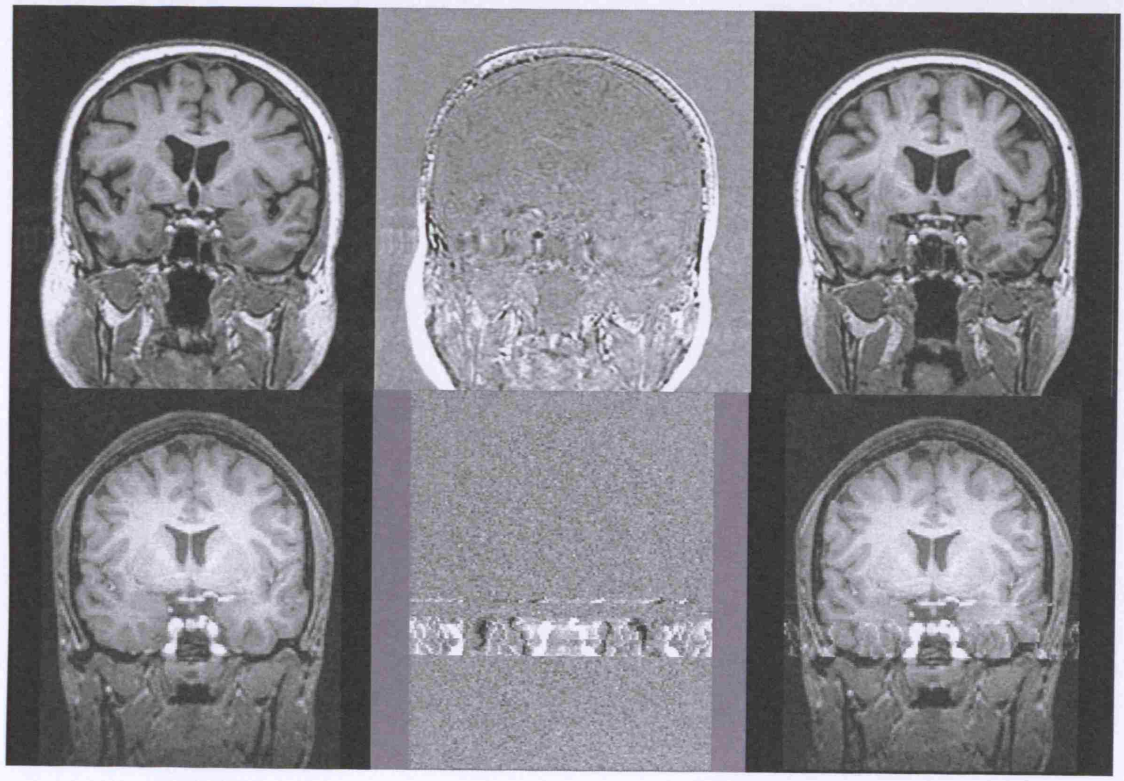

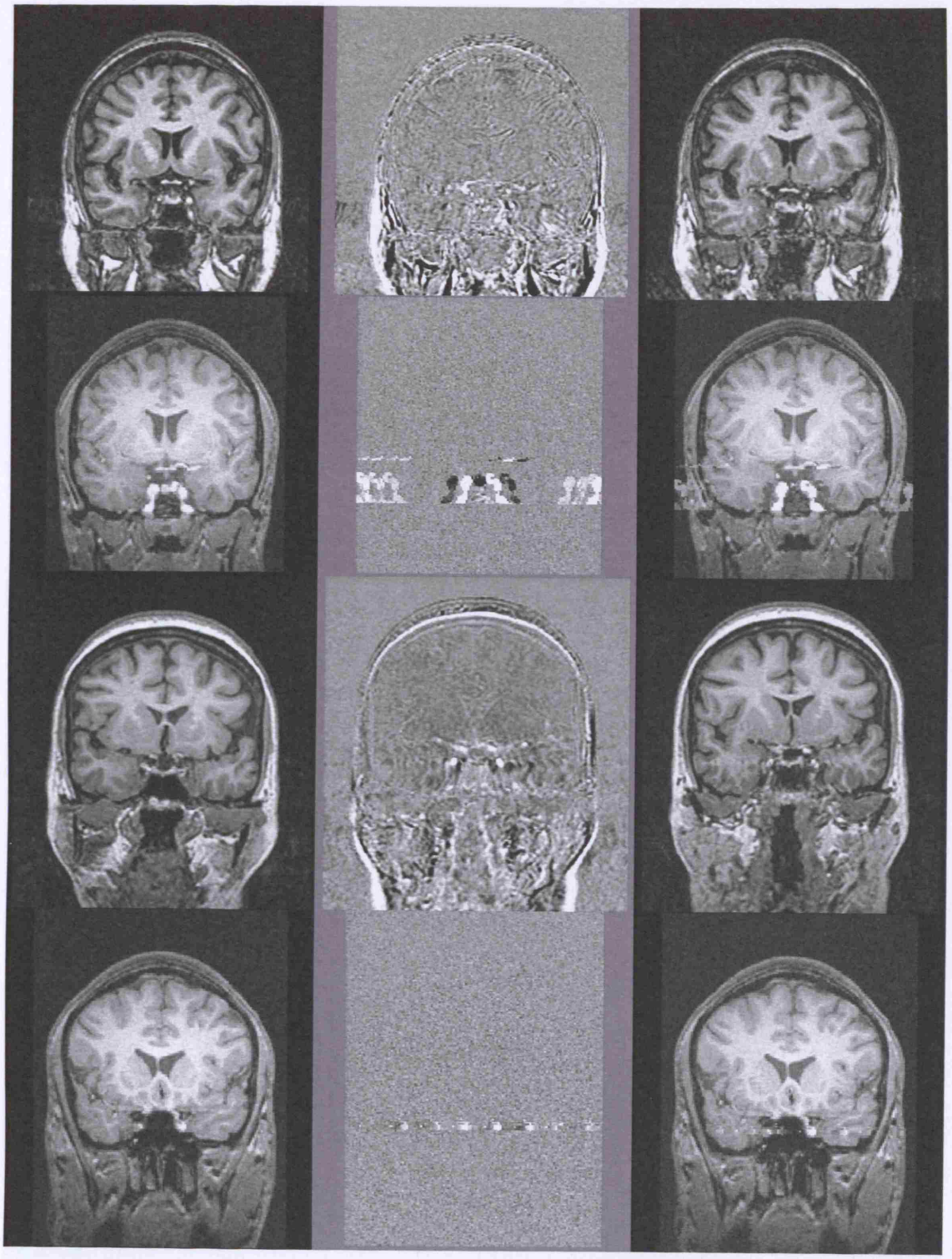

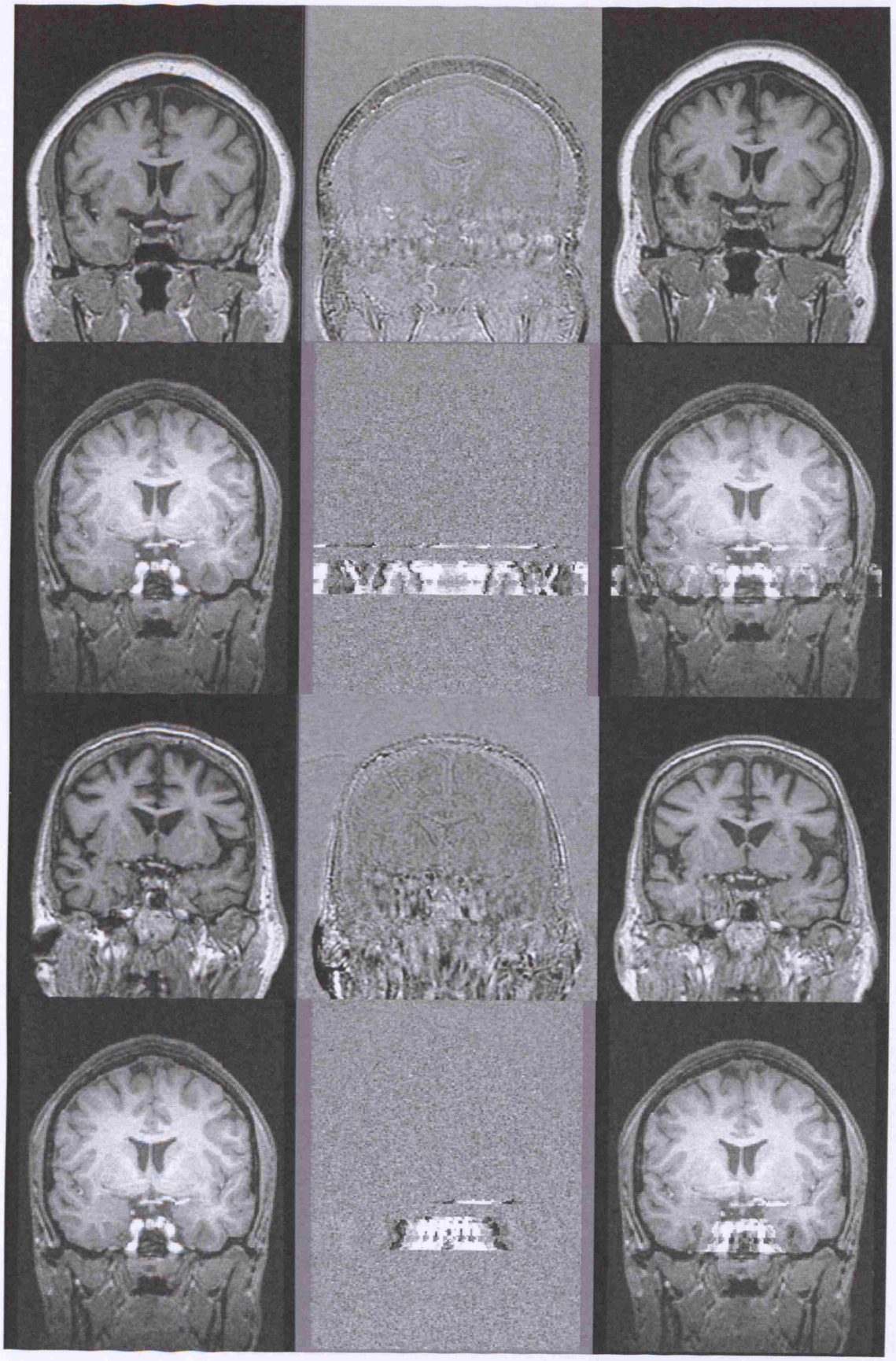

9 Conclusions

9.1 Summary of findings
9.2 Clinical Impact
9.3 Future work
9.4 Overall Summary

9.1 Summary of findings

Chapters 1 to 3 provide the introduction and background information relevant to the rest of this thesis. The following five chapters, 4 to 8, record the key methods and results of my work. In this section I will summarise the contribution of each of these chapters.

9.1.1 Chapter 4 - Artefacts in longitudinal images at different field strengths

This chapter illustrates the increase in severity of flow artefacts in images from clinical trials acquired on scanners with a magnetic field strength of 3T, whose acquisition protocols have been moved from scanners with a magnetic field strength of 1.5T without considering the issues of change in relative artefact levels.

The aims of the chapter were:

- To compare both quantitatively and qualitatively the extent of flow artefacts in both 1.5T and 3T scans acquired using a typical 3D MP-RAGE sequence, in order to assess the likely consequences of moving longitudinal imaging studies to 3T scanners.
- To develop a novel image processing technique to quantitatively compare relative artefact levels between longitudinal scans carried out at different field strengths.

To achieve these aims:

- An image intensity based artefact quantification technique was devised to quantify the comparative difference in severity of this artefact at the two field strengths. (This technique is developed further in Chapter 5)
- Using this technique it was shown that, on average, the level of this artefact more than doubled at 3T compared to 1.5T.

- Using a qualitative ranking method I devised we have also shown a visibly detectable difference between artefacts at these field strengths.

Although moving longitudinal neuroimaging trails to higher field scanners can provide higher signal to noise ratios the problem of artefacts is not eliminated but increased. Therefore as longitudinal neuroimaging trials in dementia are moving towards using 3T scanners more frequently, the elimination, or management of artefacts must be considered during the set up of these trials. The optimization of the pulse sequence protocols, the use of saturation pulses, the set up of quality control (QC) protocols, and image analysis should all be performed with the issues of artefacts in mind.

9.1.2 Chapter 5 - Prevalence and automatic quantification of artefacts affecting longitudinal neuroimaging studies

This chapter adds to the literature a more complete understanding of the prevalence of different types of artefacts which affect longitudinal neuroimaging trials. This enables future trials to prioritise the issues they consider when optimising their scanning acquisition parameters and protocols. I provide those designing MR neuro-imaging trial QC procedures with a better understanding of the most severe and the most common problems which need detecting. Also I contribute novel tools for automatically detecting and quantifying artefacts in scan pairs. These tools could form part of an automatic QC system for use in longitudinal clinical trials.

The aims of this chapter were:

- To assess the frequency of occurrence of different types of artefacts in historical and current clinical trails of dementia at 1.5T.
- To investigate the prevalence of artefacts in scans rejected from analysis, and in those accepted into analysis.
- To determine the main types of temporal lobe artefacts
- To propose a tool to automatically quantify the severity of the most common of these from longitudinal pairs of images.

To achieve these aims:

- I assessed the frequency of occurrence of different types of artefacts by investigating the quality assurance records of scans from a large number of volunteers (837) involved in historical and current clinical dementia trials at 1.5T.

- The prevalence of artefacts in scans rejected from analysis and in those accepted into analysis was also investigated.
- I have shown that temporal lobe artefact, motion and problems with image contrasts are the three most commonly occurring artefact in the two trials investigated
- The main cause of temporal lobe artefact was determined to be pulsatile flow artefact. The next most frequent causes are motion and susceptibility artefacts
- A tool to automatically quantify this pulsatile flow artefact was designed and tested. An automatic tool was also proposed to quantify motion artefact.

Quantifying artefact with automated QC systems and reducing the frequency of artefacts in longitudinal MRI trials could improve their precision, reducing the number of subjects needed to power the study, and therefore reduce the cost of MRI trials.

Quantifying artefact also has other application other than QC systems. These include acting as cost functions in artefact correction algorithms, and providing adjustments or levels of confidence for automated measures, such as local atrophy quantification techniques.

9.1.3 Chapter 6 - Simulation of a database of longitudinal MR head images with known atrophy and acquisition artefacts

The contribution of this chapter is the generation of atrophy and artefact simulations to provide a gold standard database on which to test different image analysis tools.

The aim of this chapter was:

- To generate a cohort of longitudinal MR brain images with known levels of simulated atrophy and motion artefact of different types, to provide a gold standard database on which to test different atrophy quantification techniques

To achieve this aim:

- I have designed techniques to simulate three types of rotational motion using the concept of kt space. These types of motion are a single step motion, a periodic step motion and a slow continuous drift.

- A cohort of longitudinal MR brain images was generated with known levels of simulated atrophy and motion artefact of different types. Figures demonstrating these simulations are presented in the chapter.

I have proposed the novel technique of combining artefact and atrophy simulation to provide a gold standard database. This can be effectively used to test the robustness of atrophy quantification techniques to artefact. Various artefact simulations could be used, such as the flow artefact simulation developed in Chapter 9, or eye ball motion artefacts. Simulating these localised artefacts to create a gold standard database could be used to test the robustness of local measures of atrophy.

9.1.4 Chapter 7 - Robustness assessment of global atrophy quantification techniques with a gold standard of atrophy and artefact simulated images

This chapter adds to the literature a more complete understanding of the effects of motion artefacts of global atrophy quantification techniques. It also provides a methodology for assessing the effects of different types and severities of artefacts on whole and local brain atrophy quantification tools.

The aim of this chapter was:

- To compare the robustness to artefacts of two different atrophy quantification techniques using the generated gold standard cohort with simulated atrophy and artefacts described in the previous chapter, as the evaluation cohort.

To achieve this aim:

- The widely used atrophy quantification techniques SIENA and BSI were selected as the two whole brain atrophy quantification techniques. These atrophy techniques were used to quantify atrophy between an unaltered baseline image and a follow up scan, generated from the baseline image with simulated artefact, and with and without simulated atrophy.

The results for the two techniques are as follows:

Results for SIENA, where follow up scan has no simulated atrophy

- Without motion artefact SIENA had a measurement error of under 0.2% as quoted by its creators.

- The presence of rotational motion of even 1 degree could cause the SIENA algorithm to measure atrophy when none had occurred.
- Rotational motions larger than 2 degrees can cause measurement errors of the same order as the expected difference in whole brain volume change between AD and normal ageing over a 12 month period (around 1.5%).
- Motion artefact could result in false positives for cases where no atrophy has occurred.

Results for SIENA, where follow up scan has simulated brain atrophy

- Even without motion artefact SIENA slightly underestimates atrophy of this magnitude (1% brain volume change error).
- Increase in motion artefact has very slightly different effects depending on the type of motion.
- The maximum brain volume change error is never much greater than 2%, for a 5% brain volume change atrophy, leaving the result always correctly read as atrophy.
- SIENA is fairly robust to motion artefact in correctly reading atrophy, and not providing false negatives when the motion artefact corrupts the second scan.

Results for BSI

- BSI always underestimates atrophy. It does so with increasing levels of variability as the motion artefacts increase.
- As motion artefact increases on images without simulated atrophy this appears as actual growth, this will mean that false positives brain atrophy is never reported due to motion artefact in the second scan.
- For the follow up scan with brain atrophy this usually results in the atrophy being progressively underestimated, with extreme periodic step motion appearing as slight growth, meaning that false negative maybe a problem due to motion artefact.
- False negative due to motion maybe a substantial problem as motion is more likely to occur with AD symptoms, which will get worse with progression of time, so this is likely to obscure the difference of rate of brain volume change between AD and normal progression.
- It has previously been shown that BSI underestimates atrophy, and my results from the follow up scans with atrophy but rotation angle of motion of zero confirm this (3% brain volume change error).

- As the BSI algorithm acts consistently, with increasing motion artefact, across both normal and simulated Alzheimer's brain change, it might be possible to quantify the level of artefact in an image and to compensate the BSI result proportionally.

The impact of motion artefacts is likely to be different with different algorithms, and especially for local atrophy measures (e.g.: from a non-rigid registration algorithm) or cortical thickness measurement methods.

The value of the approach presented in this chapter is in predicting the sensitivity of methods to motion artefact (potentially valuable in a power analysis used in the design of a clinical trial), and also in comparing the relative merits of alternative atrophy measuring algorithms in the presence of common image artefacts.

9.1.5 Chapter 8 - Novel approach to simulating and removing pulsatile flow artefact

The contribution of this chapter is firstly a novel simulation of pulsatile flow artefact arising from the carotid artery. This novel method can be used to determine the effects of pulsatile flow artefact on image analysis techniques. The second contribution of this chapter is a novel technique for the remove of these pulsatile flow artefacts in 3D brain imaging.

The aims of this chapter were:

- To develop a novel technique to simulate pulsatile flow artefact.
    - This simulation technique should have the potential to be used in conjunction with atrophy simulation techniques to determine the effects of this artefact on atrophy quantification techniques, similar to how the motion simulation was used in Chapter 7.
- To devise a novel, technique for the removal of flow artefacts from 3D structural head images
- To apply this novel removal technique to simulated data

To achieve these aims:

- A novel technique to simulate pulsatile flow artefact was developed using the idea of kt space. A model of blood flow in the carotid and the acquisition sequence timings were used to vary the intensity of the segmented carotid

artery across kt space. This space is then sampled to match the acquisition order, and the new k space containing the artefact is formed.

- I have devised a novel technique to remove flow artefact in 3D structural head images using the corresponding data from different elements of an array coil.
- I have tested this technique on simulated artefact and found it works well without noise, however, as the level of noise increases the correction algorithm's performance decreases.

In this chapter I have developed a novel technique to simulate pulsatile flow artefact. This simulation technique could be used in conjunction with atrophy simulation techniques to determine the effects of this artefact on different atrophy quantification techniques.

The simulation and correction methods described in this chapter could also potentially be used to simulate and correct eye ball motion artefact which can decrease image quality in longitudinal trial images when the slow phase encode direction is Anterior - Posterior.

9.2 Clinical impact

This thesis has raised several issues which should be considered in longitudinal dementia trials. The first is the potential of higher artefact levels at 3T causing problems to longitudinal neuroimaging trials, which already suffer from high levels of artefacts at 1.5T. In particular I highlight the need to consider pulsatile flow artefacts in the selection of the imaging parameters used. I have provided an insight into the most commonly occurring artefacts in clinical trials being temporal lobe artefact, motion artefact and contrast issues. This information should be used to reduce these acquisition artefacts, and provide automated quality checking systems with the most common artefacts which should be detected. I have also provided a technique to automatic quantify flow artefact and motion artefact from longitudinal data, which could also be useful for future automatic quality control systems to detect significant levels of artefacts in images.

The approach I have used of simulating a gold standard database of known atrophy and artefact is valuable in predicting the sensitivity of methods to artefact (potentially valuable in a power analysis used in the design of a clinical trial) and also in comparing the relative merits of alternative atrophy measuring algorithms in the presence of common image artefacts.

9.3 Future work

High quality imaging is important if new therapies for AD are to be developed and brought to market. The move to 3T imaging, while in general providing higher SNR images, has not made everything better. Acquisition artefacts are still a major concern as they have the potential to affect results. QC is therefore an essential component of any clinical imaging trail. A better understanding of the effects of different artefacts on image analysis tools is also highly desirable.

9.3.1 Implementation of an automated quality checking system

Future work could involve the design and implementation of an automated quality checking system. This would involve designing novel algorithms to quantify different types of artefacts and determining threshold levels above which images are rejected from analysis as they significantly distort the atrophy quantification results. The flow artefact quantification technique proposed in this thesis could be one of these algorithms. To improve this algorithm a fast non-rigid registration technique could be used to place the region of interest more accurately across subjects.

The motion quantification technique proposed in this thesis needs further testing. At present it measures the noise between scan pairs, which does correlate with motion but also with many other artefacts. If the aim is to flag poor quality image in a QC system this ambiguity is not a problem. However if the aim is to specifically quantify just motion artefact when other artefacts may be present, work would be needed to detect more specific attributes of motion, such as the lines produced by repetitions of the skull outline across the brain.

Algorithms to quantify other artefacts could include assessing any difference in gross contrast between the two scans, and local artefacts such as eye motion artefact. Such an automated QC system should also be able to verify that the correct subject, sequence and scanner were used, by verifying the acquired image header against the expected data. The results from such an automated system should be compared to the results obtained on the same data using visual QC.

9.3.2 Effect of artefacts on atrophy measurement techniques

In this thesis I investigated the effect of motion artefact of whole brain atrophy measurement techniques BSI and SIENA. Further work could be performed, investigating the effect of motion on the semi automated segmentation tool used in BSI,

and on BET (the segmentation tool used in SIENA), and the effect of motion on the separate stages of the algorithms such as the registration and the final quantification step.

There is scope for future work investigating how artefacts including localised ones, such as the pulsatile blood flow artefact or eye ball motion artefact, affect various local atrophy measures. The effect of artefacts on many other image processing techniques should also be assessed in future. These should include the use of non-rigid registration deformation fields between two serial images and post-processing artefact correction techniques incorporated into atrophy measurement methods. In particular the issue of any link between increased motion of the follow up scan and changes in atrophy measurements is important as motion often increases with disease severity and this should be accounted for if it is biasing results.

9.3.3 Improving image quality obtained from the scanners

Improvements to image quality obtained from scanners could be made in several ways. The first of these is post processing software could be installed on the scanners by the manufacturers to correct artefact. An example of this is the pulsatile flow removal technique I proposed. This removal technique needs further testing to correct acquired images with flow artefacts. First the technique needs to be made more robust to noise. For example using the data from all six coil elements, rather than just two would be likely to improve this. Using the side voxel correction technique might also improve the robustness of the correction algorithm. The method would also benefit from further work so that it could switch between different k-space acquisitions, for example when more than one plane is acquired within one TR. Another similar correction method based on the same technique could also potentially be used to remove eye ball motion artefact which can decrease image quality in longitudinal trial images when the slow phase encode direction is Anterior - Posterior. Other motion correction and susceptibility correction techniques could also be incorporated.

A second way to improve image quality obtained in scanners is to improve the hardware used. For example safe, comfortable head holding devises which are easy for the subject to escape from if they so choose, but help hold their head still if they are compliant would decrease one of the most common artefacts, that of bulk head motion.

Different artefacts, such as pulsatile flow artefact and bright artefact from the meninges or skull overlaying the brain, seem to be more prominent on scanners from certain

manufacturers. It would be helpful for setting up and running future clinical imaging trials if it was known which scanners tended to exhibit which artefacts.

To also improve the quality of images obtained in clinical trials it is imperative that the radiographers acquiring the images understand the importance and definition of high quality images. Different methods of training could be investigated to see which is most effective.

9.4 Overall summary

This thesis has met its initial aims to investigate artefacts in longitudinal MRI of the brain. The effect on artefacts of moving from a 1.5T to 3T scanner was found to be significant. Techniques for quantifying artefacts were developed. The frequency of occurrence of different types of artefacts in clinical dementia trials at 1.5T was assessed. Temporal lobe artefact, motion and contrast issues were found to be the most common. The main cause of artefact occurring in the temporal lobe in dementia trials was determined to be pulsatile flow artefact. Techniques to simulate different types of motion and pulsatile flow artefacts were developed. The robustness to artefact of two whole brain atrophy measurement techniques commonly used in clinical trials was tested, by creating a gold standard database with known levels of simulated atrophy and artefact. The results of both techniques were substantially affected by motion artefacts to such an extent that the difference between diseased and normal ageing rates could be obscured. SIENA was affected slightly less than BSI but the BSI failed in a more consistent way, so that if an accurate measure of motion could be made this result could potentially be corrected. Finally, a novel algorithm was developed to remove flow artefact and tested it on simulated data. This thesis has impact for those running clinical dementia trials and has suggested future work to further this impact.

References:

Anderson V, Fernando K, Davies G, Rashid W, Frost C, Fox N, Miller D. Cerebral Atrophy Measurement in Clinically Isolated Syndromes and Relapsing Remitting Multiple Sclerosis: A Comparison of Registration-Based Methods. Journal of Neuroimaging 17 (1): 61-68, 2007.

Atkinson D, Hill DL, Stoyle PN, Summers PE, Clare S, Bowtell R, Keevil SF. Automatic compensation of motion artefacts in MRI. Magnetic Resonance Medicine 41: 163-70, 1999.

Atkinson D, Larkman DJ, Batchelor PG, Hill DL, Hajnal JV. Coil-based artefact reduction. Magn Reson Med. 52(4):825-30, 2004.

Barra V, Frenoux E, Boire Jy. Automatic volumetric measurement of lateral ventricles on magnetic resonance images with correction of partial volume effects. J Magn Reson Imaging, 15(1):16:22, 2002.

Bernstein MA, Huston J, Lin C, Gibbs GF, Felmlee JP, High-resolution intracranial and cervical MRA at 3.0T: Technical considerations and initial experience Magnetic Resonance in Medicine 46(5):955-962, 2001.

Blumenthal JD, Zijdenbos Al, Molloy E, Giedd JN. Motion artefact in magnetic resonance imaging: implications for automated analysis. Neuroimage. 16(1): 89–92, 2002.

Bogerts B, Ashtari M, Degreef G, Alvir JM, Bilder RM, Lieberman JA. Reduced temporal limbic structure volumes on magnetic resonance images in first episode schizophrenia. Psychiatry Res. 35(1):1-13, 1990

Boyes RG, Rueckert D, Aljabar P, Whitwell J, Schott JM, Hill DLG, Fox NC. Cerebral atrophy measurements using Jacobian integration: Comparison with the boundary shift integral. NeuroImage 32(1):159-169, 2006

Braak H, Braak E. Neuropathological staging of Alzheimer's-related changes. Acta Neuropathol. 82:239-259, 1991.

Bradely WG, Waluch V. Blood flow: Magnetic Resonance Imaging. Radiology. 154:443-50, 1985.

Bremner JD, Narayan M, Anderson ER, Staib LH, Miller HL, Charney DS. Hippocampal volume reduction in major depression. American Journal of Psychiatry. 157(1):115-7, 2000.

Buxton RB, Kerber CW, Frank LR. Pulsatile flow artefacts in two-dimensional time-of-flight MR angiography: initial studies in elastic models of human carotid arteries. J Magn Reson Imaging. 3(4): 625-36, 1993.

Bydder M, Larkman DJ, Hajnal JV. Detection and elimination of motion artefacts by regeneration of k-space. Magn Reson Med. 47:677–686, 2002.

Bydder M, Atkinson D, Larkman DJ, Hill DL, Hajnal JV. SMASH navigators. Magn Reson Med. 49:493–500, 2003.

Camara O, Schweiger M, Scahill RI, Crum WR, Sneller BI, Schnabel JA, Ridgway GR, Cash DM, Hill DLG, Fox NC. Phenomenological model of diffuse global and regional atrophy using Finite-Element methods. IEEE Transactions on Medical Imaging. 2006

Camara O, Scahill R, Schnabel J, Crum W, Ridgway G, Hill D, Fox N. Accuracy assessment of global and local atrophy measurement techniques with realistic simulated longitudinal data. MICCAI. In Press. 2007.

Cendes F, Andermann F, Gloor P, Evans A. MRI volumetric measurement of amygdala and hippocampus in temporal lobe epilepsy. Neurology. 43(4):719, 1993.

Chan D, Janssen J, Whitwell J, Watt H, Jenkins R, Frost C, Rossor M, Fox N. Change in rates of cerebral atrophy over time in early-onset Alzheimer's disease: longitudinal MRI study. The Lancet 362(9390):1121-22, 2003.

Clarys JP, Martin AD, Marfell-Jones MJ, Janssens V, Caboor D, Drinkwater DT. Human Body Composition: A review of adult dissection data. American Journal of Human Biology 11:167-174, 1999.

Cohen MS, DuBois RM, Zeineh MM. Rapid and Effective Correction of RF Inhomogeneity for High Field Magnetic Resonance Imaging. Human Brain Mapping 10: 204-211, 2000.

Collins DL, Evans AC. ANIMAL: Validation and applications of nonlinear registration-based segmentation. International Journal of Pattern Recognition and Artificial Intelligence. 11(8):1271-94, 1997.

Collins DL, Zijdenbos AP, Baare WF, Evans AC. ANIMAL + INSECT: Improved cortical structure segmentation. Proceedings of the 16th International Conference on Information Processing in Medical Imageing. 210-23, 1999.

Crooks LE, Arakawa M, Hoenninger J, McCarten B, Watts J, Kaufman LRadiology. Magnetic resonance imaging: effects of magnetic field strength. 151(1):127-33, 1984.

Davatzikos C, Genc A, Xu D, Resnick S. Voxel-based Morphometry using the RAVENS maps: methods and validation using simulated longitudinal atrophy. Neuroimage 14: 1361–9, 2001.

De Leon MJ, Convit A, George AE, Golomb J, De Santi S, Tarshish C, Rusinek H, Bobinski M, Ince C, Miller D. In vivo structural studies of the hippocampus in normal ageing and in incipient Alzheimer's disease. Annals of the new york academy of sciences, 777:1-13,1996.

Deichmann R, Good CD, Josephs), Ashburner J, Turner R. Optimization of 3D MP-RAGE sequences for structural brain imaging. Neuroimage. 12(1):112-127, 2000.

Deichmann R, Schwarzbauer C, Turner R. Optimisation of the 3D MDEFT sequence for anatomical brain imaging: technical implications at 1.5 and 3 T. Neuroimage 21 (2), 757-767, 2004.

Ehman R Influence of Physiologic Motion on the appearance of tissue in mri. Radiology, 159:777-82, 1986.

Farahani K, Sinha U, Sinha S, Chiu LC, Lufkin RB. Effect of field strength on susceptibility artefacts in magnetic resonance imaging. Comput Med Imaging Graph. 14 (6), 409-13, 1990.

Felmlee JP, Ehman RL.spatial prestauration: a method for suppressing flow artefacts and improving depiction of vascular artefacts and improving depiction of vascular anatomy in MRI. Radiology. 164:559-64, 1987.

Firbank MJ, Coulthard A, Harrison RM, Williams ED. A comparison of two methods for measuring the signal to noise ratio on MR images. Phys Med Biol. 44 (12), 261-264, 1999.